



HAL
open science

Non-Gaussian states and measurements for quantum information

Olivier Morin

► **To cite this version:**

Olivier Morin. Non-Gaussian states and measurements for quantum information. Quantum Physics [quant-ph]. Université Pierre et Marie Curie - Paris VI, 2013. English. NNT : . tel-01066655v2

HAL Id: tel-01066655

<https://theses.hal.science/tel-01066655v2>

Submitted on 15 Dec 2014

HAL is a multi-disciplinary open access archive for the deposit and dissemination of scientific research documents, whether they are published or not. The documents may come from teaching and research institutions in France or abroad, or from public or private research centers.

L'archive ouverte pluridisciplinaire **HAL**, est destinée au dépôt et à la diffusion de documents scientifiques de niveau recherche, publiés ou non, émanant des établissements d'enseignement et de recherche français ou étrangers, des laboratoires publics ou privés.



Non-Gaussian States and Measurements for Quantum Information

Présenté par :
Olivier MORIN

pour obtenir le grade de docteur de l'Université Pierre et Marie Curie
Spécialité : **Physique Quantique**

Mardi 10 Décembre, 2013

M. Marco BELLINI	<i>Rapporteur</i>
M. Nicolas CERF	<i>Examineur</i>
M. Claude FABRE	<i>Membre invité</i>
M. Philippe GRANGIER	<i>Examineur</i>
M. Julien LAURAT	<i>Directeur de thèse</i>
M. Gerd LEUCHS	<i>Rapporteur</i>
Mme. Agnès MAÎTRE	<i>Président du jury</i>

Résumé

Dans ce travail de thèse nous nous sommes intéressés à une catégorie spécifique d'états quantiques de la lumière : les états non-gaussiens. Ces états ont la particularité de présenter des fonctions de Wigner à valeurs négatives. Cette propriété est indispensable pour réaliser des opérations de calcul quantique mais trouve aussi des applications variées en communication quantique ou métrologie par exemple.

Différentes stratégies peuvent être utilisées pour générer de tels états. Ici, les ressources initiales sont des états dit gaussiens produits par des oscillateurs paramétriques optiques en régime continu (i.e. vide comprimé bi-mode et mono-mode). Le caractère non-gaussien ne peut être obtenu que par des phénomènes non-linéaires (hamiltonien sur-quadratique). Dans notre cas, la non-linéarité est induite par des mesures basées sur le comptage de photon (aussi appelées mesures non-gaussiennes).

Cette étude est principalement divisée en deux parties. Tout d'abord, la génération d'états non-classiques correspondants à deux types d'encodages de qubits : le photon unique, utilisé en information quantique dite à variables discrètes, et la superposition d'états cohérents (chat de Schrödinger optique), utilisée en information quantique dite à variables continues. Ces états ont ensuite été utilisés pour mettre en œuvre deux protocoles d'information quantique. Le premier porte sur un témoin d'intrication en photon unique, l'autre sur la génération d'intrication entre deux types d'encodages (aussi appelée intrication hybride).

Mots clés

optique quantique; information quantique; photon unique; chat de Schrödinger; intrication hybride; tomographie quantique

Abstract

In the present PhD work, we focus on a specific class of quantum states of light: the non-Gaussian states. These states have the particularity of exhibiting Wigner functions with some negative values. This quantum feature is a necessary condition to perform some quantum computation task; furthermore it is also useful for various other applications, including quantum communication and metrology.

Different strategies can be used to generate these states. Here, we start from Gaussian states produced by optical parametric oscillators in the continuous wave regime, (i.e. single-mode and two-mode squeezed vacuum states). The non-Gaussian feature can only be obtained by non-linear phenomena (over-quadratic Hamiltonian). In our case, the non-linearity is induced by photon-counting-based measurements (also called non-Gaussian measurements).

This study is mainly divided into two parts. First, the generation of non-classical states associated with two types of qubit encoding: the single-photon state, used for quantum information with discrete variables, and the coherent state superposition (the so-called optical Schrödinger cat state), used for quantum information with continuous variables. These two states have then been used to perform some quantum information protocols. The first one addresses the problem of single-photon entanglement witness, and the other the generation of entanglement between the two encodings (also called hybrid entanglement).

Keywords

quantum optics; quantum information; single photon; Schrödinger's cat; hybrid entanglement; quantum tomography

Remerciements

Je voudrais tout d'abord commencer par la fin en remerciant ceux qui ont validé l'aboutissement de ces travaux de thèse, à savoir, l'ensemble des membres du jury: les deux rapporteurs *vielen Dank* Gerd Leuchs, *grazie mille* Marco Bellini, les deux examinateurs Philippe Grangier et Nicolas Cerf ainsi que la présidente de ce jury Agnès Maître. Je sais au combien ils sont occupés et sollicités, merci de m'avoir consacré un peu de votre temps.

Une thèse c'est trois ans (voir plus si affinité...), cependant un bon environnement de travail est une condition nécessaire (voir suffisante) pour obtenir des résultats. Une manip' ne marchant jamais du premier coup, il est essentiel d'être entouré de personnes compétentes et enthousiastes malgré l'adversité. C'est grâce à cela que l'on peut garder le moral, persévérer et finalement surmonter chacun des obstacles que l'on peut rencontrer. Je tiens donc à remercier mes deux encadrants qui y sont évidemment pour beaucoup dans tout ce travail chacun à leur façon. Merci à Claude pour ton expérience, ta constante rigueur mais aussi ton inébranlable bonne humeur. Merci à Julien pour m'avoir laissé tant de liberté dans l'organisation de mon travail, pour tout ce que j'ai pu apprendre à ton contact et enfin pour ta confiance. Je ne pouvais pas espérer un meilleur *matching*.

Bien que de taille modeste en comparaison d'autres expériences d'optique quantique, le dispositif sur lequel j'ai travaillé ne s'est pas fait en un jour, il est le résultat de la contribution de nombreuses personnes (stagiaires, thésards et postdocs), perfectionnant toujours un peu plus chaque élément, permettant d'aller toujours un peu plus loin et ainsi de *comprendre* toujours mieux les choses... Je remercie donc, à peu près dans l'ordre d'apparition, les différentes personnes qui ont contribué à cette expérience: Julien, Gaëlle, Taoufik, Virginia, Robert-Christopher, (moi ;-), Samuele, Marceau, Felipe, Jianli, Kun et Hanna. Je souhaite bonne chance aux deux derniers actuellement en poste.

Je dois avouer que mon enthousiasme à écrire ces lignes commence à diminuer, car quand j'y pense, j'ai côtoyé beaucoup de personnes pendant ces quelques années, et la tâche de toutes les remercier me semble finalement plus ambitieuse que ce que je pensai. Je vais donc me contenter de remerciements simples mais non moins sincères! (cette fois-ci sans ordre particulier)

Merci aux colloc' de la salle de manip Jean-François, Guillaume et Alexandre

Merci aux "*femtos*": Nicolas, Renné, Olivier, Roman, Valérian, Giulia, Clément, Shifeng, Cai Yin, Pu, Jon, Zhang, Valentin

Merci aux "*mémoires*" (qui pour des raisons historiques contient aussi les *nanofibres*): Lambert, Lucile, Michael, Adrien, Valentina, Pierre, Baptiste, Dominik, Elisabeth

Merci aux "*polaritons*" (appellation pas très exacte puisqu'elle regroupe aussi les "microcavités"): Alberto, Romain, Godefroy, Mathieu, Thomas

Je les remercie tous pour les nombreux moments partagés: échange, prêts et vols de matériels, les divers et variés Pique-niques, réunions de groupe, les discussions scientifiques ou pas, le champagne d'occasions divers, les conférences aux quatre coins du monde comme à l'autre bout de la rue...

Pour monter une expérience on a besoin de matériel et pour ça les services "techniques" sont indispensables. Merci à l'*atelier d'électronique* Brigitte et Jean-Pierre pour leur gentillesse et leur disponibilité. Merci aux "*mécanos*" Jean-Michel, Pascal, Gaël, Arnaud pour leur

bonne humeur et leur efficacité. Merci au *service administratif* Monique, Lætitia, Michel pour leur patience avec moi qui aime tant remplir des papiers... et enfin merci à la direction du labo dont son directeur Antoine Heidmann qui font que cette grande machine qu'est le LKB fonctionne et surtout vie ! (que d'évènements durant cette thèse : déménagement, prix Nobel, ERC, médaille CNRS, inspections, ...)

Je remercie nos collègues genevois Nicolas, Nicolas, Jean-Daniel, Melvin et Pavel pour notre fructueuse collaboration.

Je remercie aussi mes musiciens Manu et Yves, Bastou, Baptiste, JD et Bruno pour nos nombreux moments musicaux durant ces dernières années.

Enfin, merci à ma famille pour avoir supportée et soutenue ces interminables années d'études...

Contents

Introduction	ix
I Theoretical tools and formalism	1
1 Quantum States	3
1.1 The photon... and beyond	4
1.2 Density matrix	7
1.3 Wigner function	10
1.4 Usual states in quantum optics	13
1.5 Gaussianity	23
1.6 Conclusion	25
2 Quantum Measurements	27
2.1 Formalism of the measurement	28
2.2 Photon detectors	30
2.3 Homodyne measurement	34
2.4 State reconstructions	37
2.5 Conclusion	43
II Generation of Non-Gaussian States	45
3 Optical Parametric Oscillators	47
3.1 Theory in the continuous-wave regime	48
3.2 Experimental realizations	54
3.3 Conclusion	60
4 Generation of Heralded Single-Photon	63
4.1 Principle of the experiment and models	64
4.2 Experimental setup	69
4.3 Results and discussions	76
4.4 Beyond: the qubit	79
4.5 Conclusion	80
5 Schrödinger Cat-like State	81
5.1 Principle of the experiment and models	82
5.2 Experimental Setup	86
5.3 Results and discussion	89
5.4 What about even cat states?	90
5.5 Conclusion	93
6 Temporal Mode and Two-Photon Fock State	95
6.1 Theories of temporal modes	96
6.2 Measurement of the temporal modes	100
6.3 Two-photon Fock state: a further example	104
6.4 Conclusion	108

Complement: Negativity of the Wigner function	109
Cp.1 Negativity of the conditional states	109
Cp.2 Losses and Gaussian operations	113
Cp.3 General negativity bound for losses	114
Cp.4 Conclusion	115
III Non-Gaussian States in Quantum Information Protocols	117
7 Single-Photon Entanglement Witness	119
7.1 Motivations	120
7.2 Principle	121
7.3 Experiment with different levels of entanglement	125
7.4 Sensitivity to losses	128
7.5 Conclusion	133
8 Hybrid Entanglement	135
8.1 Hybrid strategy	136
8.2 Protocol	136
8.3 Experimental demonstration	139
8.4 Details about the experiment	142
8.5 Further discussions	150
8.6 Conclusion	151
Conclusion	153
Appendix	157
A SSPD and APD	157
B Homodyne detection: technical considerations	161
B.1 Introduction	161
B.2 Optics	161
B.3 Electronics	162
C Optical cavities	167
C.1 TEM ₀₀ Gaussian beam	167
C.2 Optical cavity	167
C.3 micro-Cavity	168
D Useful mathematical formula	169
D.1 Gauss integrals	169
D.2 Laguerre polynomial	169
D.3 Hermite polynomials (<i>physicist version</i>)	169
E Entanglement	171
E.1 PPT criterion	171
E.2 Von Neumann entropy	171
E.3 Concurrence	171
E.4 Negativity	172

F Acquisition and interface	173
F.1 Single-oscilloscope configuration	173
F.2 Two-oscilloscope configuration	174
G Numerical computing	175
G.1 Homodyne data simulation	175
G.2 MaxLik in practice	176
Bibliography	179

Introduction

If I were not a physicist, I would probably be a musician. I often think in music. I live my daydreams in music. I see my life in terms of music...

ALBERT EINSTEIN

History of quantum information

The foundations of *quantum information* have been established a few decades ago. It has been initiated by some ideas like the one of Feynman who, noticing that classical computers are not able to simulate quantum systems, suggested to use quantum systems as simulators of other quantum systems. Similarly, people wondered how could we take advantage of the “strange” features of quantum mechanics such as *quantum superposition* or *entanglement*. These ideas, extended to the realm of *information theory* science, have led more recently to some promising protocols exploiting the “quantum rules”. Indeed, they can solve difficult classical problems in a reasonable time and with a reasonable amount of resources, highlighting the high potential of processing information by using quantum mechanics [85]. During these last years, a large effort has been made theoretically and experimentally to make these ideas more accessible.

Quantum information science can be divided into mainly two purposes: to transport and to process the information. For this reason, we can distinguish *quantum communication* on one side and, *quantum computation* (also called quantum information processing) on the other side¹. Although there is an important overlap, these two fields have mostly progressed separately so far.

More specifically, quantum communication has recently shown impressive advances as exemplified by the implementation of *quantum cryptography* protocols [29]. In this latter, quantum mechanics guarantees an unconditional secure exchange of classical information. The first protocol of quantum cryptography was proposed in 1984 by Bennett and Brassard (BB84) and has been, somehow, the first real application of quantum information. Nowadays, the quantum cryptography has become a reality, not only in labs, but also as an available commercial product. Quantum communication also concerns the exchange of quantum information, indeed quantum cryptography only allows the exchange of classical information, the added value by the quantum mechanics only lies in the secure aspect of the information exchange. One can expect that in the future, quantum computation will also require techniques to exchange quantum information. In contrast to classical information, this task is very challenging as quantum information cannot be copied, as proven by the no-cloning theorem [121]. A straightforward method is to move the information carrier from one place to the other. However, quantum mechanics offers powerful alternative methods such as the teleportation protocol. Indeed, this technique enables the exchange of quantum information between two distance places without transport of the quantum information carrier. The first experimental demonstrations of teleportation between light or material systems are extremely recent (but still experimentally challenging).

¹In [85], one would notice that the subdivision of quantum computation/quantum information is proposed in order to consider more conceptual aspects linked to *information theory*.

A contrario, one can notice that for quantum computation, although the theoretical proposals are numerous, the experimental demonstrations are so far extremely limited. The experimental realizations are indeed extremely challenging. In contrast to quantum cryptography systems, quantum processing requires to control quantum systems of large sizes with a very high reliability. In particular, defects induce the so-called *decoherence* which is nowadays the main limitation to quantum computation. This effect is even stronger than the defects scale with the size of the system. Thus, fighting the decoherence by improving the quality of the experimental setups and finding more robust algorithms is the main challenge to achieve any quantum computational task.

There is still a very long way to go for the implementation of quantum algorithms. For this reason, quantum physics stays a topic of fundamental research, however new ideas and experimental demonstrations are done regularly paving the way to potential applications. Furthermore, it also permits to go through a deeper understanding of puzzling aspects of quantum mechanics: is there a trivial interpretation of entanglement, of quantum superposition, how can we define the quantum-classical limit?

The rules of the game

Let us continue this introduction by a more precise description of quantum information to show what is required for a quantum system to be a good candidate for quantum information tasks [85].

All the quantum information theory has been built by analogy with the digital information, the goal is thus to find physical systems to encode the two logical levels 0 and 1: a *qubit*. Hence, the system should have at least two states:

$$|\mathbf{0}\rangle = |\psi\rangle, \quad |\mathbf{1}\rangle = |\phi\rangle. \quad (1)$$

Furthermore, these states have to be orthogonal:

$$\langle \mathbf{0} | \mathbf{1} \rangle = \langle \psi | \phi \rangle = 0. \quad (2)$$

Indeed, these two levels have to be distinguishable without any ambiguities (with of course the appropriate measurement). These are the basic requirements that a quantum system has to fulfill to be used as a qubit.

How the quantum computation will surpass classical computation lies in the fact that we can have a superposition of these two logic levels:

$$a|\mathbf{0}\rangle + b|\mathbf{1}\rangle \quad (3)$$

(with $|a|^2 + |b|^2 = 1$ for probability conservation). Somehow, this feature enables to perform simultaneously different calculations. A qubit, as any two-level quantum system, is usually represented on the Bloch sphere via the expression

$$|\psi\rangle = \cos(\theta/2)|\mathbf{0}\rangle + e^{i\phi} \sin(\theta/2)|\mathbf{1}\rangle. \quad (4)$$

By analogy with classical computation, quantum algorithms have been decomposed with the help of *quantum gates*. In contrast to classical gates, these ones have to preserve the superposition feature. They constitute the building blocks of quantum computation. Any gate operations can also be decomposed with the help of a set of basic operations. For instance, the Pauli matrices for single-qubit operation

$$\mathbf{X} = \begin{bmatrix} 0 & 1 \\ 1 & 0 \end{bmatrix}, \quad \mathbf{Y} = \begin{bmatrix} 0 & -i \\ i & 0 \end{bmatrix}, \quad \mathbf{Z} = \begin{bmatrix} 1 & 0 \\ 0 & -1 \end{bmatrix}. \quad (5)$$

Another basis of single-qubit operation is often used

$$\mathbf{H} = \begin{bmatrix} 1 & 1 \\ 1 & -1 \end{bmatrix}, \quad \mathbf{S} = \begin{bmatrix} 1 & 0 \\ 0 & i \end{bmatrix}, \quad \mathbf{T} = \begin{bmatrix} 1 & 0 \\ 0 & e^{i\pi/4} \end{bmatrix}. \quad (6)$$

Similarly, we have also some gates involving more than one qubit. For instance, the CNOT gate for which the matrix \mathbf{X} will be applied or not, depending on the value of the control qubit. This can be expressed in the basis $\{|0, 0\rangle, |0, 1\rangle, |1, 0\rangle, |1, 1\rangle\}$, by the matrix

$$\mathbf{CNOT} = \begin{bmatrix} 1 & 0 & 0 & 0 \\ 0 & 1 & 0 & 0 \\ 0 & 0 & 0 & 1 \\ 0 & 0 & 1 & 0 \end{bmatrix}, \quad (7)$$

where the first qubit controls the gate applied on the second qubit.

Quantum Information with Quantum Optics

The undeniable advantage of light is its mobility and low interaction with the environment. Even though it seems commonplace to say that, these are strong advantages compared to the others physical systems. This is why most of the quantum communication protocols are based on light states. However, these features have their downsides. First, light is difficult to store, the photon being a massless particle it cannot be stopped. Quantum memories for light are nowadays an interesting challenge to solve this problem. Secondly, its low interaction with the environment makes it stable but difficult to manipulate.

Among the various protocols of quantum information, mainly four optical encodings are used:

- $|0\rangle, |1\rangle$ photon numbers
- $|\alpha\rangle, |-\alpha\rangle$ phase of a “classical” light
- $|t_1\rangle, |t_2\rangle$ time bin ²,
- $|\uparrow\rangle, |\rightarrow\rangle$ single-photon polarization ³.

These different encodings can be separated into two families. First, the *single-rail* qubit (two first encodings) where the qubit is defined on one mode. Secondly, the *dual-rail* qubit (the two last ones), the qubit is defined on two modes. Actually, these two are very similar, there is no particular difficulty to switch from one to the other (for instance with the help of polarizing beam-splitter and optical switch) which is not the case with the first ones as they are based on state of light of a very different nature.

Furthermore, we can also distinguish the encodings based on single-photon and vacuum states, and the one based on coherent states; the so-called *discrete* or *continuous* variables implementation. This fundamental difference of nature has important consequences. Indeed, the way to process the information involves very different protocols and optical tools.

Interaction between photons is difficult, indeed, it can be mediated by a beam-splitter but this interaction is limited. Non-linear interaction is extremely difficult to obtain efficiently. For this reason, the paradigm of *Linear Optical Quantum Computing* [48] has been developed, it is based only on standard optical elements like beam-splitter, wave- plates, delay

²the position in time of a single-photon encodes the qubit, the states being more precisely $|t_1\rangle = |1\rangle_{t_1}|0\rangle_{t_2}$, $|t_2\rangle = |0\rangle_{t_1}|1\rangle_{t_2}$

³ $|\uparrow\rangle = |1\rangle_{\uparrow}|0\rangle_{\rightarrow}$, $|\rightarrow\rangle = |0\rangle_{\uparrow}|1\rangle_{\rightarrow}$

and measurements. One complete scheme for discrete variables is the now the well-known KLM proposal [47]. There are some equivalent schemes for continuous variables [43, 95, 28].

Interestingly, these last years it has been highlighted that the combination of discrete and continuous variables, and their associated toolboxes, could yield to an improvement and/or simplification of quantum information tasks. This is the so-called *optical hybrid approach* of quantum information [25].

Context and structure of the manuscript

This PhD lies within the framework of quantum state engineering and the development of new protocols for the implementation of quantum networks. The generation of qubits is the first step of any quantum information task based on photonic systems. Moreover, for quantum information processing, these qubits have particular non-classical features. These last few years, many groups have demonstrated experimental generation of non-classical states of light such as single-photon state and optical Schrödinger cat state (almost in the chronological order: Lvovsky, Grangier, Polzik, Bellini, Furusawa, Sasaki). Now, the main goal is to use these resources in some quantum information protocols.

This PhD work is the first one in this field in the group of Quantum Optics at the Laboratoire Kastler Brossel. However, it has been started on a well-studied optical parametric oscillator [53]. Moreover, we could expect that this work will be extended to more complex systems; for instance multi-mode non-Gaussian state with frequency comb or storage in various quantum memories.

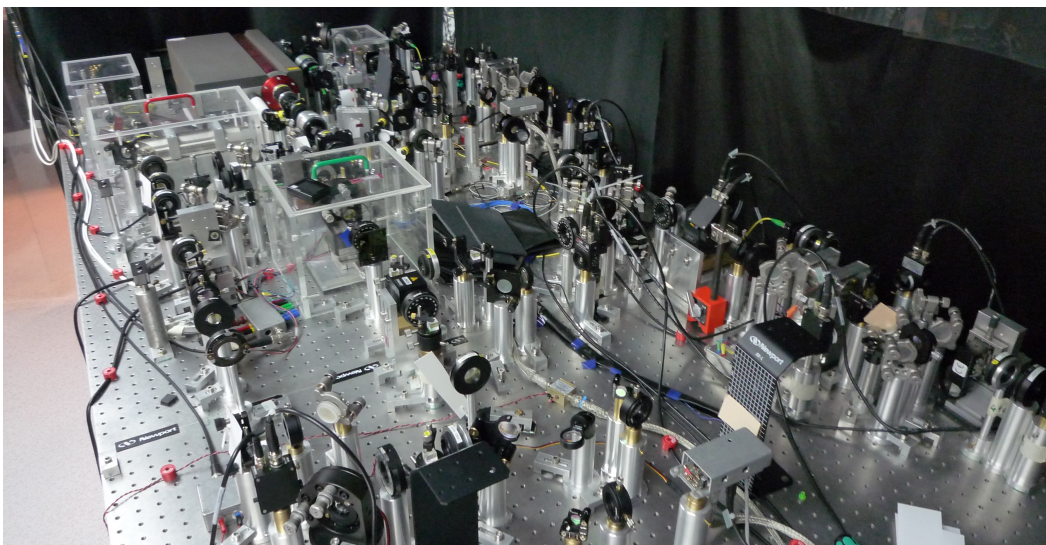
Before describing the main content of this PhD work, we introduce in **Part I** the theoretical concepts that we use and/or that justify some strategies we have chosen. In the first chapter, we introduce the Wigner function, a formalism of quantum states now widely used in quantum optics. It has the advantage to be a more familiar representation as it is a quantum analog of the Fresnel representation. More importantly, the Wigner function allows to distinguish two categories of quantum states: the *Gaussian* and *non-Gaussian* states. Although one could think that it simply results from mathematical properties, recent works shows that it seems to have a deeper physical meaning. Indeed, it has been proved that non-Gaussian states are a necessary resource for quantum computation [68]. Furthermore, we show in the second chapter that this distinction of quantum states can be extended to quantum measurements: despite the name “Gaussian/non-Gaussian” is less appropriate in that case, it can however highlight some similar important features.

As detailed in **Part II**, we thus have developed some non-Gaussian resources that correspond to the main encodings of photonic qubits, with in mind the idea to make it usable. Indeed, as we have noticed, there are many theoretical proposals but only few experimental demonstrations, this is also due to the fact that, observing strong quantum signatures some quantum features is always experimentally challenging. Starting from optical oscillators (chap. 3), we have developed two main resources of quantum information in optics: the single-photon state (chap. 4) and the coherent superposition of coherent states (chap 5). In both cases, thanks to a very-well control spatio-temporal mode, a very high fidelity has been obtained making them suitable for further experiments.

Finally in **Part III**, we have then used these resources in novel quantum information protocols. The first one is a witness for single-photon entanglement (chap. 7), which has been designed and studied for realistic quantum networks. The second uses both resources to generate an entangled state where each party uses a different encoding (chap. 8). These two latter experiments constitute some illustrations of the *optical hybrid approach* where the continuous and discrete variables toolboxes have been mixed.

List of publications

- *Witnessing single-photon entanglement with local homodyne measurements: analytical bounds and robustness to losses.*
M. Ho, O. Morin, J.-D. Bancal, N. Gisin, N. Sangouard, J. Laurat.
arxiv.org/abs/1406.0381 (2014)
- *Remote creation of hybrid entanglement between particle-like and wave-like optical qubits.*
O. Morin, K. Huang, J. Liu, H. Le Jeannic, C. Fabre, J. Laurat.
Nature Photonics **8**, 570-574 (2014), doi:10.1038/nphoton.2014.137
- *Quantum State Engineering of Light with Continuous-wave Optical Parametric Oscillators.*
O. Morin, J. Liu, K. Huang, F. Barbosa, C. Fabre, J. Laurat
www.jove.com/video/51224 (2014)
- *Experimentally accessing the optimal temporal mode of traveling quantum light states.*
O. Morin, C. Fabre, J. Laurat.
Phys. Rev. Lett. **111**, 213602 (2013), dx.doi.org/10.1103/PhysRevLett.111.213602
- *Witnessing trustworthy single-photon entanglement with local homodyne measurements.*
O. Morin, J.-D. Bancal, M. Ho, P. Sekatski, V. D'Auria, N. Gisin, J. Laurat and N. Sangouard.
Phys. Rev. Lett. **110**, 130401 (2013), dx.doi.org/10.1103/PhysRevLett.110.130401
- *High-fidelity single-photon source based on a type-II optical parametric oscillator.*
O. Morin, V. D'Auria, C. Fabre and J. Laurat.
Optics Lett. **37**, 3738-3740 (2012), dx.doi.org/10.1364/OL.37.003738
- *Effect of the heralding detector properties on the conditional generation of single-photon states.*
V. D'Auria, O. Morin, C. Fabre and J. Laurat.
Eur. Phys. Journ. D **66**:249 (2012), dx.doi.org/10.1140/epjd/e2012-30351-6



Part I

Theoretical tools and formalism

1 | Quantum States

All the arts are based on two principles: reality and ideality.

FRANTZ LISZT

This first chapter is devoted to a brief review of the descriptions of quantum states (specifically in quantum optics) through two formalisms: the *density matrix* and the *Wigner function*. Their general definitions and main mathematical properties are given. Furthermore, we highlight that in some cases one of this formalism is more appropriate than the other for calculation and/or for physical interpretations. These differences are then illustrated with various states commonly used in quantum optics. All these concepts are of course well explained in many textbooks, this chapter mainly allows us to define the notations used afterwards and to make this manuscript more accessible to non-specialists by giving the minimum background.

1.1	The photon... and beyond	4
1.1.1	Quantization	4
1.1.2	Modes	6
1.2	Density matrix	7
1.2.1	Definition	7
1.2.2	Properties	7
1.2.3	One example: effect of optical losses	9
1.3	Wigner function	10
1.3.1	Definition	10
1.3.2	Properties	11
1.3.3	Wigner function for operators	12
1.3.4	Other formulations of the Wigner function	13
1.4	Usual states in quantum optics	13
1.4.1	Fock states	13
1.4.2	Coherent states	15
1.4.3	Squeezed vacuum state	15
1.4.4	Two-mode squeezed vacuum state	17
1.4.5	Thermal states	18
1.4.6	Gaussian states	18
1.4.7	Schrödinger's cat states	19
1.5	Gaussianity	23
1.5.1	Hudson-Piquet theorem	23
1.5.2	Gaussian operations	23
1.6	Conclusion	25

1.1 The photon... and beyond

Is the light a particle or a wave? This question has been a long debate for many years; Newton was for particle, Huygens supporter of wave... When Maxwell derived his famous equations, the debate seemed closed. But, during the beginning of the 20th century the question came back. In particular, Planck found an empirical law using some particles of light and later Einstein showed that the Wien's law implies a corpuscular description of light with the fundamental *quanta* of energy $E = h\nu$. It was thus necessary to find a new mathematical description to reconcile the two descriptions by quantizing the light.

Hence, the idea initiated by Dirac was to start from the Maxwell's equations of the electromagnetic field and to apply a canonical quantization in order to add the particle feature of light, for which the energy is discretized by elementary quantity.

1.1.1 Quantization

The fundamental postulates of quantum mechanics say that a physical system is described by vector states and the electromagnetic field, being a measurable quantity, is an Hermitian operator (an *observable*). If we consider an harmonic plane wave at frequency ω with a wave vector \mathbf{k} in a volume V , the electromagnetic field is thus written

$$\hat{\mathbf{E}}(\mathbf{r}, t) = \mathbf{E}_0 \left[\hat{a} e^{-i(\omega t - \mathbf{k} \cdot \mathbf{r})} + \hat{a}^\dagger e^{i(\omega t - \mathbf{k} \cdot \mathbf{r})} \right], \quad (1.1)$$

with the operator \hat{a} and its Hermitian conjugate \hat{a}^\dagger , these two following the bosons commutation rule

$$[\hat{a}, \hat{a}^\dagger] = 1. \quad (1.2)$$

Specifically, the *creation operator* adds one photon to photon-number states

$$\hat{a}^\dagger |n\rangle = \sqrt{n+1} |n+1\rangle, \quad (1.3)$$

whereas the *annihilation operator* subtracts a photon (this operator gives 0 if applied to the vacuum state)

$$\hat{a} |n\rangle = \sqrt{n} |n-1\rangle. \quad (1.4)$$

The product of both operators forms the *photon number operator*

$$\hat{n} = \hat{a}^\dagger \hat{a}. \quad (1.5)$$

Therefore, the constant \mathbf{E}_0 can be defined from the mean value of electromagnetic energy for a state of n photons

$$\langle n | \int \varepsilon_0 |\hat{\mathbf{E}}|^2 d\mathbf{r}^3 | n \rangle = \hbar\omega(n + 1/2), \quad (1.6)$$

leading to

$$\mathbf{E}_0 = \sqrt{\frac{\hbar\omega}{2\varepsilon_0 V}} \mathbf{e}_p, \quad (1.7)$$

where \mathbf{e}_p is the polarization vector and V the volume of the quantization box.

Moreover, as we usually do with classical fields, we can rewrite the field (1.1) in the Fresnel basis, as:

$$\hat{\mathbf{E}}(\mathbf{r}, t) = \sqrt{2}\mathbf{E}_0 \left[\hat{X} \cos(\omega t - \mathbf{k} \cdot \mathbf{r}) + \hat{P} \sin(\omega t - \mathbf{k} \cdot \mathbf{r}) \right]. \quad (1.8)$$

This leads to define two Hermitian operators, called *quadrature operators* (\hat{X}, \hat{P}) , as linear combinations of the annihilation and creation operators. The commutation relation is then:

$$[\hat{X}, \hat{P}] = i . \quad (1.9)$$

The mess of conventions Different possible choices of normalization exist for the quadrature operators. Unfortunately, this choice can be different from one textbook or paper to another... Worst, none of them seems dominant. In order to stay “compatible” with any conventions, the best strategy consists in keeping a parameter that we can replace by any numerical value afterwards. Among the different conventions, one uses the Planck constant in order to get the commutation relation as $[\hat{X}, \hat{P}] = i\hbar$. However, we have done another choice here: we use as reference the standard deviation of the vacuum fluctuation in such a way that the quadrature \hat{x} (denoted with lowercase with this convention) satisfies

$$\langle 0|\hat{x}^2|0\rangle = \sigma_0^2 . \quad (1.10)$$

Therefore, the Heisenberg uncertainty relation usually written

$$\Delta x \Delta p \geq \hbar/2 , \quad (1.11)$$

where $\Delta x = \sqrt{\langle \hat{x}^2 \rangle - \langle \hat{x} \rangle^2}$ is a standard deviation, becomes in our case:

$$\sigma_x \sigma_p \geq \sigma_0^2 . \quad (1.12)$$

(We thus identify $\hbar = 2\sigma_0^2$.) The choice of the letter σ refers to the usual notation of a standard deviation in statistics (and avoids any possible confusion with the variance). Moreover, this choice has two advantages. First, it highlights the statistical meaning of the Wigner function that we introduce later. Secondly, it has a practical interest: the vacuum state being extremely easy to produce, we can calibrate our measurement device with this quantity. Hence, this notation will be used as much as possible in the whole manuscript.

Given this convention, the relationships between annihilation/creation operators and quadratures operators are thus

$$\hat{a} = \frac{\hat{x} + i\hat{p}}{2\sigma_0} , \quad \hat{x} = \sigma_0(a + a^\dagger) , \quad (1.13)$$

$$\hat{a}^\dagger = \frac{\hat{x} - i\hat{p}}{2\sigma_0} , \quad \hat{p} = -i\sigma_0(a - a^\dagger) . \quad (1.14)$$

The quadrature operators follow the commutation relation

$$[\hat{x}, \hat{p}] = i2\sigma_0^2 . \quad (1.15)$$

The relationship with the photon number operator is

$$\hat{n} = \hat{a}^\dagger \hat{a} = \frac{1}{4\sigma_0^2} (\hat{x}^2 + \hat{p}^2 - 2\sigma_0^2) . \quad (1.16)$$

The choice of the quadrature operators basis is a priori arbitrary. As for the Fresnel representation, it is possible to rotate the basis. This is realized by the basic rotation matrix for an angle θ

$$\begin{pmatrix} \hat{x}_\theta \\ \hat{p}_\theta \end{pmatrix} = \begin{pmatrix} \cos \theta & \sin \theta \\ -\sin \theta & \cos \theta \end{pmatrix} \begin{pmatrix} \hat{x} \\ \hat{p} \end{pmatrix} . \quad (1.17)$$

In other words,

$$\hat{x}_\theta = \sigma_0(\hat{a}e^{-i\theta} + \hat{a}^\dagger e^{i\theta}) . \quad (1.18)$$

Contrary to the annihilation/creation operators, \hat{x}_θ being an observable, is a Hermitian operator. It thus has some orthonormal eigenvectors $\{|x, \theta\rangle\}_{x \in \mathbb{R}}$ (for each fixed θ) satisfying $\hat{x}_\theta|x, \theta\rangle = x|x, \theta\rangle$ and the closure relation

$$\int_{\mathbb{R}} dx |x, \theta\rangle\langle x, \theta| = \mathbb{1} . \quad (1.19)$$

Hence, to avoid any confusion, instead of “*Fresnel representation*”, it will be better to talk about “*phase space*”.

1.1.2 Modes

For a complete description of the light, we should consider the different degrees of freedom of the electromagnetic field. Indeed, the light can have different polarizations, various frequencies and various phase and intensity profiles. Classically this is done by using a set of orthonormal functions $\{\mathbf{u}_k(\mathbf{r}, t)\}$ which form a basis of solution of Maxwell’s equations, each function defines what we call a *mode* of the electromagnetic field.

So far, our quantization has been applied to a specific solution of Maxwell’s equations, yielding to an Hilbert space generated by a single Fock basis. The quantization can be generalized to each mode. For instance the field operator associated to the mode k is thus written

$$\hat{\mathbf{E}}_k^{(+)}(\mathbf{r}, t) = E_k \mathbf{u}_k(\mathbf{r}, t) \cdot \hat{a}_k . \quad (1.20)$$

Now, to each solution $\mathbf{u}_k(\mathbf{r}, t)$, we associate one Hilbert space \mathcal{E}_k generated by one Fock basis $\{|0\rangle_k, |1\rangle_k, \dots\}$ thanks to the annihilation/creation operators $\hat{a}_k/\hat{a}_k^\dagger$.

It is important to note that this formulation is general and that there is no particular physics behind the index k . However, we usually work with only one degree of freedom, we thus often use one subset of functions that have all the other degrees of freedom fixed. We then talk about *polarization mode*, *spatial mode*... to focus on a particular degree of freedom. For example, the spatial degree of freedom can be expanded over the different transverse electromagnetic modes

$$\mathcal{E} = \mathcal{E}_{\text{TEM}00} \otimes \mathcal{E}_{\text{TEM}01} \otimes \dots \mathcal{E}_{\text{TEM}10} \otimes \mathcal{E}_{\text{TEM}11} \dots . \quad (1.21)$$

Each subspace being generated by a single Fock basis, we consider a family of mode which have the same temporal and polarization mode (and more rigorously the same spatial origin and direction of propagation). Now, if we consider fixed the temporal and spatial degrees of freedom, we can have for instance the following decomposition over the polarization modes:

$$\begin{aligned} \mathcal{E} &= \mathcal{E}_\uparrow \otimes \mathcal{E}_\rightarrow \\ &= \mathcal{E}_{\swarrow} \otimes \mathcal{E}_{\nearrow} \\ &= \mathcal{E}_\circ \otimes \mathcal{E}_\circ . \end{aligned} \quad (1.22)$$

As illustrated by this latter example, we can use different mode basis, nothing is necessarily fixed: one can switch from one mode expansion $\{\hat{a}_k\}_{k \in \mathbb{N}}$ to another $\{\hat{b}_m\}_{m \in \mathbb{N}}$ via the linear transformation

$$\hat{b}_m = \sum_k U_m^k \hat{a}_k . \quad (1.23)$$

In order to be physically consistent, the transformation has to preserve for instance the commutation relation $[\hat{b}_m, \hat{b}_{m'}^\dagger] = \delta_{mm'}$ in the new basis. Hence, the transformation should be unitary

$$\sum_k (U_k^m)^* U_k^{m'} = \delta_{mm'} \Leftrightarrow U^\dagger U = \mathbb{1} \Leftrightarrow U^\dagger = U^{-1} . \quad (1.24)$$

Besides, it is also true for continuous mode expansion. Indeed, we have used above integer indices but it can also be continuous variables. In that case, under the assumption that there is no mathematical “contraindication”, a discrete sum becomes an integral. For instance, we have the relationships with frequency decomposition and time decomposition with the unitary Fourier transform

$$\hat{a}(t) = \frac{1}{\sqrt{2\pi}} \int d\omega \hat{a}(\omega) e^{-i\omega t}, \quad (1.25)$$

$$\hat{a}(\omega) = \frac{1}{\sqrt{2\pi}} \int dt \hat{a}(t) e^{i\omega t}. \quad (1.26)$$

Again, it satisfies the commutation relations $[\hat{a}(t), \hat{a}(t')^\dagger] = \delta(t - t')$ and $[\hat{a}(\omega), \hat{a}(\omega')^\dagger] = \delta(\omega - \omega')$.

However, it is worth noting that, for a given system, some modes basis are sometimes more relevant/“natural”, e.g. a change of polarization basis is always possible but the same transformation applied to two spatially separated beams is a priori less appropriate. Furthermore, without discussing the mathematical difficulties that can appear in the general case, all the following will be under the *paraxial* and *narrowband* approximations, which is highly reasonable for most of the quantum optics experiments nowadays. This will ensure the orthogonality and the closure relation of the mode functions.

1.2 Density matrix

Most of the readers are probably familiar with this formalism. Nevertheless, it is never useless to remind a few of its properties as this tool is rich and thus, usually, we do not keep in mind all of these properties. Moreover, this section will be useful for the parallel with the Wigner function next defined (and extensively used afterwards).

1.2.1 Definition

The *density matrix* (also called *density operator*) has been introduced to bring an additional description that is not possible when using only state vectors. Indeed, though the state of a quantum system is always perfectly defined by a state vector, it is not necessarily well known by the observer. Hence, the system is described by a *statistical mixture* of states. In other word, this mixture of different states can be interpreted as a result of a part of “ignorance” of the observer about the system. It is of a particular importance to describe experiments: experimental setups are never perfect, and thus some “leaks of knowledge” about the system yield to this kind of states.

By definition, the density matrix of a *pure state* $|\psi\rangle$ is $\hat{\rho} = |\psi\rangle\langle\psi|$. A non-pure state (or *mixed state*) $\hat{\rho}$ is, by extension, a sum of pure states $\hat{\rho}_i$ each weighted by the probability P_i of having $\hat{\rho}_i$ in the mixture, i.e. $\hat{\rho} = \sum P_i \hat{\rho}_i$, with the probability conservation $\sum P_i = 1$.

1.2.2 Properties

As a direct consequence of its definition from state vectors, the density matrix has many properties, sometimes with a physical meaning and some others purely mathematical (or not yet physically interpreted).

Completeness of probabilities For a pure state, the normalization of the state vector $|\psi\rangle$ to one $\langle\psi|\psi\rangle = 1$ ensures the completeness of probability. The extension to the density matrix gives a trace equal to one. For the same reason, when we consider a mixed state we have $\sum P_i = 1$ and $\forall i, \text{Tr}[\hat{\rho}_i] = 1$. Thus

$$\text{Tr} \hat{\rho} = 1 . \quad (1.27)$$

Hermitian Straightforward consequence of its definition, the density matrix is an Hermitian operator

$$\hat{\rho}^\dagger = \hat{\rho} . \quad (1.28)$$

Positivity Thanks to the spectral theorem the density matrix is diagonalizable and is said *positive semi-definite*, i.e. all of its eigenvalues are positive or null. This is noted as:

$$\hat{\rho} \geq 0 . \quad (1.29)$$

Diagonalisation The density matrix is diagonal in a basis of orthogonal eigenvectors. In other words, it can be written as a sum of pure states which are pairwise orthogonal.

$$\hat{\rho} = \sum_i p_i |\psi_i\rangle\langle\psi_i| , \text{ with } \forall i, j \quad \langle i|j\rangle = \delta_{ij} . \quad (1.30)$$

According to the spectral theorem, this expansion is always possible and unique if there is non degenerate eigenvalues p_i . However, it can also be described by a mixture of pure states but not necessary orthogonal. In this case, existence and uniqueness are not guaranteed.

Expectation value The expectation value of an observable \hat{A} is equal to

$$\langle\hat{A}\rangle_{\hat{\rho}} = \text{Tr}[\hat{A}\hat{\rho}] . \quad (1.31)$$

Purity This quantity, as its name suggests, is used to give a quantitative value of the purity of a state. When it is equal to 1, the state is pure and for a mixed state this quantity is smaller than one.

$$\mathcal{P} = \text{Tr}[\hat{\rho}^2] = \sum_i p_i^2 . \quad (1.32)$$

von Neumann entropy This is another criterion for the purity. For a single-mode state, it can be written as

$$\mathcal{S}_{vN} = -\text{Tr}[\hat{\rho} \ln \hat{\rho}] = -\sum_i p_i \ln p_i . \quad (1.33)$$

This quantity is equal to zero for pure states and positive otherwise.

Fidelity It is interesting to have a quantity to measure the similarity between two states. Many quantities of this kind exist, but the most used, probably because relatively obvious, is the fidelity. For two pure states it corresponds to the projection

$$\mathcal{F} = |\langle\psi_1|\psi_2\rangle|^2 . \quad (1.34)$$

The general formulation for mixed states is more sophisticated [45] and can be written as:

$$\mathcal{F} = \left(\text{Tr} \left[\sqrt{\sqrt{\hat{\rho}_2} \hat{\rho}_1 \sqrt{\hat{\rho}_2}} \right] \right)^2 . \quad (1.35)$$

However, if at least one state is pure, it simplifies in ¹

$$\mathcal{F} = \text{Tr}[\hat{\rho}_1 \hat{\rho}_2] . \quad (1.36)$$

It is equal to 1 when the states are identical and 0 when they are orthogonal.

Marginal distribution It corresponds to the measurements distribution of a given quadrature

$$\mathcal{P}_{\hat{\rho}}(x_{\theta}) = \langle x_{\theta} | \hat{\rho} | x_{\theta} \rangle . \quad (1.37)$$

Thanks to the positive semi-definite property, this value is always real and positive.

1.2.3 One example: effect of optical losses

This is a typical situation where some information on the system are lost and yielding to a statistical mixture. The formalism of the density matrix is then necessary.

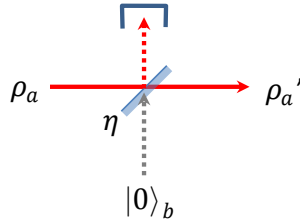


Figure 1.1: Most of the optical losses can be modeled by a fictitious beam-splitter. It result in a mixing with the vacuum state and a loss of information on one mode.

As depicted on figure 1.1, the simplest model of optical losses is a beam-splitter with a transmission η on the path of the beam (our “flying” quantum system). Hence, the state is modified as following

$$(\hat{\rho}_a \otimes |0\rangle\langle 0|_b) \xrightarrow{\hat{B}_\eta} \hat{B}_\eta (\hat{\rho}_a \otimes |0\rangle\langle 0|_b) \hat{B}_\eta^\dagger = \hat{\rho}_{ab} . \quad (1.38)$$

The reflected part, being not consider anymore, is “lost”. In other word, the experimentalist does not control this part and thus doesn’t know what is the exact effect of the beam-splitter on the output state. Consequently, we trace the density matrix of the reflected part

$$\text{Tr}_b[\hat{\rho}_{ab}] = \hat{\rho}'_a . \quad (1.39)$$

For instance, let us consider a single-photon state $|1\rangle_a = \hat{a}^\dagger |0\rangle_a$. Applying the beam-splitter operator to a pure state is equivalent to applying it on the annihilation/creation operator when the state is written as a function of these latter applied to the vacuum state (see 1.5.2).

$$\hat{B}^\dagger \hat{a}^\dagger \hat{B} = \sqrt{\eta} \hat{a}^\dagger + \sqrt{1-\eta} \hat{b}^\dagger \quad (1.40)$$

$$\hat{B}^\dagger \hat{b}^\dagger \hat{B} = \sqrt{\eta} \hat{b}^\dagger - \sqrt{1-\eta} \hat{a}^\dagger \quad (1.41)$$

Therefore, our state becomes $\sqrt{\eta} |1\rangle_a |0\rangle_b + \sqrt{1-\eta} |0\rangle_a |1\rangle_b$. After tracing the mode b , we obtain the resulting state

$$\eta |1\rangle\langle 1|_a + (1-\eta) |0\rangle\langle 0|_a . \quad (1.42)$$

With the density matrix, we can therefore make the distinction between such a statistical mixture and a coherent superposition of vacuum and single-photon. They have the same

¹If we consider the pure state $\hat{\rho}_1 = |\psi\rangle\langle\psi|$, we have $\sqrt{\hat{\rho}_1} = \hat{\rho}_1$, then $\hat{\rho}_1 \hat{\rho}_2 \hat{\rho}_1 = \hat{\rho}_1 \langle\psi|\hat{\rho}_2|\psi\rangle$ a matrix times a scalar. We obtain $(\text{Tr}[\sqrt{\hat{\rho}_1} \langle\psi|\hat{\rho}_2|\psi\rangle])^2 = \langle\psi|\hat{\rho}_2|\psi\rangle (\text{Tr}[\sqrt{\hat{\rho}_1}])^2 = \langle\psi|\hat{\rho}_2|\psi\rangle$ which corresponds to the trace of the product of the two matrices.

photon number probabilities (diagonal elements of the density matrix) but the coherent superposition has coherence terms different from zero unlike the statistical mixture.

Nevertheless, we can already notice that the information is not completely lost. The mechanism being known (the system is coupled to a vacuum state with a ratio η), it is possible to infer the state before the losses with the complete measurements of the state after the losses (this will be very useful for the states reconstruction in section 2.4).

This example is quite simple as we consider a space of size 2. For bigger states, the calculation can become more painful... In the next section, we introduce the Wigner function. With this formalism, the losses simply translate into a convolution with a Gaussian function.

1.3 Wigner function

In 1932, Eugen Wigner introduced this function in order to have a quasi-distribution probability of joint measurements of position and momentum of a particle. In our case, it applies to the quadrature operators. This function, as for the density matrix, completely characterizes a quantum state. Although it is not often used (at least less than the density matrix), this representation has many useful features. First, it yields to a more convenient representation of a state (for instance, the complex values of the density matrix are a little difficult to plot). On the other hand, it is more convenient in terms of physical meaning. Indeed, it is a “quantum” version of the Fresnel representation for the quadrature operators.

1.3.1 Definition

The Wigner function of the state $\hat{\rho}$ can be defined with the formula²

$$W_{\hat{\rho}}(x, p) = \frac{1}{2\pi\sigma_0^2} \int e^{iyp/\sigma_0^2} \langle x-y | \hat{\rho} | x+y \rangle dy . \quad (1.44)$$

As mentioned before, the convention of normalization yields to many mistakes if not manipulated carefully, that is why we give a definition with the parameter σ_0^3 .

For a pure state, the Wigner function can be expressed via the wave-function

$$W_{\hat{\rho}}(x, p) = \frac{1}{2\pi\sigma_0^2} \int e^{iyp/\sigma_0^2} \psi^*(x-y) \psi(x+y) dy . \quad (1.46)$$

The wave-function of the n -th harmonic oscillator can be read as

$$\langle n | x_\theta \rangle = e^{in\theta} \frac{1}{(\sqrt{2\pi}\sigma_0 2^n n!)^{1/2}} H_n \left(\frac{x}{\sigma_0 \sqrt{2}} \right) e^{-(x/\sigma_0 \sqrt{2})^2/2} \quad (1.47)$$

with H_n the n -th Hermite polynomial (D.3). For each elements of the density matrix [59] one can write

$$W_{|k\rangle\langle l|}(x, p) = \frac{(-1)^l}{2\pi\sigma_0^2} \sqrt{\frac{l!}{k!}} \left(\frac{x-iy}{\sigma_0} \right)^{k-l} e^{-(x^2+p^2)/2\sigma_0^2} L_l^{k-l} \left(\frac{x^2+p^2}{\sigma_0^2} \right) , \quad (1.48)$$

²we can also find the expression

$$W_{\hat{\rho}}(x, p) = \frac{1}{2\pi 2\sigma_0^2} \int e^{iyp/2\sigma_0^2} \langle x-y/2 | \hat{\rho} | x+y/2 \rangle dy . \quad (1.43)$$

³ with the convention using \hbar , we can find the following definition

$$W_{\hat{\rho}}(x, p) = \frac{1}{2\pi\hbar} \int_{\mathbb{R}} e^{ipy/\hbar} \langle x-y/2 | \hat{\rho} | x+y/2 \rangle dy \quad (1.45)$$

with L_l^{k-l} a Laguerre polynomial (D.2). This equation is true for $k \geq l$, otherwise, we exchange l by k and y becomes $-y$. This function has complex values if $l \neq k$ but, due to the Hermitian properties of the density matrix, at the end, the Wigner function has only real values. The Wigner function is thus conveniently calculated with

$$W_{\hat{\rho}}(x, y) = \sum_{k,l} \rho_{kl} W_{|k\rangle\langle l|}(x, y) . \quad (1.49)$$

The equation (1.43) can be generalized to more than one mode, with two variables x_i, p_i per mode i :

$$W_{\hat{\rho}}(x_1, p_1; \dots; x_n, p_n) = \frac{1}{(2\pi 2\sigma_0^2)^n} \int_{\mathbb{R}^{2n}} e^{iy_1 p_1/2\sigma_0^2 + \dots + iy_n p_n/2\sigma_0^2} \langle x_1 - y_1/2 | \dots \langle x_n - y_n/2 | \hat{\rho} | x_1 + y_1/2 \rangle \dots | x_n + y_n/2 \rangle dy_1 \dots dy_n . \quad (1.50)$$

We can use a matrix notation to pack all the variables of the Wigner function, but this is not much more useful if we only consider a small number of modes.

1.3.2 Properties

As for the density matrix, the Wigner function has many properties. We give below the different analogs but also some more specific features.

Hermitian operators If the operator is Hermitian (like for density matrix $\hat{\rho} = \hat{\rho}^\dagger$), the Wigner function has only real values.

Linearity The Wigner function is linear in terms of operators

$$W_{p_1 \hat{\rho}_1 + p_2 \hat{\rho}_2 + \dots} = p_1 W_{\hat{\rho}_1} + p_2 W_{\hat{\rho}_2} + \dots . \quad (1.51)$$

Marginal distribution It can be written as

$$\mathcal{P}_{\hat{\rho}}(x_\theta) = \int dp_\theta W_{\hat{\rho}}(x_\theta \cos \theta - p_\theta \sin \theta, p_\theta \cos \theta + x_\theta \sin \theta) , \quad (1.52)$$

which is the density of probability to measure x_θ with the observable \hat{x}_θ .

Probability completeness For the same reason that the trace of the density matrix sum to one, the quasi-probability distribution sums up also to one

$$\iint_{\mathbb{R}^2} W_{\hat{\rho}}(x, p) dx dp = 1 . \quad (1.53)$$

Overlap formula This is a general formula for two Hermitian operators. This is an extremely useful property enabling to make the parallel with calculations using density matrix⁴

$$\text{Tr}[\hat{O}_1 \hat{O}_2] = 4\pi\sigma_0^2 \iint dx dp W_{\hat{O}_1}(x, p) W_{\hat{O}_2}(x, p) . \quad (1.54)$$

Moreover, this formula is also valid for more than one mode. This latter remark will be extremely useful afterwards⁵. (A factor of $(4\pi\sigma_0^2)$ should be added for each integrated mode.)

⁴The demonstration can be found for instance in [59] and [105].

⁵Surprisingly, the fact that the overlap formula is also valid for more than one mode is never mentioned yet not obvious a priori.

Purity By a simple application of the overlap formula, we obtain the equivalent formulation for the Wigner function

$$\mathcal{P} = \text{Tr}[\hat{\rho}^2] = 4\pi\sigma_0^2 \iint W^2(x, p) dx dp \leq 1 . \quad (1.55)$$

Fidelity Again, by applying the overlap formula on two states, one can write

$$\mathcal{F} = \text{Tr}[\hat{\rho}_1 \hat{\rho}_2] = 4\pi\sigma_0^2 \iint W_{\hat{\rho}_1}(x, p) W_{\hat{\rho}_2}(x, p) dx dp \leq 1 . \quad (1.56)$$

In the case of mixed states, as for the density matrix, the formula is more elaborated. However, this formula is still valid if at least one of the two states is pure [23], which is often the case as we want to compare a non-perfect experimental state with a target pure state.

Origin of phase space The value of the Wigner function at the origin of the phase space only depends on the diagonal elements of the density matrix

$$2\pi\sigma_0^2 W_{\hat{\rho}}(0, 0) = \sum_n (-1)^n \rho_{nn} . \quad (1.57)$$

Transposition Since $\hat{\rho}^T = \hat{\rho}^*$, the transposition of the density matrix translated in terms of Wigner function in

$$W_{\hat{\rho}^T}(x, y) = W_{\hat{\rho}}(x, -y) . \quad (1.58)$$

Bounds The values of the Wigner function are lower and upper bounded by

$$|W(x, p)| \leq \frac{1}{2\pi\sigma_0^2} . \quad (1.59)$$

1.3.3 Wigner function for operators

The density matrix being an Hermitian operator in an Hilbert space, the mathematical definition of the Wigner function can be also applied to any Hermitian operator:

$$W_{\mathbb{1}}(x, p) = \frac{1}{2\pi\sigma_0^2} \frac{1}{2} , \quad (1.60)$$

$$W_{\hat{x}}(x, p) = \frac{1}{2\pi\sigma_0^2} \frac{x}{2} , \quad (1.61)$$

$$W_{\frac{1}{2}\{\hat{x}, \hat{p}\}}(x, p) = \frac{1}{2\pi\sigma_0^2} \frac{xp}{2} , \quad (1.62)$$

$$W_{|x_\theta\rangle\langle x_\theta|}(x, p) = \frac{1}{2\pi\sigma_0^2} \frac{1}{2} \delta(x \cos \theta + p \sin \theta - x_\theta) . \quad (1.63)$$

Of course, all the specific properties of the density matrix that we have extended to the Wigner function formalism, for instance the trace equal to one, will not necessarily be valid for these operators as they do not correspond to physical states.

Other operators and effects of non-Hermitian operators on states can be found in chapter 4 of Ref. [26].

1.3.4 Other formulations of the Wigner function

Equation (1.43) is not the only formula for the Wigner function, it exists many other formulations.

An interesting one use the equation (1.57) which can be written with the help of the *parity operator* $\hat{P} = e^{i\pi\hat{n}}$

$$2\pi\sigma_0^2 W_{\hat{\rho}}(0,0) = \text{Tr}[\hat{\rho}\hat{P}] . \quad (1.64)$$

Therefore, as applying the displacement operator is equivalent to translate the Wigner function, it appears that we can express the Wigner function by the following way [34]

$$W(\alpha) = \frac{2}{\pi} \text{Tr}[\hat{D}(-\alpha)\hat{\rho}\hat{D}(\alpha)\hat{P}] . \quad (1.65)$$

Here, we do not use the quadrature variables but a complex number as the amplitude of a coherent state. Sometimes, to avoid any ambiguities, it is also noted with the conjugated values $W(\alpha, \alpha^*)$ but the Wigner function is still a function of two real variables per mode. The relationship between quadrature and complex amplitude is

$$W(\alpha, \alpha^*) = 4\sigma_0^2 W(x, p) , \quad (1.66)$$

which is obtained by simply substituting $\alpha = (x + ip)/2\sigma_0$.

1.4 Usual states in quantum optics

In the following, we review several states that we can encounter in quantum optics. We mainly give some useful formulas, yet no particular physical discussions. Most of them are pure states. Both descriptions are used: the density matrix or state vector within the photon number basis and the Wigner function.

1.4.1 Fock states

All the photon number states can be generated from the vacuum state by iterative application of the creation operator

$$|n\rangle = \frac{(\hat{a}^\dagger)^n}{\sqrt{n!}} |0\rangle . \quad (1.67)$$

These states constitute an orthonormal eigenbasis of the photon number operator, i.e. $\forall n, \hat{n}|n\rangle = n|n\rangle$, usually named *Fock basis*. It thus verifies orthogonality and unit norm $\forall k, n \langle k|n\rangle = \delta_{k,n}$ and, since the basis is complete, it satisfies the completeness relation

$$\sum_{n=0}^{\infty} |n\rangle\langle n| = \mathbb{1} . \quad (1.68)$$

As a consequence, any state can be decomposed on this basis

$$|\psi\rangle = \left(\sum_n |n\rangle\langle n| \right) |\psi\rangle \quad (1.69)$$

$$= \sum_n c_n |n\rangle, \text{ with } c_n = \langle n|\psi\rangle . \quad (1.70)$$

For a given Fock state $|n\rangle$, the general expression of the Wigner function is

$$W_{|n\rangle}(x, p) = \frac{(-1)^n}{2\pi\sigma_0^2} e^{-(x^2+p^2)/2\sigma_0^2} L_n \left(\frac{x^2+p^2}{\sigma_0^2} \right) , \quad (1.71)$$

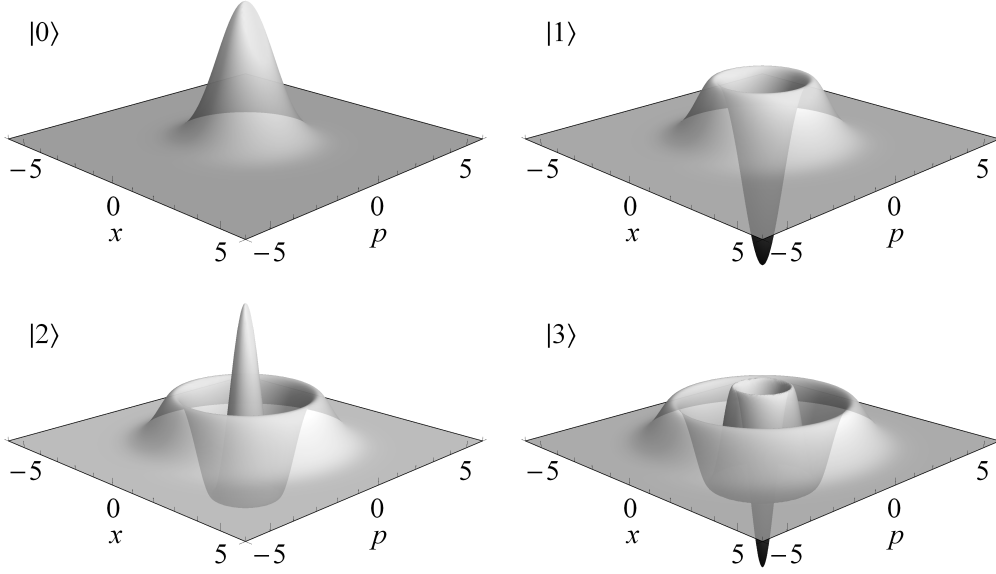


Figure 1.2: Wigner function of Fock states $|0\rangle$, $|1\rangle$, $|2\rangle$ and $|3\rangle$.

with L_n the n -th Laguerre polynomial. For instance, we give hereafter several Wigner functions of Fock states and the corresponding marginal distributions:

$$W_{|0\rangle} = \frac{1}{2\pi\sigma_0^2} e^{-(x^2+p^2)/2\sigma_0^2},$$

$$\int dp W_{|0\rangle} = \frac{1}{\sqrt{2\pi}\sigma_0} e^{-x^2/2\sigma_0^2}, \quad (1.72)$$

$$W_{|1\rangle} = \frac{1}{2\pi\sigma_0^2} e^{-(x^2+p^2)/2\sigma_0^2} \left(\frac{x^2+p^2}{\sigma_0^2} - 1 \right),$$

$$\int dp W_{|1\rangle} = \frac{1}{\sqrt{2\pi}\sigma_0} \frac{x^2}{\sigma_0^2} e^{-x^2/2\sigma_0^2}, \quad (1.73)$$

$$W_{|2\rangle} = \frac{1}{2\pi\sigma_0^2} e^{-(x^2+p^2)/2\sigma_0^2} \left(\frac{(x^2+p^2)^2}{2\sigma_0^4} - \frac{2(x^2+p^2)}{\sigma_0^2} + 1 \right),$$

$$\int dp W_{|2\rangle} = \frac{1}{\sqrt{2\pi}\sigma_0} e^{-x^2/2\sigma_0^2} \frac{1}{2} \left(\frac{x^2}{\sigma_0^2} - 1 \right)^2, \quad (1.74)$$

$$W_{|3\rangle} = \frac{1}{2\pi\sigma_0^2} e^{-(x^2+p^2)/2\sigma_0^2} \left(\frac{(x^2+p^2)^3}{6\sigma_0^6} - \frac{3(x^2+p^2)^2}{2\sigma_0^4} + \frac{3(x^2+p^2)}{\sigma_0^2} - 1 \right),$$

$$\int dp W_{|3\rangle} = \frac{1}{\sqrt{2\pi}\sigma_0} e^{-x^2/2\sigma_0^2} \frac{1}{6} \left(\frac{x^3}{\sigma_0^3} - \frac{3x}{\sigma_0} \right)^2. \quad (1.75)$$

The corresponding plots are given on figure 1.2. It is easy to see on these Wigner functions that the Fock states are phase invariant and, as a consequence, the marginal distributions do not depend on the phase.

We can also notice that all these states have a Wigner function that reaches the maximal value at the origin of the phase space with a sign given by the parity of the state

$$W_{|n\rangle}(0,0) = (-1)^n / 2\pi\sigma_0^2. \quad (1.76)$$

1.4.2 Coherent states

This is the state we have at the output of a laser (far above the threshold). It is often described as a “classical” Gaussian state (i.e. without negative values of Wigner function). Also called *Glauber state*, this state is often defined as the eigenvector of the annihilation operator

$$\hat{a}|\alpha\rangle = \alpha|\alpha\rangle . \quad (1.77)$$

The mean photon number is equal to the square of its amplitude

$$\langle \hat{n} \rangle_{|\alpha\rangle} = |\alpha|^2 . \quad (1.78)$$

We can also write the state as the action of the displacement operator on the vacuum state

$$\hat{D}(\alpha)|0\rangle = |\alpha\rangle , \quad (\alpha \in \mathbb{C}) \quad (1.79)$$

where the displacement operator is $\hat{D}(\alpha) = e^{\alpha\hat{a}^\dagger - \alpha^*\hat{a}}$. This can be simplified in the following way:

$$|\alpha\rangle = \hat{D}(\alpha)|0\rangle = e^{\alpha\hat{a}^\dagger - \alpha^*\hat{a}}|0\rangle = e^{-|\alpha|^2/2}e^{\alpha\hat{a}^\dagger}e^{-\alpha^*\hat{a}}|0\rangle = e^{-|\alpha|^2/2}e^{\alpha\hat{a}^\dagger}|0\rangle. \quad (1.80)$$

Therefore, we deduce from this expression its expansion in the Fock basis

$$|\alpha\rangle = e^{-|\alpha|^2/2} \sum_{n=0}^{+\infty} \frac{\alpha^n}{\sqrt{n!}} |n\rangle . \quad (1.81)$$

Two coherent states are not orthogonal

$$|\langle \alpha | \beta \rangle|^2 = e^{-|\beta - \alpha|^2} \quad \forall \alpha, \beta \in \mathbb{C} . \quad (1.82)$$

Nevertheless, they satisfy the completeness relation

$$\frac{1}{\pi} \int_{\mathbb{C}} d^2\alpha |\alpha\rangle \langle \alpha| = \mathbb{1} , \quad (1.83)$$

and thus constitute an over-complete non-orthogonal basis.

Now, if we look at the representation in the phase space (Fig. 1.3), it makes more sense than the state vector (or density matrix) as it correspond to a simple translation of the vacuum state Wigner function

$$W_{|\alpha\rangle}(x, p) = \frac{1}{2\pi\sigma_0^2} e^{-(x-a)^2/2\sigma_0^2 - (p-b)^2/2\sigma_0^2} , \quad (1.84)$$

with $\alpha = \frac{a + ib}{2\sigma_0}$.

Moreover, by analogy with the Fresnel representation where the state would be represented by a dot, this Gaussian shape highlights the vacuum fluctuations of the electromagnetic field around a mean value α . Note that, here, the fluctuations saturate the Heisenberg inequality $\sigma_x = \sigma_p = \sigma_0$.

1.4.3 Squeezed vacuum state

Although the vacuum state shows some fluctuations, they can be *squeezed*. The variance normalized to the variance of the vacuum fluctuation $s = \sigma_x^2/\sigma_0^2$ is called the *squeezing factor*. It is often given in a logarithmic scale

$$s_{dB} = -10 \log_{10} s = -10 \log_{10} \left(\frac{1 - \lambda}{1 + \lambda} \right) = \frac{20}{\ln 10} \zeta , \quad (1.85)$$

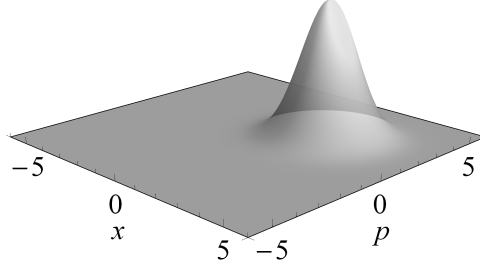


Figure 1.3: Wigner function of a coherent state

with ζ the *squeezing parameter* that we can relate to the *squeezing factor* $s = e^{-2\zeta}$ and $\lambda = \text{th}\zeta$. The state can be written as:

$$|\psi_{sq}\rangle = (1 - \lambda^2)^{1/4} \sum_{n=0}^{\infty} \binom{2n}{n}^{1/2} \left(\frac{\lambda}{2}\right)^n |2n\rangle. \quad (1.86)$$

The mean photon number of this state is

$$\langle \hat{n} \rangle = \frac{1}{4} \left(s + \frac{1}{s} - 2 \right) \quad (1.87)$$

We show on figure 1.4 how the populations change with the level of squeezing.

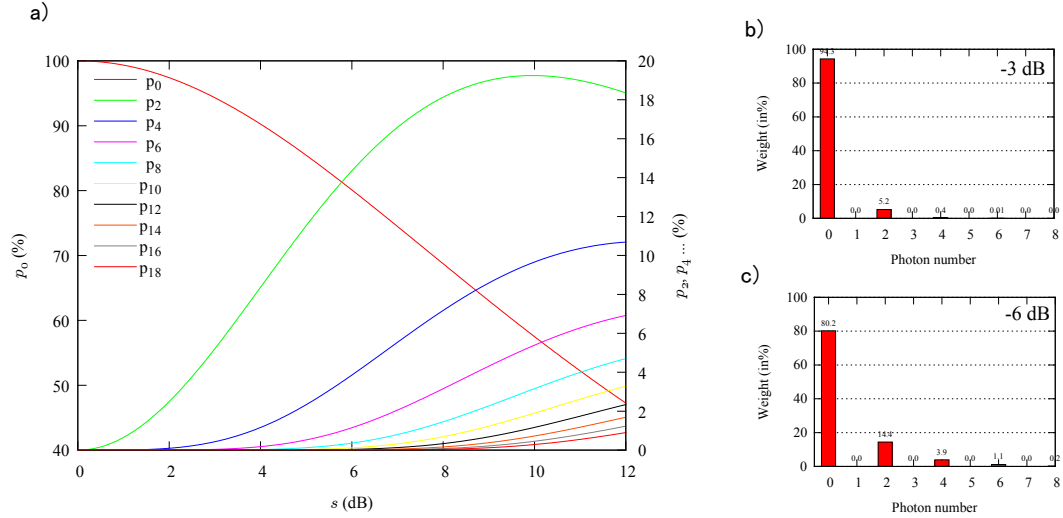


Figure 1.4: a) Evolution of the populations as a function of the squeezing value in dB scale. (left scale for p_0 and right scale for $p_{n>0}$). b) For 3 dB of squeezing, although the vacuum component is as high as 94% and the two photon component around 5% ($\langle \hat{n} \rangle = 0.12$), the vacuum fluctuations are reduced by a factor of 2. c) For 6 dB, the two photons component is more important ($\langle \hat{n} \rangle = 0.56$). The infinite squeezing corresponds to the state $|x = 0\rangle$, an eigenstate of the quadrature operator \hat{x} .

The corresponding wave-function is

$$\psi_{sq}(x) = \frac{1}{(s\pi)^{1/4}} e^{-x^2/2s} \quad (1.88)$$

The squeezing operator is

$$\hat{S}(\zeta) = e^{\frac{\zeta}{2}(a^2 - a^{\dagger 2})}. \quad (1.89)$$

More generally, if $\zeta \in \mathbb{C}$ the compression operator is written

$$\hat{S}(\zeta) = e^{\frac{\zeta^*}{2}a^2 - \frac{\zeta}{2}a^{\dagger 2}}. \quad (1.90)$$

If we note $\lambda = \text{th} |\zeta|$ and $\zeta/|\zeta| = e^{i\phi}$, the effect of this operator on the vacuum state is ⁶

$$\hat{S}(\zeta)|0\rangle = (1 - \lambda)^{1/4} e^{-\frac{\lambda}{2}e^{i\phi}a^{\dagger 2}}|0\rangle. \quad (1.91)$$

Of course, with the appropriate rotation in the phase space, we can have $\phi = 0$.

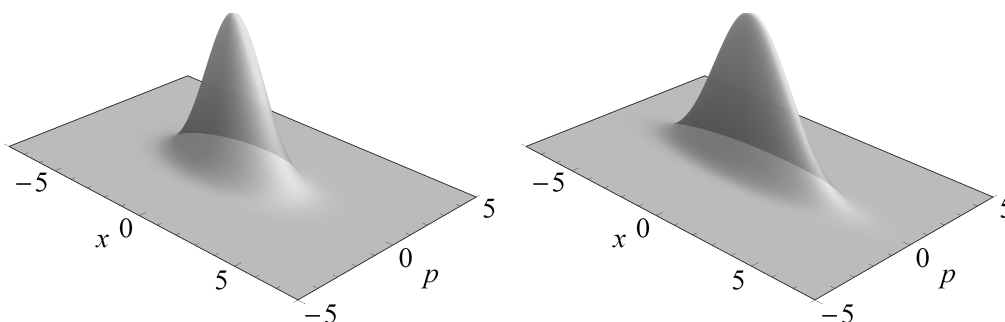


Figure 1.5: Wigner function of squeezed vacuum states for 3 dB on the left and 6 dB on the right

The Wigner function of the squeezed vacuum state is given by

$$W_{sq}(x, p) = \frac{1}{2\pi\sigma_0^2} e^{-\frac{(x-\langle x \rangle)^2}{2\sigma_0^2 s} - \frac{(p-\langle p \rangle)^2}{2\sigma_0^2/s}}. \quad (1.92)$$

It is plotted on figure 1.5. As we can notice, it corresponds to the Wigner function of the vacuum state squeezed along one axis. However, the uncertainty relation being satisfied $\sigma_x \sigma_p \geq \sigma_0^2$, the Gaussian shape is “anti-squeezed” along the orthogonal axis. As for the previous state, the vacuum state also saturates the Heisenberg inequality $\sigma_x^2 = s\sigma_0^2$ and $\sigma_p^2 = \frac{1}{s}\sigma_0^2$.

1.4.4 Two-mode squeezed vacuum state

This is a two-mode state and it is called *two-mode squeezed vacuum* since it can be simply obtain by the mixing of two squeezed vacuum states on a 50:50 beam-splitter and vice versa. It is also often called *EPR* state in reference to the paradox for entangled states, but sometimes by misuse because it not always satisfies the criteria. Written in the Fock basis, it can be read as:

$$|\psi_{sq}\rangle_{ab} = (1 - \lambda^2)^{1/2} \sum_{n=0}^{\infty} \lambda^n |n\rangle_a |n\rangle_b. \quad (1.93)$$

The Wigner function can be written as two squeezed vacuum states after combination on a beam-splitter

$$W(x_a, p_a, x_b, p_b) = \frac{1}{(2\pi\sigma_0^2)^2} e^{-\frac{(x_a - x_b)^2}{4\sigma_0^2 s} - \frac{(x_a + x_b)^2}{4\sigma_0^2/s} - \frac{(p_a - p_b)^2}{4\sigma_0^2/s} - \frac{(p_a + p_b)^2}{4\sigma_0^2 s}} \quad (1.94)$$

⁶The proof can be found in [22] and [5].

If we consider only one local mode, i.e. we lose the information of one of them, the state is integrated on the lost mode

$$\int_a W_{\text{EPR}} = \frac{1}{\pi} \frac{1}{\sigma_x^2 + \sigma_p^2} e^{-(x^2+p^2)/(\sigma_x^2+\sigma_p^2)}, \quad (1.95)$$

we obtain a thermal state as described now.

1.4.5 Thermal states

Although it is not very useful in quantum optics, we can encounter the thermal state in non-perfect experiment and other physical phenomenon (black body radiation, sunlight,...). For instance, this is the state we obtain if we trace one mode of a two-mode squeezed vacuum.

It is a statistical mixture of Fock states

$$\hat{\rho}_{th} = \sum p_T(n) |n\rangle\langle n|, \quad (1.96)$$

with $p_T(n) = (1 - e^{-\hbar\omega/k_B T}) e^{-n\hbar\omega/k_B T}$. We can also use the mean photon number

$$n_{th} = \frac{1}{e^{\hbar\omega/k_B T} - 1}. \quad (1.97)$$

Therefore, the photon number probability becomes

$$p_T(n) = \frac{n_{th}^n}{(n_{th} + 1)^{n+1}}. \quad (1.98)$$

Thanks to this expression, the state can also be expressed as the following

$$\hat{\rho}_{th} = \frac{1}{n_{th} + 1} \left(\frac{n_{th}}{n_{th} + 1} \right)^{\hat{n}}. \quad (1.99)$$

And in the basis of the coherent states it becomes

$$\hat{\rho}_{th} = \frac{1}{\pi n_{th}} \int d^2\alpha e^{-|\alpha|^2/n_{th}} |\alpha\rangle\langle\alpha| \quad (1.100)$$

The Wigner function of the thermal state is a Gaussian phase invariant function, the same as the vacuum state but with a larger standard deviation

$$W(x, p) = \frac{1}{2\pi\sigma_{th}^2} e^{-(x^2+p^2)/2\sigma_{th}^2}. \quad (1.101)$$

The variance of this state is $\sigma_{th}^2 = (2n_{th} + 1)\sigma_0^2$, i.e. the one of the vacuum with an additional noise.

1.4.6 Gaussian states

This is a more general name that encompasses the thermal state, the coherent state, the squeezed vacuum (or squeezed coherent state), the two-mode squeezed vacuum. But it also includes the mixed state of these ones. (e.g. pure Gaussian states after lossy propagation.) They are fully described with the *covariance matrix*. For a single mode state

$$\Sigma = \begin{pmatrix} \langle \hat{x}^2 \rangle - \langle \hat{x} \rangle^2 & \langle \frac{1}{2} \{ \hat{x}, \hat{p} \} \rangle - \langle \hat{x} \rangle \langle \hat{p} \rangle \\ \langle \frac{1}{2} \{ \hat{x}, \hat{p} \} \rangle - \langle \hat{x} \rangle \langle \hat{p} \rangle & \langle \hat{p}^2 \rangle - \langle \hat{p} \rangle^2 \end{pmatrix}. \quad (1.102)$$

By using the following notation

$$\mathbf{X} = \begin{pmatrix} x \\ p \end{pmatrix}, \quad \bar{\mathbf{X}} = \begin{pmatrix} \langle \hat{x} \rangle \\ \langle \hat{p} \rangle \end{pmatrix}, \quad (1.103)$$

it can be easily extended to more than one mode. We then obtain a compact form of the Wigner function

$$W_{\text{gauss}}(\mathbf{X}) = \frac{1}{(2\pi)^N \sqrt{\det(\boldsymbol{\Sigma})}} e^{-\frac{1}{2}(\mathbf{X}-\bar{\mathbf{X}})^T \boldsymbol{\Sigma}^{-1}(\mathbf{X}-\bar{\mathbf{X}})}, \quad (1.104)$$

with N the number of modes.

The covariance matrix being real and symmetric, thanks to the spectral theorem, it can be diagonalized with positive eigenvalues. Thus, we conveniently express the Wigner function in the eigenbasis of a single-mode Gaussian state

$$W_{\text{gauss}}(x, p) = \frac{1}{2\pi\sigma_x\sigma_p} e^{-\frac{(x-x_0)^2}{2\sigma_x^2} - \frac{(p-p_0)^2}{2\sigma_p^2}}. \quad (1.105)$$

It is actually a simple rotation in the phase space.

The corresponding marginal distribution is

$$\int W_{\text{gauss}}(x_\theta, p_\theta) dp_\theta = \mathcal{P}(x_\theta) = \frac{1}{\sqrt{2\pi\sigma_\theta^2}} e^{-(x_\theta - x_0(\theta))^2 / 2\sigma_\theta^2}, \quad (1.106)$$

with $\sigma_\theta^2 = \sigma_x^2 \sin^2 \theta + \sigma_p^2 \cos^2 \theta$ and $x_0(\theta) = x_0 \cos \theta + p_0 \sin \theta$.

The purity of the state, whatever its dimension, is directly obtained with the covariance matrix

$$\mathcal{P} = \text{Tr}[\hat{\rho}^2] = \frac{1}{\sqrt{\det(\boldsymbol{\Sigma})}}. \quad (1.107)$$

Hence, for a single-mode Gaussian state with the eigenvalues σ_x^2, σ_p^2 we have $\mathcal{P} = 1/\sigma_x\sigma_p$.

We can also describe this state as a squeezed thermal state:

$$\frac{\sigma_x^2}{\sigma_0^2} = (2n_{th} + 1)e^{-2r} \quad \frac{\sigma_p^2}{\sigma_0^2} = (2n_{th} + 1)e^{2r}. \quad (1.108)$$

The mean photon number is then:

$$\langle \hat{n} \rangle = \frac{1}{4\sigma_0^2} (\sigma_x^2 + \sigma_p^2 - 2\sigma_0^2) = \frac{1}{4}(s_x + s_p - 2). \quad (1.109)$$

1.4.7 Schrödinger's cat states

This state refers to the gedanken experiment of Schrödinger [106] in which he highlighted the weird consequences of quantum mechanics when extended to our world (i.e. macroscopic systems). Indeed, superposition of very different states is possible thanks to the superposition principle, for instance the two levels of an atom. How such a situation could happen in our world? In optics, the idea consists in a superposition of two orthogonal “classical” states [27], i.e. two coherent states with large amplitudes. We thus call this state *optical Schrödinger cat state*

$$|cat_\phi\rangle = \frac{1}{\mathcal{N}_\phi} (|\alpha\rangle + e^{i\phi} |-\alpha\rangle), \quad (1.110)$$

where $|\alpha\rangle$ is a coherent state of amplitude α and $\mathcal{N}_\phi = \sqrt{2(1 + \cos \phi e^{-2|\alpha|^2})}$ the normalization factor.

Nevertheless, the use this label for this state can be questionable. Does it completely match the idea of Schrödinger? We could answer “yes” about the idea: we have quantum phenomenon at the macroscopic scale. But concerning the picture used by Schrödinger, the answer could be “no”: indeed, it relies on entanglement between a quantum particle with a classical/macroscopic object. That is why *coherent state superposition* (CSS) is in principle preferred. However, when α is small we also talk about “kitten”.

Two specific cases are interesting. When the phase of the superposition $\phi = 0$, the state is a superposition of even photon-numbers only and we call this state an *even cat states*.

$$\begin{aligned} |cat_+\rangle &= \frac{1}{\mathcal{N}_+}(|\alpha\rangle + |-\alpha\rangle) \\ &= \frac{2}{\mathcal{N}_+} e^{-|\alpha|^2/2} \sum_{n=0}^{+\infty} \frac{\alpha^{2n}}{\sqrt{(2n)!}} |2n\rangle. \end{aligned} \quad (1.111)$$

With $\phi = \pi$, the state is this time a superposition of odd Fock states and logically we call it an *odd cat state*.

$$\begin{aligned} |cat_-\rangle &= \frac{1}{\mathcal{N}_-}(|\alpha\rangle - |-\alpha\rangle) \\ &= \frac{2}{\mathcal{N}_-} e^{-|\alpha|^2/2} \sum_{n=0}^{+\infty} \frac{\alpha^{2n+1}}{\sqrt{(2n+1)!}} |2n+1\rangle. \end{aligned} \quad (1.112)$$

We give on figure 1.6 and 1.7 the population of both cats as a function of the amplitude α .

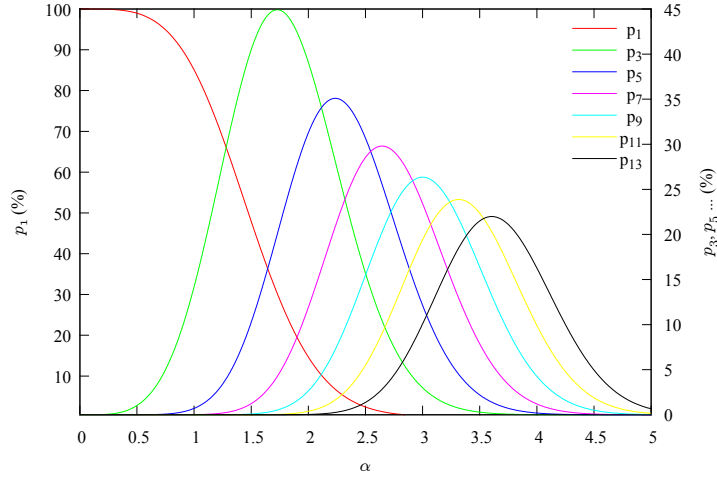


Figure 1.6: Evolution of the population of the odd cat state $|cat_-\rangle$ as a function of the amplitude α . (left scale for p_1 and right scale for $p_{n>1}$)

The marginal distribution for the quadrature \hat{x}_θ is given by:

$$\mathcal{P}_{|cat_\phi\rangle}(x, \theta) = |\langle x, \theta | cat_\phi \rangle|^2. \quad (1.113)$$

As

$$|\psi_{\pm\alpha}(x, \theta)|^2 = \frac{1}{\sqrt{2\pi}\sigma_0} \exp\left(-\left(\frac{x}{\sigma_0\sqrt{2}} \mp |\alpha|\sqrt{2}\cos(\Phi - \theta)\right)^2\right) \quad (1.114)$$

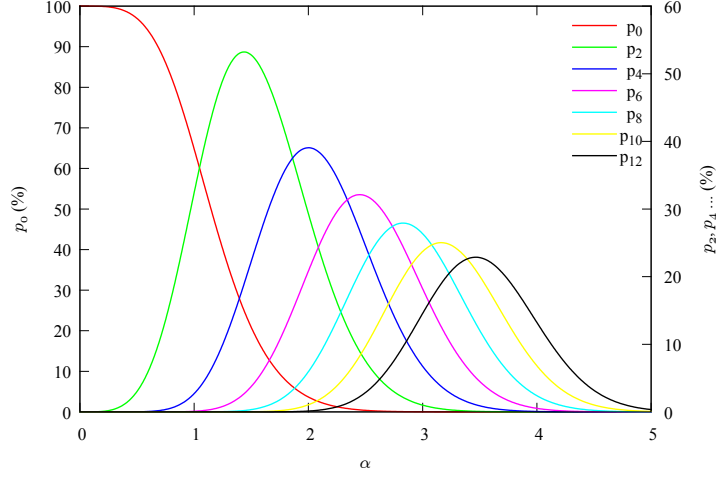


Figure 1.7: Evolution of the population of the even cat state $|cat_+\rangle$ as a function of the amplitude α . (left scale for p_1 and right scale for $p_{n>1}$)

and

$$e^{i\phi}\psi_{-\alpha}\psi_{\alpha}^* + e^{-i\phi}\psi_{\alpha}\psi_{-\alpha}^* = \frac{1}{\sqrt{2\pi}\sigma_0} \exp\left(-2|\alpha|^2 \cos^2(\Phi - \theta) - \left(\frac{x}{\sigma_0\sqrt{2}}\right)^2\right) \quad (1.115)$$

$$\times 2 \cos\left(2\sqrt{2}\frac{x}{\sigma_0\sqrt{2}}|\alpha|\sin(\Phi - \theta) + \phi\right) \quad (1.116)$$

with $\alpha = e^{i\Phi}|\alpha|$ and θ angle of the quadrature (ϕ is the phase of the superposition and Φ is the phase of the coherent state $|\alpha\rangle$). The marginal distribution is thus given by

$$\mathcal{P}_{|cat_{\phi}\rangle}(x) = \frac{|\psi_{+\alpha}(x)|^2 + e^{i\phi}\psi_{-\alpha}\psi_{\alpha}^* + e^{-i\phi}\psi_{\alpha}\psi_{-\alpha}^* + |\psi_{-\alpha}(x)|^2}{1 + \cos(\phi)e^{-2|\alpha|^2}} \quad (1.117)$$

On figure 1.8, we have plotted the marginal distributions associated with two quadratures ($\theta = 0$ and $\theta = \pi/2$). For one, we see a profile of a mixture of two coherent states with opposite phases but, on the other quadrature, the Gaussian shape of the expected mixture of coherent state is modulated by some fringes.

If we choose a quadrature basis such as the amplitude is real ($\alpha \in \mathbb{R}_+$), the Wigner function of the cat state is

$$W_{|cat_{\phi}\rangle}(x, p) = \frac{e^{-(x^2+p^2)/2\sigma_0^2}}{2\pi\sigma_0^2(1 + \cos\phi e^{-2\alpha^2})} \left[e^{-2\alpha^2} \text{ch}(2\alpha x/\sigma_0) + \cos(2\alpha p/\sigma_0 - \phi) \right] \quad (1.118)$$

$$= \frac{1}{1 + \cos\phi e^{-2\alpha^2}} \left[\frac{1}{2}W_{|\alpha\rangle}(x, p) + \frac{1}{2}W_{|-\alpha\rangle}(x, p) + W_{|0\rangle}(x, p) \cos(2\alpha p/\sigma_0 - \phi) \right]. \quad (1.119)$$

By looking at this expression and the associated plots on figure 1.9, we can recognize the two coherent states via the Gaussian function times the hyperbolic cosine. They correspond to the terms $|\alpha\rangle\langle\alpha|$ and $|-\alpha\rangle\langle-\alpha|$. The second part, the cosine function modulated by a Gaussian function, gives the fringes of the “quantum interference” in the phase space. It corresponds to the cross terms (or coherences) $|-\alpha\rangle\langle\alpha|$ and $|\alpha\rangle\langle-\alpha|$. As we can see in this latter the phase ϕ of the superposition simply shift the cosine pattern (but the Gaussian

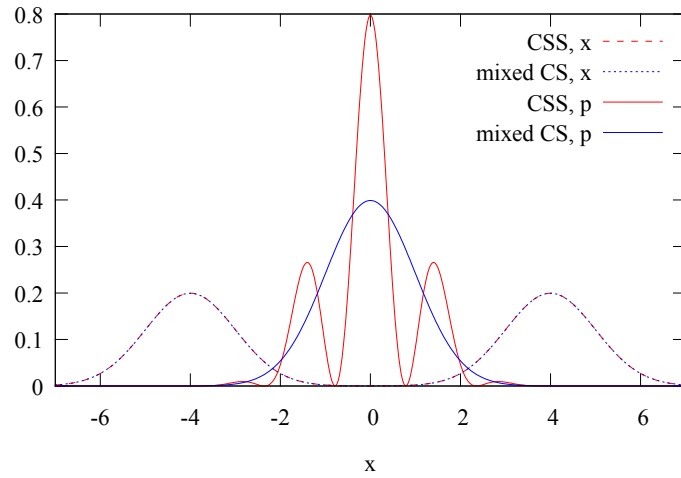


Figure 1.8: Marginal distributions of even cat state (CSS) and mixture of two coherent states of opposite phases for two conjugated quadratures. ($\alpha = 2$) For the quadrature x it is not possible to distinguish both states whereas they are completely different for the conjugate quadrature.

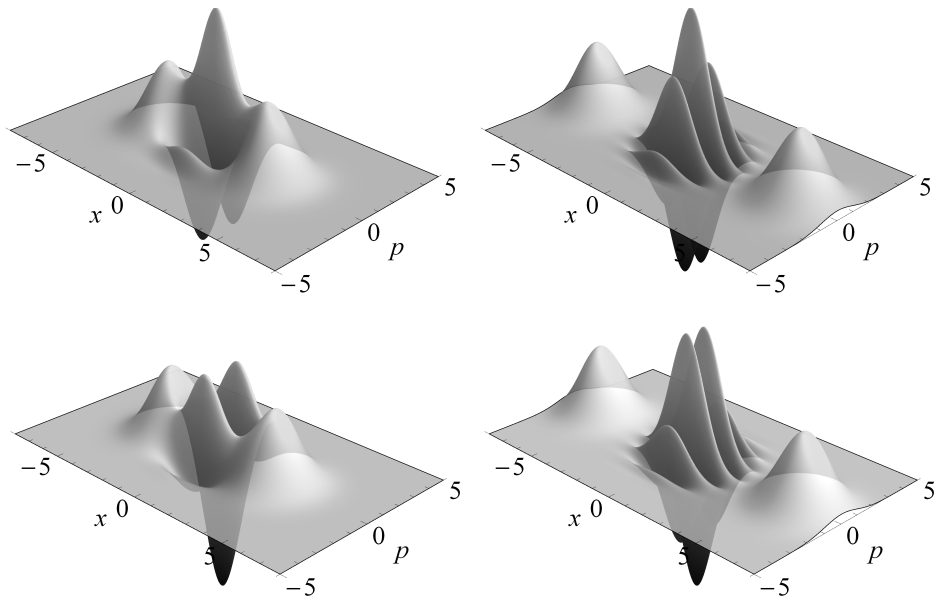


Figure 1.9: Wigner function of the even cat states $|cat_+\rangle$ on the top and odd cat states $|cat_-\rangle$ at the bottom, for a size $\alpha = 1.5$ on the left and $\alpha = 3$ on the right.

envelop stay the same). Hence, we switch from the even cat state to the odd cat state with a π drift of the fringes.

1.5 Gaussianity

Amongst the various states presented before, we have noticed that some of them have Wigner functions with negative values whereas some others are everywhere positive. Interestingly, most of the states that have a positive Wigner function have actually a gaussian Wigner function. We show below that gaussianity constitute an important criteria to, some how, “classify” quantum states.

1.5.1 Hudson-Piquet theorem

The negativity is a crucial property of the Wigner function, but what can we say about this property? What does it mean physically? Failing to find a satisfying answer to this question, an interesting theorem called the *Hudson-Piquet’s theorem* gives a beginning of answer. This theorem states [50]:

A necessary and sufficient condition for the Wigner density W corresponding to the Schrödinger state vector ψ to be a true probability is that ψ be the exponential of quadratic polynomial.

Where ψ denotes the wave function of the state. This can be rephrased: *For a pure state, the Wigner function is everywhere positive if and only if it is a Gaussian function.* The corresponding states are then logically called Gaussian states. As a consequence, any state with some negative values is called *non-Gaussian* state. Hence, the states are now separated into two categories.

Moreover, it is important to point out that this theorem is only valid for pure states. Indeed, it exists some non-Gaussian mixed states without negative values of the Wigner function. Moreover, it doesn’t exist a generalization of this theorem (i.e. to mixed states) [66]. For this reason, the negativity still keeps a part of “mystery”.

1.5.2 Gaussian operations

We have seen various operators that generate some Gaussian states, these are called *Gaussian operations*. Interestingly, they map Gaussian states to other Gaussian states. Thus, all the pure Gaussian states can be expressed as a combination of these operators applied to the vacuum state.

There are four operations [119], three are single-mode and one spans on two modes. This forms a complete basis of unitary affine application on quadratures variables $\hat{\mathbf{X}} = (\hat{x}_1, \hat{p}_1, \hat{x}_2, \hat{p}_2, \dots)$

$$\mathcal{O}_G : \hat{\mathbf{X}} \mapsto \mathbf{U}\hat{\mathbf{X}} + \mathbf{X}_0 . \quad (1.120)$$

Interestingly, this feature translates to the Wigner function by simply applying the transformation \mathcal{O}_G on the variables of the Wigner function (instead of the quadrature with the density matrix). All of these operators are unitary, $\hat{U}^\dagger \hat{U} = \mathbf{1}$. They are described by interaction Hamiltonian with at maximum quadratic annihilation/creation operators.

Beam-splitter This two-mode operator is written

$$\hat{B}(\theta) = e^{\theta(\hat{a}^\dagger \hat{b} - \hat{a} \hat{b}^\dagger)} , \quad (1.121)$$

where $t = \cos \theta$ and $r = \sin \theta$ are the transmission and reflection coefficients in amplitude (thus the square for energy coefficients). The effect on the creation/annihilation operators

is similar to one on the classical field

$$\hat{B}^\dagger \hat{a} \hat{B} = t\hat{a} + r\hat{b} \quad \hat{B}^\dagger \hat{a}^\dagger \hat{B} = t\hat{a}^\dagger + r\hat{b}^\dagger \quad (1.122)$$

$$\hat{B}^\dagger \hat{b} \hat{B} = t\hat{b} - r\hat{a} \quad \hat{B}^\dagger \hat{b}^\dagger \hat{B} = t\hat{b}^\dagger - r\hat{a}^\dagger \quad (1.123)$$

The action on the quadrature is similar to the ones on the annihilation/creation operators:

$$\hat{B}^\dagger \hat{x}_a \hat{B} = t\hat{x}_a + r\hat{x}_b \quad \hat{B}^\dagger \hat{p}_a \hat{B} = t\hat{p}_a + r\hat{p}_b \quad (1.124)$$

$$\hat{B}^\dagger \hat{x}_b \hat{B} = t\hat{x}_b - r\hat{x}_a \quad \hat{B}^\dagger \hat{p}_b \hat{B} = t\hat{p}_b - r\hat{p}_a \quad (1.125)$$

This operator can also describe the change of polarization basis.⁷

Displacement Already introduced previously, the displacement operator is

$$\hat{D}(\alpha) = e^{\alpha \hat{a}^\dagger - \alpha^* \hat{a}} . \quad (1.129)$$

Its action on the annihilation/creation operators is sum up by

$$\hat{D}(\alpha)^\dagger \hat{a} \hat{D}(\alpha) = \hat{a} + \alpha , \quad \hat{D}(\alpha)^\dagger \hat{a}^\dagger \hat{D}(\alpha) = \hat{a}^\dagger + \alpha^* . \quad (1.130)$$

The effect on the phase space is more intuitive, it corresponds indeed to a translation in the phase space

$$\hat{D}(\alpha)^\dagger \hat{x} \hat{D}(\alpha) = \hat{x} + 2\sigma_0 \Re[\alpha] , \quad \hat{D}(\alpha)^\dagger \hat{p} \hat{D}(\alpha) = \hat{p} + 2\sigma_0 \Im[\alpha] . \quad (1.131)$$

This transformation can be obtained by mixing a state $|\psi\rangle$ and a bright coherent state on a high transmission beam-splitter $1 - \eta \ll 1$.

$$\hat{B}_\eta |\alpha\rangle_a |\psi\rangle_b = \hat{B}_\eta \hat{D}_a(\alpha) |0\rangle_a |\psi\rangle_b \quad (1.132)$$

$$= \hat{B}_\eta \hat{D}_a(\alpha) \hat{B}_\eta^\dagger \hat{B}_\eta |0\rangle_a |\psi\rangle_b \quad (1.133)$$

$$\sim \hat{D}_a(\alpha) \hat{D}_b(\sqrt{1-\eta}\alpha) \hat{B}_\eta |0\rangle_a |\psi\rangle_b . \quad (1.134)$$

The mode b is displaced in the phase space of $\sqrt{1-T}\alpha$.

Phase-shift The phase shift operator is

$$\hat{U}(\theta) = e^{-i\theta \hat{n}} . \quad (1.135)$$

It adds a phase term on the annihilation/creation operators

$$\hat{U}^\dagger \hat{a} \hat{U} = \hat{a} e^{-i\theta} , \quad \hat{U}^\dagger \hat{a}^\dagger \hat{U} = \hat{a}^\dagger e^{i\theta} . \quad (1.136)$$

The quadrature operators are changed by a rotation

$$\hat{x}_\theta = \hat{U}^\dagger \hat{x} \hat{U} = \hat{x} \cos \theta + \hat{p} \sin \theta , \quad \hat{p}_\theta = \hat{U}^\dagger \hat{p} \hat{U} = -\hat{x} \sin \theta + \hat{p} \cos \theta , \quad (1.137)$$

7

$$\hat{B}(\theta, \phi) = e^{\theta(e^{i\phi} \hat{a}^\dagger \hat{b} - e^{-i\phi} \hat{a} \hat{b}^\dagger)} , \quad (1.126)$$

$$\hat{B}^\dagger \hat{a} \hat{B} = t\hat{a} + r e^{i\phi} \hat{b} \quad \hat{B}^\dagger \hat{a}^\dagger \hat{B} = t\hat{a}^\dagger + r e^{-i\phi} \hat{b}^\dagger \quad (1.127)$$

$$\hat{B}^\dagger \hat{b} \hat{B} = t\hat{b} - r e^{-i\phi} \hat{a} \quad \hat{B}^\dagger \hat{b}^\dagger \hat{B} = t\hat{b}^\dagger - r e^{i\phi} \hat{a}^\dagger \quad (1.128)$$

$$\hat{x}_\theta = \sigma_0(\hat{a}e^{-i\theta} + \hat{a}^\dagger e^{i\theta}) . \quad (1.138)$$

The state is rotated in the phase space by an angle $-\theta$ (clockwise) which is also equivalent to rotate the quadrature (counterclockwise) by an angle θ .

We note that it corresponds to the evolution of the free Hamiltonian $\hat{H} = \hbar\omega[\hat{n} + 1/2]$. Indeed, with the Heisenberg picture we have the time evolution $\hat{U}(t) = e^{-i\hat{H}t/\hbar} = e^{-i\omega t[\hat{n}+1/2]}$ (the 1/2 can be removed as it only changes the global phase). This evolution is relative to a reference. Practically, if the two beams are on the same spatial mode we can use some combination of wave-plates, otherwise a simple small change of path length is enough. Usually, this is realized by using piezoelectric stacks to increase of few wavelengths the optical path.

Squeezing The squeezing operator is⁸

$$\hat{S}(\zeta) = e^{\frac{\zeta}{2}(\hat{a}^2 - \hat{a}^{\dagger 2})} . \quad (1.139)$$

The effect on the creation and annihilation operators is

$$\hat{S}^\dagger \hat{a} \hat{S} = \hat{a} \operatorname{ch} \zeta - \hat{a}^\dagger \operatorname{sh} \zeta , \quad \hat{S}^\dagger \hat{a}^\dagger \hat{S} = \hat{a}^\dagger \operatorname{ch} \zeta - \hat{a} \operatorname{sh} \zeta . \quad (1.140)$$

The effect on the quadratures is equivalent to a rescaling with invert factors

$$\hat{S}^\dagger \hat{x} \hat{S} = \hat{x} e^{-\zeta} , \quad \hat{S}^\dagger \hat{p} \hat{S} = \hat{p} e^{+\zeta} . \quad (1.141)$$

This operation is obtained by parametric interaction. It is experimentally more difficult to realize. In contrast with all the previous ones, this operation requires non-linear optics, as it will be seen in chapter 3.

1.6 Conclusion

We have recalled the main descriptions of quantum states: the density matrix which is particularly appropriate when a system is not perfectly controlled; and the Wigner function for which the physical interpretation is often easier than the density matrix. Furthermore the density matrix appear to be a “natural” description when dealing with the corpuscular aspect of the quantum mechanics (*discrete*) and the Wigner function when dealing with waves (*continuous*). We have also used these two descriptions to present the quantum states that are often encountered in quantum optics in theory and experiments.

However, in contrast to the density matrix, the Wigner has the singular feature to have negative values (whereas it is mostly interpreted as a kind of probability density). Interestingly, not all the states show this particularity. Thanks to the Hudson-Piquet theorem, quantum state can be divided in two categories: the Gaussian and the non-Gaussian states. On the other hand, it turns out that Gaussian states can be generated, and are stable, with a set of operators, thus called Gaussian operators.

Since we have defined the various quantum states we are going to work with, we need to interact (manipulate, probe,...) with them. This can be efficiently performed by measurements. In the following chapter, we present various kind of measurements and how they give information about a quantum states, but also how they modify it. Again, we will use both formalisms, Fock basis and Wigner functions.

⁸if ζ is a complex number the operator is written $\hat{S}(\zeta) = \exp[\frac{\zeta}{2}\hat{a}^2 - \frac{\zeta^*}{2}\hat{a}^{\dagger 2}]$ which is equivalent to apply a phase shift $\hat{U}^\dagger \hat{S} \hat{U}$

2 | Quantum Measurements

Without craftsmanship, inspiration is a mere reed shaken in the wind.

JOHANNES BRAHMS

In quantum information protocols, the measurement is a key element: the result of the measurement is as important as the physical effect on the measured state. Indeed, as in classical physics, the measurement gives some information about a system but, in the quantum theory the measurement also affect the measured system. Here, we describe the measurement with in mind these two aspects. More specifically, we will distinguish, as for quantum states, Gaussian and non-Gaussian measurements where the Wigner function associated to a measurement can also show some negative values. One will be useful to manipulate/modified quantum state of light whereas the other will be used to characterized the quantum state of light.

We remind here the formalism of *Positive Operator Valued Measures* (POVM) to generally describe a measurement. Then, we discuss two widely used detectors: the single-photon detector and the homodyne detection. We end by a brief review of the different techniques of states reconstruction, the so-called *quantum state tomography*, with an emphasis on the different possible processings. (Non-demolition measurements are not considered here as they will be not used afterwards.)

2.1	Formalism of the measurement	28
2.1.1	Positive Operator Valued Measures	28
2.1.2	Conditional preparation of quantum state	29
2.2	Photon detectors	30
2.2.1	<i>on/off</i> detectors	30
2.2.2	Limited efficiency	31
2.2.3	Noisy detector	32
2.2.4	Detection of two photons	33
2.3	Homodyne measurement	34
2.3.1	Principle of the homodyne detection	35
2.3.2	POVM of the homodyne measurement	37
2.4	State reconstructions	37
2.4.1	Radon transform	38
2.4.2	Abel transform	38
2.4.3	Phase averaging and moments	39
2.4.4	Pattern functions	40
2.4.5	MaxLik algorithm	42
2.5	Conclusion	43

2.1 Formalism of the measurement

This topic gives rise mainly two difficulties: the physical interpretation of the quantum measurement on one hand and its formalism on the other hand. Even though the first one is still difficult conceptually, the formalism of the measurement is nowadays satisfying, the measurement apparatus can be simply described as a black box giving different possible outputs.

For more details, the reader can refer to the book of Nielsen and Chuang [85] section 2.2 where are detailed the different approaches of measurement formalism.

2.1.1 Positive Operator Valued Measures

Often, the basics of measurement are introduced via the so-called *observable* operators which are associated with physical quantity. These operators are Hermitian and can be thus decomposed in the basis of eigenstates. For instance, the observable \hat{A} is written in its eigenbasis $\{|\psi_\lambda\rangle\}$

$$\hat{A} = \sum_{\lambda} \lambda |\psi_\lambda\rangle\langle\psi_\lambda| , \quad (2.1)$$

with each eigenvalue λ stand for the measurement results. Each element being a projector, we talk about *projective measurements*. Moreover, they are all orthogonal. Hence, if one measures λ and the eigenvalue is not degenerate, the state after the measurement will be in the eigenstate $|\psi_\lambda\rangle$.

However, this model for measurements is not fully satisfying, at least from an experimental point of view. Indeed, the link with a realistic device in the lab is not straightforward, this approach focuses more on what we would like to measure than what the apparatus measures in reality. In the so-called *generalized measurement*, the approach is different and, as expected, more general.

Let us define a set of measurement operators $\{\hat{M}_m\}$ where each index corresponds to a measurement outcome. Again, here, we do not start from the physical quantity we would like to measure but, given an answer from the measurement apparatus, we focus on the information it gives. Moreover, compared to the projective measurements, the measurement operators are now not necessarily Hermitian, neither orthogonal nor projectors. The measurement probability is

$$p(m) = \langle\psi|\hat{M}_m^\dagger\hat{M}_m|\psi\rangle . \quad (2.2)$$

Thus these operators follow the completeness relation (to conserve the probability)

$$\sum_m \hat{M}_m^\dagger\hat{M}_m = \hat{\mathbb{1}} . \quad (2.3)$$

After measurement, the state becomes¹

$$|\psi_m\rangle = \frac{\hat{M}_m|\psi\rangle}{\sqrt{p(m)}} . \quad (2.4)$$

These expressions can be extended to the density matrix formalism

$$\hat{\rho}_m = \frac{\hat{M}_m\hat{\rho}\hat{M}_m^\dagger}{p(m)} , \quad (2.5)$$

with the outcome probability

$$p(m) = \text{Tr}[\hat{M}_m\hat{\rho}\hat{M}_m^\dagger] . \quad (2.6)$$

¹to go further, we should use the Kraus formalism [54]

Based on these measurement operators, we now defined a set of Hermitian operators, called *POVM* such as

$$\hat{\Pi}_m = \hat{M}_m^\dagger \hat{M}_m . \quad (2.7)$$

We do not discuss here the meaning of “*Positive Operator Valued Measures*” (this designation refers to mathematical properties and no physics). We talk about *POVM* for the complete set of operators and *POVM element* for one operator that corresponds to a specific outcome of the measurement apparatus. By extension of the generalized measurement properties, we have

$$p(m) = \text{Tr}[\hat{\Pi}_m \hat{\rho}] \quad (2.8)$$

These operators also follow the completeness relation

$$\sum_m \hat{\Pi}_m = \hat{\mathbb{1}} . \quad (2.9)$$

Although the POVM elements are Hermitian and positive operators, they are not necessarily projectors. The use of these operators is motivated by the fact that, most of the time, the measured mode is destroyed or not considered anymore and we consequently apply the trace on this mode. POVM cannot describe a non-destructive measurement². On the other hand, it is important to note that observables are actually a specific case of this formalism. Indeed, the POVM elements correspond to the projectors associated with the eigenstates of the observable. We give examples of POVM in the next two sections to illustrate its interest.

We close this section with another important remark. These operators being Hermitian we can compute their corresponding Wigner functions (i.e. it will be a function with values in \mathbb{R}). This phase space representation of a measurement can be sometime extremely convenient to understand it. Nevertheless, the POVM elements are not normalized i.e. the trace is not necessarily finite and thus do not represent some physical states. Only in the case of observables, the POVM correspond to a physical state (eigenstate of the observable).

2.1.2 Conditional preparation of quantum state

As underlined in the introduction of the chapter, a measurement gives us information on quantum states but we can also take advantage of the measurement projectivity to modify states. With the appropriate strategy, we can *engineer* some states: the state will be projected onto the desired one for a specific result of measurement. This is why we talk about *conditional preparation*. However, this strategy remains probabilistic and the success rate thus becomes an important parameter.

A general picture could be the following. We start from a two-mode state $\hat{\rho}_{\text{in},a,b}$ which is entangled. On one of the mode, we perform a measurement $\hat{\Pi}_a$ and, when the measurement apparatus gives the desired answer, the state in the other mode is $\hat{\rho}_{\text{cond},b}$ (cf figure 2.1). Thanks to the formalism of POVM, this conditional state can be written as (with a simplified notation³):

$$\hat{\rho}_{\text{cond},b} = \text{Tr}_{a/a,b}[\hat{\Pi}_a \hat{\rho}_{ab}] . \quad (2.11)$$

²However, this needs to be further discussed. It is not completely true to talk about non-destructive measurement, if we look into details the measurement apparatus, we will see that the measurement is mediated by an auxiliary system which will be destroyed... actually, it is more a question of where we define the limit between the system and the environment. This is part of a larger debate of the interest or not of POVM as it is possible to obtain the same results with observables and unitary evolution [85]. In contrast, the main idea of POVM is at the end to have a description of the different interactions between the system and the measurement apparatus as a black box and not to describe what happens inside.

³We omit $\mathbb{1}_b$ and use a more compact notation of the normalization. The exact writing should be

$$\hat{\rho}_{\text{cond},b} = \frac{\text{Tr}_a[\hat{\Pi}_a \otimes \mathbb{1}_b \hat{\rho}_{ab}]}{\text{Tr}_{a,b}[\hat{\Pi}_a \otimes \mathbb{1}_b \hat{\rho}_{ab}]} . \quad (2.10)$$

Equivalently, for the Wigner function formalism, we apply the generalized overlap formula for partial trace on a multi-mode state (1.54)⁴ and obtain the simple and very convenient expression:

$$W_{\hat{\rho}_{\text{cond},b}} = \int_{a/a,b} W_{\hat{\Pi}_a} W_{\hat{\rho}_{ab}} . \quad (2.13)$$

This last relation shows an important consequence. Indeed, if the input state has a Wigner function with only positive values, this strategy will produce states with negative values only if the Wigner function of the POVM element has some negative values. Hence, despite the fact that Wigner function of the POVM does not necessarily represent a physical state, the negativity of its Wigner function is also an important feature.

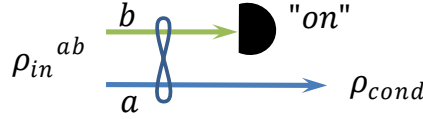


Figure 2.1: Conceptual scheme of a conditional preparation. A measurement is performed on one mode of an entangled state. The measurement outcome then heralds the preparation of a new state.

We will now study two types of detector usually used in quantum optics experiments: the single-photon detector and the homodyne detection. These can be used in conditional preparation. The important point, for this purpose, is to know what are the POVM elements corresponding to the different outcomes of the devices.

2.2 Photon detectors

We call “photon detector” a device which can detect at least a single-photon. These detectors are basically characterized by two parameters: the *quantum efficiency* and the *dark count*⁵. Experimentally, the quantum efficiency often strongly depends on the wavelength for various reasons (material, coating,...). On the other hand, the noise is intrinsic to the detector: it does not depend on the wavelength of the measured beam.

A “good” detector should have a high efficiency and a low dark count. However, as we will see below, it is not really possible to give absolute values to define whether a detector is “good” or “bad”. Actually, it depends a lot on the experiment in which we use it. The typical characteristics of nowadays detector of different technologies are given in appendix A.

2.2.1 *on/off* detectors

This model is typically used for avalanche photodiodes (APD). These detectors having only two possible outputs, we call them “*on/off* detectors”: detection of at least one photon, or no

⁴As for the expression with the density matrix, we simplify the notation by removing the normalization and the variables. The rigorous writing is

$$W_{\hat{\rho}_{\text{cond},b}}(x_b, p_b) = \frac{\iint_{\mathbb{R}^2} dx_a dp_a W_{\hat{\Pi}_a}(x_a, p_a) W_{\hat{\rho}_{ab}}(x_a, p_a, x_b, p_b)}{\iiint_{\mathbb{R}^4} dx_a dp_a dx_b dp_b W_{\hat{\Pi}_a}(x_a, p_a) W_{\hat{\rho}_{ab}}(x_a, p_a, x_b, p_b)} . \quad (2.12)$$

⁵i.e. counts that do not come from light, however background light can also contribute to unwanted photon detection events and is in practice included into this parameter.

detection. Ideally, the output *off* corresponds to the projector on the vacuum state $\hat{\Pi}_{\text{off}} = |0\rangle\langle 0|$ and thus the output *on* the projector on all the other Fock states $\hat{\Pi}_{\text{on}} = \sum_{n=1}^{\infty} |n\rangle\langle n|$.

(Note that the completeness relation is satisfied because the sum of the POVM is equal to the identity $\hat{\Pi}_{\text{off}} + \hat{\Pi}_{\text{on}} = \mathbb{1}$.) The associated Wigner functions in this case are obvious: the output *off* is the vacuum state and for the output *on* we use the completeness relation

$$W_{\hat{\Pi}_{\text{on}}} = W_{\mathbb{1}} - W_{|0\rangle\langle 0|} = \frac{1}{2\pi\sigma_0^2} \left(\frac{1}{2} - e^{-(x^2+p^2)/2\sigma_0^2} \right). \quad (2.14)$$

We remind that the POVM element being not a physical state, it has not necessarily a trace equal to one. Here, it is clear for instance that the integral does not converge.

2.2.2 Limited efficiency

As underlined previously, the detectors are actually not perfect and have, most of the time, a limited quantum efficiency η . This can be simply modeling by a black box containing a perfect detector with some optical losses upstream. In that case, the POVM element of the output *off* is given by:

$$\hat{\Pi}_{\text{off}} = \sum_{n=0}^{+\infty} (1-\eta)^n |n\rangle\langle n|. \quad (2.15)$$

The detector becomes less sensitive to low photon-number, the weight is higher for the outcome *off* than for the high photon number. More precisely, the probability to have the answer *on* with an input state $|n\rangle\langle n|$ is $1-(1-\eta)^n$, i.e. the probability that any photon reaches the detector (supposed perfect inside the black box).

To calculate the corresponding Wigner function, we use the formula

$$W_{|n\rangle} = \frac{(-1)^n}{2\pi\sigma_0^2} e^{-(x^2+p^2)/2\sigma_0^2} L_n \left(\frac{x^2+p^2}{\sigma_0^2} \right). \quad (2.16)$$

Thus, we have

$$W_{\hat{\Pi}_{\text{off}}} = \frac{1}{2\pi\sigma_0^2} e^{-(x^2+p^2)/2\sigma_0^2} \sum_{n=0}^{+\infty} (1-\eta)^n L_n \left(\frac{x^2+p^2}{\sigma_0^2} \right). \quad (2.17)$$

Then, with the help of the generating function $\frac{e^{-xt/(1-t)}}{1-t} = \sum_{n=0}^{+\infty} L_n(x)t^n$ we obtain

$$W_{\hat{\Pi}_{\text{off}}} = \frac{1}{2-\eta} \frac{1}{2\pi\sigma_0^2} \exp \left[-\frac{x^2+p^2}{\sigma_0^2} \left(\frac{1}{2} - \frac{1-\eta}{2-\eta} \right) \right]. \quad (2.18)$$

We note $\sigma_\eta^2 = \frac{2-\eta}{\eta} \sigma_0^2$. The previous expression is simplified in

$$W_{\hat{\Pi}_{\text{on}}} = W_{\mathbb{1}} - W_{\hat{\Pi}_{\text{off}}} = \frac{1}{2\pi\sigma_0^2} \left(\frac{1}{2} - \frac{1}{2-\eta} e^{-(x^2+p^2)/2\sigma_\eta^2} \right). \quad (2.19)$$

This Wigner function has negative values in particular at the origin of the phase space. However, this negativity is degraded by the efficiency but still exist if $\eta > 0$ which is of course always the case (figure 2.2 left). We talk therefore about *non-Gaussian detectors*.

2.2.3 Noisy detector

Another usual drawback of these detectors is the noise. Different types of distributions can be used, this mainly depends on the physical nature of the noise. However, the poissonian distribution is relevant in most of the cases and the POVM element of the *off* outcome can be rewritten in the following form

$$\hat{\Pi}_{\text{off}} = e^{-\nu} \sum_{n=0}^{+\infty} (1-\eta)^n |n\rangle\langle n|, \quad (2.20)$$

where ν is the mean value of the noise. Therefore, we adapt the equation (2.19) and obtain the general Wigner function

$$W_{\hat{\Pi}_{\text{on}}} = W_{\mathbb{1}} - W_{\hat{\Pi}_{\text{off}}} = \frac{1}{2\pi\sigma_0^2} \left(\frac{1}{2} - \frac{e^{-\nu}}{2-\eta} e^{-(x^2+p^2)/2\sigma_\eta^2} \right). \quad (2.21)$$

It is important to underline that, in practice, the value of the noise ν is not completely intrinsic to the detector, it also depends on the dynamic of the state impinging on the detector. Indeed, $e^{-\nu}$ is the mean number of photon in the detection window.

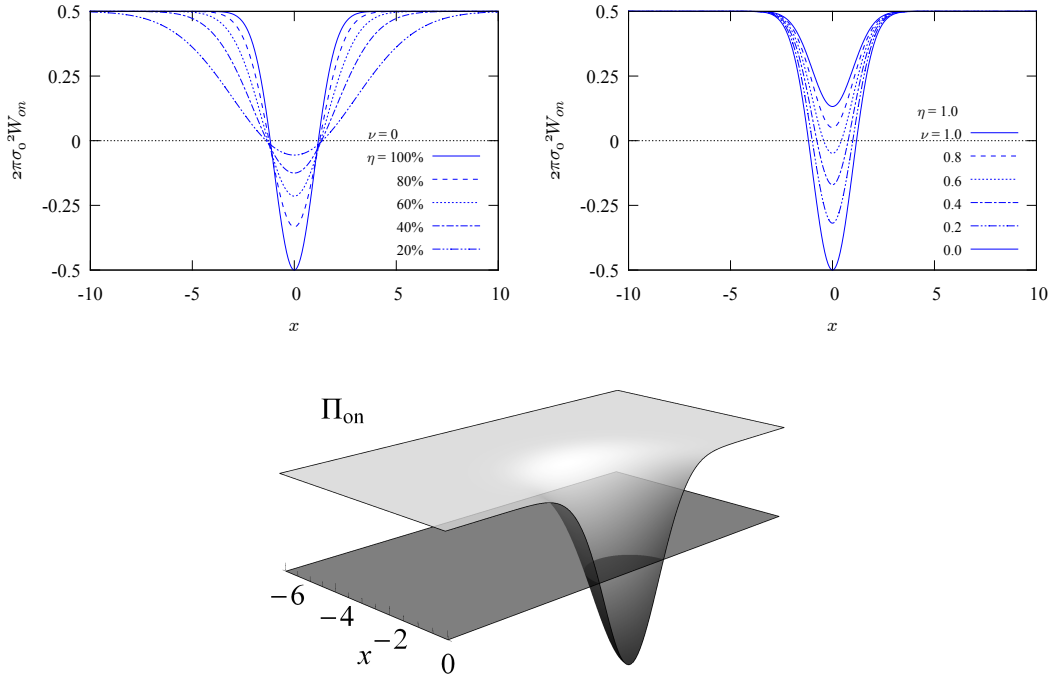


Figure 2.2: On the top, cross sections of the Wigner function for the POVM element $\hat{\Pi}_{\text{on}}$. On the left, no noise $\nu = 0$ and various efficiencies η from 100% down to 20%. On the right, perfect efficiency $\eta = 1$, and variable noise ν from 0 to 1. On the bottom, the Wigner function with perfect detection efficiency and no noise.

Now, with a noise ν , the negativity of the Wigner function can be lost (figure 2.2 right). Indeed, the negativity is preserved only if $1 - \eta/2 < e^{-\nu}$; in other words, in the limit of low noise $\nu \ll 1$, since

$$\nu < \eta/2. \quad (2.22)$$

2.2.4 Detection of two photons

In the previous section we did not really explain how we have determined the POVM. Let us use the example of the two-photon detection to show a method. Generally speaking, any phase insensitive detector has a POVM element of the form

$$\hat{\Pi}_m = \sum_{k=0}^{\infty} r_{k,m} |k\rangle\langle k|, \quad (2.23)$$

where the weighting term $r_{k,m}$ corresponds to the probability to have the outcome “m” when measuring the state $|k\rangle$. This term can be expressed as:

$$r_{k,m} = \text{Tr}[\hat{\Pi}_m |k\rangle\langle k|] = P(m|k). \quad (2.24)$$

An intuitive strategy to detect more than one photon is to combine single-photon detectors and beam-splitters. Of course, even if the efficiencies are equal to unity and the noise equal to zero, it is still not equivalent to a photon-number resolved detector. Indeed, the detector can detect many $|n > 0\rangle\langle n > 0|$ but not specific $|n\rangle\langle n|$. However, these photon-number resolved detectors are not yet well working (and not yet really available cf. appendix A), the combination of several non-photon-number-resolved detectors is a good alternative.

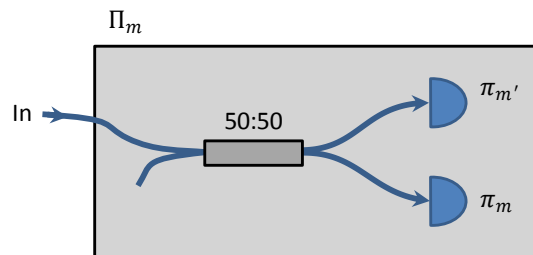


Figure 2.3: The measured beam is sent to a 50:50 beam-splitter with two single-photon detector connected at each output. These two detectors have the POVM element $\hat{\pi}_m$ and $\hat{\pi}_{m'}$. This device can be seen as a single detector with POVM elements $\hat{\Pi}_m$.

As depicted on figure 2.3, we now consider a device made of a beam-splitter and two detectors. The idea is the following, when we have two clicks, we have a kind of detector $|2\rangle\langle 2|$ for low photon number states. An alternative scheme uses a time delay and recombines the two outputs with another beam-splitter in order to save one detector. The two modes are distinguished with a time delay. Hence, the detector now looks at two different time windows separated by a time delay τ (we talk about “Time Multiplexed Detectors”). Nevertheless, with the second beam-splitter, half of the beam is lost and the count rate reduced. More precisely using the TMD with a detector of efficiency η of scheme (c) is equivalent to the scheme (a) with two detectors of efficiencies $\eta/2$. We “pay” the use of only one detector (instead of two) by a diminution of a factor 2 on the efficiency. However, a possible trick to save this efficiency is to recombine the two beams in polarization: instead of 50:50 beam splitter, we use a polarizing beam-splitter [17].

This setup can be described globally as a single detector. To avoid any confusion, let us now note by upper case the POVM element of the complete device $\hat{\Pi}_m$ and by lower case the POVM elements of each single-photon detectors $\hat{\pi}_m$ that we have described in the previous section. This new detector has three possible outcomes: no clicks $\hat{\Pi}_0$, two clicks $\hat{\Pi}_{\geq 2}$ and one click $\hat{\Pi}_1$. Concerning the last one, we underline that the symmetry of the setup makes

identical the outcomes “one click on detector 1, no one on 2” and “one click on detector 2, no one on 1”.

We can calculate each POVM element by using its definition in equations (2.23) and (2.24). We obtain the following expressions

$$\hat{\Pi}_0 = \sum_n e^{-2\nu} (1 - \eta)^n |n\rangle\langle n|, \quad (2.25)$$

$$\hat{\Pi}_1 = 2 \sum_n (e^{-\nu} (1 - \eta/2)^n - e^{-2\nu} (1 - \eta)^n) |n\rangle\langle n|, \quad (2.26)$$

$$\hat{\Pi}_{\geq 2} = \sum_n (1 + e^{-2\nu} (1 - \eta)^n - 2e^{-\nu} (1 - \eta/2)^n) |n\rangle\langle n|, \quad (2.27)$$

where η and ν are the efficiency and noise of each single-photon detector as described in the previous section. We easily check that these operators satisfy the completeness relation $\hat{\Pi}_0 + \hat{\Pi}_1 + \hat{\Pi}_{\geq 2} = \mathbb{1}$.

The Wigner function is expressed by using the function

$$\overline{W}_{\eta,\nu} = \frac{e^{-\nu}}{2 - \eta} e^{-(x^2 + p^2)/2\sigma_\eta^2}, \quad (2.28)$$

where we still defined $\sigma_\eta^2 = \frac{2 - \eta}{\eta} \sigma_0^2$. Thus

$$W_{\hat{\Pi}_1} = \frac{2}{2\pi\sigma_0^2} (\overline{W}_{\eta/2,\nu} - \overline{W}_{\eta,2\nu}), \quad (2.29)$$

$$W_{\hat{\Pi}_{\geq 2}} = \frac{1}{2\pi\sigma_0^2} \left(\frac{1}{2} + \overline{W}_{\eta,2\nu} - 2\overline{W}_{\eta/2,\nu} \right), \quad (2.30)$$

In contrast to the simple single-photon detector, we can see on figure 2.4 left that the shape of the Wigner function associated with the POVM element $\hat{\Pi}_1$ is now closer to the single-photon projector $|1\rangle\langle 1|$. This is the improvement of the second detection: it allows a better discrimination of the higher photon number as witness by the absence of plateau for large x . As for the single-photon, we can see on figure 2.4 right that the output “ ≥ 2 ” shows a plateau for large x owing to the fact that it doesn’t discriminate $n > 2$ [17, 16].

These different models of detectors allow to understand how they can modify quantum states of light, how the defects change their effects, in a conditional preparation scheme. However, it is also possible to experimentally measure the POVM of a detector. As performed in Ref. [17, 16], it basically consist in recording the response of a detector probed by a set of coherent states (i.e. of different amplitudes). These different measurements of input/output (of the detector) allow us to then reconstruct its POVM by using a technique similar to the one used to reconstruct a quantum state (that we present in section 2.4.5).

2.3 Homodyne measurement

The previous detector shows POVM elements with negative Wigner function, and can therefore be called *non-Gaussian* detectors. Now, the detector we consider in this section does not show such a feature, however it yields to useful measurements in particular to characterize a state. This measurement has been widely used so far, surprisingly it allows to perform quantum measurements with *a priori* classical devices: photodiodes and standard

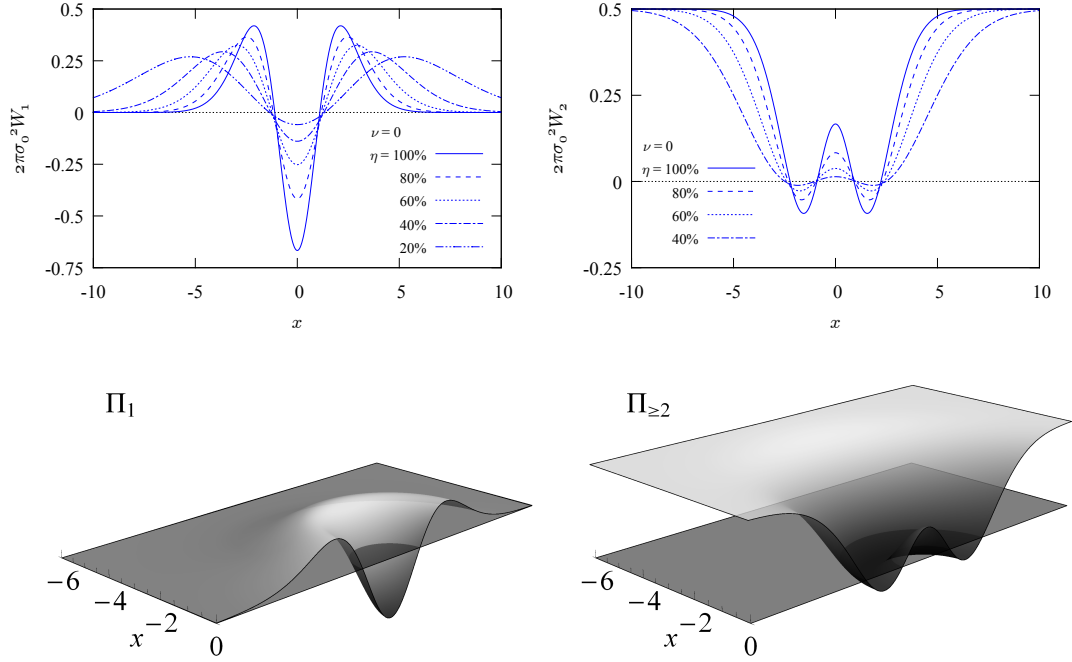


Figure 2.4: On the top, cross sections of the Wigner function associated with the POVM element $\hat{\Pi}_1$ on the left and $\hat{\Pi}_2$ on the right without noise $\nu = 0$ and various efficiencies η from 100% down to 20%. On the bottom Wigner functions for perfect detector ($\eta = 1, \nu = 0$).

electronics. (Despite photodiodes are based on quantum phenomenon, they cannot resolve the discrete nature of light.)

In the following, we discuss the different modeling and other theoretical aspects of the homodyne detection. The technical details are discussed in the Appendix B.

2.3.1 Principle of the homodyne detection

The state $\hat{\rho}_s$ we want to measure, called *signal*, is mixed with a bright beam, called *local oscillator*, on a 50:50 beam-splitter (cf. figure 2.5). This bright beam is a coherent state $|e^{-i\theta}\alpha\rangle$ with a large amplitude $\alpha \in \mathbb{R}_+$ and a phase θ . In terms of operators, we have after the beam-splitter

$$\hat{a}_1 = (\hat{a}_{LO} + \hat{a}_s)/\sqrt{2}, \quad (2.31)$$

$$\hat{a}_2 = (\hat{a}_{LO} - \hat{a}_s)/\sqrt{2}. \quad (2.32)$$

The two resulting beams are measured with photodiodes, which provide a current proportional to the number of photons i.e. $\hat{i} \propto \hat{n}$ (one photon gives one electron in the ideal case)

$$\hat{n}_{1,2} = \frac{1}{2}[\hat{a}_{LO}^\dagger \hat{a}_{LO} + \hat{a}_s^\dagger \hat{a}_s \pm \hat{a}_{LO}^\dagger \hat{a}_s \pm \hat{a}_s^\dagger \hat{a}_{LO}]. \quad (2.33)$$

The subtraction of the two photocurrents results in a signal proportional to

$$\hat{n}_1 - \hat{n}_2 = \hat{a}_s^\dagger \hat{a}_{LO} + \hat{a}_{LO}^\dagger \hat{a}_s. \quad (2.34)$$

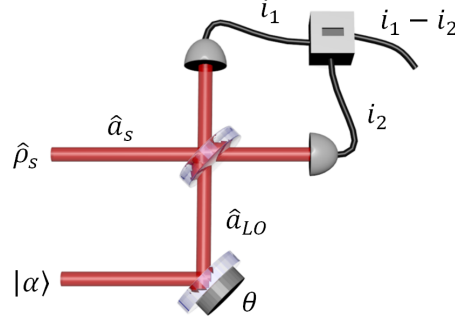


Figure 2.5: Homodyne detection. The measured beam is mixed with a bright coherent state called *local oscillator* on a 50:50 beam-splitter. The two outputs are measured with two photodiodes. The resulting photocurrents are subtracted and provide an output signal proportional to a quadrature measurement amplified by the amplitude of the local oscillator. Most of the time, the phase of the quadrature is adjusted with a PZT on the path of the local oscillator.

The coherent state being bright, the observable mainly gives its mean value. As a result, we can take the expected value of the local oscillator mode i.e. to replace the operator by the amplitude of the coherent state⁶ :

$$\hat{n}_1 - \hat{n}_2 \approx \alpha e^{-i\theta} \hat{a}_s^\dagger + \alpha e^{i\theta} \hat{a}_s . \quad (2.35)$$

We finally recognize a quadrature observable with a phase defined by the phase of the local oscillator

$$i_1 - i_2 \propto \alpha \hat{x}_{\theta} . \quad (2.36)$$

We can notice that this measurement at the quantum scale is enabled by the gain on the measurement provided by the amplitude of local oscillator. The bigger is α , the better is the sensitivity of the measurement.

However, one could underline that assuming the photodiode as a photon counter is questionable. Indeed, stating $\hat{i} \propto \hat{n}$ means that if we can measure precisely the current we have detector able to resolve the number of photon! Actually, a more precise model would be to consider this detector with a large noise compared to the single-photon scale. However, at the end, even though the contribution of this noise is important it will be canceled out by the fact that the local oscillator is a bright beam.

This general description is actually what the experimental apparatus tries to aim at. One aspect that we do not consider here is the dynamical degree of freedom. This will be the topic of chapter 6.

⁶This approximation can be justified in the following way. If we consider the mean observable on the signal mode by taking the mean value on the local oscillator mode

$$\langle \alpha | (\hat{n}_1 - \hat{n}_2) | \alpha \rangle_{LO} = \alpha \hat{x}_{s,\theta} ,$$

and we compare it to the mean value of its square

$$\langle \alpha | (\hat{n}_1 - \hat{n}_2)^2 | \alpha \rangle_{LO} = \alpha^2 \hat{x}_{s,\theta}^2 + \hat{a}_s^\dagger \hat{a}_s .$$

We note that the standard deviation of the observable of the signal mode is negligible if its mean photon number is negligible compare to the local oscillator. In other word, under this assumption we always have the same observable on the signal mode.

2.3.2 POVM of the homodyne measurement

The POVM elements are given by the eigenvectors of the quadrature observable. Here, in the $\{\hat{x}, \hat{p}\}$ quadrature basis we consider the general quadrature $\hat{x}_\theta = \cos\theta\hat{x} + \sin\theta\hat{p}$. The POVM element associated with the outcome x_θ is

$$\hat{\Pi}(x_\theta) = |x_\theta\rangle\langle x_\theta|, \quad (2.37)$$

$\hat{x}_\theta|x_\theta\rangle = x_\theta|x_\theta\rangle$. An homodyne detection with a fixed phase (i.e. which measures a fixed quadrature) is a detector associated with a given POVM, hence, all the different answers satisfy the completeness relation. $\int \hat{\Pi}(x_\theta)dx_\theta = \int |x_\theta\rangle\langle x_\theta|dx_\theta = \mathbb{1}$. Note that this relation is true for each phase, two different phases yielding to two different POVMs (hence, it would be wrong to sum also on all the phases). The corresponding Wigner function is

$$W_{\hat{\Pi}(x_\theta)}(x, p) = \frac{1}{2\pi\sigma_0^2} \frac{1}{2} \delta(x \cos\theta + p \sin\theta - x_\theta). \quad (2.38)$$

In practice, the homodyne detection is not perfect and can suffer from inefficiency, i.e. $\eta < 1$. More precisely, if each arm has the same limited efficiency η , this is equivalent to consider a beam-splitter of transmission η before a perfect homodyne detection (see [59]). Thus we can write the measured marginal distribution \mathcal{P}_η as a function of the marginal distribution with a perfect efficiency \mathcal{P} :

$$\mathcal{P}_\eta(x_\theta) = \frac{1}{\sqrt{2\pi\sigma_0^2(1-\eta)}} \int \exp\left(-\frac{(x_\theta - \sqrt{\eta}y_\theta)^2}{2\sigma_0^2(1-\eta)}\right) \mathcal{P}(y_\theta)dy_\theta \quad (2.39)$$

where $\mathcal{P}_\eta(x_\theta) = \text{Tr}[\hat{\Pi}_\eta(x_\theta)\hat{\rho}]$ and $\mathcal{P}(x_\theta) = \text{Tr}[\hat{\Pi}(x_\theta)\hat{\rho}]$. Thus, being true for any states we deduce the corresponding POVM element

$$\hat{\Pi}_\eta(x_\theta) = \frac{1}{\sqrt{2\pi\sigma_0^2(1-\eta)}} \int \exp\left(-\frac{(x_\theta - \sqrt{\eta}y_\theta)^2}{2\sigma_0^2(1-\eta)}\right) |y_\theta\rangle\langle y_\theta|dy_\theta, \quad (2.40)$$

as a function of the POVM element for perfect efficiency. We obtain the Wigner function by using equation (2.38)

$$W_{\hat{\Pi}_\eta(x_\theta)}(x, p) = \frac{1}{\sqrt{2\pi\sigma_0^2(1-\eta)}} \exp\left(-\frac{(x_\theta - \sqrt{\eta}(x \cos\theta + p \sin\theta))^2}{2\sigma_0^2(1-\eta)}\right) \frac{1}{2\pi\sigma_0^2} \frac{1}{2}. \quad (2.41)$$

The limited efficiency broadens the Gaussian Wigner function which can be interpreted by the fact that the contamination by the vacuum state is not controlled and makes the measurement less precise.

All these measurements have positive Wigner functions and for this reason are called *Gaussian measurements*.

2.4 State reconstructions

In free-space optics, the *quantum state tomography* with homodyne detection is a powerful method to fully characterize a quantum state. The term of *tomography* comes from the analogy with the medical imaging technique. Indeed, the mathematical description of the reconstruction is exactly the same. For different angles θ , we measure the transmitted X-ray by a body. We can write it $I(x_\theta) = \int dy_\theta T(x_\theta, y_\theta)$ with T the transmission function of the

body, y_θ the propagation axis of the X-ray and $I(x_\theta)$ the measured intensity profile. The problem is to reconstruct the function T . In our case, the measurements of the quadrature \hat{x}_θ give the marginal distribution $\mathcal{P}(x_\theta) = \int dy_\theta W(x_\theta, y_\theta)$ and, we want to reconstruct the Wigner function W .

The first used algorithm was the Radon transform. But now, in quantum optics, the MaxLik algorithm is most of the time preferred as it allows to compensate optical losses, and also because it intrinsically leads to a lower numerical noise.

Below, we describe various techniques of reconstruction. The first two ones are not detailed as we will not use them. We mention them in order to justify why we prefer to use the others. Unfortunately, for the next ones, we will see that none all of them is really better than the other. Actually, there is always a compromise between the accuracy and the speed of the calculation.

Among the following techniques, there are two possible strategies: reconstruct the Wigner function first or the density matrix first. Moreover, we will see that we have simpler techniques under the assumption of phase-invariant states. Importantly, this invariance can be “artificial” by a phase averaging of the measurements, which can be use to access to the diagonal elements of any state.

2.4.1 Radon transform

It is actually the analytical solution of the problem. Nevertheless, this reconstruction is sensitive to the sampling which is unavoidable in real experiment. Rigorously, we call *Radon transform* the marginal distribution from the Wigner function. On the other hand, it reconstructs the Wigner function first and not the density matrix. This is not the best choice as the conversion from the Wigner function to the density matrix is a little difficult.

With a rigorous notation the marginal distribution is

$$\mathcal{P}(x_\theta) = \int W(x_\theta \cos \theta + y_\theta \sin \theta, y_\theta \cos \theta - x_\theta \sin \theta) dy_\theta \quad (2.42)$$

The Radon transform provides the following relation in the Fourier space

$$\tilde{W}(k_\theta \cos \theta, k_\theta \sin \theta) = \tilde{\mathcal{P}}(k_\theta) \quad (2.43)$$

For each angle, the Fourier transform of the marginal distribution gives a radial cross section of the Fourier transform of the Wigner function. Accumulating different angles gives then the complete Wigner function in the Fourier space, and the invert Fourier transform provides the Wigner function of the state.

2.4.2 Abel transform

It is a specific case of the Radon transform. Indeed, we assume that the state is phase invariant or it will give a phase-randomized state. This assumption makes the problem analytically simpler. As before, we start from a marginal distribution measurement

$$\mathcal{P}(x) = \int W(x, y) dy, \quad (2.44)$$

and the goal is to reconstruct the corresponding Wigner function. The one we consider here has an axial symmetry. We can thus write it as a function of a single variable

$$W(x, y) = W(\sqrt{x^2 + y^2}) = W(r) . \quad (2.45)$$

Thus, by using the change of variable $dy = r dr / \sqrt{r^2 - x^2}$ the expression of the marginal distribution becomes

$$\mathcal{P}(x) = 2 \int_x^\infty \frac{W(r)r dr}{\sqrt{r^2 - x^2}}. \quad (2.46)$$

The inverse of the Abel transform ⁷ is

$$W(r) = -\frac{1}{\pi} \int_r^\infty \frac{d\mathcal{P}}{dx} \frac{dx}{\sqrt{x^2 - r^2}}. \quad (2.47)$$

The advantage, compared to the Radon transform, is that this operation does not require to perform any Fourier transform.

2.4.3 Phase averaging and moments

The idea here, as for the next techniques, is quite different: we want to directly infer the density matrix and not first the Wigner function. To do so, we use the different even orders of quadratures to infer the diagonal elements of the state. Therefore, this technique, as the previous one, requires an assumption of phase invariance of the measured state, or a phase averaging. It also requires an assumption on the size of the Hilbert space. However, it is extremely light in terms of computation resources (memory depth and computation speed), and extremely simple to implement.

Nevertheless, one important issue is the possibility to obtain negative values which is physically meaningless. But, on the other hand, this artifact happens mainly when the measurement is not good enough (noise, too small Hilbert space, ...). This can be an advantage somehow to detect some potential problems in the measurement.

The even moments of quadrature are used for the reconstruction

$$\langle x^{2k} \rangle_{|n\rangle} = \frac{1}{\sqrt{2\pi}\sigma_0 2^n n!} \int x^{2k} H_n^2\left(\frac{x}{\sigma_0\sqrt{2}}\right) e^{-x^2/2\sigma_0^2} dx, \quad (2.48)$$

and follows the recurrence relation ⁸:

$$\langle x^{2k} \rangle_{|n\rangle} = (2k - 1) \left(\langle x^{2(k-1)} \rangle_{|n\rangle} + \langle x^{2(k-1)} \rangle_{|n-1\rangle} \right) + \langle x^{2k} \rangle_{|n-1\rangle} \quad (2.50)$$

⁷the marginal distribution should drop to 0 faster than $1/r$ but this is the case because the general form of the marginal distribution is a Gaussian function times a polynomial

⁸a simple demonstration consists in simplifying with the Hermite polynomials called "statistic", choose $\sigma_0 = 1$, then do an integration by parts and use the recurrence relation of the Hermite polynomials.

⁹Actually provides the numbers of Henri Delannoy, they follow the recurrence relation

$$D(m, n) = D(n - 1, m) + D(n - 1, m - 1) + D(n, m - 1), \quad (2.50)$$

then each row k is multiplied by $(k - 1)!! = (k - 1)(k - 3) \dots$ (ie $\langle x^{2k} \rangle_{|0\rangle}$).

For instance, we obtain the matrix

$$\mathbf{M} = \begin{bmatrix} \langle x^0 \rangle_{|0\rangle} & \langle x^0 \rangle_{|1\rangle} & \langle x^0 \rangle_{|2\rangle} & \cdots & \langle x^0 \rangle_{|n\rangle} & \cdots \\ \langle x^2 \rangle_{|0\rangle} & \langle x^2 \rangle_{|1\rangle} & \langle x^2 \rangle_{|2\rangle} & \cdots & \langle x^2 \rangle_{|n\rangle} & \cdots \\ \langle x^4 \rangle_{|0\rangle} & \langle x^4 \rangle_{|1\rangle} & \langle x^4 \rangle_{|2\rangle} & \cdots & \langle x^4 \rangle_{|n\rangle} & \cdots \\ \vdots & \vdots & \vdots & \ddots & \vdots & \vdots \\ \langle x^{2k} \rangle_{|0\rangle} & \langle x^{2k} \rangle_{|1\rangle} & \langle x^{2k} \rangle_{|2\rangle} & \cdots & \langle x^{2k} \rangle_{|n\rangle} & \cdots \\ \vdots & \vdots & \vdots & & & \ddots \end{bmatrix} = \begin{bmatrix} 1 & 1 & 1 & 1 & 1 & 1 & 1 & \cdots \\ 1 & 3 & 5 & 7 & 9 & 11 & 13 & \cdots \\ 3 & 15 & 39 & 75 & 123 & 183 & 255 & \\ 15 & 105 & 375 & 945 & 1935 & 3465 & 5655 & \\ 105 & 945 & 4305 & 13545 & 33705 & 71505 & 135345 & \\ 945 & 10395 & 57645 & 218295 & 643545 & 1590435 & 3452085 & \\ 10395 & 135135 & 883575 & 3918915 & 13399155 & 37972935 & 93440655 & \\ \vdots & \vdots & \vdots & & & & & \ddots \end{bmatrix} . \quad (2.51)$$

Let us call the vector of the even quadrature moments of the measured state

$$\mathbf{X}_{\hat{\rho}} = \begin{bmatrix} \langle x^0 \rangle_{\hat{\rho}} \\ \langle x^2 \rangle_{\hat{\rho}} \\ \langle x^4 \rangle_{\hat{\rho}} \\ \vdots \\ \langle x^{2k} \rangle_{\hat{\rho}} \\ \vdots \end{bmatrix} . \quad (2.52)$$

Thus, it is clear that

$$\mathbf{M} \text{diag}[\hat{\rho}] = \mathbf{X}_{\hat{\rho}} . \quad (2.53)$$

Hence, we simply infer the diagonal elements of the density matrix by inverting the latter equation

$$\text{diag}[\hat{\rho}] = \mathbf{M}^{-1} \mathbf{X}_{\hat{\rho}} . \quad (2.54)$$

We remind again that this reconstruction, as the Abel transform, gives access to the diagonal elements only. Moreover, if the measured state is not phase invariant, it requires a phase averaging: the phase associated with the quadrature measurement should be equally distributed. Interestingly, such a measurement cancels the coherences of the density matrix whereas the diagonal elements remain unchanged.

2.4.4 Pattern functions

We only give here the reconstruction technique and not any proof of it. For a complete demonstration of the formulas and more details the reader is invited to refer to Ref. [59].

The pattern function method is actually an extension of the Radon transform but it enables us to directly infer the elements of the density matrix. Let us now call the marginal distribution $w_{\theta}(x; s)$ with $s = 1 - \eta^{-1}$ the parametrization to compensate the detection efficiency η . The elements can be written as:

$$\langle a | \hat{\rho} | b \rangle = \int_0^{\pi} \int_{-\infty}^{+\infty} w_{\theta}(x; s) F_{ab}(x, \theta; s) dx d\theta , \quad (2.55)$$

where F_{ab} is the pattern function associated with $|a\rangle\langle b|$. Note that the relevance of the reconstruction is not guaranteed for an efficiency $\eta < 1/2$. For N measurements $\{x_n, \theta_n\}$ with θ_n equally distributed on $[0, \pi]$

$$\langle a|\hat{\rho}|b\rangle = \frac{\pi}{N} \sum_{n=1}^N F_{ab}(x_n, \theta_n, s) . \quad (2.56)$$

Fock basis The pattern functions in the Fock basis are given by:

$$F_{mn}(x, \theta; s) = e^{i(m-n)\theta} f_{mn}(x, s) , \quad (2.57)$$

with

$$f_{mn}(x, s) = \sqrt{m!n!2^{m-n}} \sum_{p=0}^m \frac{h_{2p+n-m+1}(x, s)}{2^p p!(m-p)!(n-m+p)!} , \quad (2.58)$$

if $n \geq m$, otherwise we use the same function and invert n and m . This function can be computed with

$$h_n(x, s) = h_n(x/\sqrt{1+s}) / (1+s)^{(n+1)/2} , \quad (2.59)$$

which follows the recurrence relation

$$h_{n+1}(x) - 2xh_n(x) + 2nh_{n-1}(x) = 0 , \quad (2.60)$$

with the first terms

$$h_0(x) = -\frac{1}{\sqrt{\pi}} e^{-x^2} \operatorname{erfi}(x) = -\frac{2}{\pi} D_w(x) , \quad (2.61)$$

and

$$h_1(x) = \frac{2}{\pi} \left[1 - \sqrt{\pi} x e^{-x^2} \operatorname{erfi}(x) \right] \quad (2.62)$$

$$= (1 - 2x D_w(x)) \frac{2}{\pi} . \quad (2.63)$$

The erfi is the imaginary error function but it is more convenient to use the Dawson function D_w ¹⁰ as given in the last expression.

Coherent state basis A particular interest of this technique is the possibility to use different basis (nevertheless, without guarantee that the formal expression will be easy to derive or to compute numerically). Here, we give the example of the pattern function for the coherent states basis.

$$F_{\alpha\beta}(x_\theta, \theta; s) = \frac{1}{1+s} h_1(\tilde{x}_\theta - x_\theta/\sqrt{1+s}) e^{-|\alpha-\beta|^2/2} , \quad (2.64)$$

where

$$\tilde{x}_\theta = (\alpha^* e^{i\theta} + \beta e^{-i\theta}) / \sqrt{2} . \quad (2.65)$$

Extension to two modes This technique can easily be extended to two modes. Indeed,

$$\rho_{nmjk} = \int_0^\pi \int_{-\infty}^{+\infty} \int_0^\pi \int_{-\infty}^{+\infty} w_{\theta_1, \theta_2}(x_1, x_2; s_1, s_2) F_{nm}(x_1, \theta_1; s_1) F_{jk}(x_2, \theta_2; s_2) dx_1 d\theta_1 dx_2 d\theta_2 \quad (2.66)$$

with $w_{\theta_1, \theta_2}(x_1, x_2; s_1, s_2)$ which is the two-mode marginal distribution (or joint density probability distribution). The matrix elements are then given by:

$$\langle c|\langle a|\hat{\rho}|b\rangle|d\rangle = \frac{\pi^2}{N} \sum_{n=1}^N F_{ab}(x_{1,n}, \theta_{1,n}, s) F_{cd}(x_{2,n}, \theta_{2,n}, s) . \quad (2.67)$$

¹⁰Note that the function erfi diverges extremely fast and its product with e^{-x^2} is numerically unstable. The use of the interpolation of D_w is numerically safer.

Convention For all the previous formulas, note that the choice of convention should be adapted. Indeed, for a standard deviation of the vacuum fluctuation given by σ_0 , the quadrature measurement should be modified as follows

$$x \longrightarrow \frac{x\sigma_0}{\sqrt{2}}, \quad (2.68)$$

to be used in the previous formulas.

2.4.5 MaxLik algorithm

This last method, introduced recently [63, 62], is now widely used. It results from a statistical approach, while the previous ones are based on analytical solution. As suggested by its name, this is an algorithm which maximize the likelihood (the most powerful tool for statistical estimation): it gives the “most compatible” state for a given set of measurement results. As for the pattern function, it enables to correct for the detection losses. However, in contrast to the previous techniques, the advantage of this reconstruction is the constraint on the diagonal elements, which are always positive. It also gives the highest accuracy (Cramer-Rao bound).

Nevertheless, this method has some drawbacks. At last, the main drawbacks we can mention are the requirement of an assumption on the size of the Hilbert space and secondly, it is heavier in terms of computation resources.

We start from a set of N measurements $\{x_k, \theta_k\}$. Depending on the sampling of the measured signal, we have for x and θ , we can reorganize the results of the measurements by packing them together when they are equal into another set of measurements $\{f_j, x_j, \theta_j\}$ with f_j the frequency of the result j (if we obtain n_j times the results $\{x_j, \theta_j\}$ among a total number of N measurements $f_j = n_j/N$). The likelihood is then equal to

$$\mathcal{L}(\hat{\rho}) = \prod_j pr(\theta_j, x_j)^{f_j} \quad (2.69)$$

with $pr(\theta_j, x_j) = \text{Tr}[\hat{\Pi}(\theta_j, x_j)\hat{\rho}]$ the probability to obtain the result $\{x_j, \theta_j\}$ for the state $\hat{\rho}$. We use the projector $\hat{\Pi}(\theta, x) = |\theta, x\rangle\langle\theta, x|$ corresponding to the measurement result x, θ . Its elements in the Fock basis are

$$\Pi_{nm} = \langle n|\hat{\Pi}(\theta, x)|m\rangle = \langle n|\theta, x\rangle\langle\theta, x|m\rangle, \quad (2.70)$$

which can be computed via the following formula (Fock state wave function)

$$\langle n|x, \theta\rangle = e^{in\theta} \frac{1}{(\sqrt{2\pi}\sigma_0 2^n n!)^{1/2}} H_n\left(\frac{x}{\sigma_0\sqrt{2}}\right) e^{-(x/\sigma_0\sqrt{2})^2/2}, \quad (2.71)$$

with H_n the n -th Hermite polynomial.

The algorithm consists in iterating the following recurrence

$$\hat{\rho}^{(k+1)} = \mathcal{N} \left[\hat{R}(\hat{\rho}^{(k)}) \hat{\rho}^{(k)} \hat{R}(\hat{\rho}^{(k)}) \right], \quad (2.72)$$

with \mathcal{N} the normalization factor to have a trace equal to 1. For each iteration, we can compute the iteration operator

$$\hat{R}(\hat{\rho}) = \sum_j \frac{f_j}{pr(\theta_j, x_j)} \hat{\Pi}_j(\theta_j, x_j). \quad (2.73)$$

The state is initialized with the matrix $\hat{\rho}^{(0)} = \mathcal{N}[\mathbb{1}]$. If the algorithm converges, we have $f_j \propto pr_j$ and $\sum_j \hat{\Pi}_j \propto \mathbb{1}$. So at the end $\hat{R}(\hat{\rho}_0) \propto \mathbb{1}$, i.e.

$$\hat{R}(\hat{\rho}_0) \hat{\rho}_0 \hat{R}(\hat{\rho}_0) \propto \hat{\rho}_0 . \quad (2.74)$$

Losses correction The other interest of this algorithm is the possibility to compensate the optical losses. Indeed, if the state $\hat{\rho}_0$ is propagated into a channel of transmission η , the state we measure is $\hat{\rho}_\eta$. The relationship we have between these two state is

$$\langle m | \hat{\rho}_\eta | n \rangle = \sum_{k=0}^{\infty} B_{m+k,m}(\eta) B_{n+k,n}(\eta) \langle m+k | \hat{\rho}_0 | n+k \rangle . \quad (2.75)$$

with

$$B_{n+k,n} = \sqrt{\binom{n+k}{n} \eta^n (1-\eta)^k} . \quad (2.76)$$

The probability of measurement is thus changed in

$$pr_\theta^n(x) = \langle \theta, x | \hat{\rho}_\eta | \theta, x \rangle \quad (2.77)$$

$$= \sum_{m,n=0}^{\infty} \sum_{k=0}^{\infty} B_{m+k,m}(\eta) B_{n+k,n}(\eta) \langle n | \theta, x \rangle \langle \theta, x | m \rangle \langle m+k | \hat{\rho}_0 | n+k \rangle . \quad (2.78)$$

And we replace the previous projectors $\hat{\Pi}(\theta, x)$ by

$$\hat{\Pi}_\eta(\theta, x) = \sum_{m,n,k} B_{m+k,m}(\eta) B_{n+k,n}(\eta) \langle n | \theta, x \rangle \langle \theta, x | m \rangle |n+k\rangle \langle m+k| . \quad (2.79)$$

Extension to two modes The extension to a two-mode state is quite straightforward. The state being expanded in the Fock bases as

$$\hat{\rho} = \sum_{ijpq} \rho_{ijpq} |i\rangle \langle j| \otimes |p\rangle \langle q| . \quad (2.80)$$

We should now consider one projector per mode

$$\hat{\rho} \cdot (\hat{\Pi}_1 \otimes \hat{\Pi}_2) = \sum_{i,j,p,q,l,n} \rho_{ijpq} \Pi_{jn} \Pi_{ql} |i\rangle \langle n| \otimes |p\rangle \langle l| , \quad (2.81)$$

Or, if we consider the density matrix elements

$$\rho_{ijkl} = \sum_{m,n} \rho_{imkn} \Pi_{mj} \Pi_{nl} . \quad (2.82)$$

2.5 Conclusion

We have seen the two main aspects of measurements in quantum optics. First, it can be used to prepare, engineer quantum states. In this case, the ability depends on the “non-classicality” of the used measurements, for this reason we will see in the further chapters that non-gaussian measurement are of a big importance. Secondly, we have shown a more basic aspect of the measurement: how to use it to obtain information on a state and more specifically the quantum tomography via homodyne measurements. It is worth noting that,

each measurement has its own advantages and drawbacks for a given task. In our few examples, non-gaussian states can be conveniently prepared with non-Gaussian measurements whereas it is not possible with a homodyne detection. Conversely, a homodyne detection being a phase sensitive measurement, it allows to fully characterize a state. A photon-counter does not provide phase information (this is a key point of the work presented in the chapter 7).

All the performed experiments described in this manuscript take advantages of these two aspects: conditional preparation and characterization.

Part II

Generation of Non-Gaussian States

3 | Optical Parametric Oscillators

I frequently hear music in the heart of noise.

GEORGE GERSHWIN

Mainly used and known for frequency conversion, the optical parametric oscillators exhibit nevertheless some fundamental quantum properties and are largely used in quantum optics. Indeed, they can squeeze the vacuum fluctuations but also produce quantum correlated beams. Two different types of OPO exist given a non-linear crystal phase matching. The type-I is the most used whereas the type II OPO is less known. This latter can produce a two-mode squeezed vacuum (i.e. a source of entangled state) or, with another polarization basis, two independent squeezed vacuum states.

The study of OPO's quantum properties and their use in various applications has been an important activity of the Quantum Optics group at Laboratoire Kastler-Brossel, in continuous-wave (cw) regime and more recently in pulsed regime. The type-II OPO we use has been previously elaborated during the PhD of Julien Laurat [53]. A second OPO, with a type-I phase matching, has been built during this PhD work with the same characteristics as the type-II OPO. The initial idea was to make them compatible in order to be used together in subsequent experiments.

We first give a description and a theoretical study of the OPO in cw-regime, operated below the oscillation threshold. We thus obtain the basic properties that we use afterwards. Then, we describe the practical implementation and characterizations of the two available OPOs.

OPOs having being widely studied in many papers and PhD work, the aim of this chapter is first to give the basics of OPO's physics, secondly to emphasize some important points for our further experiments and finally to give a description of the setups with the corresponding results.

3.1	Theory in the continuous-wave regime	48
3.1.1	Single-pass non-linear interaction	48
3.1.2	Non-linear crystal in a cavity	49
3.1.3	Noise spectrum	51
3.2	Experimental realizations	54
3.2.1	Global setup	54
3.2.2	Crystal phase-matching	55
3.2.3	Type-II OPO	55
3.2.4	Type-I OPO	57
3.3	Conclusion	60

3.1 Theory in the continuous-wave regime

3.1.1 Single-pass non-linear interaction

The crystal used in an OPO is a *non-linear* medium with in particular $\chi^{(2)}$ susceptibility. This can induce some frequency conversion. In our case, a *pump* photon is divided into two, a *signal* and a *idler*, we talk about *down-conversion*. Such phenomenon happens only under two conditions:

$$\begin{aligned} \omega_p &= \omega_s + \omega_i && \text{energy conservation,} \\ n_p \omega_p &\approx n_s \omega_s + n_i \omega_i && \text{momentum conservation.} \end{aligned}$$

The second condition is commonly called *phase matching*. It can be obtained thanks to the birefringence (different optical indexes for two polarizations) feature of the medium. Hence, two situations can be considered

- *Type-I phase matching* : $o \longleftrightarrow e + e$
the pump is polarized along the ordinary axis and, signal and idler are on the extraordinary axis. (degenerate in polarization).
- *Type-II phase matching* : $e \longleftrightarrow o + e$
the pump is along the extraordinary axis and, signal and idler on different axis, one along the ordinary axis the other on the extraordinary axis. It is non-degenerate in polarization and s and i can be easily separated.

The corpuscular description gives us an easy understanding of the form of the Hamiltonian of interaction: for one annihilation of pump photon we create one photon signal and one photon idler. We add to that the Hermitian conjugate, which actually corresponds to the opposite process i.e. the *up-conversion*:

$$\mathcal{H}_{int} = i \frac{\hbar g}{2} \hat{a}_s^\dagger \hat{a}_i^\dagger \hat{a}_p + h.c. \quad (3.1)$$

Under the hypothesis of bright coherent state for the pump beam, $|\alpha\rangle$, the Hamiltonian is rewritten

$$\mathcal{H}_{int} = i \frac{\hbar \kappa}{2} \hat{a}_s^\dagger \hat{a}_i^\dagger + h.c. \quad \text{where } \kappa = \alpha g \quad (3.2)$$

Therefore, the evolution equation is

$$i\hbar \frac{d}{dt} \hat{a}_l = [\mathcal{H}_{int}, \hat{a}_l] \quad (3.3)$$

In the degenerate case $\hat{a}_s = \hat{a}_i$ (that we then write \hat{a}) we obtain $\frac{d}{dt} \hat{a} = -\kappa \hat{a}^\dagger$ for which the solution is

$$\hat{a}(t) = \hat{a}(0) \text{ch}(\kappa t) - \hat{a}^\dagger(0) \text{sh}(\kappa t) \quad (3.4)$$

We then obtain the quadratures, with $\zeta = \kappa \tau$ where τ is the interaction time with the non-linear crystal

$$\hat{x}_{out} = e^{-\zeta} \hat{x}_{in} \quad (3.5)$$

$$\hat{p}_{out} = e^{\zeta} \hat{p}_{in} \quad (3.6)$$

from which we deduce a *compression factor* $s = e^{-2\zeta}$. The effect of the non-linear crystal can also be written as the evolution operator

$$\hat{S}(\zeta) = e^{\frac{\zeta}{2}(\hat{a}^2 - \hat{a}^{\dagger 2})} \quad (3.7)$$

Concerning a type-II phase matching, signal and idler are not degenerate. The interaction is then given by

$$\hat{S}_{si}(\zeta) = e^{\frac{\zeta}{2}(\hat{a}_s \hat{a}_i - \hat{a}_s^\dagger \hat{a}_i^\dagger)}. \quad (3.8)$$

However, if we rotate the polarization basis i.e. at 45° of the ordinary and extraordinary axis, we obtain the following transformation

$$\hat{a}_s \hat{a}_i - h.c. \longrightarrow \frac{1}{\sqrt{2}}(\hat{a}_2 + i\hat{a}_1)(\hat{a}_1 + i\hat{a}_2) - h.c. = \frac{1}{2}i(\hat{a}_1^2 + \hat{a}_2^2) - h.c. \quad (3.9)$$

at the end

$$\hat{S}_{si} \longrightarrow \hat{S}_1 \hat{S}_2. \quad (3.10)$$

Thus, we have two squeezing operators. Hence, applied to a vacuum state, we obtain *two-mode squeezed vacuum state*.

3.1.2 Non-linear crystal in a cavity

The non-linear process is an extremely weak effect. To enhance it, two strategies are possible. The first one consists in increasing the pump power, but in that case, the required power is possible only in the pulsed regime. The other possibility is to increase the interaction time, not by increasing the size of the crystal (which is not impossible but extremely challenging) but, by putting the crystal in a cavity. However, in this case the dynamics of the output state, i.e. the effect of the cavity, has to be considered.

The idea is thus to write the different dynamical relationships of the fields inside the cavity. First, we denote by T the intensity transmission of the output coupler and L the intra-cavity losses for the signal and idler fields that can be considered as coming from a fictitious beam-splitter inserted in the cavity. This coefficient being small, the reflection in amplitude is $r = \sqrt{1-T} \approx 1 - T/2$.

Secondly, let's label the different fields. We use the letter $\hat{a}(t)$ for the annihilation operator at time t . We use the indices to define the various fields: with p for the pump, s for the signal and i for the idler; sL , iL for the modes coupled to the vacuum by the losses, and iIn , sIn for the input modes outside of the cavity of figure 3.1).

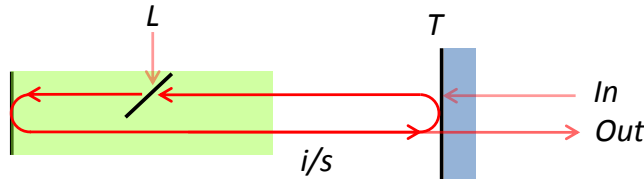


Figure 3.1: Loop of the fields inside the OPO cavity. L denotes the intra cavity losses, In the input fields (a priori vacuum) and Out the output fields (a priori squeezed vacuum).

Modes equation round-trip The dynamical relationships can be found by applying the quantum Langevin equation [26]. Here we use another approach by considering the equations with one round-trip [53]. The idea is to write the field, let say just before the output coupler, before and after one round-trip. First, we consider a cavity resonant for the two fields s and i , therefore, they accumulate a phase-shift of an integer number of 2π after one round-trip. Secondly, during one round-trip the field is reflected on the output coupler, then submitted to the non-linear interaction in the crystal (see previous section). Moreover, during one round-trip the field is partly degraded by some losses inside the cavity. Finally, we call τ

the time for one round-trip and we have also the non-linear gain through the whole crystal $\mathbf{g} = 2\mathcal{L} \cdot g^{-1}$ (\mathcal{L} the length of the crystal). We thus have for the signal and idler modes

$$\hat{a}_s(t + \tau) = (1 - T'/2) \left[\hat{a}_s(t) + \mathbf{g}\hat{a}_p(t)\hat{a}_i^\dagger(t) \right] + \sqrt{L}\hat{a}_{sL}(t) + \sqrt{T}\hat{a}_{sIn}(t), \quad (3.11)$$

$$\hat{a}_i(t + \tau) = (1 - T'/2) \left[\hat{a}_i(t) + \mathbf{g}\hat{a}_p(t)\hat{a}_s^\dagger(t) \right] + \sqrt{L}\hat{a}_{iL}(t) + \sqrt{T}\hat{a}_{iIn}(t), \quad (3.12)$$

with the simplification (low transmission and low losses) $r \cdot t_L = (1 - T/2)(1 - L/2) \approx 1 - T/2 - L/2 = 1 - T'/2$ with $T' = L + T$. The time constant being small, a Taylor development leads to

$$\tau \frac{d\hat{a}_s}{dt} = -T'/2\hat{a}_s + \mathbf{g}\hat{a}_p\hat{a}_i^\dagger + \sqrt{L}\hat{a}_{sL} + \sqrt{T}\hat{a}_{sIn}, \quad (3.13)$$

$$\tau \frac{d\hat{a}_i}{dt} = -T'/2\hat{a}_i + \mathbf{g}\hat{a}_p\hat{a}_s^\dagger + \sqrt{L}\hat{a}_{iL} + \sqrt{T}\hat{a}_{iIn}. \quad (3.14)$$

These two equations can be decoupled by the following change of modes $\hat{a}_1 = (\hat{a}_s + \hat{a}_i)/\sqrt{2}$, $\hat{a}_2 = (\hat{a}_s - \hat{a}_i)/\sqrt{2}$. The loop equations can be rewritten

$$\tau \frac{d\hat{a}_1}{dt} = -T'/2\hat{a}_1 + \mathbf{g}\hat{a}_p\hat{a}_1^\dagger + \sqrt{L}\hat{a}_{1L} + \sqrt{T}\hat{a}_{1In}, \quad (3.15)$$

$$\tau \frac{d\hat{a}_2}{dt} = -T'/2\hat{a}_2 - \mathbf{g}\hat{a}_p\hat{a}_2^\dagger + \sqrt{L}\hat{a}_{2L} + \sqrt{T}\hat{a}_{2In}. \quad (3.16)$$

Hence, we obtain the same equations as two independent type-I OPOs. We note also that the two fields “see” the pump with opposite phases, leading to squeezing on orthogonal quadrature.

Threshold The pump is a bright coherent state, we thus can replace \hat{a}_p by $e^{i(\omega_p t + \phi_p)}|\alpha\rangle$. Hence, the equation shows a threshold, i.e. a value of the pump for which the losses of the cavity compensate the gain. $-T'/2 + \mathbf{g}|\alpha| > 0$. We thus define the threshold:

$$|\alpha_{th}|^2 = \frac{(T + L)^2}{4\mathbf{g}^2}. \quad (3.17)$$

In addition to that, if the pump is resonant, it doesn't affect the intra-cavity equation for the down-converted beams, it only changes the relationship between intra and extra-cavity beam pump and yields to a higher intra-cavity power (compared to the input beam power). In that case, we have the relation between the intra-cavity pump threshold and the extra-cavity one (field inside a resonant Fabry-Perot cavity)

$$\mathcal{P}_{th}^{ext} = \frac{(T_p + L_p)^2}{4T_p} \mathcal{P}_{th}^{int}, \quad (3.18)$$

with T_p the transmission of the mirror for the pump. The pump enhancement enables to drastically reduce the threshold. The cavity being also resonant for s and i , we have here a *triple resonant* OPO.

If we consider the losses negligible compared to the mirror transmissions, we have the scaling

$$\mathcal{P}_{th}^{ext} \propto T_p \cdot \frac{T^2}{L^2}. \quad (3.19)$$

¹with a factor 2 for the linear cavity as the effective length of the crystal is twice the length of the crystal \mathcal{L} (round-trip of the beam inside the crystal)

In the following, we will note the pump normalized to the threshold $\varepsilon = |\alpha|2\mathbf{g}/T' = \sqrt{P/P_{th}}$. It can be interpreted as a strength of the pumping.

NB: We will always operate the OPO below threshold. Hence, it is not completely true to talk about OPO as it is below the oscillation threshold, that is why sometime squeezer (or two-mode squeezer) is preferred.

Correlation function After few manipulations of the loop equation, one obtains the correlation equations

$$\langle \hat{a}_{s/i}(t)\hat{a}_{i/s}(t') \rangle = \frac{\lambda^2 - \mu^2}{4} \left(\frac{e^{-\mu|t-t'|}}{2\mu} + \frac{e^{-\lambda|t-t'|}}{2\lambda} \right), \quad (3.20)$$

$$\langle \hat{a}_{s/i}^\dagger(t)\hat{a}_{i/s}(t') \rangle = \frac{\lambda^2 - \mu^2}{4} \left(\frac{e^{-\mu|t-t'|}}{2\mu} - \frac{e^{-\lambda|t-t'|}}{2\lambda} \right), \quad (3.21)$$

$$\langle \hat{a}_{s/i}(t)\hat{a}_{i/s}(t') \rangle = \langle \hat{a}_{s/i}^\dagger(t)\hat{a}_{i/s}(t') \rangle = 0. \quad (3.22)$$

with $\lambda = \frac{T'}{2\tau}(1/2 + \varepsilon)$ and $\mu = \frac{T'}{2\tau}(1/2 - \varepsilon)$.

3.1.3 Noise spectrum

In order to study the noise spectrum of the OPO output, we do the following linear combination within the rotating frame (aligned on the pump phase) to obtain the quadrature observables

$$\hat{x}(t) = (e^{-i(\omega_0 t + \phi_p/2)}\hat{a}(t) + e^{+i(\omega_0 t + \phi_p/2)}\hat{a}^\dagger(t))\sigma_0, \quad (3.23)$$

where $\omega_0 = \omega_p/2$ is the down-converted frequency in the degenerate case. This yields to the mode loop equations for the quadratures:

$$\tau \frac{d\hat{x}_1}{dt} = -T'/2\hat{x}_1 + \mathbf{g}|\alpha|\hat{x}_1 + \sqrt{L}\hat{x}_{1L} + \sqrt{T}\hat{x}_{1In}, \quad (3.24)$$

$$\tau \frac{d\hat{p}_1}{dt} = -T'/2\hat{p}_1 - \mathbf{g}|\alpha|\hat{p}_1 + \sqrt{L}\hat{p}_{1L} + \sqrt{T}\hat{p}_{1In}. \quad (3.25)$$

After a Fourier transform, we obtain

$$\left(1 - \frac{\tau i\omega}{T'/2}\right)\hat{x}_1(\omega) = \frac{\mathbf{g}|\alpha|}{T'/2}\hat{x}_1(-\omega) + \frac{\sqrt{L}}{T'/2}\hat{x}_{1L}(\omega) + \frac{\sqrt{T}}{T'/2}\hat{x}_{1In}(\omega). \quad (3.26)$$

By denoting $\omega_c = T'/(2\tau)$, we finally obtain:

$$(1 + \varepsilon - i\omega/\omega_c)\hat{x}_1(\omega) = \frac{\sqrt{L}}{T'/2}\hat{x}_{1L}(\omega) + \frac{\sqrt{T}}{T'/2}\hat{x}_{1In}(\omega). \quad (3.27)$$

We have a similar equation with the conjugate quadratures by exchanging $\varepsilon \rightarrow -\varepsilon$.

Moreover, in order to have the output quadrature and to remove the intra-cavity quadrature, we use the relation

$$\hat{x}_{1Out} = \sqrt{T}\hat{x}_1 - (1 - T/2)\hat{x}_{1In}. \quad (3.28)$$

Note that here we have a minus sign owing to our previous choice for the other output mirror equation.

On the other hand, we have a vacuum state on mode $1In$ and $1L$, thus $\langle \hat{x}_{1L}(\omega)\hat{x}_{1L}(-\omega) \rangle = \sigma_0^2$ and $\langle \hat{x}_{1In}(\omega)\hat{x}_{1In}(-\omega) \rangle = \sigma_0^2$ but these two are not correlated $\langle \hat{x}_{1L}(\omega)\hat{x}_{1In}(-\omega) \rangle = 0$.

Finally, we obtain the Lorentzian shaped spectral density of noise normalized to the vacuum noise $s_x = \langle \hat{x}_{1Out}(\omega)\hat{x}_{1Out}(-\omega) \rangle / \sigma_0^2$

$$s_x(\omega) = 1 + \eta \frac{4\varepsilon}{(1 - \varepsilon)^2 + 4(\omega/\omega_c)^2}, \quad (3.29)$$

$$s_p(\omega) = 1 - \eta \frac{4\varepsilon}{(1 + \varepsilon)^2 + 4(\omega/\omega_c)^2}, \quad (3.30)$$

with $\eta = T/(T+L)$ the *escape efficiency*. This quantity can be interpreted as the conditional probability that if one photon escapes from the cavity it is by the output coupler T (and not due to the losses L). More interestingly, this escape efficiency can be seen as the transmission of a beam-splitter of losses η right after a perfect OPO (i.e. without internal losses).

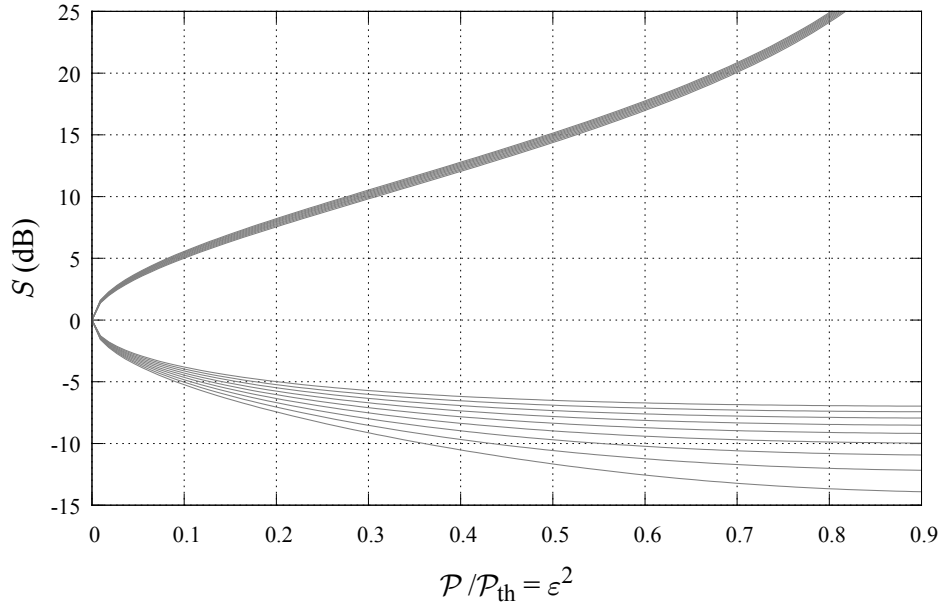


Figure 3.2: Squeezing and anti-squeezing versus pump power at zero frequency for different values of the escape efficiency (from 0.8 up to 0.96)

Figure 3.2 gives the squeezing and anti-squeezing versus the pump power. Owing to the logarithmic scale, the anti-squeezing is not very sensitive to the escape efficiency contrary to the squeezing (see figure). Furthermore, the squeezing doesn't change a lot with a pump power above 50% of the power threshold when $\eta = 0.8$. For high escape efficiency, the evolution is more significant.

We can also note that the purity of the state decreases. Indeed, for a Gaussian state $\mathcal{P} = 1/\sqrt{s_+s_-}$. Hence, with a logarithmic scale the state is pure only if $s_+^{dB} = -s_-^{dB}$.

The maximum of squeezing is reached at the threshold $s_-^{max} = s_-(\Omega = 0, \varepsilon = 1) = 1 - \eta$. Moreover, as the anti-squeezing diverges to $+\infty$ when the pump power goes to the threshold, the purity of the state decreases with the pump power.

On figure 3.3, we illustrate the effect of the losses on the squeezing and the anti-squeezing. Indeed, in addition to the escape efficiency the subsequent losses (detection for instance) also contribute to degrade the squeezing level. One interesting limit, that we will highlight in the *Complement*, is the -3 dB. If this limit is crossed, we can say that the overall efficiency of the setup is greater than 50%.

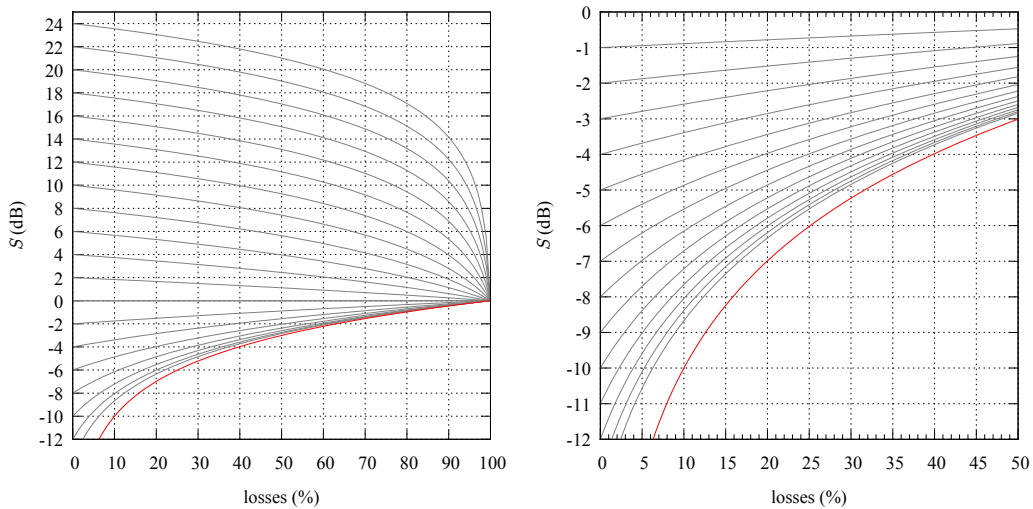


Figure 3.3: Effect of the losses on the squeezing and anti-squeezing in logarithmic scale the initial squeezing values corresponding to no losses). In red, the infinite squeezing.

The question that arises is: how to improve the quality of the state? Concerning the detection efficiency, the only trade-off is on the electronic noise versus the bandwidth of the homodyne detection as detailed in appendix B. Concerning the OPO, the intra-cavity losses should be reduced at the minimum. However, as shown figure 3.4, the transmission of the output coupler can have a strong effect. Basically, if the losses are small compared to the transmission of the output coupler, the escape efficiency is high.

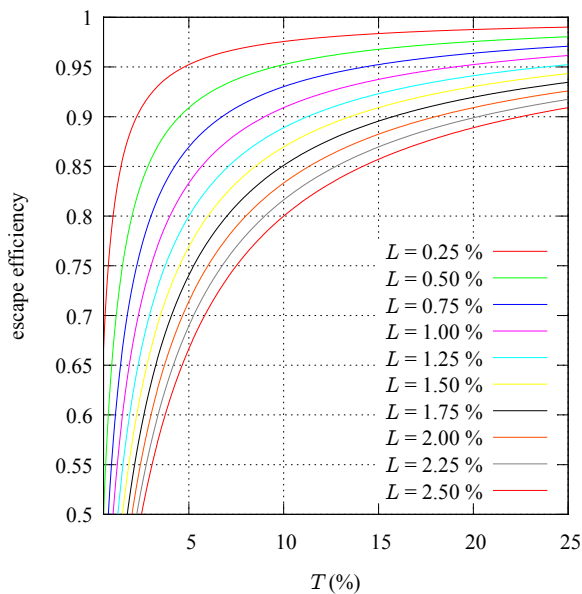


Figure 3.4: Effect of the transmission output on the escape efficiency for different values of intra-cavity losses.

3.2 Experimental realizations

The two OPOs we are going to describe are identical, only the type of crystal differs leading to type I and type II phase matching. They are both operated below threshold.

3.2.1 Global setup

The OPO is made of a semi-monolithic cavity. One face of the crystal is used as a mirror of the cavity by directly coating it. This geometry has the advantage to reduce the number of interfaces and thus the intra-cavity losses. Additionally, it reduces the number of optical elements, and thus increases the overall stability of the setup. It is pumped by a 532 nm frequency doubled Nd:YAG laser (doubling crystal LiNbO_3)².

Let us start by the optical description of the OPO (see figure 3.5). The KTP and ppKTP crystals are from the company Raicol, the coatings on the crystal have been made by the company Layertech. One face (input of the OPO) has a high-reflection at 1064 nm for both polarizations and 5% transmission at 532 nm. The other face (in the middle of the OPO) has a double anti-reflection coating for 532 nm and both polarizations at 1064 nm (DBAR).

As stated before, the intra-cavity losses are extremely important. The figure 3.4 shows that these losses have strong effect on the escape efficiency $\eta = T/(T + L)$ with L the intra-cavity losses and T the output coupler transmission. For instance, with $T = 10\%$ only 0.5% of losses yields to 5% of losses. Here, HR, AR coatings and absorption at 1064 nm contribute to the intra-cavity losses. The output coupler has a high-reflection (HR) coating at 532 nm and 10% transmission at 1064 nm. Note that this value is a good trade-off between a high escape efficiency, a not too large bandwidth, and a reasonable threshold.

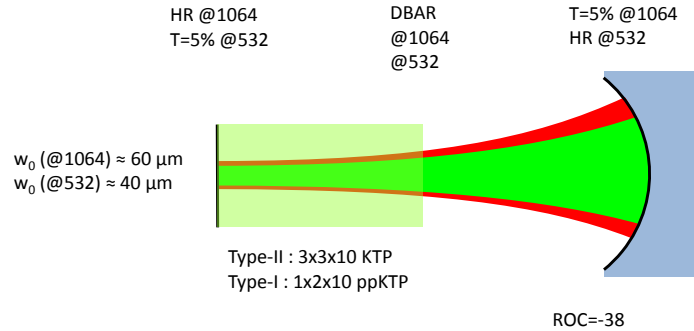


Figure 3.5: Optical description of the OPO.

The length of the cavity is locked by a PZT on which the output coupler is mounted by using the Pound-Drever-Hall technique. We use a Faraday isolator to get back the reflection of the pump beam that is reflected on the input mirror of the OPO (and also to protect the laser from back reflections). The Diabolo laser beam is phase modulated at 12 MHz. The reflected beam measured by a photodiode and demodulated at 12 MHz, the resulting signal is then used as an error signal in a proportional-integrate circuit. The output is then sent to a high voltage amplifier to set the PZT position. (For a detailed description see [53]).

The temperature of the crystal is controlled and stabilized with a PID locking. This one heats up or cools down a copper oven via of a Peltier element. The temperature is measured by a thermistor close to the crystal inserted into the oven (see figure 3.6).

²Diabolo Laser from Innolight. The useful feature of this laser is its second output: a part of the 1064 nm beam used to pump the doubling cavity is directly accessible. This beam is therefore perfectly coherent with the output state of the OPO.

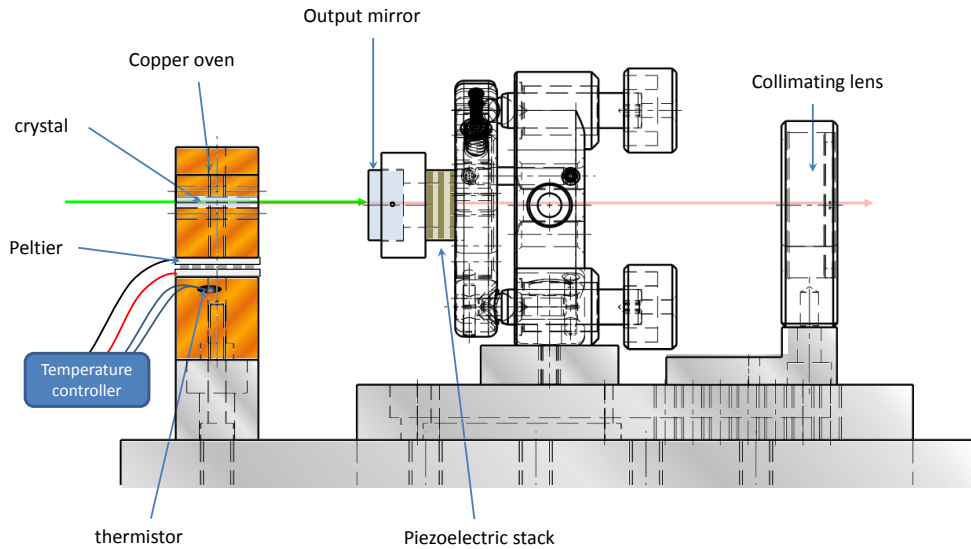


Figure 3.6: OPO layout. The non-linear crystal is inserted in a oven made of copper. The temperature is controlled thanks a thermistor feedback to a Peltier element. The output mirror is handled in a plastic mount glued on a piezo itself placed in a high stability mirror mount. A lens is placed right after in order to collimate the beam to a size of almost 1 mm.

3.2.2 Crystal phase-matching

Being in a semi-monolithic configuration, it is not possible to use the tilt of the crystal to adjust the phase-matching. The crystal should be directly cut with the good phase-matching angle. As described in [53], this angle is extremely precise. Nevertheless, it is possible to correct it by adjusting the cutting angle. A first measurement of phase-matching versus temperature via up-conversion gives us the actual phase-matching temperature. As shown on figure 3.7, if we pump the crystal with a 1064 nm beam, we obtain a 532 nm beam by up-conversion (second harmonic generation). When we vary the temperature, the phase-matching condition varies and, as a consequence, the power of the 532 nm emitted light changes. This temperature will be of course the same for the down-conversion. By knowing the value of the temperature of phase-matching, we can compute how much the cutting angle of the crystal should be corrected in order to shift this temperature to the desired one. In practice, the targeted temperature is around 25°C. Indeed, a temperature close to the room temperature enables a better thermal stability.

3.2.3 Type-II OPO

Triply resonant OPO The triple resonance is probably the main difficulty of the setup. Our cavity is necessary resonant for the signal and idler, but the resonance for the pump offers two advantages. First, this yields to a lower threshold. Secondly, we can use the pump to lock the cavity, otherwise it would be necessary to use an infrared beam. The OPO has one geometric length but three optical lengths (for the pump, the signal and the idler). To be resonant, each length should be an integer number of the corresponding wavelength. We thus need at least three degrees of freedom. Here we use the geometric size of the cavity (via a PZT), the relative change of index induced by the crystal temperature and the wavelength

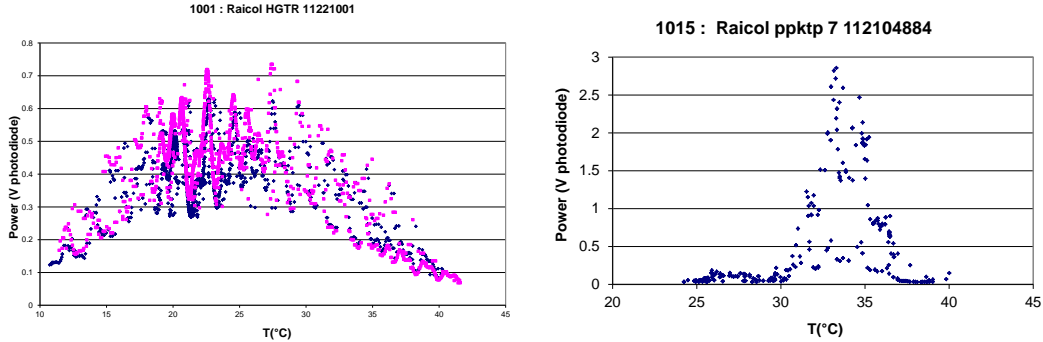


Figure 3.7: Up-conversion from 1064 nm versus temperature (in normal incidence). The range of temperature for phase-matching is broader for the type-II than the type-I. The substructure we can observe is due the reflection on the non-coated surfaces (effect of cavity, when at least one of the face is AR coated the substructures vanish. These measurements have been performed on crystals before coatings.)

of the pump laser. Note that being a semi-monolithic cavity, there is no degree of freedom on the angle of the crystal, all the beams are necessarily with a normal incidence. Thus, as demonstrated in [53], there is not anymore degree of freedom, and the triple resonance condition is unique.

To find the good settings of the triple resonance condition, a seed is impinged on the OPO for both polarizations 45° and separated at the output with a polarizing beam-splitter. The cavity is then swept in order to see the different peaks of resonance for the pump and the two infrared lights. The goal is then to adjust these three optical lengths in order to superpose the three resonances. Practically, the temperature of the OPO changes differently the indices of the two polarizations (one changes faster than the other one) whereas the temperature of the laser changes the two indices in the same way. We first adjust the temperature of the laser to superpose the pump and the “slow” polarization and then, adjust the temperature of the OPO to superpose the “fast” polarization. Of course, these two steps should be iterated few times in order to converge to the good settings. However, if it is not possible to find some stable settings we can use another input on the crystal. Indeed, the small heterogeneity of the crystal leads to specific parameters for each position.

Measured output state Depending on the chosen polarization basis, the output state has different properties. In the basis of the crystal axis we have an EPR state. This state being entangled, the relevant properties are obtained when the two modes are measured together. When the polarization basis is rotated at 45° , the output state is a squeezed vacuum state on each polarization. The state being separable, we can focus on only one.

In both cases, we didn’t try to perform the best measurement in terms of noise reduction. Indeed, this is possible only close to the threshold. But the KTP crystal suffers of *gray tracking* for high pump power. So, to preserve the performance of the crystal, we didn’t try to see the highest level of squeezing. In addition to that, the triply resonance condition is not often easy to find.

With a 5% transmission output coupler the threshold is around 20 mW, so we expect that for a 10% transmission output coupler it would be around 80 mW. Again, since we use a new crystal, we never operate the OPO with high pump power in order to avoid any gray tracking.

Besides, this OPO has been fully characterized in [53]. To sum up the different results: 9.7 dB of noise compression on the intensity difference has been obtained above threshold (10% transmission output coupler), and two squeezed vacuum states at -5 dB have been obtained below threshold (5% transmission output coupler). Note that the homodyne detection has also been largely improved since this time. Hence, we could expect higher performances now.

3.2.4 Type-I OPO

Resonance The settings for the resonance are easier to tune than for the type-II OPO as the cavity is only doubly resonant (s and i are degenerate in polarization). We simply optimize the value of the squeezing by changing the temperature of the crystal.

Phase noise Beyond a certain level of squeezing the effect of phase noise is not at all negligible. Indeed, the state is more phase sensitive. Although we discuss this in the type-I OPO section, it is of course an issue for the type-II OPO too. However, it is one of the main possible limitation of our type-I OPO. For instance, for the type-II OPO, the triple resonance tuning is a limitation that the type-I doesn't have.

Depending on the physical phenomenon at the origin of the phase noise, the way to model it can be very different. In all the cases, the measured state is a statistical mixture of the same squeezed vacuum state but with different phases. If this different phases follow a distribution $f(\theta)$, the state can be written as $\hat{\rho}_f = \int d\theta f(\theta) \hat{\rho}_\theta$ with $\hat{\rho}_\theta$ a squeezed vacuum state rotated by an angle θ . The measured squeezing is thus $s_f = \int d\theta f(\theta) s(\theta)$ with $s(\theta) = s_x \sin^2 \theta + s_p \cos^2 \theta$.

On figure 3.8, we compare two types of distribution: a square distribution³ and a Gaussian distributions⁴ which can correspond to a Brownian motion. In both, for small values of squeezing up to -5 dB typically the effect is not really important, but for high values the squeezing is degraded extremely fast.⁵ The effect is extremely close as for the Gaussian distribution with $\delta\theta = \sigma_\theta$ (the two models become different for higher amplitude of noise).

In our experiment, we did not try to measure the phase noise precisely. The idea was mainly to find a way to “diagnose” the possible sources of noise and afterwards to fix them. We do not detail what we did here but explain the general idea.

A phase fluctuation cannot be measured directly with a photodetector. Hence, we need some interference to “translate” the phase fluctuations into amplitude fluctuations. First, we have looked at the interferences between the local oscillator and the seed (infrared beam

³

$$s'_x(\delta\theta) = \frac{(2\delta\theta + \sin(2\delta\theta))s_x + (2\delta\theta - \sin(2\delta\theta))s_y}{4\delta\theta} \quad (3.31)$$

⁴

$$s'_x(\sigma_\theta) = \frac{(1 + e^{-2\sigma_\theta^2})s_x + (1 - e^{-2\sigma_\theta^2})s_y}{2} \quad (3.32)$$

⁵The case of a harmonic noise is more delicate to treat. The phase oscillates between $-\delta\theta$ and $\delta\theta$, but the measurement is random in time. Thus the distribution in this case is $f(\theta) = 1/\pi\sqrt{\delta\theta^2 - \theta^2}$. It is obvious that the calculation will be more difficult... However, we can assume the diverging part with Dirac function i.e. $f(\theta) = (\delta(\theta - \delta\theta) + \delta(\theta + \delta\theta))/2$ we obtain in that case

$$s(\delta\theta) = s_x \sin^2 \delta\theta + s_p \cos^2 \delta\theta \quad (3.33)$$

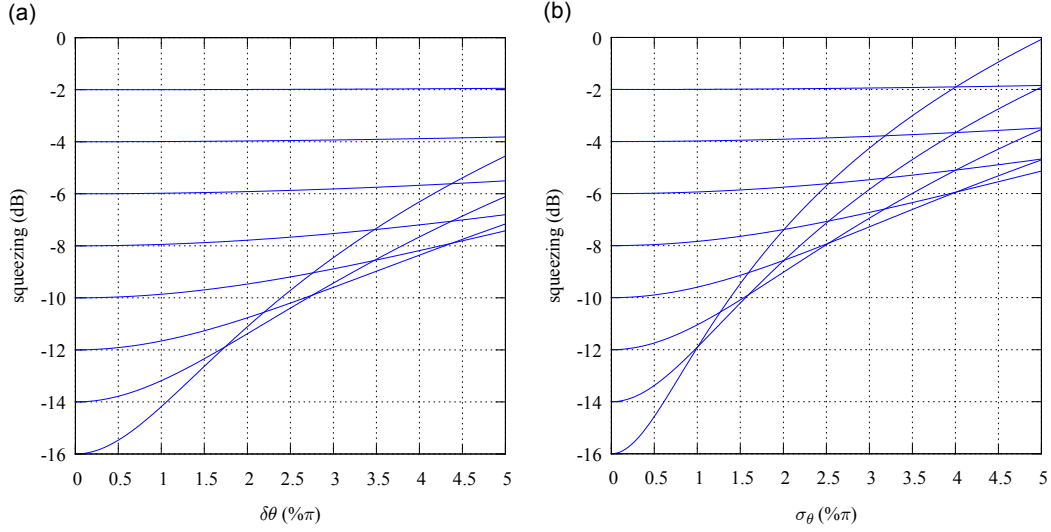


Figure 3.8: Effect of phase noise on the measured level of squeezing. Evolution of the squeezing versus the amplitude of noise. (a) for a square distribution of $2\delta\theta$ large. (b) for a normal distribution with σ_θ standard deviation. For a large value of squeezing the state is extremely sensitive to the noise. Moreover, these curves only consider pure states.

injected in the OPO). Of course, some noises can come from the upstream of the seed, and in that case, this noise is not present in our measurement. However, this technique shows at least the noise on our measurement. As we can see on figure 3.9 (a), the Fourier transform of the interference signal contains interesting information. We have some broad peaks at 15 Hz and one at 130 Hz. The first one is not obvious to discuss because not always reproducible. The second one, well defined, is attributed to mechanical vibrations but its source is unknown. We have checked individually each beam to make sure they do not already contain any amplitude noise.

In order to remove the broad peaks, we have adjusted the air pressure of the optical table by taking into account the weight of the elements on it (laser, mounts, ...). This procedure strongly reduced the peaks and, after that, only the 50 Hz and harmonics peaks remained. In conclusion, we can suspect that this noise was induced by coupling to the floor and not by acoustic in the air (at least in a quiet room).

Thereafter, we have suspected that the remaining noise was linked the pump light. This was all the more confirmed given the fact that without locking and with the pump (i.e. only maintained the resonance by hand) the 50 Hz and harmonics noise disappear. Therefore, we have also checked this possibility of phase noise on the pump. For this purpose, we use the parametric gain on the seed. Indeed, the amplification/desamplification is a function of the relative phase between the pump and the seed. Once again, we observed the same peaks.

At the end, it turns out that this noise came from the laser. Indeed, when the doubling cavity is not precisely locked on the top of the transmission peaks, we can observe a 50 Hz pattern fluctuations on the light. When locked on the side, we confirmed that the amplitude is stronger. It seems intrinsic to the electronics of the locking of the doubling cavity. Actually, we have observed the same kind of noise with another Diabolo laser.

Eventually, a better setting of the optical table air pressure and a better locking of the laser, as we can see on figure 3.9 (b), have led to a reduction of all the peaks. Although the obtained quantitative values are not obvious to compare, if we use the background noise as reference we clearly see the improvement.

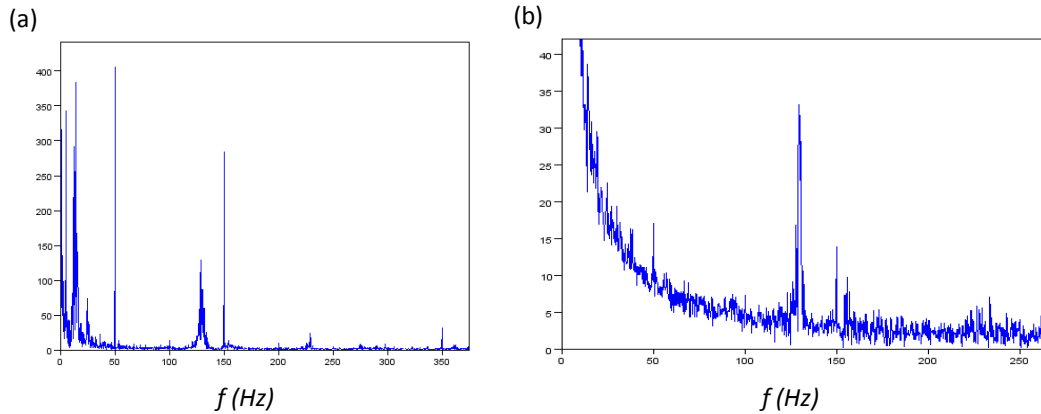


Figure 3.9: Phase noise analysis: Fourier transform of the interferences between the seed and the local oscillator. (a) First measurement. We can see mainly 3 peaks. One is broad and attributed to mechanical vibrations/relaxations. The two others are extremely narrow (pure sine) one at 50 Hz and the other one at 150 Hz and we can distinguish some other odd harmonics. These peaks are attributed to the electronics. (b) After improvements. The peaks do not completely disappear, but their amplitudes, compared to the background, have been strongly reduced (the scale is divided by 10).

Nevertheless, it remains not completely clear whether the induced noise was in amplitude only or also in phase and how did it affect the locking of the OPO. Anyway, as the problem was fixed, and not very important for the next experiments, we didn't do further investigations.

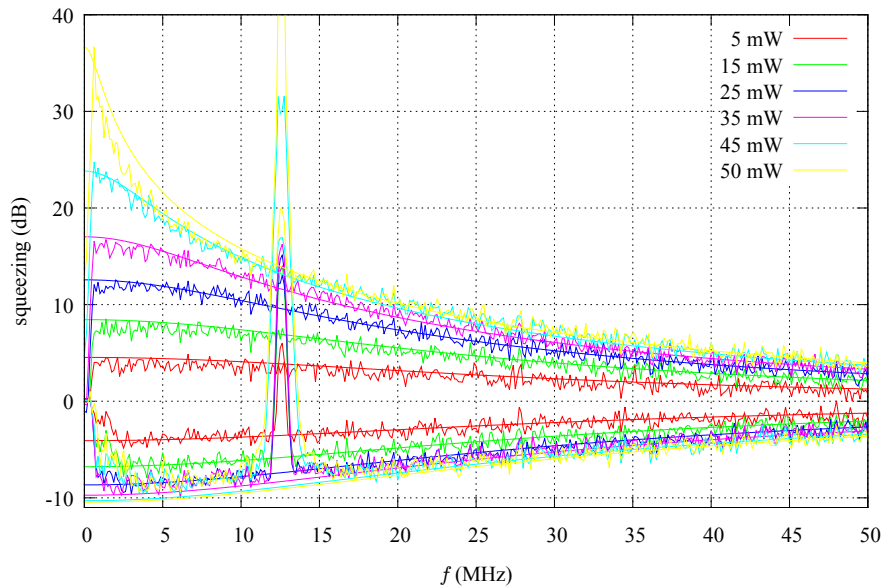


Figure 3.10: Squeezing and anti-squeezing versus frequency for different values of the pump power. The smooth lines are theoretical fitting using equations 3.29 and 3.30 (with parameters $\eta = 91\%$, $\omega_c = 65$ MHz). All traces are normalized to the shot noise (i.e. $S(\omega)/SN(\omega)$).

Squeezing measurements On figure 3.10, we show the measured squeezing and anti-squeezing for different values of pump power. We also add the theoretical curves and optimized the different parameters: global efficiency of $\eta = 91\%$ and $\omega_c = 65$ MHz. We can note that close to the threshold, the theory does not fit as well as for lower pump power. Moreover the fitting is not perfect because these curves have been obtained “hand-made”, i.e. there is no locking.

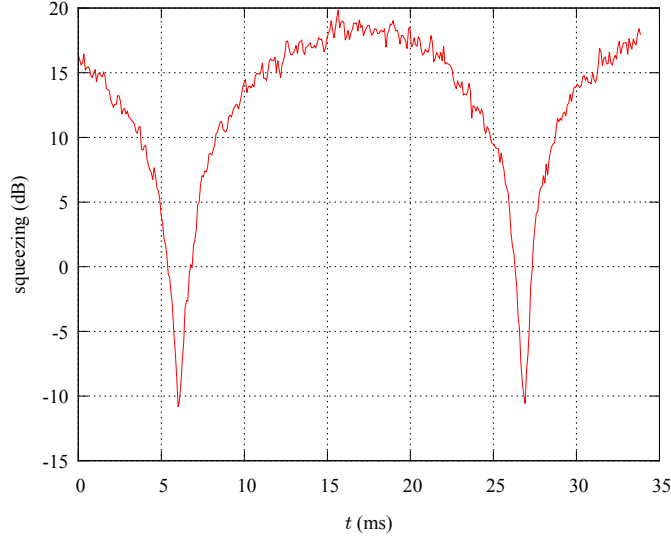


Figure 3.11: Arches of squeezing. The various parameters are: the pump power $P = 40$ mW for a threshold $P_{th} = 50$ mW, with a visibility 99% for the homodyne detection. The spectrum analyser parameters are $RBW = 300$ kHz, $VBW = 3$ kHz, $F = 4$ MHz.

The best measurement of squeezing is reported on figure 3.11 and shows a value as high as 10.5 dB which means a global losses (OPO, propagation, detection) below 10%. We can roughly estimate the different losses: the visibility squared is $V^2 = 99\%$, the photodiode of the homodyne detection $\eta_{pd} = 97\%$, the electronic noise $\eta_e = 99\%$ and the propagation (i.e. non perfect AR coating of the various optics on the path) $\eta_{prop} = 99\%$. All of this yields to a detection efficiency of 93%, hence we estimate the squeezing at the output of the OPO to be -16.5 dB.

3.3 Conclusion

In this chapter, we have described the starting point of all the later experiments: the optical parametric oscillators. Two types of OPO have been studied: a type-I phase matched OPO with a ppKTP crystal in a doubly resonant cavity and a type-II phase matched OPO with a KTP crystal in a triply resonant cavity. The type-II OPO has been widely studied during the previous PhD works, and has shown some good performances. The type-I OPO being new, it has been more investigated. This latter has shown comparable good performances according to the different enhancements performed on the homodyne detection.

In practice, the semi-monolithic architecture for a type-II OPO has some advantages but also some drawbacks. It is easy to align and optically very stable. It also minimize the intra-cavity losses which leads to a very good “quality” of the output state. However, this has a “price”. Indeed, the triple resonance condition can be sometimes very difficult to

achieve. Moreover, these parameters have to be adjusted when the level of the pump power is changed. On the other hand, it seems quite impossible to build a second type-II OPO which would work with exactly the same parameters, it would require a perfectly identical crystal. However, these possible drawbacks have to be balanced by the fact that a type-II OPO is actually equivalent to two perfect copies of a type-I OPO, i.e. with the same level of squeezing, perfectly mode-matched output, spectrally matched and phase locked, which seems experimentally more challenging.

With the type-I OPO, we have shown high squeezing value measurements, confirming the high efficiency of the overall setup (up to 90%). At this level, the limitation does not only come from the optical losses but also from the phase noise. The remaining losses are almost half from the escape efficiency, and the other half from the detection, in particular the photodiode efficiency and the mode matching.

To go further in terms of performances, the first possible solution would be to shorten the crystal to reduce the absorption losses. Of course, this will lead to a significant enhancement only if the absorption is the main contribution of the intra cavity losses. Indeed, there is not enough precise measurement concerning the coatings to know its contribution in the intra-cavity losses. Actually, all the possible improvements will need optical characterizations improved by one order of magnitude better compared to what we can do with standard optics.

4 | Generation of Heralded Single-Photon

*I think there's a great beauty to having problems.
That's one of the ways we learn.*

HERBIE HANCOCK

The single photon was at the origin of the quantum theory. It has been used to illustrate many thought experiments. In particular, it highlights the wave-particle duality of light. Being an extremely simple state, it has also been used as a basic element in many different protocols of quantum information. Nowadays, the reliable generation of single-photon states is a central resource for the development of quantum information sciences and technologies, including quantum communication and computing [10, 103]. For instance, since the seminal proposal by Knill, Laflamme and Milburn [47], single-photons are indeed at the heart of linear-optical quantum computation (LOQC) [48]; it is a key element of discrete variable quantum information. Practical implementations however require to generate such states with a low admixture of vacuum as efficient LOQC protocols are constrained by loss thresholds [114]. Indeed, losses induce some errors but this can be compensated with quantum error correction algorithms. Nevertheless, these algorithms are efficient up to a certain level of losses. For instance, the best known figure to date, which applies to cluster state computation, is a 1/2 overall loss tolerance [30], i.e. the product of the source fidelity and detector efficiency has to be above this value. This constraint puts a challenging demand on single-photon generation. Additionally, linear-optical processing cannot increase the fidelity of the state, even with multiple imperfect sources [6]. Moreover, gates implementation requires to make single-photons interfere with a high visibility and thus to be emitted into a well-controlled spatio-temporal mode.

This experiment is the first milestone of this PhD thesis work [74]. This is the simplest conditional preparation: the state is phase invariant, the losses are easy to estimate, the different defects are simple to model and understand.

This chapter is divided into three parts. In the first one, we describe the principle of the experiment and derive different models taking into account the realistic aspects of the experiment. Then, we describe the experimental setup and we finally present the experimental results.

4.1	Principle of the experiment and models	64
4.1.1	Basic scheme	64
4.1.2	Model of the experiment	64
4.2	Experimental setup	69
4.2.1	Type-II OPO	70
4.2.2	Conditioning path	70
4.2.3	Homodyne measurement, data acquisition and processing	74
4.3	Results and discussions	76
4.3.1	Results	76
4.3.2	Global efficiency	77
4.3.3	Asymmetric marginal distributions	77
4.4	Beyond: the qubit	79
4.5	Conclusion	80

4.1 Principle of the experiment and models

The generation technique consists in using photon pairs emitted in two distinct modes: the detection of a single-photon on one mode heralds the preparation of a single-photon into the other one [40]. This conditional preparation technique has been widely used so far with a variety of physical systems, including atomic cascade, atomic ensemble [52] and pulsed single-pass parametric down-conversion (PDC) [64, 123, 88, 42]. More recently, continuous-wave OPOs, where PDC occurs in cavity, have also been considered for this purpose [82].

In this latter case, two methods can be used to obtain the two distinct modes. The first one is based on tapping a very small fraction of a squeezed vacuum [118], leading intrinsically to a low count rate. The other method consists in using non-degenerate modes emitted into the same spatial mode of the OPO cavity. Using a type-I non-linear interaction, signal and idler have the same polarization: the only degree of freedom is thus the frequency. The two correlated modes can be then two modes with frequencies separated by multiples of the cavity free spectral range, as demonstrated in [79]. However, this configuration requires for the homodyne tomography to use local oscillators with shifted frequencies. Here we use another possibility with a type-II interaction: the frequency-degenerate signal and idler modes have orthogonal polarizations and can be easily separated. This configuration has been commonly used with pulsed system in single-pass OPA, however this is the first time that it is used with a cavity.

4.1.1 Basic scheme

We use here a strategy of conditional preparation. The generation of the state is probabilistic but heralded. The output state of the type-II OPO is described by¹

$$|\psi_{sq}\rangle_{ab} = (1 - \lambda^2)^{1/2} \sum_{n=0}^{\infty} \lambda^n |n\rangle_a |n\rangle_b, \quad (4.1)$$

where a and b denote the two correlated modes. These modes have orthogonal polarizations at the output of the OPO and become two different spatial modes after a polarizing beam-splitter.

From this expression, one can see immediately that any photon-number measurement $|n\rangle\langle n|$ on one mode will project the other mode onto the corresponding Fock state $|n\rangle$. Therefore, one beam is sent to a single-photon detector $|1\rangle\langle 1|$. Each detection event heralds the preparation of a single-photon on the other mode. The generated state is then characterized by quantum state tomography (Chap. 2) with quadrature measurements, which provide a marginal distribution

$$\mathcal{P}(x) = \text{Tr}[\hat{\rho}_{\text{cond}} |x\rangle\langle x|]. \quad (4.2)$$

With this distribution we can reconstruct the state $\hat{\rho}_{\text{cond}}$. The prepared state being phase invariant one can notice that this distribution will be the same whatever the phase of the measured quadrature.

4.1.2 Model of the experiment

Unfortunately, many experimental defects exist and can “damage” the state. We can divide the experiment defects into three parts

- the conditioning path,

¹with $\sigma_x^2/\sigma_0 = s = (1 - \lambda)/(1 + \lambda)$ the squeezing factor cf. section 1.4.3

- the state of the OPO output,
- the characterization.

In the following, we are going to consider the defects of each part more or less independently, in order to estimate the importance of each of them. In other words, the goal is not to give a precise and exhaustive model of this experiment but more a study of the “symptomatic” effects of the different parts. For this purpose, we are going to use the POVM formalism (cf Chap 2) where the conditional preparation is written²

$$\hat{\rho}_{\text{cond},b} = \text{Tr}_{a/a,b}[\hat{\Pi}_a \hat{\rho}_{ab}] , \quad (4.3)$$

Otherwise, we use the equation (2.13)³:

$$W_{\hat{\rho}_{\text{cond},b}} = \int_{a/a,b} W_{\hat{\Pi}_a} W_{\hat{\rho}_{ab}} , \quad (4.4)$$

when using the Wigner function formalism. Ideally, the POVM element of the detector is $\hat{\Pi}_{\text{on}} = |1\rangle\langle 1|$. We first study the effect of the detector when considering different models described in section 2.2, then the effect of the output state of the OPO and finally the characterization of the state.

Perfect, non-resolved photon detector We first consider a photon detector which cannot resolve the number of photons but with a perfect quantum efficiency and without noise. The POVM element corresponding to a detection event is

$$\hat{\Pi}_{\text{on}} = \sum_{k=1}^{\infty} |k\rangle\langle k| . \quad (4.5)$$

The resulting conditional state is

$$\hat{\rho}_{\text{cond}} = (1 - \lambda^2) \sum_{k=1}^{\infty} \lambda^{2(k-1)} |k\rangle\langle k| . \quad (4.6)$$

Being not photon-number resolved, the detector not only heralds a single-photon state but also higher Fock states. Nevertheless, the contribution of the higher photon-number depends on the level of the squeezing parameter λ of the EPR state. This latter can be expressed as a function of the squeezing with the relation $\lambda = \frac{1-s}{1+s}$. We can see on figure 4.1 that only for a low squeezing the p_2 and upper photon number are small. For instance, with a relative pump of at 10%, we have 4% of $|2\rangle\langle 2|$ with a perfect detector and if the efficiency is as low as 1% the two-photon component is equal to 8%.

²we remind that we use a condensed notation of

$$\hat{\rho}_{\text{cond},b} = \text{Tr}_a[\hat{\Pi}_a \otimes \mathbb{1}_b \hat{\rho}_{ab}] / \text{Tr}_{a,b}[\hat{\Pi}_a \otimes \mathbb{1}_b \hat{\rho}_{ab}]$$

³again, we use a condensed notation of

$$W_{\hat{\rho}_{\text{cond},b}}(x_b, p_b) = \frac{\iint_{\mathbb{R}^2} dx_a dp_a W_{\hat{\Pi}_a}(x_a, p_a) W_{\hat{\rho}_{ab}}(x_a, p_a, x_b, p_b)}{\iiint_{\mathbb{R}^4} dx_a dp_a dx_b dp_b W_{\hat{\Pi}_a}(x_a, p_a) W_{\hat{\rho}_{ab}}(x_a, p_a, x_b, p_b)}$$

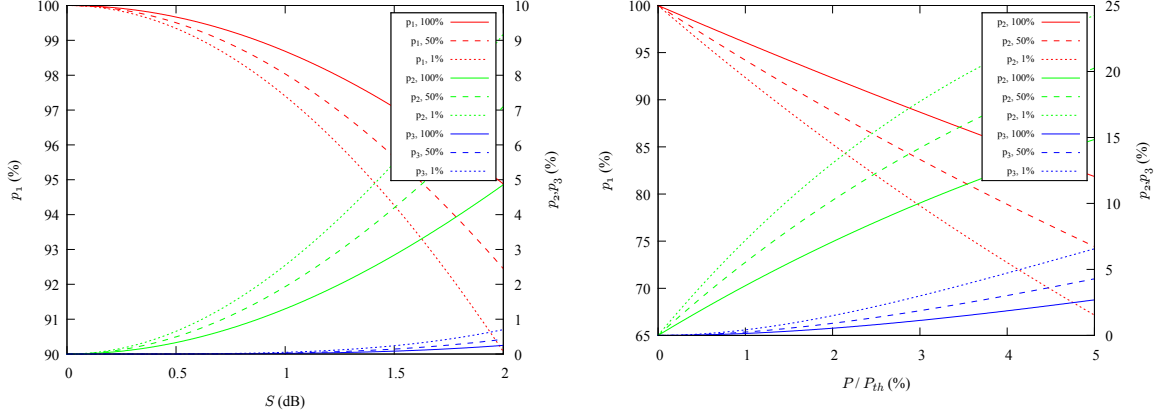


Figure 4.1: Photon number probability of the conditional state $\hat{\rho}_{\text{cond}}$ (p_1 on the left scale, p_2, p_3 on the right scale) as a function of the squeezing of the input state on the left and as a function of the pump power on the right. These plots are done for different levels of detector efficiency. The effect of the non-resolution of the photon detector is already strong for a small pump.

Lossy non-resolved photon detector Of course, our detector is not perfect and at our wavelength (1064 nm) the quantum efficiency is probably the main weakness of nowadays single-photon detectors. It is important to remark that the losses we consider here can also include the propagation losses within the conditioning path. The POVM element in this case is given by:

$$\hat{\Pi}_{\text{on}} = \sum_{k=1}^{\infty} [1 - (1 - \eta)^k] |k\rangle\langle k|, \quad (4.7)$$

with η the overall efficiency of the detector.

If the efficiency of the detector decreases, it becomes less sensitive to low-photon numbers: a part of the high-photon numbers survives through the lossy path more often than the low photon numbers. Thereby, the contribution of higher-photon numbers is even bigger as the efficiency of the conditioning path is low. The conditional state becomes

$$\hat{\rho}_{\text{cond}} = (1 - \lambda^2) \frac{1 - \lambda^2(1 - \eta)}{\eta} \sum_{k=1}^{\infty} \lambda^{2(k-1)} [1 - (1 - \eta)^k] |k\rangle\langle k|. \quad (4.8)$$

We show on figure 4.1 the photon number probabilities for different efficiencies. Moreover, the level of squeezing is not always accessible experimentally, so it is also interesting to consider the pump level. We use the equation (3.30) and, for simplicity, only consider squeezing value at zero frequency

$$s_- = 1 - \frac{4\varepsilon}{(1 + \varepsilon)^2}, \quad (4.9)$$

which is a function of the power normalized to the threshold $\varepsilon^2 = \mathcal{P}/\mathcal{P}_{th}$. This way, we have roughly the dependency of the state with the pump power. We do not consider here the effect of the imperfection of the OPO (i.e. escape efficiency).

Noisy photon detector In contrast to the effect of the efficiency, the effect of the noise is probably more intuitive. If the “click” of the detector comes from the noise, the heralded

state is the partial trace of the EPR state (a thermal state): if the click comes from a “true” detected photon(s) the state is the one corresponding to the previous case (lossy detector without noise). These two different clicks being not coherent, the resulting state is a mixed state weighted by the statistics of the different clicks

$$\hat{\rho}'_{\text{cond}} = \frac{N_{\text{sig}} - N_{\text{dk}}}{N_{\text{sig}}} \hat{\rho}_{\text{cond}} + \frac{N_{\text{dk}}}{N_{\text{sig}}} \text{Tr}_a[\hat{\rho}_{\text{EPR}}^{ab}] , \quad (4.10)$$

where N_{dk} is the dark count rate, i.e. the rate of clicks when no beam is send to the detector, and N_{sig} the count rate from the detection events, i.e. the rate of clicks when the experiment is running (so, it includes the dark count events).

The POVM element of the noisy detector (noted as a function of ν) is (see section 2.2.3 for details)

$$\hat{\Pi}_{\text{on}}(\nu) = \sum_{k=0}^{\infty} [1 - e^{-\nu}(1 - \eta)^k] |k\rangle\langle k|. \quad (4.11)$$

The relationship between the noise ν and the experimental parameters is a priori not straightforward. We should actually rewrite this POVM element as a function of $\hat{\Pi}_{\text{on}}(0)$ the POVM element without noise

$$\begin{aligned} \hat{\Pi}_{\text{on}}(\nu) &= \mathbb{1} - e^{-\nu} \hat{\Pi}_{\text{off}}(0) \\ &= \mathbb{1} - e^{-\nu} \mathbb{1} + e^{-\nu} \mathbb{1} - e^{-\nu} \hat{\Pi}_{\text{off}}(0) \\ &= (1 - e^{-\nu}) \mathbb{1} + e^{-\nu} \hat{\Pi}_{\text{on}}(0) . \end{aligned} \quad (4.12)$$

The conditional state is thus

$$\hat{\rho}'_{\text{cond}} = \frac{e^{-\nu} \hat{\rho}_{\text{cond}} + (1 - e^{-\nu}) \text{Tr}_a[\hat{\rho}_{\text{EPR}}^{ab}]}{e^{-\nu} \frac{1 - \lambda^2(1 - \eta)}{\eta \lambda^2} + 1 - e^{-\nu}} . \quad (4.13)$$

We can then identify $1 - e^{-\nu} = N_{\text{dk}}/N_{\text{sig}}$ which, for a small noise, gives $\nu \approx N_{\text{dk}}/N_{\text{sig}}$.

It is obvious to say that the noise should be as low as possible, but for a given dark count rate, it is not possible to say if the detector is good or not as it should be compared to the count rate of “true” events, which also depends on the efficiency of the detector.

Lossy OPO To study the effect of the output state of the OPO on the final heralded state, we are going to use the formalism of the Wigner function. It will be easier for this calculation, but also because the output of an OPO being a Gaussian state, we experimentally characterize it by measuring its covariance matrix. Moreover, we will assume that the OPO losses are the same for both modes.

A non-pure EPR state can be written as a mixing of two non-pure squeezed vacuum (that we assume identical) on a 50:50 beam-splitter

$$\begin{aligned} &\frac{1}{2\pi\sigma_x\sigma_p} e^{-x_a^2/2\sigma_x^2 - p_a^2/2\sigma_p^2} \frac{1}{2\pi\sigma_x\sigma_p} e^{-p_b^2/2\sigma_x^2 - x_b^2/2\sigma_p^2} \underline{BS}_{50:50} \\ W_{\text{EPR}} &= \frac{1}{(2\pi\sigma_x\sigma_p)^2} \exp \left[-\frac{(x_a - x_b)^2}{4\sigma_x^2} - \frac{(p_a - p_b)^2}{4\sigma_p^2} - \frac{(x_a + x_b)^2}{4\sigma_x^2} - \frac{(p_a + p_b)^2}{4\sigma_p^2} \right] . \end{aligned} \quad (4.14)$$

We reorganize the terms in the exponential to directly apply the Gaussian integral formula⁴

$$W_{\text{EPR}} = \frac{1}{(2\pi\sigma_x\sigma_p)^2} \exp \left[-(x_a^2 + x_b^2 + p_a^2 + p_b^2) \left(\frac{1}{4\sigma_x^2} + \frac{1}{4\sigma_p^2} \right) + (x_a x_b - p_a p_b) \left(\frac{1}{2\sigma_x^2} - \frac{1}{2\sigma_p^2} \right) \right] . \quad (4.15)$$

⁴ $\int_{\mathbb{R}} e^{-ax^2+bx} = \sqrt{\frac{\pi}{a}} e^{b^2/4a}$

First, we consider that the photon-detector is not photon-number resolved but with a perfect efficiency $\eta = 1$. The Wigner function associated with its POVM element is

$$W_{\hat{\Pi}_{\text{on}}} = W_{\mathbb{1}} - W_{|0\rangle\langle 0|} = \frac{1}{2\pi\sigma_0^2} \left(\frac{1}{2} - e^{-(x^2+p^2)/2\sigma_0^2} \right). \quad (4.16)$$

Hence, we obtain

$$\int_b W_{\text{EPR}} W_{\hat{\Pi}_{\text{on}}} = \frac{1}{2\pi\sigma_0^2} \frac{1}{(2\pi\sigma_x\sigma_p)^2} \left[\frac{1}{2} \frac{\pi}{\frac{1}{4\sigma_x^2} + \frac{1}{4\sigma_p^2}} \exp\left(-\frac{x^2+p^2}{\sigma_x^2 + \sigma_p^2}\right) - \frac{\pi}{\frac{1}{4\sigma_x^2} + \frac{1}{4\sigma_p^2} + \frac{1}{2\sigma_0^2}} \exp\left(-(x^2+p^2) \frac{2\sigma_0^2 + \sigma_p^2 + \sigma_x^2}{2\sigma_0^2(\sigma_x^2 + \sigma_p^2) + 4\sigma_x^2\sigma_p^2}\right) \right]. \quad (4.17)$$

After normalization and simplification, we obtain the value at the origin of the phase space ($2\pi\sigma_0^2 W = \bar{W}$)

$$\bar{W}_{\hat{\rho}_{\text{cond}}}(0,0) = -\frac{s_+^{-1} + s_-^{-1} - 2}{s_+ + s_- - 2} \cdot \frac{2 + s_+ + s_-}{2 + s_+^{-1} + s_-^{-1}} \cdot \frac{2}{s_+ + s_-}. \quad (4.18)$$

The first two terms limit the negativity as the EPR state is not pure (i.e. when $s_+s_- > 1$) while the third one translates the fact that the detector is not photon-number resolved and limits the negativity even if the EPR state is pure.

We now consider the complete model of the photon detector including the efficiency η and the noise ν . We use the equation (2.21)

$$W_{\hat{\Pi}_{\text{on}}} = W_{\mathbb{1}} - W_{\hat{\Pi}_{\text{off}}} = \frac{1}{2\pi\sigma_\eta^2} \left(\frac{1}{2} - \frac{e^{-\nu}}{2-\eta} e^{-(x^2+p^2)/2\sigma_\eta^2} \right), \quad (4.19)$$

with $\sigma_\eta^2 = \frac{2-\eta}{\eta} \sigma_0^2$. Compared to the previous case, the derivation is slightly modified: we change the weighting of $\hat{\Pi}_{\text{off}}$ and the standard deviation of the Gaussian function

$$\int_b W_{\text{EPR}} W_{\hat{\Pi}_{\text{on}}} = \frac{1}{2\pi\sigma_\eta^2} \frac{1}{(2\pi\sigma_x\sigma_p)^2} \left[\frac{1}{2} \frac{\pi}{\frac{1}{4\sigma_x^2} + \frac{1}{4\sigma_p^2}} \exp\left(-\frac{x^2+p^2}{\sigma_x^2 + \sigma_p^2}\right) - \frac{e^{-\nu}}{2-\eta} \frac{\pi}{\frac{1}{4\sigma_x^2} + \frac{1}{4\sigma_p^2} + \frac{1}{2\sigma_\eta^2}} \exp\left(-(x^2+p^2) \frac{2\sigma_\eta^2 + \sigma_p^2 + \sigma_x^2}{2\sigma_\eta^2(\sigma_x^2 + \sigma_p^2) + 4\sigma_x^2\sigma_p^2}\right) \right]. \quad (4.20)$$

After normalization of the state and simplifications, we obtain⁵

$$\bar{W}_{\hat{\rho}_{\text{cond}}}(0,0) = -\frac{s_+^{-1} + s_-^{-1} - 2s_\eta^{-1} \left(\frac{e^{-\nu}}{1-\eta/2} - 1 \right)^{-1}}{s_+ + s_- - 2s_\eta \left(\frac{e^{-\nu}}{1-\eta/2} - 1 \right)} \cdot \frac{2 + s_+ + s_-}{2 + s_+^{-1} + s_-^{-1}} \cdot \frac{2 \left(\frac{e^{-\nu}}{1-\eta/2} - 1 \right)}{s_+ + s_-}. \quad (4.23)$$

⁵an alternative writing can be the following

$$\int_b W_{\text{EPR}} W_{\hat{\Pi}_{\text{on}}} = \frac{1}{2\pi\sigma_0^2} \left[\frac{1}{2} \frac{1}{\pi(\sigma_x^2 + \sigma_p^2)} \exp\left(-\frac{x^2+p^2}{\sigma_x^2 + \sigma_p^2}\right) - \frac{e^{-\nu}}{2-\eta} \frac{1}{\pi(\sigma_x^2 + \sigma_p^2 + 2\frac{\sigma_x^2\sigma_p^2}{2\sigma_\eta^2})} \exp\left(-(x^2+p^2) \frac{1 + (\sigma_p^2 + \sigma_x^2)/2\sigma_\eta^2}{\sigma_x^2 + \sigma_p^2 + 2\sigma_x^2\sigma_p^2/2\sigma_\eta^2}\right) \right]$$

“thermal” standard deviation $\sigma_{th}^2 = \frac{\sigma_x^2 + \sigma_p^2}{2}$

negativity standard deviation $\sigma_n^2 = \frac{\sigma_{th}^2 + \sigma_x^2\sigma_p^2/\sigma_\eta^2}{1 + \sigma_{th}^2/\sigma_\eta^2}$

Lossy homodyne detection This loss leads to a more complex model (analytically speaking) but actually, it can be included in the losses of the OPO. Indeed, as depicted on figure 4.2, we can model the different losses with fictitious beam-splitters. η_{OPO} for the OPO (equal to the escape efficiency), η_{PD} the efficiency of the single-photon detector and η_{HD} the efficiency of the homodyne detection. If $\eta_{PD} < \eta_{HD}$ we can decompose the efficiency of the photon detector into two factors, with one equal to the homodyne detection efficiency i.e. $\eta_{PD} = \eta'_{PD} \cdot \eta_{HD}$. Therefore, we can “move” back the two beam-splitters of efficiency η_{HD} before the PBS and add these two to the efficiency of the OPO i.e. $\eta'_{OPO} = \eta_{OPO} \cdot \eta_{HD}$. This way we show that the situation is analytically equivalent to the case of a perfect homodyne detection. The only assumption $\eta_{PD} < \eta_{HD}$ is, in practice, always satisfied.

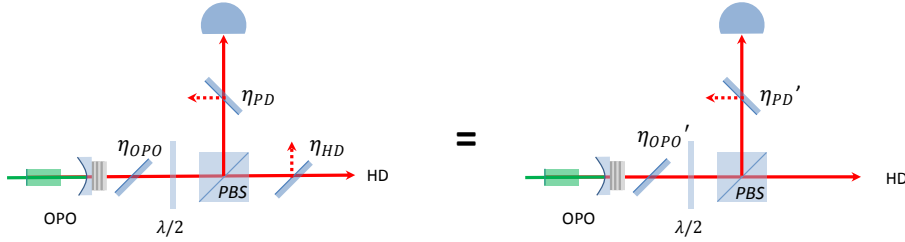


Figure 4.2: Loss model of the experiment. We consider a perfect OPO, single-photon detector,(PD) and homodyne detection (HD). The limited efficiency of each is modeled by fictitious beam-splitters. Because the losses of the conditioning part are higher than the homodyne detection, we can consider a model (to simplify the calculation) where only the OPO and the conditioning path are not perfect.

Conclusion We can conclude by summing up the important points. First, we should work at a very low pump level for two reasons: to avoid the multi-photon components (owing to the detector that cannot resolve the number of photons) and the purity of the EPR state that decreases as the pump increases (this would make an admixture of vacuum). However, the pump level cannot be too low, otherwise the count rate would be small and the dark count of the detector would have a non-negligible effect (also an admixture of vacuum). Secondly, the losses of the conditional state from the OPO to the homodyne detection should be as low as possible, the fidelity of the state being extremely sensitive to these losses.

4.2 Experimental setup

The experimental setup is sketched on figure 4.3. Only the important elements are represented, we omit wave-plates, beam-splitters, mirrors, lenses, etc. The laser has two outputs. One at 532 nm pumps the type-II OPO. The two modes of the EPR state from the OPO are separated via a polarizing beam-splitter. One mode is sent through the *conditioning path*. In this part, the correlated photon is selected by a two-stage optical filtering and then detected by a *superconducting single-photon detector* (SSPD). Each detection event heralds the preparation of a single-photon state which is afterwards characterized by *quantum state*

$$\int_b W_{\text{EPR}} W_{\hat{\Gamma}_{\text{on}}} = \left[\frac{1}{2} \frac{1}{2\pi\sigma_{th}^2} e^{-(x^2+p^2)/2\sigma_{th}^2} - \frac{e^{-\nu}}{2-\eta} \frac{1}{1+\sigma_{th}^2/\sigma_\eta} \frac{1}{2\pi\sigma_n^2} e^{-(x^2+p^2)/2\sigma_n^2} \right], \quad (4.21)$$

normalized with

$$\int_{ab} W_{\text{EPR}} W_{\hat{\Gamma}_{\text{on}}} = \left[\frac{1}{2} - \frac{e^{-\nu}}{2-\eta} \frac{1}{1+\sigma_{th}^2/\sigma_\eta} \right]. \quad (4.22)$$

tomography with the help of a homodyne detection. The second output of the laser provides the local oscillator (at 1064 nm). All the measurements are then acquired and processed by an oscilloscope/computer.

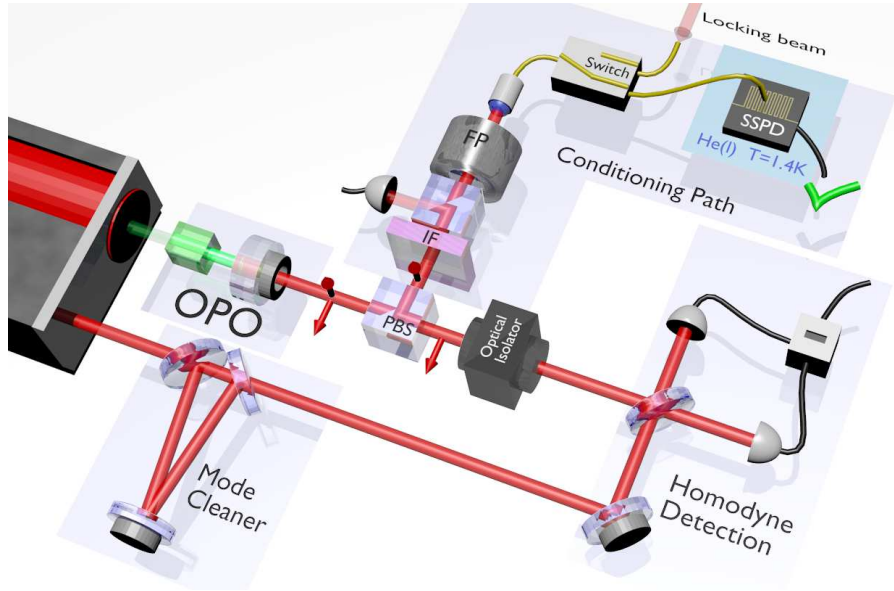


Figure 4.3: General picture of the experiment. A 532 nm beam from a Diabolo Laser pumps a type II OPO. The generated EPR state is separated by a polarizing beam-splitter. One polarization is sent through a filtering stage made of an interferential filter (IF) and a Fabry-Pérot cavity (FP) and then to a superconducting single-photon detector. The resulting state, on the other beam, is then characterized by homodyne measurement: for each detection event on the SSPD the homodyne signal is recorded by an oscilloscope. This signal is then post-processed to reconstruct the state.

4.2.1 Type-II OPO

The OPO we use has been already described in the Chapter 3, we remind the main characteristics of this OPO. The pump is at 532 nm and the OPO, degenerate in frequency, gives an output at 1064 nm. As seen in the modeling (cf previous section) the OPO should be operated at low pump power for two main reasons. First, to reduce the multi-photon components due to the non-resolution in photon of the detector. Secondly, to increase the purity of the output state. Here, for a mirror with 10% of transmission, the threshold is around 80 mW of pump power. In order to have a reasonable count rate, we use a pump power of 1 mW.

The separation of the two polarization-modes can be monitored by injecting a *seed* beam (1064 nm) into the OPO. When the length of the cavity is swept and the OPO set out of the triple resonance condition, the peaks of transmission of each polarization appear for different cavity lengths. We can thus easily separate with precision the two modes.

4.2.2 Conditioning path

One point that we have not consider hitherto is the fact that the parametric down conversion process occurs over a wide range of the spectrum, especially for a KTP crystal with type-II

phase-matching. The down-conversion process converts a pump-photon into two photons at two frequencies $\omega_0 - \nu$ and $\omega_0 + \nu$ (following the energy conservation rule with the pump frequency $\omega_p = 2\omega_0$). In our case, we want to herald a photon at ω_0 by detecting a photon at the same frequency. The cavity of the OPO acts as a filter and allows only some specific frequencies $\omega_0 \pm p\Delta$ separated by the free spectral range of the cavity Δ (and $p \in \mathbb{N}$). The phase-matching being broader than the free spectral range of the cavity, many other modes, not only the degenerate pairs of frequencies, are emitted at the output of the OPO. In order to make sure that the detected photon comes from the degenerate frequencies, it is thus necessary to eliminate all the other frequencies.

Filtering The chosen method uses a two-stage of filtering. The strategy is depicted on Figure 4.4. The first stage is an interferential filter (from Barr Associates) with a bandwidth equal to 0.5 nm and a transmission of 80% at 1064 nm and $8 \cdot 10^{-6}$ outside of the transmission band. A large part of the unwanted frequencies are removed. With a free spectral range of 4.3 GHz for the OPO, around 60 non-degenerate peaks remain. The second stage is a homemade Fabry-Perot cavity. In order to eliminate the remaining frequencies, the free spectral range should be larger than the bandwidth of the interference filter. We need a cavity with a free spectral range at least twice the bandwidth of the filter: this constraint leads to a maximal value of the cavity length $2 \cdot \text{FSR}_{cav} = 265 \text{ GHz} = c/L > \text{BW}_{filter} \rightarrow L/2 < 0.5 \text{ mm}$ (with $L/2$ the size of the cavity, the optical length L being two times this value). Experimentally, we have measured a free spectral range of 330 GHz and a length of 0.45 mm (more details in Appendix.C). We thus call it μCavity in the next. Moreover, the bandwidth of the cavity should be broader than the one of the OPO cavity to transmit the entire degenerate mode to the single-photon detector (for instance, 4 times broader), but of course, small compared to the free spectral range of the OPO cavity. $\text{FSR}_{OPO} \gg \Delta_{cav} \geq 4\Delta_{OPO}$ with $\Delta_{cav} = \text{FSR}_{cav} \cdot T/\pi$ and T the sum of the transmission $T = T_1 + T_2$. We obtain $10\% \gg T \geq 0.6\%$. Finally, the reflection should be high enough to strongly reject the other frequencies, so we choose two mirrors with $T = 0.3\%$ which gives a cavity bandwidth of 320 MHz.

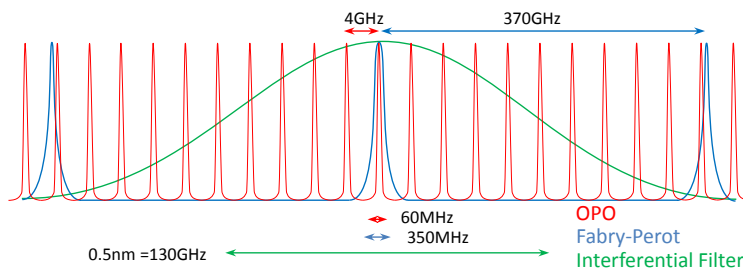


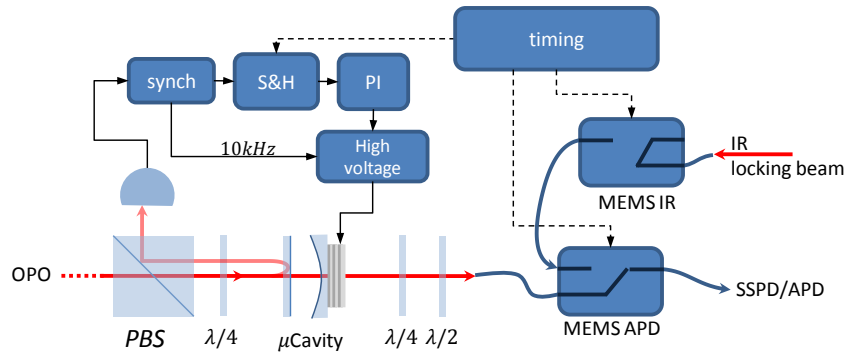
Figure 4.4: Conditioning path. The frequency-degenerate mode is selected by two filtering stages, first a narrow interferential filter then a Fabry-Perot cavity with a bandwidth broader than the OPO cavity bandwidth and a free spectral range bigger than the bandwidth of the interferential filter.

Relatively to the degenerate mode, we can roughly estimate that among the 60 non-degenerate peaks only $T^2 \cdot 60 = 0.05\%$ of the overall is transmitted. A more precise calculation, taking into account the spectrum of the filtering cavity, gives a contribution of 0.3% i.e. a -25dB rejection of the non-degenerate modes.

Although the size of the cavity is a bit challenging, it simplifies the setup of the conditional path as it only needs one active stabilization. Indeed, similar experiments require 3 cavities to realize the filtering of all the non-degenerate modes [80].

Locking and optical path A quarter-wave plate combined with the input mirror of the cavity plays the role of a Faraday mirror. This avoids any extended cavity with the OPO. Indeed, when the mode matching is well realized a cavity can be formed between the output mirror of the OPO and the input mirror of the μ Cavity, or some more complex configurations. Nevertheless, it appears extremely hard to have a reproducible good isolation all the time, especially if the mode matching is well done. So, it has been finally more convenient to add a Faraday rotator.

a) measurements



b) locking

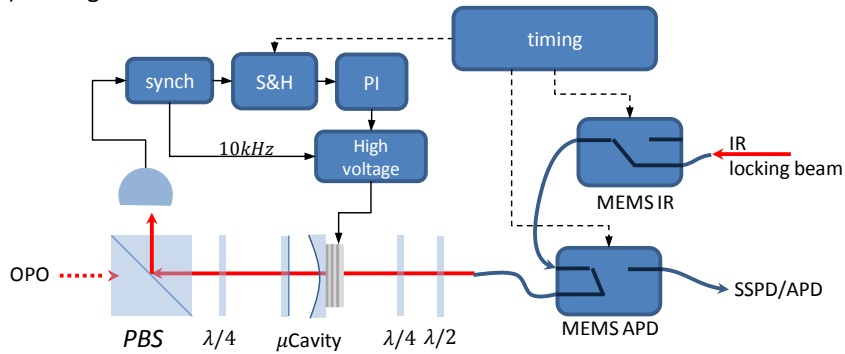


Figure 4.5: The length of the μ Cavity is modulated at 10kHz. The transmitted beam is then demodulated. The error signal is sampled during the locking time and turn to 0 during the measurement thanks to the sampler-and-holder (S&H). The error signal is integrated, amplified and fed back to PZT of the μ Cavity. All the timing is adjusted by a digital delay generator (timing). a) During the measurement time, the locking beam is blocked by the “MEMS IR” and the “MEMS APD” connects the conditioning path to the single-photon detector. b) During the locking time, the MEMS are switched in order to connect the locking beam and disconnect the single-photon detector.

The cavity is locked with the Dither-and-Lock technique [53]. This requires a bright beam (few μ W). Here we use a contra-propagating beam in the same optical path than the OPO output. This is achieved by using a micro-mechanical fiber switch called *MEMS* (stands for *Micro-Electro-Mechanical Systems*). A quarter-wave plate and a half-wave plate are used to control and/or compensate the polarization of the beam from the fiber output. These

two plates are adjusted in order to completely reject the locking beam by the polarizing beam-splitter also used in the Faraday circulator. The PZT of the cavity is modulated by a sine signal at 10 kHz. The transmission signal measured by a photodiode is demodulated at the same frequency. Hence, we obtain the derivative of the cavity transmission as a function of the piezo position. This signal is used as error signal and send to a proportional-integral (PI). The integrated signal is at the end amplified at a high voltage and send to the piezo of the cavity.

NB: Actually, we use a second MEMS. In principle, one is enough because the isolation between the two paths is extremely high. Moreover, the locking beam can be very weak (few μW). However, during the transition some light from the locking beam can go to the photon detector. We thus use another MEMS to turn on and off the locking beam to overcome any bright beam during the transition time (Fig. 4.5).

An alternative setup has been implemented later in which we can remove the MEMS, this in order to increase the transmission efficiency of the conditioning path, see Fig. 6.6 in Chap. 6.

Timing We cannot lock the μCavity and perform measurements at the same time. So, the experiment is conducted in a cyclic fashion: one period to lock the μCavity and the other for the measurement. For this purpose, the locking system of the cavity is “frozen”. During this period the homodyne measurements can be performed.

The choice of the two durations is at least constrained by the locking. The measurement time should be smaller than the time of stability of the cavity and the locking period long enough to lock again the cavity. Here, we typically use 40 ms for the locking and 60 ms for the measurement. But, in a reasonably quiet condition, it can be adjusted to 10 ms of locking and 90 ms of measurements.

To avoid any unexpected behavior of the locking, a small delay is adjusted between each transitions (see Fig. 4.6). Starting from a measurement step, first the MEMS is switched on and send the locking beam to the cavity, then the second MEMS turns on the locking beam and finally the locking is released. To switch back to the measurement period we do exactly the opposite sequence as depicted on Fig. 4.6.

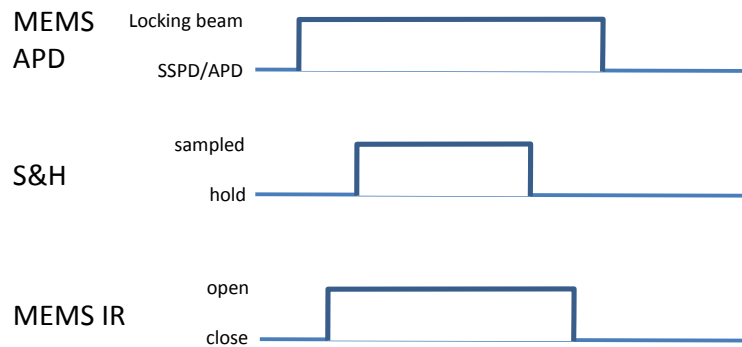


Figure 4.6: Some small delays are used to adjust the order of each element to avoid some unexpected behavior. The APD is disconnected prior to any locking step. Then the locking beam is send to the cavity. The size of the cavity is thus adjusted within a short time by releasing the proportional-integrate.

In *hold* position, the output signal of the lockin’ amplifier (our error signal) is 0 in such a way that the PI does not change its output value and, at the end, keeps the position of the piezo fixed during the measurement period.

4.2.3 Homodyne measurement, data acquisition and processing

Given a detection event on the conditioning path, the heralded state is then characterized by quantum state tomography performed via a homodyne detection. The 6 mW local oscillator is provided by the 1064 nm output of the laser, after spatial mode filtering by a high-finesse cavity⁶. The homodyne detection is based on a pair of high-quantum efficiency InGaAs photodiodes (Fermionics) with a diameter of 500 μm and a quantum efficiency of above 97%. More details on the homodyne detection are given in the Appendix B. An optical isolator just before the homodyne detection is required in our setup to remove the light from the local oscillator backscattered by the photodiodes. Unfortunately, this weak light can go back to the OPO, then to the single-photon detector and finally induces some “false” events.

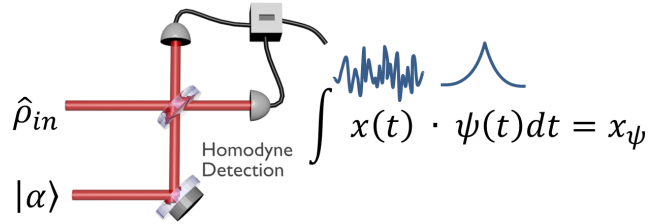


Figure 4.7: Processing of the homodyne detection. The quadrature measurement of the conditional state is obtained by applying a temporal mode on the output signal of the homodyne detection at each trigger event.

A C++ program controls the acquisition with an oscilloscope (Lecroy Wavepro 7300A) (Appendix F), post processes the data and displays the results of the experiment in quasi-real-time (the main limitation of the speed being the data transfer and the rate of events). For each trigger event, the photocurrent is recorded with the oscilloscope at a sampling rate of 5 GS/s during 100 ns.

The output signal from the homodyne detection $x(t)$ is continuous. Each measurement corresponds to a quadrature measurement in a subspace generated by the annihilation/creation operator $\hat{a}(t)/\hat{a}^\dagger(t)$ at a time t . However, the heralded state will be in a different temporal mode [82]. This part will be studied in more detail in a further chapter (Chap.6). Nevertheless, an intuitive picture could be the following: the two photons are emitted at the same time and one of them is detected by the single-photon detector but, being in a cavity, the twin photons can escape from the cavity at different time following a double exponential decay function. This being in an indistinguishable fashion, it leads to a superposition of single-photon at different times $\int f(t)|1\rangle_t dt = \int f(t)\hat{a}^\dagger(t)dt|0\rangle = \hat{a}_f^\dagger|0\rangle$.

The temporal mode is the Fourier transform of the cavity spectrum, i.e. a Lorentzian $\tilde{f}(\nu) = \frac{1}{\sqrt{\pi\nu_0}} \frac{1}{1 + (\nu/\nu_0)^2}$ with ν_0 the -3 dB bandwidth (HWHM), related to the cavity by $2\nu_0 = \gamma = 65\text{MHz}$ (FWHM). The temporal mode is thus $f(t) = \sqrt{\pi\gamma}e^{-\pi\gamma|t|}$.

Hence, with a continuous quadrature measurement we can obtain a quadrature measurement specifically in this temporal mode by applying the same transformation $\hat{x}_f = \int f(t)\hat{x}(t)$ (cf figure 4.7). This is an intuitive picture and is only relevant in an ideal case. Indeed, we do not consider the effect of the μCavity .

⁶The filtering cavity is a priori not important here. The classical noise is removed in the homodyne measurement. Indeed, the subtraction of the two signals remove all classical noises. Secondly, the spatial mode of the laser is already good, so it is not really improved by the filtering cavity. Nevertheless, we never tried to run the experiment without this cavity, which was necessary in previous experiment performed above threshold.

All the acquired waveforms are processed by applying such a temporal mode. We have thus a set of quadrature measurements in this specific mode. The time delay between the photon detector and the homodyne detection can be adjusted with the help of the temporal variance of the homodyne detection signal $\langle x(t)^2 \rangle = \frac{1}{N} \sum_{k=1}^N x_k(t)^2$ plotted on figure 4.8, which easily indicates at which time the temporal mode should be centered.

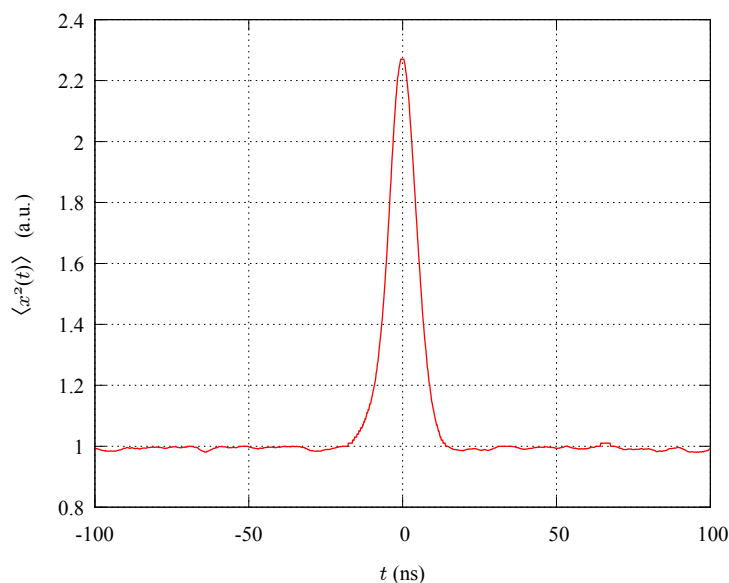


Figure 4.8: Temporal variance of the homodyne signal. We use it to adjust the delay between the SSPD trigger event and the temporal mode function on the homodyne signal.

NB: This temporal mode could be directly applied by electronics or shaping of the local oscillator to avoid any post-processing. But, this has no real interest here as the speed of measurement is not a limitation. Moreover, this would require more experimental abilities and we will see in the chapter 6 that recording the complete signal can give useful additional information.

Moreover, a calibration of the homodyne measurement signal is required. Indeed, the signal is proportional to a quadrature measurement but not equal. To perform this calibration, we use the vacuum fluctuation as reference: the signal path is blocked, we thus obtain quadrature measurements of the vacuum state. The same temporal mode is applied to each recorded waveform, then we compute the variance of the measured quadratures which gives us the normalization factor to use.

Practically, to summarize the process, if we call $s_k(t)$ the output signal of the homodyne detection related to the k -th heralding event, we compute with each waveform $s_k = \int dt f(t) s_k(t)$, then we obtain the normalization factor $\mathcal{N}_0 = \sqrt{\langle s^2 \rangle} / \sigma_0$, and we use it to obtain the quadrature measurement $x_k = s_k / \mathcal{N}_0$. This calibration is achieved with typically 50,000 points and repeated for each run⁷.

The state is reconstructed by using the MaxLik algorithm with typically 50,000 points. For this state, a size of the Fock space up to $|6\rangle$ is quite enough, and 200 iterations of the

⁷In principle it is not necessary to repeat this operation but the power of the local oscillator can change, and it is thus preferable to do this calibration regularly.

algorithm gives a reasonable accuracy. We also monitor in real time the experiment with the method of the moments described in sec.2.4.3.

4.3 Results and discussions

All the different parts have been optimized in order to have a state as pure as possible. However, the light from the local oscillator scattered by the photodiodes, has appeared to be a big issue to solve, and is probably the main limitation of the purity in the actual setup. Below we present the best obtained results.

4.3.1 Results

Results are displayed on Fig. 4.9:(a) gives the histogram of the measured quadrature values, while (b) and (c) show respectively the diagonal elements of the reconstructed density matrix and the corresponding Wigner function.

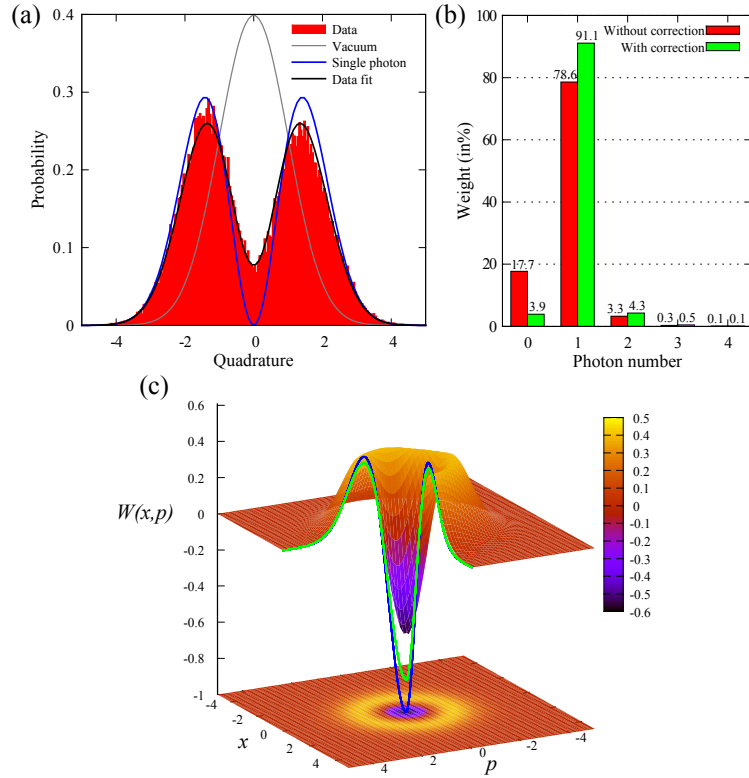


Figure 4.9: High-fidelity single-photon state. (a) Marginal distribution from 50,000 quadrature measurements with average phases. The black solid line is a fit of the experimental data, while the blue solid line provides the distribution for a perfect single-photon state and the gray line for the vacuum. (b) Diagonal elements of the density matrix of the generated state, with and without correction for detection losses. (c) Corresponding Wigner function. The solid lines give the theoretical cross-section for a perfect single-photon and the experimental cross-section after correction.

The state is, in a good approximation, a mixture of vacuum and single-photon state.

The two-photon component is around 3%, resulting from multi-photon pairs created by the down-conversion process and the non-resolution of photon number by the SSPD. The OPO is operated far below threshold (1 mW for a threshold of 80 mW) to limit this contribution. Without any corrections, the single-photon component reaches $78.6 \pm 0.5\%$ (Error bar is estimated by following the method in [73]). By taking into account the detection losses, we infer a state just before the homodyne detection with value as high as 91%.

The heralding rate for single-photon generation is 30 kHz. Given the bandwidth of the OPO, it corresponds to a brightness of 400 photons/s per MHz. This rate is mainly limited by the losses in the conditioning path, which reaches 97%: the quantum efficiency of the SSPD is 7% and the overall transmission (including optical switch and filtering elements) is 40%. Corrected for the losses in this path, the rate can be close to 750 kHz.

The value of the bandwidth γ of the temporal mode has been optimized to maximize the single-photon component.

4.3.2 Global efficiency

Table 4.1 gives the various efficiencies affecting the final result. Two contributions have to be distinguished. A first one comes from the overall losses along the propagation and the detection. This includes the propagation efficiency η_{prop} , the mode overlap limited by the visibility V of the local oscillator-signal interference $\eta_{\text{vis}} = V^2$ [4], the efficiency of the photodiodes η_{phot} and the electronic noise of the detection $\eta_{\text{noise}} = 96\%$ (the electronic noise is 20 dB below vacuum noise at the central frequency) [49]. They sum up to an overall detection loss of $1 - \eta_{\text{tot}} = 15\%$, which is taken into account to give the values with correction. The second contribution is more fundamental and cannot be corrected as it is related to the generation process. It depends on the OPO escape efficiency, given by $\eta_{\text{OPO}} = T/(T + L)$, where T is the transmission of the output coupler and L the intracavity loss. This value is estimated to be here $\eta_{\text{OPO}} = 96\%$. Given these estimated parameters, the expected vacuum component is 18%, in very good agreement with the measured value.

η_{noise}	η_{phot}	η_{vis}	η_{prop}	η_{tot}	η_{OPO}
96%	97%	$(98\%)^2$	95%	85%	96%

Table 4.1: Experimental efficiencies

4.3.3 Asymmetric marginal distributions

One can notice that the marginal distribution is not perfectly symmetric, contrary to what we could expect. Actually, it can also be much worse (see Fig. 4.10). This cannot be explained by some statistical effects as the number of points is large enough to have relevant statistics: it has physical origin.

This asymmetry can be explained by a weak displacement on the triggering mode, which would come from the backscattered light,

$${}_b\langle 1 | \hat{D}_b(\beta) (|0\rangle_a |0\rangle_b + \lambda |1\rangle_a |1\rangle_b) . \quad (4.24)$$

The approximation of a weak displacement gives $\hat{D}(\beta) = e^{\beta \hat{b}^\dagger - \beta^* \hat{b}} \sim \mathbb{1} + \beta \hat{b}^\dagger - \beta^* \hat{b}$, we thus obtain for the first order in λ and β the conditional state

$$\beta |0\rangle + \lambda |1\rangle , \quad (4.25)$$

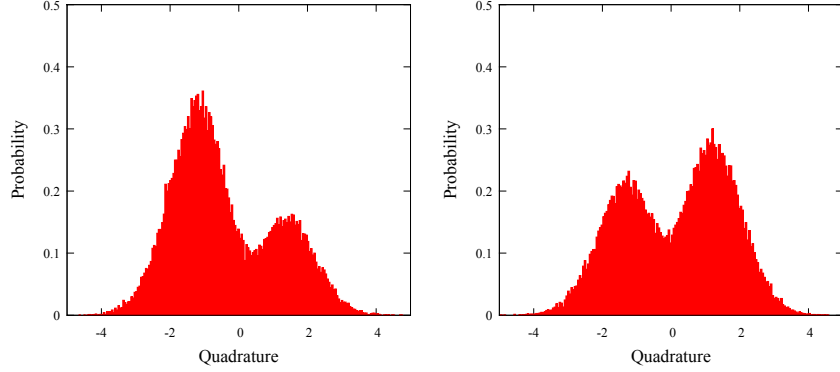


Figure 4.10: Two examples of asymmetric marginal distributions. This situation happens when the isolation is not efficient enough and/or the sources of scattering are not controlled or too numerous.

a coherent superposition of single-photon and vacuum state. We rewrite the state in the general form with two reals α and β (following $\alpha^2 + \beta^2 = 1$) with a relative phase ϕ

$$\alpha|0\rangle + \beta e^{i\phi}|1\rangle. \quad (4.26)$$

The wave function of this state is

$$\langle x_\theta|\psi\rangle = \psi(x) = \frac{e^{-x^2/4\sigma_0^2}}{(\sqrt{2\pi}\sigma_0)^{1/2}} \left(\alpha + \beta \frac{x}{\sigma_0} e^{i(\theta+\phi)} \right). \quad (4.27)$$

The corresponding marginal distribution is thus

$$\begin{aligned} \psi(x)\psi^*(x) &= \frac{e^{-x^2/2\sigma_0^2}}{\sqrt{2\pi}\sigma_0} \left(\alpha + \beta \frac{x}{\sigma_0} e^{i(\theta+\phi)} \right) \left(\alpha + \beta \frac{x}{\sigma_0} e^{-i(\theta+\phi)} \right) \\ &= \frac{e^{-x^2/2\sigma_0^2}}{\sqrt{2\pi}\sigma_0} \left(\alpha^2 + \beta^2 \frac{x^2}{\sigma_0^2} + 2\alpha\beta x \cos(\theta + \phi) \right). \end{aligned}$$

By choosing $\sigma_0 = 1$ and including a detection efficiency of η , we finally obtain

$$\mathcal{P}(x_\theta) = \frac{e^{-x^2/2}}{\sqrt{2\pi}} \left[\eta (\alpha^2 + \beta^2 x^2 + 2\alpha\beta x \cos(\theta + \phi)) + 1 - \eta \right]. \quad (4.28)$$

Depending on the phase of the local oscillator (i.e. the measured quadrature), the marginal distribution can be asymmetric. We show on figure 4.11 that the effect is easy to see for small values of α .

Surprisingly, the shape of this asymmetry is the same whatever the phase of the local oscillator. Moreover, it changes only after a long time (typically tens of minutes). This is not physically possible because the averaging of the phase should compensate it. This is why we should find an explanation linked to the local oscillator. Indeed, the light inducing this displacement comes from the local oscillator. So, when we change the phase of the local oscillator to measure another quadrature, the phase of the displacement follows. That is why, despite we sweep the phase, we actually always measure the same quadrature. This quadrature is defined by the relative phase between the local oscillator and the path to the point of displacement. The experimental setup being (mechanically) extremely stable, this relative phase changes extremely slowly and thus the asymmetry changes slowly too. Hence,

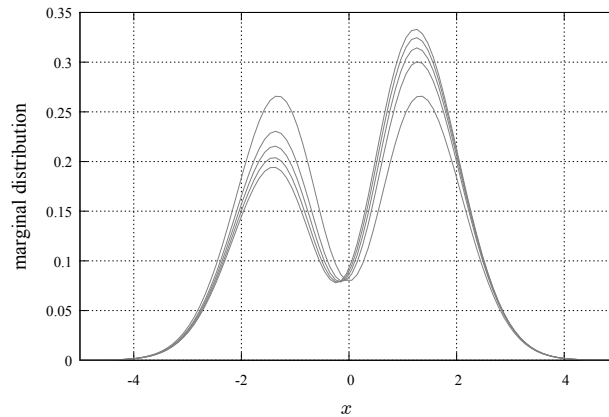


Figure 4.11: Effect of the scattering for $\alpha^2 = 0\%, 1\% \dots 4\%$ (cf eq. (4.26)). We also include the limited efficiency with typically $\eta = 80\%$. The asymmetry appears clearly even from a very small amount of superposed vacuum state. (see eq. (4.28)).

if we do not measure all the quadrature of a state which is not phase invariant, one can wonder how “true” is our quantum state tomography. Actually, at least in this particular case and with this reasonable asymmetry, this can only lead to an underestimation of the single-photon component.

Unfortunately, two points are still not completely explained. First, by which mechanism(s) the light can go back to the OPO? It seems clear that the photodiodes of the homodyne detection contribute but, is it from some scattering by the surface of the sensitive area? does it depend on the wave front of the beam? It also seems that the surface of the mirrors can play an important role. Secondly, where exactly the displacement takes place? On the output mirror of the OPO? Does this weak beam enter into the OPO and is then amplified by the parametric gain? The main difficulty, to study this problem, is the fact that the asymmetry appears more or less strongly as it depends on the measured quadrature, but we cannot control it!

Moreover, the accuracy and particularly the stability of the count rate is not enough to study the problem. In other words, we should be able to resolve few percents of fluctuation in the count rate. Some interferences between the scattered light on each part of the homodyne detection are possibly making the global scattered light going to the OPO sometimes and, back to the local oscillator the other times.

To conclude, this issue is difficult to understand as it involves some scattering phenomenon at the single-photon scale! Nevertheless, we figure out recently that the use of mirrors with IBS⁸ coatings reduces the problem.

4.4 Beyond: the qubit

It has not been implemented here but our source is a starting point to many protocols with discrete variables as different encodings use the single-photon state. For instance, the polarization encoding (dual rail) a simple combination of wave-plate can transform the single-photon state in any qubit of the Bloch sphere.

⁸Ion-Beam-Sputtered

If we consider the photon number encoding⁹, the setting of the qubit is less straightforward. One possibility is to displace the conditioning beam: the indistinguishable detection of a photon from the displacement or the EPR state will lead to a coherent superposition of vacuum and single-photon. The relative complex amplitude is thus tuned by the amplitude and phase of the displacement relatively to the EPR beam. Another strategy consists in sending the single-photon onto a 50:50 beam-splitter. A quadrature measurement is realized by an homodyne detection on one output. The selection of specific results gives the desired superposition. The main disadvantage of this last method is its probabilistic nature in addition to the single-photon heralding. For this reason, the previous one would be preferable.

4.5 Conclusion

In conclusion, we have generated of high-fidelity heralded single-photons, using a configuration based on a type-II optical parametric oscillator below threshold. A 79% fidelity has been demonstrated, mainly limited by the losses in the detection path. Corrected for this limited efficiency, the state just before the homodyne detection is above 92%. Thanks to the OPO cavity, the spatial mode enables to reach high interference visibilities without the need of additional filterings. Moreover, the frequency-degenerate interaction makes the operation much simpler than previous realizations. This practical tool can facilitate the implementation of various new experiments in quantum information processing [73]. The technique developed in [84] could be extended to our efficient scheme if time-gating of the single-photons is required.

The novelty of this experiment relies on the use of a degenerate (in frequency) type-II down conversion and the simplicity of the setup. The reported value is also one of the highest reported to date. The main criticism we can make about this setup is its wavelength. Indeed, it is neither telecoms one nor for an atomic transition. The other possible criticism is the probabilistic nature of the source, however nowadays deterministic sources are extremely impure, and thus are somehow, more probabilistic than ours.

Besides, there are numerous demonstrations of single-photon sources based on spontaneous parametric down conversion. In contrast to many of them, the important feature of our source is the well control of the mode in which lies the single-photon state. This is highlighted by the characterization via an homodyne detection. Indeed, the detector performed a measurement in a precise mode (actually the one of the local oscillator). Moreover, this prove that homodyne detection can be used with this source, which, as we will see in the next, open up some possible protocols.

This source will be used in the next experiments performed in this PhD work. One concerns a single-photon entanglement witness, presented in Chap.7, and in the generation of hybrid entanglement, presented in Chap.8.

⁹ $|0\rangle$ to encode 0 and $|1\rangle$ to encode 1

5 | Generation of Schrödinger Cat-Like State

I start in the middle of a sentence and move both directions at once.

JOHN COLTRANE

As introduced in the chapter 1, we call optical Schrödinger cat state the superposition of two coherent states with opposite phases

$$|cat_{\pm}\rangle = \frac{|\alpha\rangle \pm |-\alpha\rangle}{\sqrt{2(1 \pm e^{-2|\alpha|^2})}}, \quad (5.1)$$

where $|\alpha\rangle$ is a coherent state of amplitude α . These states are of large interest for continuous variable quantum computation where the qubit is encoded on the phase of a coherent state. Indeed, this qubit being easy to measure with a homodyne detection, numerous protocols of quantum information based on this encoding have been proposed (see [95] and references therein). Thus, the cat states as defined here correspond to the equator of the Bloch sphere.

There are different strategies to generate these states but all of them require high non-linearities. For instance, in Ref. [18] a phase shift of a cavity field is induced by interaction with an atom and depends on its state. Another possible strategy, in free space, is analytically similar to the previous example. It consists in replacing the atomic levels by vacuum and single-photon state and mediating the interaction by a cross-Kerr effect [44]. Nevertheless, so far, no known material provides a sufficient Kerr non-linearity. At least one order of magnitude more is necessary. Here, the non-linearity will be induced by a measurement. It consists in subtracting one photon from a squeezed vacuum state [15]. Nevertheless, the states produced here are an approximation: it is not rigorously the cat state. More rigorously, we saw in chapter 1 that this state does not exactly “map” the idea of Schrödinger and that it is preferable to talk about *coherent state superposition* (CSS). Hence, we would label the state generated in this chapter *CSS-like* state.

The technique implemented here has been widely used so far and realized in many groups: Grangier in the pulsed regime and Furusawa, Polzik, Sasaki in the continuous wave regime [89, 78, 118]. There is no particular novelty in our experimental realization. However, the quality of the OPO plus the very efficient detection, make us expect a state of a “high quality”, as we will see.

This chapter will be shorter as there are many things in common with the previous one. The experimental setup varies only a little, and the main difference will be the phase information required for the tomography of the state.

5.1	Principle of the experiment and models	82
5.1.1	Basic scheme	82
5.1.2	Models	83
5.1.3	What we learnt	85
5.2	Experimental Setup	86
5.2.1	Phase information	86
5.3	Results and discussion	89
5.4	What about even cat states?	90
5.5	Conclusion	93

5.1 Principle of the experiment and models

The experiment here is similar to the single-photon one: we use a measurement-induced non-linearity with the same single-photon detector and start from a Gaussian state. However, the initial resource, here, is a squeezed vacuum state.

5.1.1 Basic scheme

The experiment follows the initial idea suggested by Dakna *et al* [15]: by subtracting a single-photon from a squeezed vacuum state, one can obtain the following state

$$|cat_-\rangle \approx \frac{\hat{a}\hat{S}|0\rangle}{\sqrt{|\langle 0|\hat{S}^\dagger\hat{a}^\dagger\hat{a}\hat{S}|0\rangle|}} . \quad (5.2)$$

For this purpose, the idea is to tap a small part of the squeezed vacuum with a beam-splitter, and to detect a single-photon on this part. In the limit of infinitely small tapping ratio, this is equivalent to apply the annihilation operator. Indeed, the beam-splitter operator is written $\hat{B} = e^{\theta(\hat{a}\hat{b}^\dagger - \hat{a}^\dagger\hat{b})} \approx 1 + \theta(\hat{b}^\dagger\hat{a} - \hat{b}\hat{a}^\dagger)$ in the limit of a small reflection ($\sin\theta \approx \theta$). We thus have

$$\hat{B}\hat{S}|0\rangle_a|0\rangle_b \approx \hat{S}|0\rangle_a|0\rangle_b + \theta\hat{a}\hat{S}|0\rangle_a|1\rangle_b . \quad (5.3)$$

We clearly see that the detection of one photon on the tapped mode b heralds the annihilation of one photon on mode a .¹ Moreover, we can conveniently rewrite the state as a squeezed single-photon $\hat{a}\hat{S}|0\rangle \propto \hat{S}\hat{S}^\dagger\hat{a}\hat{S}|0\rangle = \hat{S}(\hat{a}\operatorname{ch}r - \hat{a}^\dagger\operatorname{sh}r)|0\rangle \propto \hat{S}|1\rangle$. The state is written in the Fock basis as:

$$\hat{S}|1\rangle = \frac{(1-\lambda^2)^{3/4}}{\lambda} \sum_{n=1} \frac{\sqrt{(2n)!}}{n!} (\lambda/2)^n \sqrt{2n} |2n-1\rangle . \quad (5.4)$$

Of course, approximating a cat state with this state is not valid for any parameters. The reliability of the approximation can be evaluated via the fidelity. Hence, we compare the squeezed single-photon with the odd cat state (with the amplitude α). The fidelity is given by

$$\mathcal{F}_1 = \left\| \langle cat_- | \hat{S}|1\rangle \right\|^2 \quad (5.5)$$

$$= \frac{2\alpha^2 e^{\alpha^2(\operatorname{th}r-1)}}{(\operatorname{ch}r)^3 (1 - e^{-2\alpha^2})} . \quad (5.6)$$

We more conveniently express it as a function of the squeezing factor s

$$\mathcal{F}_1 = \frac{2\alpha^2 e^{\alpha^2(\operatorname{th}r-1)}}{(\operatorname{ch}r)^3 (1 - e^{-2\alpha^2})} \quad (5.7)$$

$$= \frac{16\alpha^2 e^{-2\alpha^2/(1+1/s)}}{(1 - e^{-2\alpha^2})(s^{-1/2} + s^{1/2})^3} , \quad (5.8)$$

and find that this fidelity is maximal for

$$s_{\text{opt}} = \sqrt{1 + (2\alpha^2/3)^2} - 2\alpha^2/3 . \quad (5.9)$$

As we can see on figure 5.1, the approximation is almost valid up to $|\alpha|^2 = 1.5$ with $\mathcal{F} > 98\%$. This is an important result as the overlap between two coherent states $|\langle \alpha | -\alpha \rangle|^2 = e^{-4|\alpha|^2}$ is below 2% for $|\alpha|^2 > 1$ and we remind that the two states encoding the qubit have to be orthogonal.

¹Although the physics is exactly the same as the previous experiment - by splitting a part of the squeezed vacuum we obtain an entangled state - the idea is different in the sense that the goal is to apply the annihilation operator, the entanglement is not really exploited.

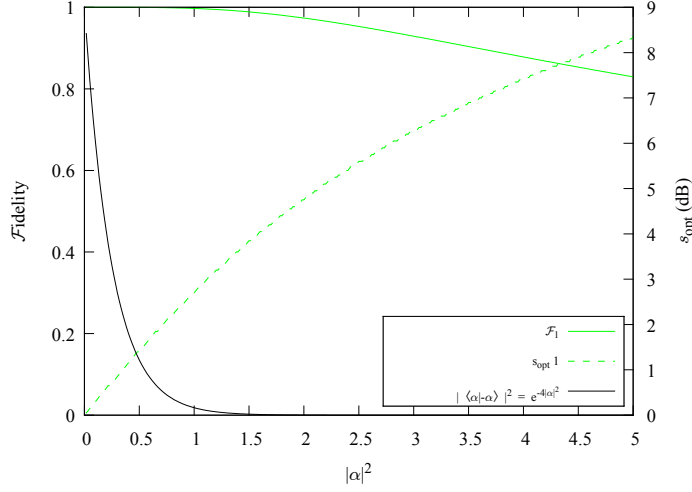


Figure 5.1: Fidelity between photon subtracted squeezed vacuum and odd Schrödinger cat state.

5.1.2 Models

Also in this experiment, we need to model the setup in order to understand the effect of the different parameters, at least qualitatively. Indeed, the non-perfect single-photon detector and the various optical losses will affect the quality of the prepared state.

Ideal single-photon subtraction The effect of the photon subtraction for the density matrix can be written as $\hat{\rho}' \propto \hat{a}\hat{\rho}\hat{a}^\dagger$. With the Wigner function formalism, this is equivalent to apply the operator \hat{D} , $W_{\hat{a}\hat{\rho}\hat{a}^\dagger} = \hat{D}W_{\hat{\rho}}$, as detailed in [59]. This operator is

$$\hat{D} = \frac{1}{2} \left[1 + \frac{x^2 + p^2}{2\sigma_0^2} + x\partial_x + p\partial_p + \frac{\sigma_0^2}{2}(\partial_x^2 + \partial_p^2) \right]. \quad (5.10)$$

Any Gaussian state is written

$$W_G(x, p) = \frac{1}{2\pi\sigma_x\sigma_p} e^{-x^2/2\sigma_x^2 - p^2/2\sigma_p^2}. \quad (5.11)$$

When we apply the annihilation of one photon, we obtain

$$\hat{D}W_G = \frac{1}{2} \left[1 - \frac{\sigma_0^2}{2\sigma_x^2} - \frac{\sigma_0^2}{2\sigma_p^2} + \left(\frac{1}{2\sigma_0^2} - \frac{1}{\sigma_x^2} + \frac{\sigma_0^2}{2\sigma_x^4} \right) x^2 + \left(\frac{1}{2\sigma_0^2} - \frac{1}{\sigma_p^2} + \frac{\sigma_0^2}{2\sigma_p^4} \right) p^2 \right] W_G \quad (5.12)$$

$$= \frac{1}{2} \left[1 - \frac{\sigma_0^2}{2\sigma_x^2} - \frac{\sigma_0^2}{2\sigma_p^2} + \left(1 - \frac{\sigma_0^2}{\sigma_x^2} \right)^2 \frac{x^2}{2\sigma_0^2} + \left(1 - \frac{\sigma_0^2}{\sigma_p^2} \right)^2 \frac{p^2}{2\sigma_0^2} \right] W_G. \quad (5.13)$$

To normalized the state, i.e. $\text{Tr}[\hat{\rho}'] = 1$, we should divide by

$$\iint dx dp \hat{D}W_G(x, p) = \frac{1}{2} \left[\frac{\sigma_x^2 + \sigma_p^2}{2\sigma_0^2} - 1 \right]. \quad (5.14)$$

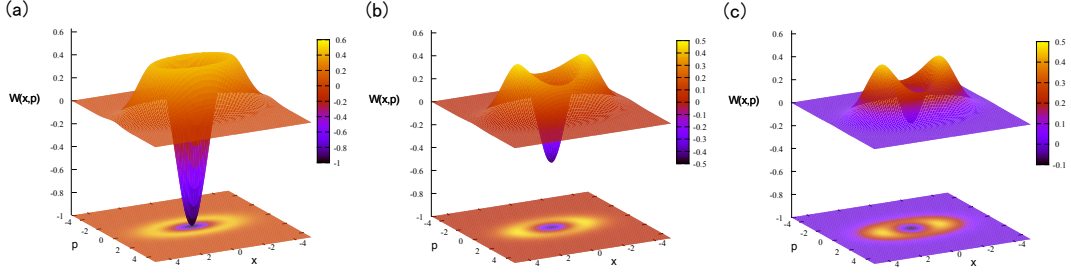


Figure 5.2: Effect of losses on the conditional state. (a) 100% efficiency, (b) 75%, (c) 55%. One can notice that it does not only affect the negativity of the state but also the shape of the Wigner function.

We have started from a general Gaussian state and applied a perfect photon subtraction. Hence, this model only gives the effect of the losses on the states (i.e. by adapting the covariance elements of the Gaussian states) and does not include neither the imperfections of the single-photon detector (efficiency, noise, not photon-number resolved) nor the value of the tapping ratio. However, here, we do not need any estimation of these losses and we can directly use the Gaussian parameters that we measure usually, i.e. squeezing and anti-squeezing. Although this model is derived in a single-mode description, it is actually not so far from the reality. On figure 5.2, we can see how the losses affect the Wigner function of the conditional state.

Overall model We start from the most general single-mode Gaussian state. We mix it with the vacuum state via a beam-splitter of reflection r ($t^2 + r^2 = 1$)

$$\frac{1}{2\pi\sigma_x\sigma_p} e^{-x_a^2/2\sigma_x^2 - p_a^2/2\sigma_p^2} \frac{1}{2\pi\sigma_x\sigma_p} e^{-x_b^2/2\sigma_0^2 - p_b^2/2\sigma_0^2} \rightarrow \frac{1}{(2\pi)^2\sigma_x\sigma_p\sigma_0^2} e^{-(tx_a+rx_b)^2/2\sigma_x^2 - (tp_a+rp_b)^2/2\sigma_p^2 - (tx_b-rx_a)^2/2\sigma_0^2 - (tp_b-rp_a)^2/2\sigma_0^2}. \quad (5.15)$$

Then, we apply the POVM element corresponding to a detection event of the detector. For this purpose, we use the model of a noisy inefficient non-resolving photon detector given in chapter 2:

$$W_{\hat{\Pi}_{\text{on}}} = W_{\mathbb{1}} - W_{\hat{\Pi}_{\text{off}}} = \frac{1}{2\pi\sigma_0^2} \left(\frac{1}{2} - \frac{e^{-\nu}}{2-\eta} e^{-(x^2+p^2)/2\sigma_\eta^2} \right), \quad (5.16)$$

with $\sigma_\eta^2 = \frac{2-\eta}{\eta}\sigma_0^2$, η the efficiency of the detector (note that we also include in this efficiency the full transmission of the conditioning path i.e. $\eta = \eta_{\text{path}} \cdot \eta_{\text{SSPD}}$), and ν the noise. The conditional state is then written

$$\int_b W_G(a, b) W_{\hat{\Pi}_{\text{on}}}(b) = \frac{1}{2\pi\sigma_0^2} \left[\frac{1}{2} \frac{\exp\left(-\frac{x^2}{2(r^2\sigma_0^2 + t^2\sigma_x^2)} - \dots p\right)}{2\pi\sqrt{(r^2\sigma_0^2 + t^2\sigma_x^2)}(\dots p)} - \frac{e^{-\nu}}{2-\eta} \frac{\exp\left(-x^2 \frac{1+(t^2\sigma_0^2+r^2\sigma_x^2)/\sigma_\eta^2}{2(r^2\sigma_0^2+t^2\sigma_x^2+\sigma_0^2\sigma_x^2/\sigma_\eta^2)} - \dots p\right)}{2\pi\sqrt{(r^2\sigma_0^2 + t^2\sigma_x^2 + \frac{\sigma_0^2\sigma_x^2}{\sigma_\eta^2})}(\dots p)} \right] \quad (5.17)$$

(where $\dots p$ denotes that we have the same expression as x for the variable p). This conditional state should be normalized by

$$\int_a \int_b W_G(a, b) W_{\hat{\Pi}_{\text{on}}}(b) = \frac{1}{2\pi\sigma_0^2} \left[\frac{1}{2} - \frac{e^{-\nu}}{2-\eta} \frac{1}{\sqrt{(1 + (t^2\sigma_0^2 + r^2\sigma_x^2)/\sigma_\eta^2)(\dots p)}} \right]. \quad (5.18)$$

For $\nu = 0$ et $\eta = 1$ the Wigner function at the origin of the phase space is

$$\overline{W}(0, 0) = \frac{\frac{1}{2} \frac{1}{\sqrt{(t^2 s_x + r^2)(t^2 s_p + r^2)}} - \frac{1}{\sqrt{(r^2 + t^2 s_x + s_x)(r^2 + t^2 s_p + s_p)}}}{\frac{1}{2} - \frac{1}{\sqrt{(1+t^2+r^2 s_x)(1+t^2+r^2 s_p)}}}. \quad (5.19)$$

As for the single-photon experiment the noise induced some “false” events, i.e. heralds a squeezed vacuum. The dark count has to be as small as possible compared to the “true” event count rate.

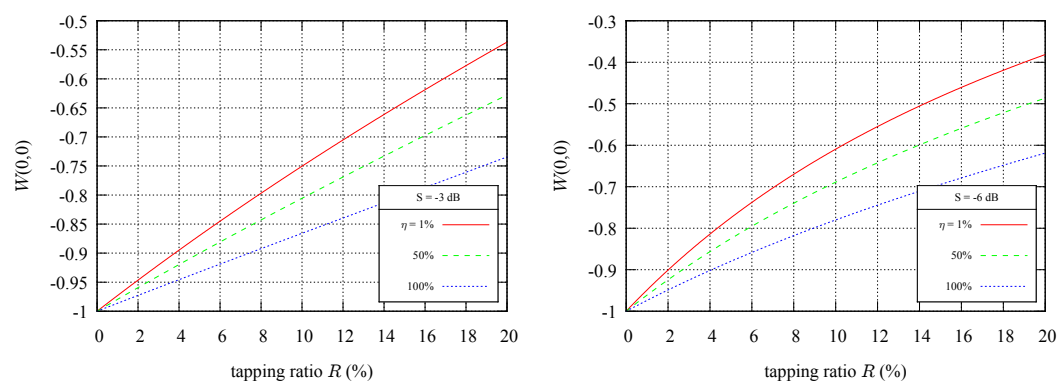


Figure 5.3: Effect of the tapping ratio on the Wigner function at the origin of the phase space for different efficiencies of the conditioning path. (Without noise $\nu = 0$ and for a pure input squeezed vacuum state.) Left: -3 dB squeezed vacuum state. Right: -6 dB.

The limited efficiency and the non-resolution in photon-number is less simple to interpret. Indeed, it should be considered with the tapping ratio. As highlighted by figure 5.3, if the efficiency decreases, the detector is less sensitive to low photon-numbers, in other words, more sensitive to high photon-number than low photon number. Hence, this can be compensated by lowering the tapping ratio, because the reflection of n photon scales as r^n . We thus lower the probability of high photon-number. Moreover, if the squeezing increases, we should lower it because the state populates higher photon-number.

5.1.3 What we learnt

These different models provide a more precise idea of how we should operate the experiment. First, we should pump the OPO within the region of -3 dB of squeezing in order to have a good fidelity with a “true” cat state. On the other hand, the tapping ratio has to be adjusted in order to have a reasonable count rate, especially compared to the dark count rate. However, the tapping ratio cannot be too large. Actually, the tapping ratio has to be as small as possible to avoid the detection of more than one photon *a fortiori* if the efficiency of the detector is low. As for the previous experiment, there is a trade-off to find between the targeted quality of the state and the contribution of the noise.

5.2 Experimental Setup

According to the previous section, we should tap at maximum 10%, but the lower is better. Practically, we use a tunable beam-splitter made of a half-wave plate and a polarizing beam-splitter in order to adjust the tapping ratio to the minimum value. The tapped beam is then sent to the conditioning path. As explained previously, we use a combination of an etalon and a very short cavity to filter out all photons at frequencies different from 1064 nm (cf figure 5.4). This ensures that the detected photon comes from the degenerate mode only. Each detection event of the single-photon detector heralds the preparation of the target state.

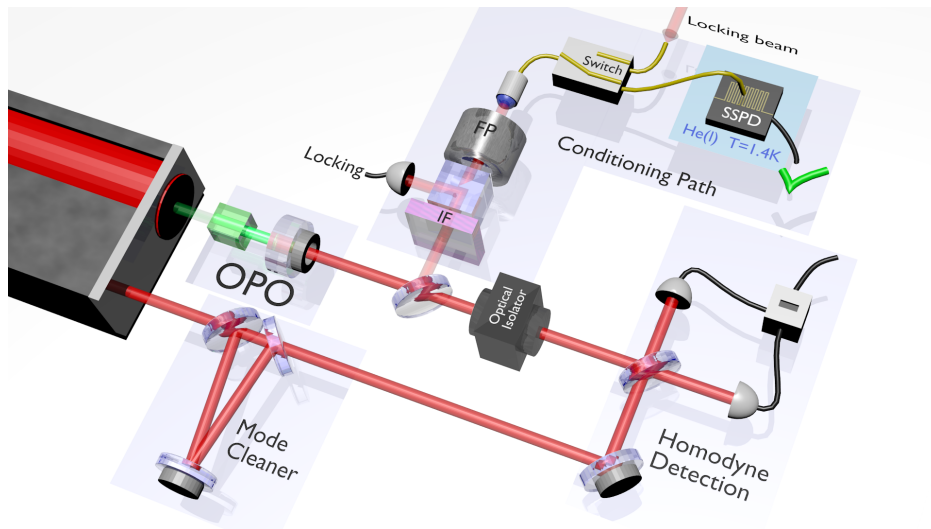


Figure 5.4: A small part of the squeezed vacuum state at the output of a type I OPO is tapped. Then, similarly to the generation described in Chap.4, the beam is filtered out with an interferential filter and a Fabry-Perot cavity in order to detect a photon in the degenerate mode of the OPO. For each detection event on the single photon detector, the homodyne signal is recorded. All the signals are then post-processed to extract the quadrature measurements to be used in the tomographic reconstruction algorithm.

The state is also characterized by quantum state tomography. We thus record the homodyne signal for each detection event and apply to it the temporal mode. Besides, contrary to the single-photon state, the one we generate here is not phase-invariant, we should at least acquire the information of phase of the measured quadrature. For this purpose, we have tried different methods. Two are described below and another one in Chap. 8.

5.2.1 Phase information

For experimental convenience, instead of locking the phase we use the randomness of the event detection to make sure that we perform measurements for all phases. However, the phase for each event has to be known.

Fitting of stable phase What we use is the variance of the quadrature measurement. For each event, we compute the variance of the recorded segment. Indeed, this value for the squeezed vacuum state is a sine function of the phase. The sweep of the phase is synchronized

with the cycle of measurement and with a duty cycle adjusted in order to have one direction of sweep during the measurement time of one cycle.

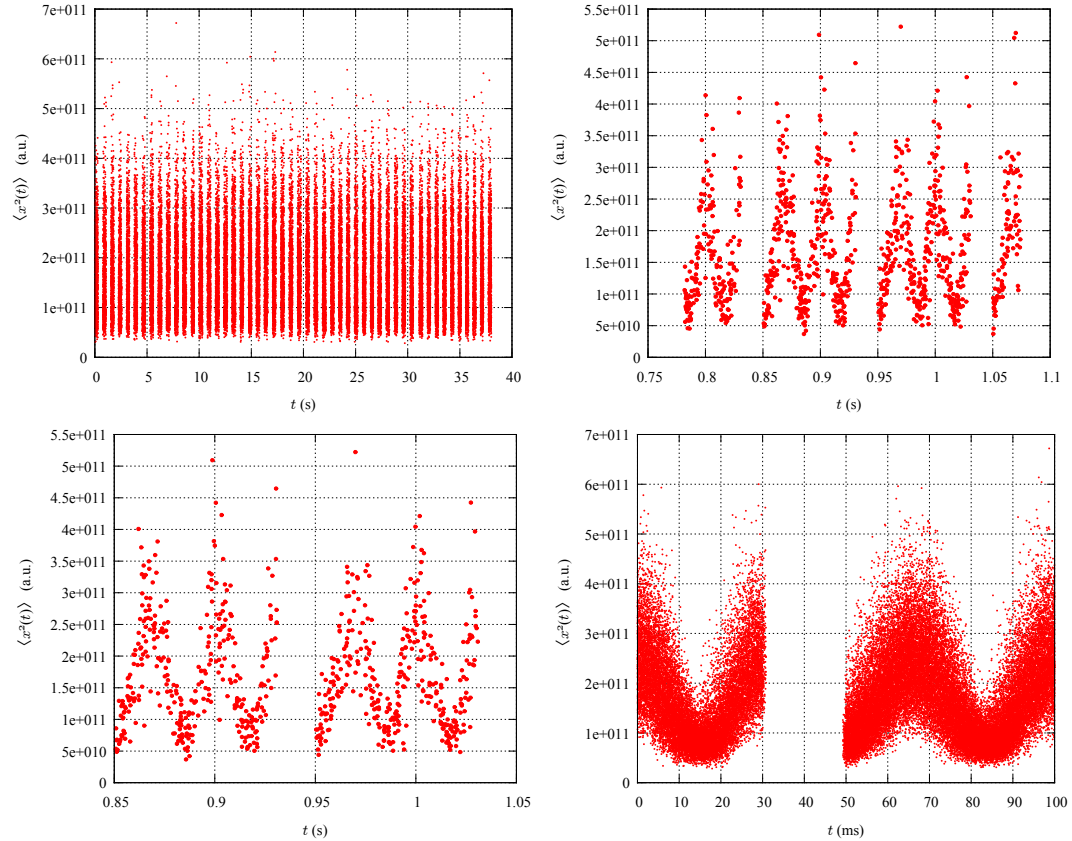


Figure 5.5: Phase estimation with variance in time. Top left, full time of a single tomography. We can see the packs of events that correspond to the “sequence” mode of the oscilloscope acquisition. Top right, zoom on one sequence. We can see the cycle of the experiment with 20 ms of locking and 80 ms of measurement for each cycle. Bottom left, second zoom on two cycles. We can see the fringes of squeezing due to the phase sweep. Bottom right, superposition of all the cycles. The fringes become more obvious.

On figure 5.5, we illustrate the way we extract the phase of each measurements. On top left is the full time of a single tomography. We can see that events are packed in time at regular intervals. This corresponds to the “sequence” mode of the oscilloscope: N measurements are accumulated in the memory and then accessible for processing. The dead-time corresponds to the processing and mainly to the backup of the data. (The times of acquisition and processing seem to be equal but this is by chance). On the top left, we zoom on one of the sequence (i.e. N measurement). We can again see some packs of events with the same duration of 80 ms. This actually corresponds to the different cycles of measurement: the μ Cavity is locked during 20 ms and “frozen” during 80 ms, the measurements are performed during this time. On bottom left, we zoom again onto two cycles. We can see that the same fringes pattern for each cycle. Eventually, we superpose all the cycle (bottom right figure), the fringes pattern becomes more obvious. We can also clearly see the different step of the cycle. Note that the locking step is in the middle because

the first measurement does not necessarily happen at the beginning of this step. Practically, if t_i is the timestamp² of the i -th detection event, we overlap all the cycle by using the modulo of the timestamp $t'_i = (t_i - t_0) \bmod T$ with T the period of the cycles (here 100ms). We can shift the time with $t'_i = (t_i - t_0 + t_{\text{offset}}) \bmod T$. In order to fit this sine, we reduce the statistical noise by taking the mean value of 0.1 ms bin (see figure 5.6 left). The sweep is linear but the response of the piezo is not linear. Hence, the fit we use is of second order in the sine ($\sin(at^2 + bt + c)$).

This strategy is only possible because the phase is stable over the time necessary to accumulate enough quadrature measurements for one tomography, in our case, few minutes. The other necessary assumption is that the state is not extremely phase sensitive. This last assumption is reasonable when we look at the mean phase drift during one experiment on figure 5.6 right.

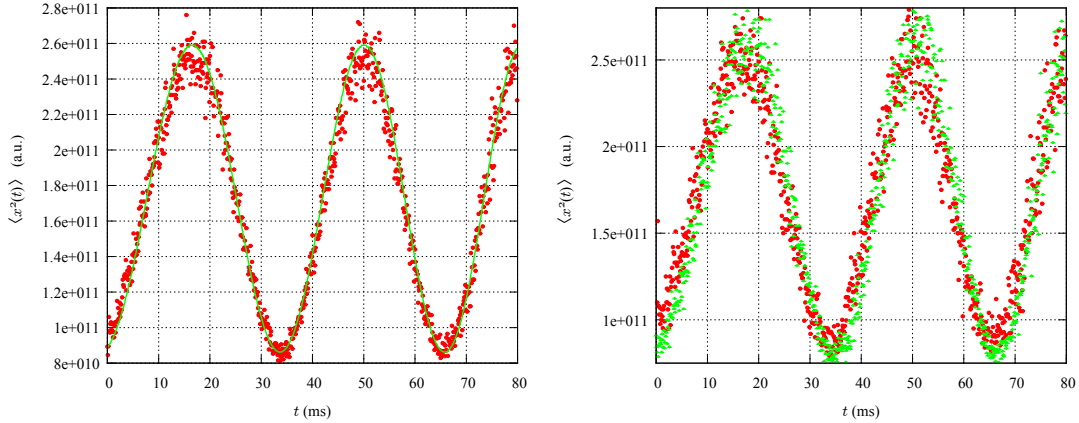


Figure 5.6: Temporal variance of the homodyne signal. Mean values of the variance for 0.1 ms long bins. On the left, the phase sweep is fitted with a second order non-linear model. On the right: two sets of data are represented, the first 15 s in red and in green the last 15 s of the measurement. We can see that the phase drift is very small (a little on the right). This confirms the reliability of the assumption that the phase is stable during one measurement.

Parallel monitoring Another possibility is to monitor the arches of squeezing in parallel. The output of the homodyne detection is also connected to a spectrum analyzer. For each sequence, we acquire the complete signal and use it to infer the phases. In this case, we assume the stability of the phase during one sequence. The difficulty is more the synchronization and the impedance matching when we connect the homodyne signal to the spectrum analyzer and the oscilloscope. (Two follower circuits would be appropriate; nevertheless using high impedance for the oscilloscope and low impedance for the spectrum analyzer works fine.)

²The absolute time of each event is systematically recorded by the oscilloscope. This time is called “timestamps”. It is an absolute time (equal to 0 for the 1st of January 2000) with a resolution of 1 ns. Most of the high-speed oscilloscopes have this feature.

5.3 Results and discussion

First of all, despite the different configuration of polarizations, we have observed the same phenomenon of back scattering from the local oscillator to the single-photon detector (cf section 4.3.3). Worst, this time, one isolator was not enough: a second isolator was necessary to get rid of the back scattered photons.

On table 5.1, we give the various parameters of the reconstructed states obtained with various pump powers. As expected, the state is less pure and thus the negativity of the Wigner function decreases (we will see in the appendix 6.4 that purity is nevertheless not a relevant parameter). The tapping ratio used for this set of measurements is around 5% (3° for the half-wave plate). This being fixed, the count rate also increases with the pump power.

\mathcal{P} (mW)	$2\pi\sigma_0^2 W(0,0)$	count rate (kHz)	S_-/S_+
6	-0.37 -0.58	1.5	-3.0 4.0
9	-0.38 -0.60	2.7	-3.5 5.0
12	-0.32 -0.52	3.5	-4.0 6.0
15	-0.29 -0.51	5.6	-4.5 7.0
21	-0.30 -0.51	6.5	-5.0 8.0
27	-0.24 -0.40	8.0	-5.5 9.5
33	-0.14 -0.30	13	-6.0 11

Table 5.1: Typical parameters of the reconstructed states for various pump powers, i.e. for various squeezed vacuum states. We can see that the Wigner function at the origin is given without correction on the left and with 85% correction on the right. As expected the negativity decreases with the pump power as the purity decreases. S_-/S_+ are the squeezing and anti-squeezing of the initial state.

On figure 5.7, we show typical results with -3 dB and -6 dB of squeezing without correction for losses for both. We can see, as expected, a domination of the odd terms. However, the losses contribute to populate the even photon-number. The fidelity is maximal for $\alpha^2 \approx 1$ as expected and equal to 65% without correction and 77% with 85% correction for losses. These results are a little disappointing. Indeed, the setup is extremely similar to the single-photon experiment but with a fidelity more than 10% lower. In addition to that, the measurement of the squeezed vacuum (cf. chapter 3) was good enough to expect a higher fidelity. Actually, this is not completely surprising when we go into details. Compared to the single-photon experiment we have added one more isolator. Secondly, the tapping ratio affects also the quality of the state (cf. figure 5.3). Working with 3% would be better³. We cannot work far from the threshold because we need to start with a -3 dB squeezed vacuum state so the state we use is less pure. In addition to that, this state is more sensitive to losses than the single-photon state (see appendix 6.4). We can also suspect a contribution of the non-perfect phase measurement but probably negligible compared to the others.

³5% was necessary to have a reasonable count rate

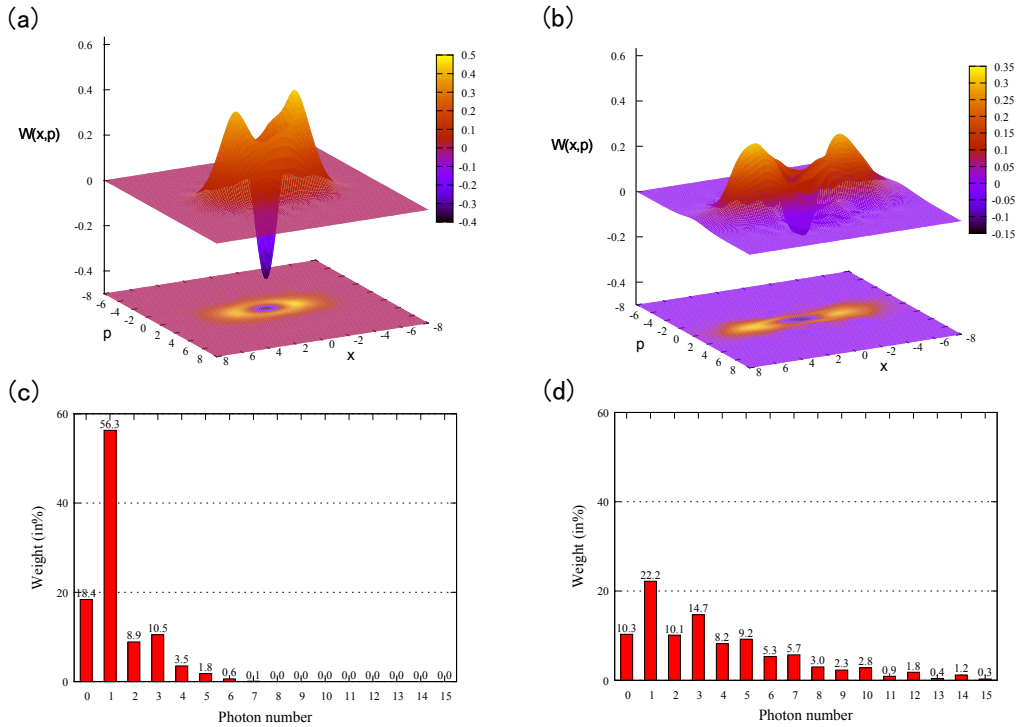


Figure 5.7: Reconstructed state without corrections. (a) Wigner function from a squeezed vacuum state of -3 dB, (c) corresponding photon-number distribution. (b) Wigner function from -6 dB of squeezed vacuum state (d) corresponding photon-number distribution.

Beyond 4 dB, the generated states have a priori no particular interest. We have mainly generated them to obtain an overall picture of the setup abilities and to see how far the negativity can be kept.

On the other hand, one can notice that the shape of the Wigner function is not completely smooth for the -6 dB of squeezing. This is probably due to the technique use to infer the phase. Indeed, this state is more sensitive to the phase and thus the non-perfect measure of phase is more obvious here.

5.4 What about even cat states?

The motivation for generating cat state is its potential to be used in quantum protocols with continuous variables. However, the next step is the ability to generate any qubit of the Bloch sphere. When we look at the state vector of an even cat state and squeezed vacuum it seems obvious that for a good choice of parameters the fidelity between the two states will be good. Nevertheless, one can wonder: how is it possible? or is it relevant? Indeed, according to the Hudson-Piquet theorem, one is negative and not the other. Actually, when we plot the even cat state, we see some negative regions but these are very small and the state looks like a squeezed vacuum state.

We end this chapter with few words on the possible extension of this protocol by subtracting one more photon. Indeed, the approximation of the squeezing as an even cat state is not completely satisfactory even though it seems to work in many cases with α small.

Double subtraction To obtain a state even closer to the even cat state with negative region, it is possible to subtract two photons from a squeezed vacuum ([83] and others). After two subtractions, the state is

$$|2PS\rangle = \frac{\hat{a}^2 \hat{S}|0\rangle}{\|\hat{a}^2 \hat{S}|0\rangle\|} \quad (5.20)$$

$$= \frac{(1-\lambda^2)^{5/4}}{\lambda\sqrt{1+2\lambda^2}} \sum_{n=1}^{\infty} \binom{2n}{n}^{1/2} \left(\frac{\lambda}{2}\right)^n \sqrt{2n(2n-1)} |2(n-1)\rangle. \quad (5.21)$$

This state gives a fidelity with an even cat state equal to:

$$\mathcal{F}_2 = \frac{2e^{-\alpha^2(1-\lambda)}}{1+e^{-2\alpha^2}} \frac{(1-\lambda^2)^{5/2}}{1+2\lambda^2} (1+\alpha^2\lambda)^2. \quad (5.22)$$

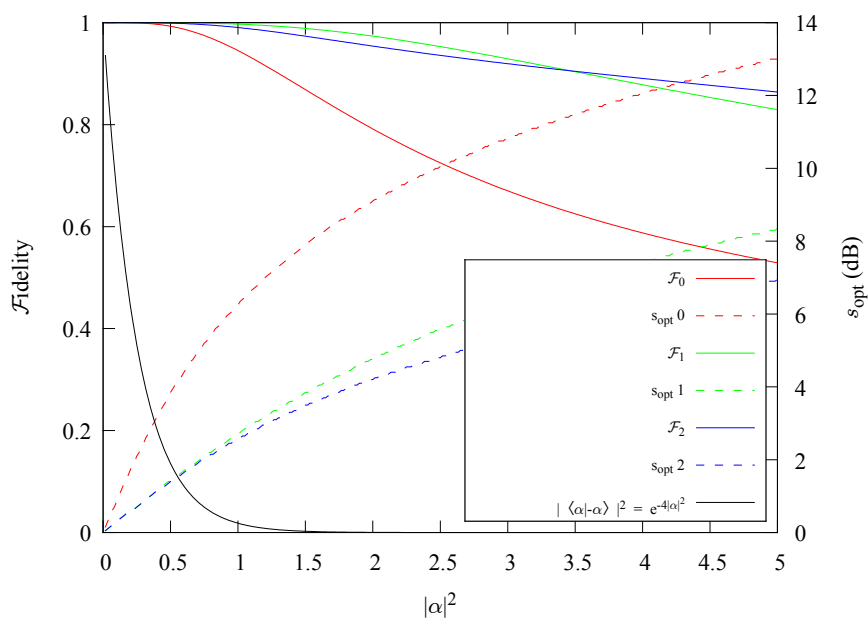


Figure 5.8: Fidelity between “true” cat state and photon subtracted form squeezed vacuum and the corresponding optimal values of squeezing

On figure 5.8, we see that, compared to the squeezed vacuum, with a two-photon subtraction we can achieve a fidelity close to unit for a higher range of amplitude α . Thus, the orthogonality of the encoding state will be better satisfied. More interestingly, on figure 5.9 we note that for a fixed squeezing, the optimal α is not the same for the squeezed vacuum and for the squeezed single-photon state. In contrast, the optimal amplitude is reasonably the same for the state obtained by two subtractions and the squeezed single-photon. This important feature means that we can work starting with the same squeezed vacuum state.

Similarly to the calculation of one photon subtraction on a Gaussian state (section 5.1.2), we can calculate the double subtraction. We first note the state after the first subtraction

$$\hat{D}W = \frac{1}{2} [A + B_x x^2 + B_p p^2] W_G, \quad (5.23)$$

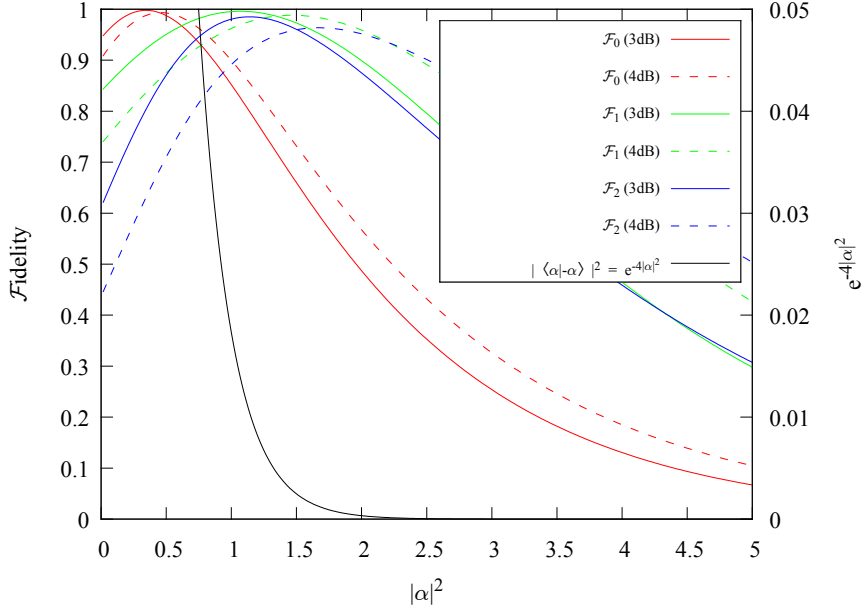


Figure 5.9: Fidelity between “true” even cat state and photon subtracted form squeezed vacuum for fixed values of squeezing.

by applying again the subtraction operator we obtain

$$\hat{D}\hat{D}W_G = \frac{1}{4} \left[(A + B_x x^2 + B_p p^2)^2 + (B_x + B_p)\sigma_0^2 + 2B_x \left(1 - \frac{\sigma_0^2}{\sigma_x^2}\right) x^2 + 2B_p \left(1 - \frac{\sigma_0^2}{\sigma_p^2}\right) p^2 \right] W_G, \quad (5.24)$$

that we normalize with

$$\iint \hat{D}\hat{D}W = \frac{3\sigma_x^4 + 3\sigma_p^4 + 2\sigma_p^2\sigma_x^2 - 8\sigma_0^2(\sigma_x^2 + \sigma_p^2) + 8\sigma_0^4}{(4\sigma_0^2)^2}. \quad (5.25)$$

Continuous variables qubits To go further, one could ask how to generate any qubit with the continuous variable encoding of the kind $c_0|\alpha\rangle + c_1|-\alpha\rangle$? This could be done by mixing a weak beam to the conditioning path to realize a displacement. This would yield to a state $a|cat_+\rangle + b|cat_-\rangle$ where the weights and coherences of the superposition depends on the phase and the amplitude of the weak beam.

Interestingly, this is a good way to “see” the limit of the approximation $|cat_+\rangle \approx \hat{S}|0\rangle$ and how two subtractions is better. Indeed, we can look at the pole of the Bloch sphere i.e. $(|cat_+\rangle + |cat_-\rangle)/\sqrt{2} = |\alpha\rangle$ or $(|cat_+\rangle - |cat_-\rangle)/\sqrt{2} = |-\alpha\rangle$. To illustrate this point, Fig. 5.10 gives the comparison between the superposition with the approximation $|cat_+\rangle \sim \hat{S}|0\rangle$ (a) and $|cat_+\rangle \sim \hat{a}^2\hat{S}|0\rangle$ (b) for the even cat state, (with still for the odd cat state $|cat_-\rangle \sim \hat{a}\hat{S}|0\rangle$). As can be seen in Fig. 5.10, the fidelity with a coherent state is better with a second subtraction. Indeed, on figure (a) we have clearly a negative part whereas for (b) it is almost positive and with a shape the that better filled the one of the coherent state.

The double subtraction has not been realized so far, mainly because the SSPD didn’t show sufficient efficiency. However, some very significant progresses have been recently

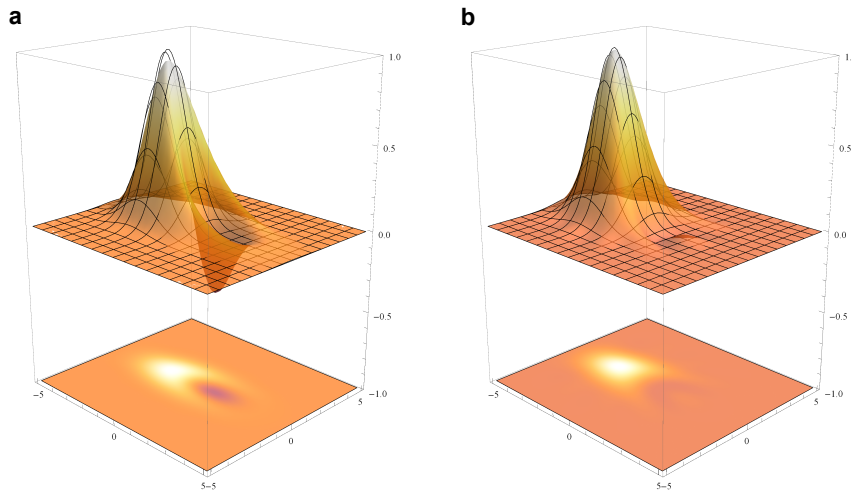


Figure 5.10: Superposition of optical Schrödinger cats. Plot of the Wigner function associated with $(|\text{cat}_+\rangle + |\text{cat}_-\rangle)/\sqrt{2}$, which is a coherent state in the ideal case. (a) The even cat state is approximated by a squeezed vacuum state $|\text{cat}_+\rangle \sim \hat{S}|0\rangle$. (b) The even cat state is approximated by a squeezed vacuum state on which we subtracted two photons $|\text{cat}_+\rangle \sim \hat{a}^2 \hat{S}|0\rangle$. The black grid corresponds to a coherent state.

obtained in the field of superconducting detector with typically some efficiencies above 50% (compared to the 7% of our detector). Note that, only the group of Sasaki has realized a double subtraction experiment [108]. However, the scope was different and now the next challenge is to generate any qubit on the Bloch sphere with a double subtraction in order to enhance the reliability of the generated states.

5.5 Conclusion

In this chapter, we have presented the generation of optical Schrödinger cat state by subtracting a single-photon from a squeezed vacuum state. Starting from a -3 dB squeezed vacuum state generated by a type-I OPO, and subtracting a single-photon from it, we have obtained a state with 65% of fidelity with a cat state of amplitude $|\alpha|^2 \approx 1$. The main limitation that decreases this fidelity comes from the detection losses (two optical isolators). Indeed, in the ideal case we expect a fidelity up to 99%.

These results were expected given the ones obtained in the previous chapter for single-photon state generation with a type II OPO. Indeed, although we consider states of very different natures, the setups are quite similar and thus the performances are comparable. Here, a new limitation could be the phase measurement, however it is manageable because it does not require a high precision for the size of cat we consider. Nevertheless, it is worth noting that the technique we use to measure the phase works well here but it is neither robust nor perennial. Therefore, it has been modified for the next experiments, as we will see in chapter 8.

6 | Temporal Mode and Two-Photons Fock State Generation

Only play what you hear. If you don't hear anything, don't play anything.

CHICK COREA

In quantum state engineering, a precise knowledge of the modal structure of the generated states is essential as it strongly influences the success of the targeted operations. Indeed, the detection or the processing mode has to be precisely adapted to the resource. For instance, homodyne detection [59] projects the impinging state into the mode of a so-called local oscillator, which has thus to be perfectly matched. Any mode mismatch will translate to losses. Similarly, in quantum information processing schemes, such as linear optical computing where light states are combined in optical circuits, the modal structure plays a central role [97]. Defining this mode structure very often relies on a detailed a priori knowledge of the used resources, when available, and can additionally call for an involved theoretical modeling. In contrast, we investigated a method based on homodyne measurements with a continuous-wave local oscillator, which enables to realize a multimode expansion via the autocorrelation function. The optimal temporal mode, or the existence of various independent modes, can then be inferred.

In this chapter, we describe in more details the temporal mode that we have assumed in the previous experiments [75]. We first review the two main theoretical approaches to determine the temporal modes in some specific experiments. Then, we investigate a practical and direct method to experimentally infer the temporal mode profile of traveling quantum light states, not only single-photon states, without prior information and without any optimization procedure. We implemented this approach in the single-photon Fock states and Schrödinger cat-like states preparation presented in the previous chapters 4 and 5. Such a technique enables a high-fidelity quantum state preparation and provides a variety of information about the multimode structure of a given state, as highlighted later by the case of a two-photon Fock state generation presented at the end of the chapter.

6.1 Theories of temporal modes	96
6.1.1 Time- and band-limited signal expansion	96
6.1.2 Optimal mode for a maximal fidelity	98
6.2 Measurement of the temporal modes	100
6.2.1 Eigenmode expansion	100
6.2.2 Example of the single-photon and cat-like state preparations	102
6.2.3 Theoretical expression	103
6.3 Two-photon Fock state: a further example	104
6.3.1 Experimental setup	105
6.3.2 Results	106
6.3.3 Temporal mode theory	108
6.4 Conclusion	108

6.1 Theories of temporal modes

Let us formulate the problem from a practical point of view. We consider a setup which heralds the preparation of a state and we would like to characterize the state by quantum state tomography. For this purpose, we use a homodyne detection, with a continuous-wave local oscillator, that performs some quadrature measurements. The output of the homodyne detection is continuous and provides the measurement of the observable $\hat{x}(t)$. So, how to process the signal $x(t)$ that we record for each detection event to obtain a quadrature measurement of the generated state? We should consider the “good” temporal mode $f(t)$ that we apply to the signal $x_f \int dt f(t)x(t)$. The question that arise is: what is the optimal temporal mode?

Mainly two approaches have been proposed to study theoretically the temporal mode in a conditional preparation within the continuous wave regime. To briefly compare, the first one is based one a temporal mode expansion adapted to the different characteristic times of the experimental setup. The other one optimizes the mode to maximize the fidelity with the target state.

In the following, we detail a little bit more these two approaches to highlight their main differences. For more details, the reader is invited to refer to Ref. [82, 81, 72] for the first one, and [104] for the second one.

6.1.1 Time- and band-limited signal expansion

In Ref. [104], the main idea is to find a mode expansion appropriate to the different dynamics of the experiment: the OPO cavity, the conditioning path, the photon detector and the homodyne detection (cf figure 6.1). The OPO and the conditioning path are frequency limited, and we note B the corresponding bandwidth. As the detector and the homodyne detection are time limited, we note T this characteristic time (practically, it basically corresponds to the time jitter of the single-photon detector).

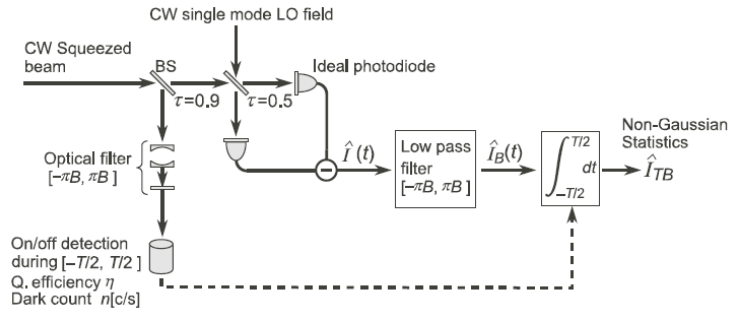


Figure 6.1: Time limited measurement and frequency limited cavity in a coherent state preparation scheme. *Extracted from [104].*

Hence, we want to find a mode expansion appropriate to the time- and frequency-limited system. If we consider some rectangle modes $[-T/2; T/2]$ in time and $[-\pi B; \pi B]$ in frequency. The relevant expansion in this case uses a basis of *prolate spheroidal functions*. They are solutions of the equations

$$\chi_k(c)\Psi_k(c, t) = \int_{-T/2}^{T/2} dt' \frac{\sin \pi B(t-t')}{\pi(t-t')} \Psi_k(c, t'), \quad (6.1)$$

$$\chi_k(c)\Phi_k(c, \Omega) = \int_{-\pi B}^{\pi B} d\Omega' \frac{\sin\left(\frac{\Omega-\Omega'}{2}T\right)}{\pi(\Omega-\Omega')} \Phi_k(c, \Omega') . \quad (6.2)$$

Ψ_k and Φ_k are linked by the relation

$$\chi_k(c)\Phi_k(c, \Omega) = \int_{-T/2}^{T/2} dt \Psi_k(c, t) e^{i\Omega t} , \quad (6.3)$$

where $\chi_k(c)$ (where $c = \pi BT/2$) is the eigenvalue of the mode k and corresponds to the weight of this mode compared to the others.

On the other hand, the annihilation operator noted

$$\hat{a}(t) = \frac{1}{2\pi} \int_{-\infty}^{+\infty} d\Omega \hat{a}(\omega_0 + \Omega) e^{-i(\omega_0 + \Omega)t} , \quad (6.4)$$

can be rewritten in the basis rotating at the pulsation ω_0 of the degenerate mode of the OPO

$$\hat{A}(t) = \hat{a}(t) e^{i\omega_0 t} = \frac{1}{2\pi} \int_{-\infty}^{+\infty} d\Omega \hat{A}(\Omega) e^{-i\Omega t} . \quad (6.5)$$

The squeezing operator is thus written

$$\hat{S} = \exp \left[\frac{1}{2\pi} \int_{-\pi B}^{+\pi B} d\Omega \frac{\gamma(\Omega)}{2} [\hat{A}(\Omega)\hat{A}(-\Omega) - \hat{A}^\dagger(\Omega)\hat{A}^\dagger(-\Omega)] \right] \quad (6.6)$$

with γ the squeezing factor which will later be supposed constant. But, the expansion on time and frequency limited modes is written

$$\hat{A}(\Omega) = \sum_{k=0}^{\infty} \hat{A}_k \Phi_k(c, \Omega) , \quad (6.7)$$

with

$$\hat{A}_k = \frac{1}{2\pi} \int_{-\pi B}^{\pi B} d\Omega \hat{A}(\Omega) \Phi_k(c, \Omega) = \int_{-\infty}^{\infty} dt \hat{A}(t) \Psi_k^*(c, t) , \quad (6.8)$$

verifying the commutation relation $[\hat{A}_k, \hat{A}_l^\dagger] = \delta_{kl}$. The squeezing operator is thus written

$$\hat{S} = \bigotimes_{k=0}^{\infty} \hat{S}_k , \quad \text{avec} \quad \hat{S}_k = \exp \left[\frac{\eta_k}{2} (\hat{A}_k^2 - \hat{A}_k^{\dagger 2}) \right] , \quad (6.9)$$

where the squeezing parameter of the mode k is $\eta_k = (-1)^k \gamma$.

This decomposition highlights the multimode aspect of the experiment. Actually, it mainly depends on the factor $\chi_k(c)$, but this latter goes suddenly to 0 for $k > 2c/\pi = BT$ (Fig.6.2). Hence, we understand that for $BT \ll 1$ only the mode $k = 0$ will stay, in such a way that we can consider only one mode. We should thus try to adjust these two parameters in order to be in this situation. Typically, for the μ Cavity $B_{\mu\text{Cav}} \approx 300$ MHz $>$ $B_{\text{OPO}} \approx 30$ MHz and a characteristic time $T \approx 0.5$ ns we have $BT \approx 0.015$. So, only the mode $k = 0$ matters. Eventually, we obtain

$$\Psi_0(t) = \sqrt{\zeta} e^{-\zeta|t|} , \quad (6.10)$$

with $t = 0$ the detection event on the photon detector, and ζ the characteristic bandwidth of the whole OPO and μ Cavity. This way, we obtain the quadrature measured by the homodyne detection

$$\hat{x}_\phi \sim \int_{-T/2}^{T/2} dt \Psi_0(t) \hat{x}_\phi(t) . \quad (6.11)$$

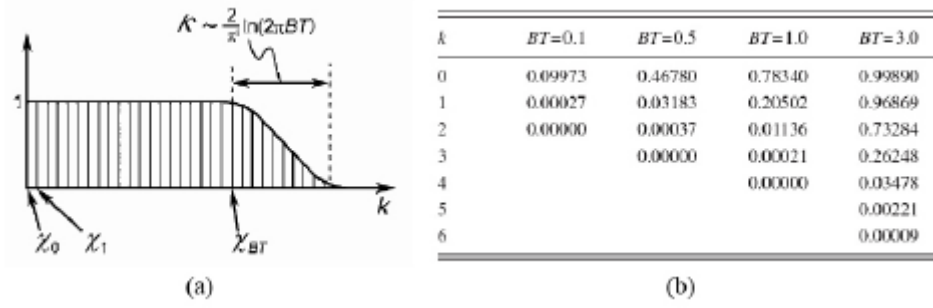


Figure 6.2: Eigenvalues $\chi_k(c)$ for different product BT . Extract from [104]. We note that only one eigenvalues dominate if $BT \ll 1$.

6.1.2 Optimal mode for a maximal fidelity

The second approach proposed in Ref. [82] is very different. The idea is to find the temporal mode which will give the highest fidelity with a single-photon state.

We consider that the single-photon detector will make a measurement on a given temporal mode 1 (i.e. the trigger mode) assumed to be a rectangle

$$f_1(t) = \begin{cases} \frac{1}{\sqrt{\Delta t_c}} & \text{if } t_c - \Delta t_c/2 < t < t_c + \Delta t_c/2, \\ 0 & \text{otherwise.} \end{cases} \quad (6.12)$$

With as previously Δt the characteristic time of the detector. On its side, the heralded state will be in another mode 2 (i.e. the signal mode). We can thus describe the state with a two-mode covariance matrix. We start from the correlation at the OPO output by

$$\langle \hat{a}_\pm(t) \hat{a}_\mp(t') \rangle = \frac{\lambda^2 - \mu^2}{4} \left(\frac{e^{-\mu|t-t'|}}{2\mu} + \frac{e^{-\lambda|t-t'|}}{2\lambda} \right), \quad (6.13)$$

$$\langle \hat{a}_\pm^\dagger(t) \hat{a}_\pm(t') \rangle = \frac{\lambda^2 - \mu^2}{4} \left(\frac{e^{-\mu|t-t'|}}{2\mu} - \frac{e^{-\lambda|t-t'|}}{2\lambda} \right), \quad (6.14)$$

$$\langle \hat{a}_\pm(t) \hat{a}_\pm(t') \rangle = \langle \hat{a}_\pm^\dagger(t) \hat{a}_\mp(t') \rangle = 0, \quad (6.15)$$

with $\lambda = \gamma/2 + \epsilon$ et $\mu = \gamma/2 - \epsilon$ et $\epsilon/\gamma = \sqrt{P/P_{th}}$. Then, we apply the two temporal modes

$$\hat{a}_1 = \int f_1(t) \hat{a}_+(t) dt, \quad (6.16)$$

$$\hat{a}_2 = \int f_2(t) \hat{a}_-(t) dt. \quad (6.17)$$

Hence, we obtain the coefficient of the covariance matrix:

$$V_{11} = V_{22} = 1 + 2\langle \hat{a}_1^\dagger \hat{a}_1 \rangle, \quad (6.18)$$

$$V_{33} = V_{44} = 1 + 2\langle \hat{a}_2^\dagger \hat{a}_2 \rangle, \quad (6.19)$$

$$V_{13} = V_{31} = -V_{24} = -V_{42} = 2 \Re(\langle \hat{a}_1 \hat{a}_2 \rangle), \quad (6.20)$$

$$V_{14} = V_{41} = V_{23} = V_{32} = 2 \Im(\langle \hat{a}_1 \hat{a}_2 \rangle), \quad (6.21)$$

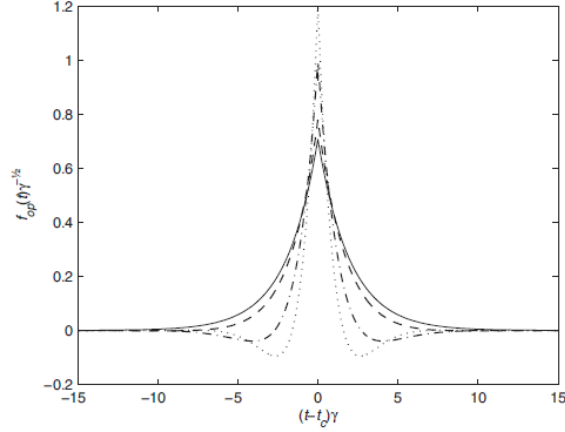


Figure 6.3: Optimal mode function for $\epsilon/\gamma = 0$ (solid line), $\epsilon/\gamma = 0.1$ (dashed line), $\epsilon/\gamma = 0.2$ (dot-dashed line), and $\epsilon/\gamma = 0.3$ (dotted line). *Extracted from [82].*

$$V_{12} = V_{21} = V_{34} = V_{43} = 0 . \quad (6.22)$$

The annihilation of one photon in the trigger mode (and traced out because the mode is lost) yields to the Wigner function of the conditional state

$$W(x, p) = [A_1 + A_2(x^2 + p^2)] e^{-A_3(x^2 + p^2)} , \quad (6.23)$$

where the coefficients are function of the covariance matrix elements

$$A_1 = \frac{V_{11}V_{33} - V_{13}^2 - V_{14}^2 - V_{33}}{\pi(V_{11} - 1)V_{33}^2} , \quad (6.24)$$

$$A_2 = \frac{V_{13}^2 + V_{14}^2}{\pi(V_{11} - 1)V_{33}^2} , \quad (6.25)$$

$$A_3 = 1/V_{33} . \quad (6.26)$$

We also assume that the characteristic time of the detector is small compared to the decay rate of the OPO cavity. At the end, the fidelity $\iint dx dp W(x, p) W_{|1\rangle}(x, p)$ is maximized by optimizing the temporal mode of the signal $f_2(t)$. Figure 6.3 shows the optimal modes for different pump power. Furthermore, in the limit of zero pump, the mode takes the shape of a double exponential function and that this shape changes with the pump power. However, we have seen that it is preferable to operate the OPO far from the threshold. So, the effect of the pump power on the temporal mode is not a concern in the reported experiments.

6.2 Measurement of the temporal modes

Precisely controlling this modal structure has been a long quest for quantum optics. In some experiments, the temporal mode profile can be easily inferred from the setup features. In pulsed parametric down conversion for instance, the temporal mode is defined by the pulse shape. When using a continuous-wave optical parametric oscillator, the cavity bandwidth leads to a double-decaying exponential profile [82]. However, even in these simple cases, the theoretical mode is only approximated given the imperfections and complexity of the setups. Indeed, it requires questionable assumptions: in the examples we detailed in the previous section, the first one assumes rectangular shape for the cavity spectrum, in the other one the possible effect of the filtering on the conditioning path is not taken into account. More critically, the pulse shape can also be strongly altered after its generation due to some propagation effects or additional frequency filtering may also change the optimal profile, leading to large mismatch between the expected mode and the actual one. In some experiments, the mode in which the light is emitted can even be harder to predict. This is the case for instance for photonic states generated from atomic systems, including from large atomic ensembles [21].

Furthermore, although the theoretical mode yields to good experimental results, it seems interesting to find a way to measure this mode in order to compare it with the theory. Various techniques have been developed to infer the temporal wavepacket of single-photon states. One technique can rely on the use of photon counting to access the temporal statistics [39]. However, this straightforward approach is not always easy to implement due to low count rates and can be constrained by the limited photon-number resolution of available detectors for characterizing states involving higher photon-number contributions. Furthermore, it does not give access to any sign information in the modal structure. Recently, another technique based on homodyne detection, which enables a full tomographic reconstruction, has been proposed for ultrashort single-photon pulses. It relies on an adaptive scheme to iteratively map the mode into the one of the local oscillator using pulse shaping techniques [93, 98].

In the following, the idea is to take advantage of the continuous-wave regime of our homodyne detection and exploit all the available information in the homodyne detection signal to recover the temporal mode.

6.2.1 Eigenmode expansion

To introduce the method, we first consider the case of a light field containing a single-photon state in a well-defined spatial mode. It can be shown that single-photon states can always be considered as single mode states, in a mode that has to be determined [109]. The question is to determine the temporal mode occupied by the single-photon by directly using the raw homodyne data. For each realization of the experiment, the homodyne detection, as illustrated in Fig. 6.4, provides a continuous measurement $x(t)$. This homodyne signal can then be processed with a temporal mode $f(t)$ to give a single quadrature outcome $x_f = \int f(t)x(t)dt$. Various quantity could be use as parameter to maximize. Here, the initial idea is to to maximize the variance of the measured quadrature in a given time interval. Indeed, the variance of the vacuum is $\langle \hat{x}^2 \rangle_{|0\rangle} = \sigma_0^2$ while it is three times larger for the single-photon state, $\langle \hat{x}^2 \rangle_{|1\rangle} = 3\sigma_0^2$. The variance $\langle \hat{x}_f^2 \rangle$ is thus a good parameter to maximize in order to infer the optimal temporal mode function.

Interestingly, it can be shown that the variance $\langle \hat{x}_f^2 \rangle$ of the filtered mode and the temporal mode $f(t)$ are linked to the autocorrelation function of the unfiltered homodyne signal by the expression:

$$\langle \hat{x}_f^2 \rangle = \iint dt dt' f(t) f(t') \langle \hat{x}(t) \hat{x}(t') \rangle. \quad (6.27)$$

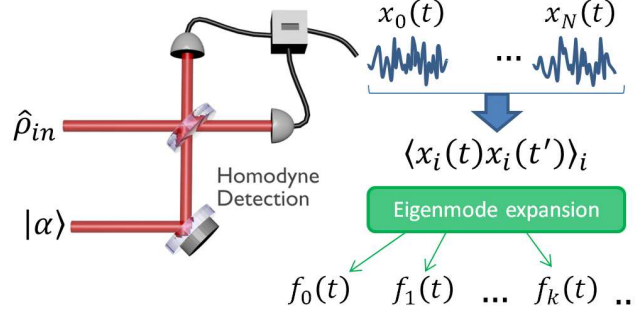


Figure 6.4: (color online). Schematic sketch. The propagating quantum state $\hat{\rho}_{in}$ is measured by homodyne detection with a continuous-wave local oscillator. The reported method consists in accessing the optimal temporal mode via a multimode analysis using eigenfunction expansion of the autocorrelation function $\langle x(t)x(t') \rangle$.

The variance is thus expressed as a quadratic integral form. The kernel, given here by the autocorrelation function, $K(t, t') = \langle \hat{x}(t)\hat{x}(t') \rangle$, is symmetric and positive definite. As a result of the Mercer's theorem, it can be expanded in a series [14]:

$$K(t, t') = \sum_{k=0}^{\infty} \kappa_k f_k(t) f_k(t'), \quad (6.28)$$

where $f_k(t)$ are orthonormal eigenfunctions satisfying the completeness relation

$$\sum_{k=0}^{\infty} f_k(t) f_k(t') = \delta(t - t') \quad (6.29)$$

and the eigenvalue equation

$$\int f_k(t') K(t, t') dt' = \kappa_k f_k(t). \quad (6.30)$$

Any temporal mode $f(t)$ can be expressed as a linear combination of the eigenmodes, i.e. $f(t) = \sum_{k=0}^{\infty} \lambda_k f_k(t)$ with $\sum_{k=0}^{\infty} \lambda_k^2 = 1$. The quadrature operator of each mode is then defined by

$$\hat{x}_{f_k} = \int f_k(t) \hat{x}(t) dt. \quad (6.31)$$

Given this expansion, the variance for a given temporal mode $f(t)$ can be written as

$$\langle \hat{x}_f^2 \rangle = \sum_{k=0}^{\infty} \lambda_k^2 \kappa_k \leq \max_{k \in \mathbb{N}} \kappa_k. \quad (6.32)$$

It results from this expression that the maximum of variance is obtained for the eigenmode with the largest eigenvalue.

Actually this multimode expansion has a deeper a more general physical meaning. As $\langle \hat{x}_{f_k} \hat{x}_{f_{k'}} \rangle = 0$ for $k \neq k'$, it corresponds to an expansion over non-correlated modes. Choosing a temporal mode indeed realizes a single-mode measurement: the state is thus traced over all the other modes and the process would result in a statistical mixture if there were some correlations with other modes.

The method introduced here is thus general and not only restricted to the single-photon case presented above. It can be applied to various quantum state engineering experiment for which extracting the optimal temporal mode is a central issue. Nevertheless, it is worth noting that we only consider here in phase correlation and the uniqueness of the expansion is only true if the eigenvalues are different. When eigenvalues are equal, but different from the one of the vacuum, this expansion does not guarantee that all the modes are separable and results in a *partial* Schmidt-like decomposition. Indeed, it does not ensure that $\langle \hat{x}_k \hat{p}_{k'} \rangle = 0$ if $k \neq k'$. More over it arises more fundamental questions: is the expansion based on $\langle \hat{x}(t) \hat{x}(t') \rangle$ and the one on $\langle \hat{p}(t) \hat{p}(t') \rangle$ yields always to the same expansion? Of course, this question is beyond our scope as we want to engineered states a priori single-mode.

6.2.2 Example of the single-photon and cat-like state preparations

As a first example, we illustrate this approach with the heralded preparation of single-photon from a two-mode squeezed vacuum emitted by a continuous-wave frequency degenerated type-II optical parametric oscillator (OPO) (cf. Ref. [74]). As described in Chap. 4, the detection of a single-photon in one beam heralds the generation of a single-photon in the other one [40]. Due to the continuous-wave nature of the pump, the temporal mode in which the single-photon is generated has to be determined.

Experimentally, for each heralding event, the homodyne signal is recorded during 200 ns. The auto-correlation function is then computed from the recorded segments. This measurement being sampled (5 Gs/s rate) the homodyne signal of the i -th trigger event is a vector \mathbf{X}_i of 1000 elements, the experimental autocorrelation function is thus a 1000×1000 real and symmetric matrix

$$\mathbf{M} = \frac{1}{N} \sum_{i=1}^N \mathbf{X}_i \mathbf{X}_i^T . \quad (6.33)$$

The eigenfunctions and their corresponding eigenvalues are then computed numerically. Figure 6.5(a) provides such eigenvalues for the vacuum state and for the heralded single-photon. Let us first note that the eigenvalues for the vacuum are not all equal. This decrease for the modes with higher frequency components results from the finite bandwidth of the homodyne detection. Secondly, for the single-photon state, we observed that only the first eigenvalue is largely above the values of the vacuum state, as expected theoretically for such a state [109]. The associated eigenfunction provides thereby the optimal temporal mode, as plotted in Fig. 6.5(b). This mode is then used for the state reconstruction [62] and the Wigner function corresponding to the heralded state is displayed in Fig. 6.5(c), together with the diagonal elements of the density matrix.

We also applied this practical method to the generation of a Schrödinger cat-like state, which includes higher photon numbers. This generation is heralded by the subtraction of a single-photon from a squeezed vacuum. For this purpose, we tap out with a beam splitter 5% of a 3 dB-squeezed vacuum generated by a type-I optical parametric oscillator as detailed in Chap. 5 and, as previously, heralds the preparation by a detection event given by the superconducting single-photon detector. In contrast to the previous case, the generated state is not phase invariant but the autocorrelation function is computed with a phase-average of the quadrature measurements. The eigenvalues are given in Fig. 6.5(a) and only one mode with a large eigenvalue appears. The other modes are squeezed vacuum leading to eigenvalues slightly larger than the vacuum state. The associated temporal profile is given in Fig. 6.5(b) and the Wigner function corresponding to the heralded single-mode state is displayed in Fig. 6.5(d).

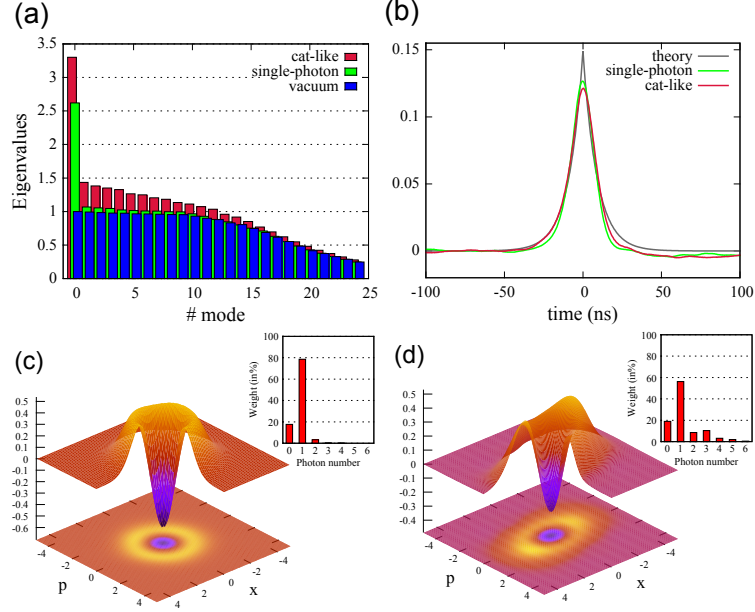


Figure 6.5: (color online). Single-photon and Schrödinger cat-like state generation. (a) Eigenvalues of the autocorrelation function $\langle x(t)x(t') \rangle$ given in blue for a vacuum state, in green for a single-photon and in red for a Schrödinger cat-like state. Due to the finite bandwidth of the detection, the eigenvalues decrease for the modes with higher frequency components. (b) First eigenmode for single-photon in green and Schrödinger cat-like state in red. The black line gives the theoretical temporal mode corresponding to a double-decaying exponential profile. (c) and (d) Associated Wigner functions using the optimal temporal modes. The insets show the diagonal elements of the density matrices, without correction from detection losses.

6.2.3 Theoretical expression

In order to compare to a model, we derive below the theoretical expression of the optimal temporal mode using the method based on the autocorrelation function expansion. To derive the theoretical expression of the autocorrelation function, we start from equation (6.23) (derived in [82]). The Wigner function of the conditional state is

$$W(x, p) = [A_1 + A_2(x^2 + p^2)] e^{-A_3(x^2 + p^2)}, \quad (6.34)$$

where the different coefficients are function of the elements of the covariance matrix (reduced to the specific temporal modes of the conditioning path and signal path)

$$A_1 = \frac{V_{11}V_{33} - V_{13}^2 - V_{14}^2 - V_{33}}{\pi(V_{11} - 1)V_{33}^2}, \quad (6.35)$$

$$A_2 = \frac{V_{13}^2 + V_{14}^2}{\pi(V_{11} - 1)V_{33}^2}, \quad (6.36)$$

$$A_3 = 1/V_{33}. \quad (6.37)$$

We can thus compute the variance of the state as

$$\langle \hat{x}^2 \rangle = \iint x^2 W(x, p) dx dp = \pi \left[\frac{A_1}{2A_3^2} + \frac{A_2}{A_3^3} \right] = \frac{1}{2} \left(V_{33} + \frac{V_{13}^2 + V_{14}^2}{V_{11} - 1} \right). \quad (6.38)$$

After simplification and identification with equation (6.27), we obtain the autocorrelation function

$$\langle \hat{x}(t)\hat{x}(t') \rangle = \delta(t-t') + 2\langle \hat{a}_s^\dagger(t)\hat{a}_s(t') \rangle + 2\frac{\langle \hat{a}_{trig}\hat{a}_s(t) \rangle \langle \hat{a}_{trig}\hat{a}_s(t') \rangle}{\langle \hat{a}_{trig}^\dagger\hat{a}_{trig} \rangle}, \quad (6.39)$$

where \hat{a}_{trig} corresponds to the operator associated with the idler photon in the mode in which the heralding detection takes place. The first and second terms of Eq. (6.39) are functions of $|t-t'|$ and thus do not come from the conditional operation. The first one corresponds indeed to the vacuum and the second one to the thermal state.

In a type-II OPO, the signal and idler photons are emitted pairwise, leading to quantum correlations. Using the correlation functions for the annihilation and creation operators for the two modes, well-known for an OPO [19, 82]. In the case of a low pump power $\epsilon \rightarrow 0$ ($\lambda = \mu = \gamma$), - which is the case in the experiment in order to limit higher photon number contamination - the contribution from the thermal state is negligible and the autocorrelation function simplifies as:

$$\langle \hat{x}(t)\hat{x}(t') \rangle = \delta(t-t') + 2\Phi(t)\Phi(t') \quad (6.40)$$

with $\Phi(t) = \frac{\langle \hat{a}_{trig}\hat{a}_s(t) \rangle}{\sqrt{\langle \hat{a}_{trig}^\dagger\hat{a}_{trig} \rangle}}$. Given this form, $\Phi(t)$ is the only eigenfunction with an eigenvalue different from unity. It thus corresponds to the mode of the heralded single-photon. Moreover, if we consider an extremely fast detector, leading to $\hat{a}_{trig} = \int dt \hat{a}_i(t)\delta(t)$, by using equation (6.13), we obtain the temporal mode $\Phi(t) = \sqrt{\gamma}e^{-|t|\gamma}$ where γ is the bandwidth of the OPO cavity. This double-decaying exponential profile was already demonstrated in [82, 104] but using different methods, as shown in the first section of the chapter.

Given the experimental bandwidth of the OPO used here ($\gamma = 60$ MHz), the theoretical temporal profile is superimposed on Fig. 6.5(b). Due to a very optimized experimental setup, the results are very closed to this simplest theoretical model: the overlap between experimental and theoretical temporal modes is above 99%. A tiny difference can however be observed on the profile. The experimental functions are indeed smoother on the top. This could be explained by some jitter on the detection signal but the superconducting single-photon detector used for this experiment is around 50 ps. The main reason comes from the limited bandwidth of the homodyne detection which is larger but not much larger than the one of the OPO cavity. This result clearly confirms the efficiency of the method, providing the optimal temporal mode without prior information.

6.3 Two-photon Fock state: a further example

As a third illustrative experiment, we consider the more complex case corresponding to the generation of a two-photon Fock state. Such generation has already been demonstrated in the pulse regime [88, 122, 7] but never in the continuous-wave regime. The setup is the same as for the single-photon generation but instead of detecting one photon we detect two photons. For this purpose, the conditioning path is now split into two in order to detect two single-photons as heralding events.

As we work in the continuous wave regime, some question arises: what can be the delay between the two detection events? what is exactly the state and the temporal mode structure for a given time delay?

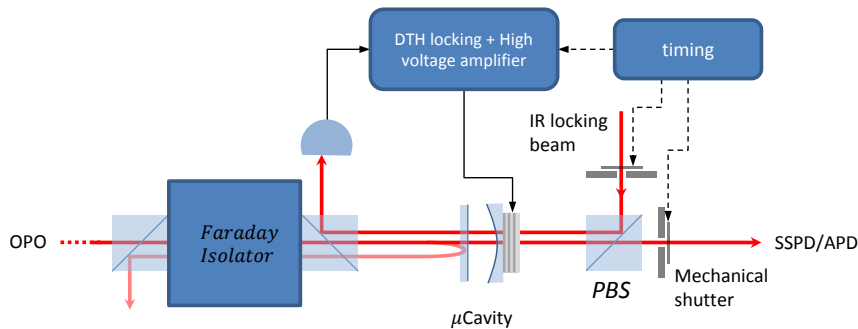


Figure 6.6: Conditioning path setup optimized for the transmission. A Faraday isolator avoids any reflection from the μ Cavity input mirror to go back to the OPO (otherwise, it would form an extended cavity with the OPO). One polarization is used for the signal beam from the OPO and the other for the locking beam. The cavity is locked with the Dither-and-lock technique. Some mechanical shutters are used to block the beams depending on the locking or measurement step. Beams have been obviously shifted for clarity.

6.3.1 Experimental setup

Starting from the single-photon generation experiment (cf Chap. 4), we modified the conditioning path to detect two photons. We explain in the following the changes operated and how the data have been obtained efficiently.

Enhancing the conditioning path efficiency

The MEMS fiber switch has the advantage to simplify the setup but, on the other hand, the actual technology does not provide devices with a good transmission (in our case 60%). This becomes a critical issue to detect more than one photon. Indeed, for multi-photon detection the count rate can be extremely small. Some parts of the conditioning path, like the μ Cavity or the detector, are difficult to improve but, the transmission of the MEMS can be replaced.

Now, we use two polarizations: one for the signal beam send to the single-photon detector and the other for the locking beam (see figure 6.6). Of course, the isolation between the two polarizations is not enough to avoid any light from the locking beam to reach the single-photon detector. We thus use free-space mechanical shutters. They are slower than the MEMS (around 5 ms of transition) but this is clearly not a limitation for our setup. The timing is pushed at the limit of stability to have a measurement time as long as possible compared to the locking time and, increases the global count rate.

All delays in one experiment

Contrary to the pulsed regime, the two heralding events can occur at different times, t and $t + \Delta t$, and the modal structure strongly depends on this delay. The idea is to record in one experiment different delays. To do so, we should trigger each time that $|\Delta t|$ is below a certain duration.¹

¹Let us note that with our oscilloscope it is not possible to do conditional triggering exactly in this way. Only one sign is possible i.e. for a given event, only the trigger with a second event after (limited to a certain time) or a second event before. But we would like to select both. In principle, it is useless, the behavior is supposed to be symmetric, but we want to check that also. The trick that we use is to delay, with a longer cable, one of the detector signal of twice the characteristic time of the temporal mode (in our case 75 ns).

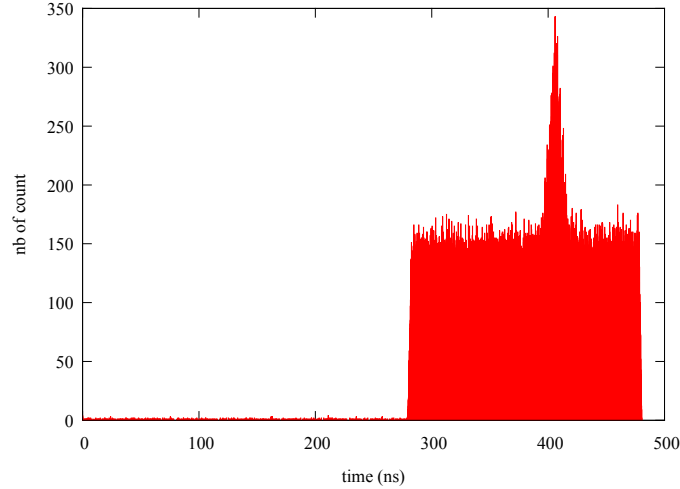


Figure 6.7: Time distribution of the second detection event. We can see the acceptance window set in the oscilloscope trigger setup. Interestingly, the double detection happens with a higher probability. This bunching is explained in the equations developed in [81].

We post-process the data by selecting a given delay between the two detection events and use them for the state reconstruction. On figure 6.7, we give the time distribution of the second detection event.

Long time shot noise calibration The calibration of the shot noise is done once before the two-photon acquisition. However, the power of the local oscillator can fluctuate during few hours of experiment. To compensate these fluctuations, we record for each event the level of the local oscillator. Thanks to this information, we can apply the relevant normalization factor of the shot noise to compensate the small fluctuations.

6.3.2 Results

Figure 6.8(a) gives the results obtained for $\Delta t = 0$ (with typically 10,000 quadrature measurements). In this case, only one eigenvalue is above the vacuum level and the corresponding temporal profile is similar to the one obtained previously for the single-photon state or the Schrödinger cat-like state. Figure 6.8(b) gives the associated Wigner function and the diagonal elements of the reconstructed density matrix. To the best of our knowledge, this is the first generation of a two-photon Fock state with a two-photon component around 50% without correction ($49 \pm 1\%$). By taking into account the detection losses, we infer a value as high as $73 \pm 1\%$.

Interestingly, when the time delay Δt is different from zero, the situation becomes very different. A second eigenvalue above the vacuum appears: the two-photon Fock state is continuously split into two single-photon states in a symmetric and an antisymmetric modes. We give in Fig. 6.9(a) and Fig. 6.9(b) the experimental results for $\Delta t = 20$ ns. One can notice that the symmetric mode is not perfectly symmetric. This can be explained by the dark noise being more important on one heralding detector than on the other. This is an example of experimental defaults difficult to take into account into a model. Figure

For instance, if the two events arrive at the same time, this means that the “true” event has a delay of 75 ns, if the delay event is 75 ns earlier this means the two “true” detections have happen at the same time.

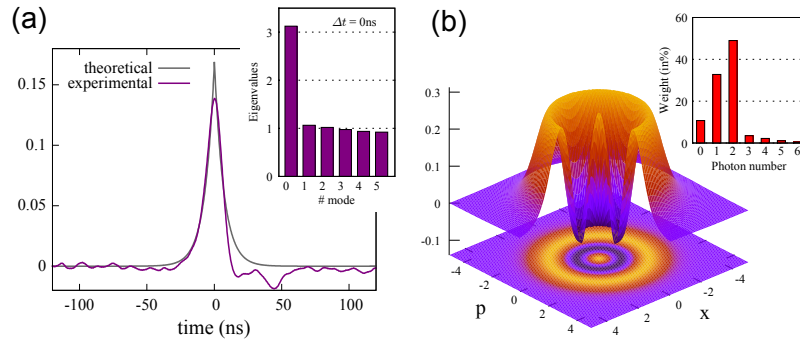


Figure 6.8: (color online). Two-photon Fock state generation with a delay $\Delta t = 0$ between the two heralding events. (a) Eigenvalues of the experimental autocorrelation function and optimal temporal mode. (b) Associated Wigner function. The inset shows the diagonal elements of the density matrix, without correction for detection losses.

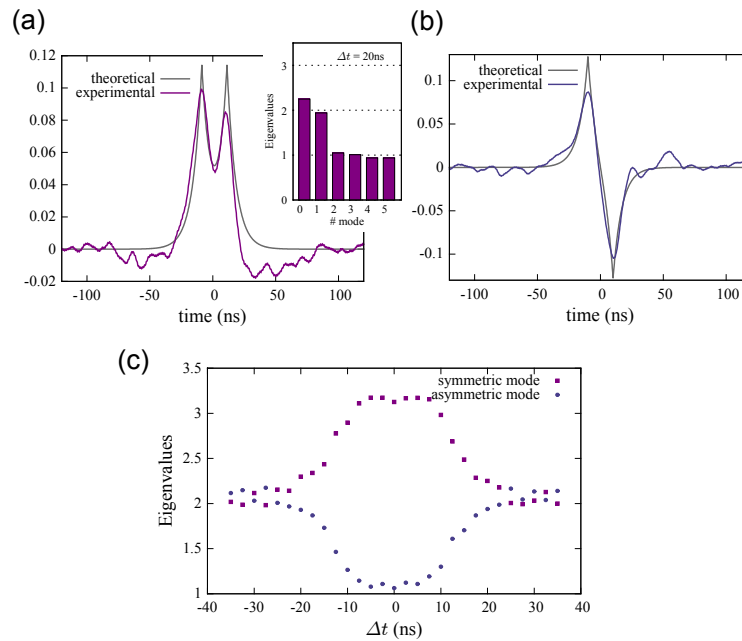


Figure 6.9: Two-photon Fock state generation with a delay Δt between the two heralding events. In this case, two eigenvalues largely above the vacuum ones appear, as shown in the inset. (a) and (b) provide for $\Delta t = 20$ ns the two first eigenmodes, respectively symmetric and antisymmetric. (c) shows the two eigenvalues as a function of the delay. Around $\Delta t = 0$, only the symmetric mode has an eigenvalue distinct from the one of a vacuum mode.

6.9(c) provides the two eigenvalues as a function of the delay Δt . Around $\Delta t = 0$, only the symmetric mode has an eigenvalue distinct from the one of a vacuum mode. Significantly, our method directly provides the exact multimode content of the measured state, and therefore allows us to define an optimal mode.

6.3.3 Temporal mode theory

As before, to compare with a theoretical model, one can use the autocorrelation function defined in Eq.(6.39) and adapt the heralding mode, which now depends on the time separation between the two detection events. For this purpose, we follow the same reasoning as 6.2.3. After two single-photon detections at different times, the corresponding Wigner function is

$$W(x, p) = \frac{1}{C_1} [C_2 + C_3(x_3^2 + p_3^2) + C_4(x_3^2 + p_3^2)^2] e^{-C_5(x_3^2 + p_3^2)}. \quad (6.41)$$

Thereby, the variance is given by

$$\begin{aligned} \langle \hat{x}^2 \rangle &= \iint x^2 W(x, p) dx dp \\ &= \pi \frac{C_2 C_5^2 + 2C_3 C_5 + 6C_4}{2C_1 C_5^4} \\ &= \frac{1}{2} V_{55} + \frac{2V_{15} V_{35} V_{13} + V_{15}^2 (V_{33} - 1) + V_{35}^2 (V_{11} - 1)}{2((V_{11} - 1)(V_{33} - 1) + V_{13}^2)}. \end{aligned}$$

Here, 1 and 2 correspond to the trigger mode of the first subtracted photon at time $t = 0$. As we consider a fast detector, the temporal mode we choose is $\delta(t)$. 3 and 4 correspond to the second subtracting photon with a time delay (respectively to the first one) Δt the temporal mode in this case is $\delta(t - \Delta t)$. Eventually, we identify the autocorrelation function

$$\langle \hat{x}(t) \hat{x}(t') \rangle = \frac{1}{2} \delta(t - t') + \langle \hat{a}_-^\dagger(t) \hat{a}_-(t') \rangle + \frac{\langle \hat{a}_1 \hat{a}_-(t) \rangle \langle \hat{a}_1 \hat{a}_-(t') \rangle}{\langle \hat{a}_1^\dagger \hat{a}_1 \rangle} + \frac{\langle \hat{a}_3 \hat{a}_-(t) \rangle \langle \hat{a}_3 \hat{a}_-(t') \rangle}{\langle \hat{a}_3^\dagger \hat{a}_3 \rangle}. \quad (6.42)$$

In the limit of a low pump power $\epsilon \rightarrow 0$ and by considering two fast detection events separated by a delay Δt , it can be written as:

$$\langle \hat{x}(t) \hat{x}(t') \rangle = \delta(t - t') + 2\Phi(t)\Phi(t') + 2\Phi(t + \Delta t)\Phi(t' + \Delta t), \quad (6.43)$$

where $\Phi(t)$ has been defined earlier in the single-photon case. Like in Eq. (6.40), the first term corresponds to the vacuum, and the others to the heralding. The two main eigenfunctions of this kernel are given by:

$$\Psi_\pm(t) = \frac{1}{N_\pm(\Delta t)} (\Phi(t) \pm \Phi(t + \Delta t)), \quad (6.44)$$

with $N_\pm(\Delta t)$ the normalization factor. All other functions orthogonal to these modes are eigenfunctions for the vacuum. The theoretical profiles are superimposed in Fig. 6.9.

6.4 Conclusion

In conclusion, we have introduced a method to directly access the complete modal content of traveling quantum light states, using raw measurements obtained by homodyning with a continuous-wave local oscillator. This continuous measurement enables a multimode expansion using the autocorrelation function, without making any assumptions on the experimental setup. We provided a detailed study of this method for various quantum state engineering experiments, leading therefore to a very high fidelity state generation. These examples clearly show the efficiency of the procedure to achieve an optimal mode matching taking directly into account all practical aspects. Apart from this crucial aspect, this approach also reveals the single-mode or multimode character of the field states.

Finally, the theoretical temporal mode is in a good agreement with the experimental one. It confirms the good control we have on the generated state: our various engineered quantum states lie within the same temporal mode which makes them “compatible” if we combine both experiments.

Complement: Negativity of the Wigner function

Einstein said that "the most beautiful experience we can have is the mysterious." So why do so many of us try to explain the beauty of music, thus depriving it of its mystery?

LEONARD BERNSTEIN

The negativity of the Wigner function is often called a *signature of non-classicality*. Does it mean that any state with positive Wigner function is *classical*? Yes and no, it depends where we define the boundary. If we call non-classical any state which cannot be described by the classical theory (for instance the Maxwell equations in optics), in this case the vacuum itself is non-classical as it shows some fluctuations. If we call non-classical any state which allows to do some quantum computation, in that case the negativity of the Wigner function is probably a good criteria [68, 116]. Actually it seems difficult to defined a boundary and maybe the better approach is to consider a classification of the states: from the more classical to the more non-classical. However, up to now, no commonly admitted criteria enable such an ordering, a fortiori when we consider multimode states with entanglement and mixed states.

In this complement, we will focus on the main limitation to quantum features in our experimental setup: the optical losses. It is actually a specific case of a broader topic, the *decoherence* phenomenon. Hence, we will go back to the previous experiments in order to draw a more general picture of non-Gaussian state under experimental conditions. Despite the absence of real novelty in the following, our main purpose is to emphasize some properties of the non-Gaussian states too poorly-known or not clearly understood.

Cp.1 Negativity of the conditional states	109
Cp.1.1 Negativity at the origin	109
Cp.1.2 Negativity versus pump	111
Cp.1.3 Losses on Gaussian states	112
Cp.2 Losses and Gaussian operations	113
Cp.3 General negativity bound for losses	114
Cp.4 Conclusion	115

Cp.1 Negativity of the conditional states

In the previous chapters, we have derived some models as a function of the input state; we now go back on to focus on the negativity of the generated state. Here, the term *negativity* refers to the minimal value of the Wigner function.

Cp.1.1 Negativity at the origin

In the chapter about the generation of Schrödinger cat state (chap. 5), we have obtained the equation (5.13) and (5.14) corresponding to an ideal photon subtraction from a Gaussian

state

$$2\pi\sigma_0^2 W_{\text{sp}}(0,0) = -\frac{s_x^{-1} + s_p^{-1} - 2}{s_x + s_p - 2}, \quad (\text{Cp.45})$$

with $s_x = \sigma_x^2/\sigma_0^2$, $s_p = \sigma_p^2/\sigma_0^2$ the normalized quadrature variances of the initial state.

Similarly, we have obtained the equation (4.18) for the generation of single-photon state (chap. 4):

$$2\pi\sigma_0^2 W_{\text{sp}}(0,0) = -\frac{s_+^{-1} + s_-^{-1} - 2}{s_+ + s_- - 2} \cdot \frac{2 + s_+ + s_-}{2 + s_+^{-1} + s_-^{-1}} \cdot \frac{2}{s_+ + s_-}. \quad (\text{Cp.46})$$

Interestingly, both equations have one identical term. Moreover, this term is the only one that can be negative, and thus yield to $W(0,0) < 0$. Furthermore, if the initial state is pure, i.e. $s_x s_p = 1$, we have $W_{\text{cat}} = -1$. This is not the case for the single-photon state, but this is due to the model used for the detector, being not able to resolve the number of photons. The negativity is therefore degraded by the higher photon-numbers as s_+ increases. In the limit of small squeezing, $s_- \approx 1$, we have $W(0,0) = -1$. Nevertheless, we are going to use the cat state generation model afterwards, to detail this specific term.

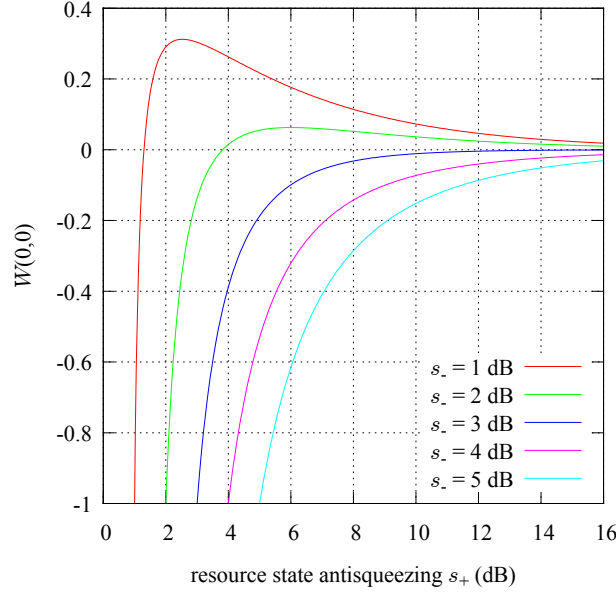


Figure Cp.10: Wigner function of the conditional state as a function of the anti-squeezing for various values of squeezing. For small values of squeezing, the negativity is extremely sensitive to the value of the anti-squeezing. Interestingly, for -3 dB of squeezing and beyond, the state is always negative whatever the anti-squeezing.

On figure Cp.10, we have plotted the value of the Wigner function at the origin versus the values of the anti-squeezing for various value of squeezing. As noted with the equation, when the state is pure i.e. $s_+ s_- = 1$, the conditional state reaches the highest negativity ($2\pi\sigma_0^2 W(0,0) = -1$), but decreases as the anti-squeezing increases and thus the state becomes less pure. However, the value at the origin is always negative when we start from more than 3 dB of squeezing. This can be directly proved from the equation. The condition

of negativity is written $s_-^{-1} - 2 > 0$ for any value of anti-squeezing (i.e. $s_+ > 1/s_-$), this yields to $s_-^{\text{dB}} < -3\text{dB}$ (rigorously $-10 \log_{10}(2)$).

Cp.1.2 Negativity versus pump

In chapter 3, we have studied the state generated by an OPO. Here, we remind the equations of the squeezing/anti-squeezing as a functions of all the different parameters of the OPO

$$s_+(\Omega) = 1 + \eta \frac{4\varepsilon}{(1-\varepsilon)^2 + 4\Omega^2/\Omega_c^2} \quad (\text{Cp.47})$$

$$s_-(\Omega) = 1 - \eta \frac{4\varepsilon}{(1+\varepsilon)^2 + 4\Omega^2/\Omega_c^2} \quad (\text{Cp.48})$$

With

- $\Omega_c = 2\gamma/\tau$ the bandwidth of the cavity,
- $\eta = T_1/(T_1 + L)$ the escape efficiency,
- $\varepsilon = \sqrt{\mathcal{P}/\mathcal{P}_{\text{th}}}$ the strength of pumping relative to the threshold.

According to these equations, the purity of the state decreases with the pump power (s_+ is diverging close to the threshold): the OPO should be thus operated with a pump power as low as possible.

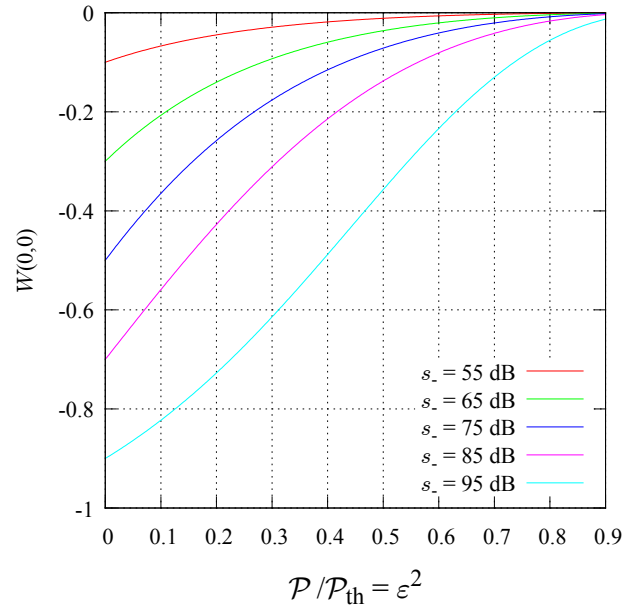


Figure Cp.11: Evolution of the negativity of the conditional state as a function of the pump power. If the pump power increases, the purity of the initial state decreases and thus the negativity decreases too. However, when the pump power goes to 0, the purity goes to 1 but the negativity does not go to -1.

On figure Cp.11, we have plotted $2\pi\sigma_0^2 W(0,0)$ as a function of the pump power of the OPO. As expected, when the pump increases, the purity of the state decreases and thus the

negativity is degraded. However, even in the limit of a zero pump power, which means in the limit of a pure state, we do not converge to a perfect negativity. Indeed, we obtain the limit (with $\varepsilon \rightarrow 0$)

$$2\pi\sigma_0^2 W(0,0) \geq -(2\eta - 1) \quad (\text{Cp.49})$$

Note that hitherto, we have used the model of the cat state generation but actually we have the same limit for the two conditional states (cat and single-photon).

Furthermore, the escape efficiency can be easily inferred (or at least lower bounded). Indeed we have $s_-^{max} = s_-(\Omega = 0, \varepsilon = 1) = 1 - \eta$. Hence, the negativity bound can also be written

$$2\pi\sigma_0^2 W(0,0) \geq 2s_-^{max} - 1. \quad (\text{Cp.50})$$

Finally, the result is not really surprising: if there are some losses, the generated state cannot be perfect. The a priori close to unity purity actually hides this parameter. We can thus conclude that the purity is not a relevant parameter in the case of conditional preparation (at least not enough). An alternative criteria could be the *equivalent losses*. However this will be not always appropriate as all mixed states do not necessarily come from pure states affected by losses.

Cp.1.3 Losses on Gaussian states

If the loss is the key parameter, how can we evaluate it from the variance of a given Gaussian state? Let us consider a Gaussian state with the quadrature variances s_x, s_p . After propagation in a lossy channel, the variances become

$$s'_x = 1 - \eta + \eta s_x, \quad (\text{Cp.51})$$

$$s'_p = 1 - \eta + \eta s_p. \quad (\text{Cp.52})$$

If the initial state is a pure Gaussian state, it saturates the Heisenberg relation i.e. $s_x s_p = 1$. With the previous equations, we obtain

$$\eta = \frac{1 + s'_x s'_p - s'_x - s'_p}{2 - s'_x - s'_p}. \quad (\text{Cp.53})$$

As one can note again, it cannot be expressed as a function of the purity only.

It is also possible to go back to the state before any losses but there is no simple formula as for the Gaussian states. The density matrix after losses can be computed with the following formula

$$\langle m | \hat{\rho}_\eta | n \rangle = \sum_{k=0}^{\infty} B_{m+k,m}(\eta) B_{n+k,n}(\eta) \langle m+k | \hat{\rho}_0 | n+k \rangle. \quad (\text{Cp.54})$$

with

$$B_{n+k,n} = \sqrt{\binom{n+k}{n} \eta^n (1-\eta)^k}. \quad (\text{Cp.55})$$

However, it can be inverted

$$\langle m | \hat{\rho}_0 | n \rangle = \sum_{k=0}^{\infty} B'_{m+k,m}(\eta) B'_{n+k,n}(\eta) \langle m+k | \hat{\rho}_\eta | n+k \rangle. \quad (\text{Cp.56})$$

with

$$B'_{n+k,n} = \sqrt{\binom{n+k}{n} \eta^{-n} (1-1/\eta)^k}. \quad (\text{Cp.57})$$

Nevertheless, in practice, i.e. when a state is reconstructed from a set of measurements, it seems not guaranteed that the state can be corrected for more than 50% of losses [59].

Cp.2 Losses and Gaussian operations

It is usually stated that a quantum state loses its negativity faster as its mean photon-number is high. However, this statement should be understood with caution. We are thus going to illustrate this point in the following.

On figure Cp.12, we can see how the losses degrade the negativity of a non-Gaussian state. Interestingly, in the case of a squeezed single-photon state $\hat{S}|1\rangle$, the negativity decreases faster as the squeezing is high. We can also see a similar behavior on Fock states.

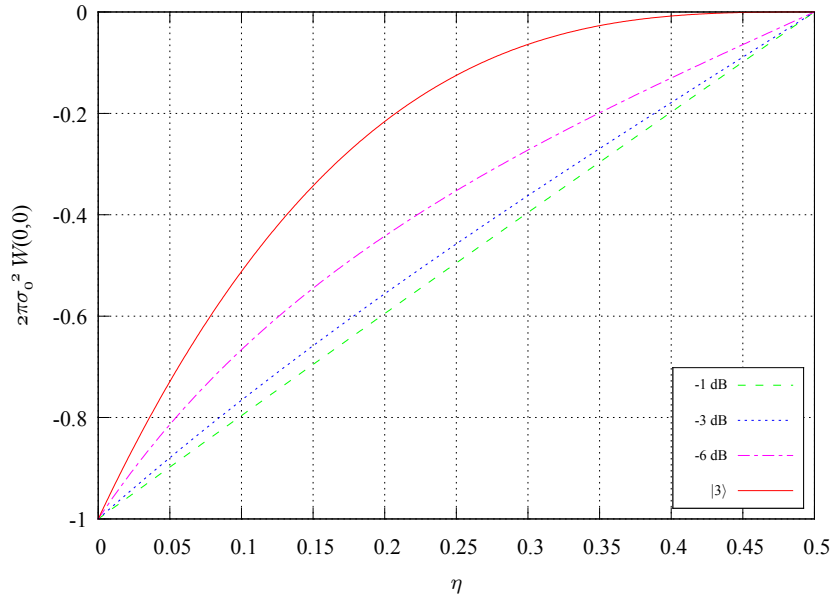


Figure Cp.12: Effect of decoherence on the negativity of a squeezed single photon for various values of squeezing.

Now, one can wonder if the displacement of a state, which increases the mean photon number, will yield to a similar behavior. Let us consider a state first displaced and then impinging on a beam splitter of transmission η , this beam-splitter being actually some losses

$$\hat{B}_\eta \hat{D}_a |\psi\rangle_a |0\rangle_b = \hat{B}_\eta \hat{D}_a (\hat{B}_\eta^\dagger \hat{B}_\eta) |\psi\rangle_a |0\rangle_b . \quad (\text{Cp.58})$$

The action of the beam-splitter on the prior displacement can be written

$$\hat{B}_\eta \hat{D}_a(\alpha) \hat{B}_\eta^\dagger = \exp(\alpha(\sqrt{\eta}\hat{a}^\dagger + \sqrt{1-\eta}\hat{b}^\dagger) - \alpha^*(\sqrt{\eta}\hat{a} + \sqrt{1-\eta}\hat{b})) \quad (\text{Cp.59})$$

$$= \hat{D}_a(\sqrt{\eta}\alpha) \hat{D}_b(\sqrt{1-\eta}\alpha). \quad (\text{Cp.60})$$

We thus obtain

$$\hat{B}_\eta \hat{D}_a(\alpha) |\psi\rangle_a |0\rangle_b = \hat{D}_a(\sqrt{\eta}\alpha) \hat{D}_b(\sqrt{1-\eta}\alpha) \hat{B}_\eta |\psi\rangle_a |0\rangle_b \quad (\text{Cp.61})$$

Of course, the mode b being lost its displacement has no importance. This is easy to prove mathematically, being a single mode operator, the displacement can be permuted inside the trace. Thus we obtain the general results

$$\text{Tr}_b \left[\hat{B}_\eta \hat{D}_a(\alpha) (\hat{\rho} \otimes |0\rangle\langle 0|) \hat{D}_a^\dagger(\alpha) \hat{B}_\eta^\dagger \right] = \hat{D}_a(\sqrt{\eta}\alpha) \text{Tr}_b \left[\hat{B}_\eta (\hat{\rho} \otimes |0\rangle\langle 0|) \hat{B}_\eta^\dagger \right] \hat{D}_a^\dagger(\sqrt{\eta}\alpha) \quad (\text{Cp.62})$$

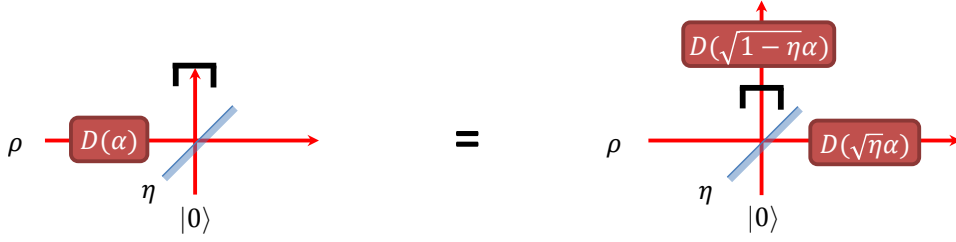


Figure Cp.13: The displacement of amplitude α of any state before a lossy channel of transmission η is perfectly equivalent to a displacement of amplitude $\sqrt{\eta}\alpha$.

In conclusion, any displacement before losses is equivalent to a smaller displacement after the losses, it means that the displacement has no effect on the decoherence and the shape of the Wigner function is the same. Only the value of the mean field changes.

Cp.3 General negativity bound for losses

The previous plot Cp.12 shows another interesting characteristics of the decoherence process. Indeed, in all the previous examples, we can note that the bound of negativity is always reached for 50% of losses. On the other hand, it is also the case for “true” cat states. However, the even cat state is less negative than the odd cat state (in terms of $\min[W(x, p), \mathbb{R}^2]$), but the bound is the same. At first sight we could be tempted to say that this value of the Wigner function is roughly the mean value of the non-Gaussian state and the one of the vacuum state. But more surprisingly, if we consider the qubit $a|0\rangle + b|1\rangle$, the bound is also 50% even if the state exhibit small negative values of the Wigner function, i.e. $1 \gg b \neq 0$.

The 50% bound is actually general for any pure state. The proof has been almost done in [61]. For this, we use the parameterized Wigner function, $W(\alpha, s)$. With $s = 1 - 1/\eta$, we have the Wigner function of any state after a lossy channel of transmission η . When the transmission decreases the parameter s also decreases. For $\eta = 1/2$ we have $s = -1$. The Wigner function of the state after losses is equal to the Q function of the state (without losses). Or, the Q function is everywhere positive for any state. This proves that after 50% of losses, any state has a positive Wigner function. Now, we want to prove that, for pure non-Gaussian states the negative values of the Wigner function remains until this limit.

Ref. [61] gives the following theorem

If $W(\alpha, s) \geq 0$ for all α and $W(\alpha, s) = 0$ for at least one α_0 , then there is no s' with $s' > s$ and $W(\alpha, s') \geq 0$ for all α

Using a similar demonstration as the Hudson one (via the Hadamard theorem), they show that:

The only pure state with $Q(\alpha) > 0$ (i.e. non zeros) are Gaussian states.

Under our scope of decoherence, this means that the only pure states which have positive Wigner function after $\eta > 1/2$ are Gaussian states. This yields to the final formulation:

Any pure non-Gaussian state still have Wigner function with negative values after a lossy channel of transmission $\eta > 0.5$ but none if $\eta \leq 0.5$.

We have noted, in the models of our experiment, that if we start from squeezing higher than -3 dB, the conditional state will be always negative whatever the value of the anti-squeezing. Actually, -3 dB ensure that the losses are lower than 50%, that is why, thanks to the general bound, we have obtained this result.

Cp.4 Conclusion

This study gives mainly three take-home messages. First, the purity appears to be an irrelevant quantity, at least when conditional operation are involved. Second, the idea that a state is more fragile under decoherence when it is big should be clarified. The “size” to consider is $n' = (\langle \hat{x}^2 \rangle - \langle \hat{x} \rangle^2 + \langle \hat{p}^2 \rangle - \langle \hat{p} \rangle^2 - 2\sigma_0^2)/4\sigma_0^2$. It is important to note that the mean field does not affect the decoherence of any state. However, this is not true for all Gaussian operation as the squeezing can increase the rate of decoherence. Finally, there is a general bound for which the negativity disappears. Interestingly, this bound is the same for any pure non-Gaussian state and the negativity only disappears after the limit (not before). This last statement leads to the conclusion that we can a priori see quantum features like the negativity of the Wigner function, if the system has an overall efficiency above 50%.

Moreover, it leads to a more fundamental question. To the best of our knowledge, the most efficient quantum error correction known today is limited at 50% [30] (it applies to cluster state computation). On the other hand, it is known that pure Gaussian state, and a fortiori mixed state, cannot be used for quantum computing and thus the negativity of the Wigner function is a necessary condition. Does it mean that the negativity of the Wigner function is a sufficient condition for quantum computing [115]?

Part III

Non-Gaussian States in Quantum Information Protocols

7 | Single-Photon Entanglement Witness

Talking about music is like dancing about architecture.

THELONIOUS MONK

Many proposals of quantum network architectures are based on discrete variables. In particular, they allow to share/transfer/teleport some information between two distant sites with the help of single-photon entanglement, i.e. entanglement of the form:

$$\frac{1}{\sqrt{2}} (|1\rangle_A|0\rangle_B + |0\rangle_A|1\rangle_B) . \quad (7.1)$$

Although, this state is easy to produce by impinging a single photon on a 50:50 beam-splitter, it is less obvious to characterize in particular without any a priori assumption on the measured state. In this chapter we study a new single-photon entanglement witness designed for realistic quantum networks [73]. The important feature of this protocol is that it only relies on local homodyne detections, i.e. on continuous quadrature measurements and not on photon counting, and offers significant advantages relative to other detection methods [3, 51]. Indeed, it does not require post-selection and the measurements are operated only locally on the entangled modes, an important feature if applied to large scale networks [46, 101]. Besides, this protocol is an illustration of the promising optical hybrid approach in which we take advantage of the continuous variables and discrete variables: here we witness a discrete variable entanglement with the measurement tools of the continuous variables. Another illustration will be given in Chap.8.

After giving the different motivations, we detail the witness protocol. Then, we investigate two aspects of the proposed witness. First, how sensitive it is to the “level” of entanglement. Secondly, how robust it is to losses, which is one of the main limitations in a network.

We note that this protocol has been developed in the context of the European project *QScale* that we collaborate with the *Group of Applied Physics* (GAP) from Université de Genève to develop this new single-photon entanglement witness. This was well appropriate to the experimental abilities in the laboratory.

7.1	Motivations	120
7.2	Principle	121
7.2.1	Starting idea	121
7.2.2	Suitability for a realistic network	122
7.2.3	Simplification and summary of the protocol	123
7.3	Experiment with different levels of entanglement	125
7.4	Sensitivity to losses	128
7.4.1	Theoretical study	128
7.4.2	Experiment	130
7.5	Conclusion	133

7.1 Motivations

We consider a quantum network in which Alice and Bob share as entanglement resource the single-photon state $(|1\rangle|0\rangle + |0\rangle|1\rangle)/\sqrt{2}$. The question is how one can check the entanglement in the case of a realistic quantum network (ie distant places, lossy channels,...)? Hitherto, there are four prescribed methods to detect single-photon entanglement.

1- post-selective projection The first one converts two copies of a single-photon entangled state into one copy of two-particle entanglement. Starting from entanglement $(|1\rangle_{A_1}|0\rangle_{B_1} + |0\rangle_{A_1}|1\rangle_{B_1}) \otimes (|1\rangle_{A_2}|0\rangle_{B_2} + |0\rangle_{A_2}|1\rangle_{B_2})$ between the modes A_1 and B_1 and between A_2 and B_2 , it basically consists of a post-selective projection onto the subspace with one excitation in each location, yielding $|1\rangle_{A_1}|1\rangle_{B_2} + |1\rangle_{A_2}|1\rangle_{B_1}$ [20]. The latter is analogous to conventional polarization or time-bin entanglement and any witness suited for such entanglement, Bell inequality for instance, can thus be used to post-selectively detect single-photon entanglement. Nevertheless, this approach is not fully satisfying conceptually because it relies on post-selection. Furthermore, for practical implementation, the need to create two copies requires twice the number of resources at each node.

2- partial quantum state tomography The second method is based on partial quantum state tomography. Specifically, one can reconstruct a reduced density matrix that corresponds to a projection of the full density matrix into a subspace with at most one photon locally. The presence of entanglement is then inferred from an entanglement measure computed from the reduced density matrix [12]. Specifically, this tomographic approach requires the knowledge of probabilities p_{mn} of having m photons in mode A and n in mode B, where $m, n \in \{0, 1\}$, and the visibility V of the single-photon interference pattern obtained by combining the modes A & B into a beam-splitter. Although it has triggered highly successful experiments [12, 11, 110, 55], this approach presented in Ref. [12] cannot be directly used in large scale networks when one needs to check the entanglement between far away locations, since the knowledge of V relies on a joint measurement of A & B modes. Recombining the two modes is indeed not suitable for a realistic network.

3- Homodyne tomography In principle, a state can be fully characterized by homodyne tomography, and consequently this procedure enables to conclude whether a state is entangled or not [3]. But what is the reliability of the reconstructed state? This is a difficult question and an active topic of research. The main issues are the reconstruction technique, the number of measurements, the choice of quadratures. However, the tomographic approach requires a number of measurements that increases with the dimension of the state being measured [57]. In practice, one could be tempted to make an assumption on the regularity of the measured Wigner function to reduce the number of measurements or, equivalently, on the dimension of the system's Hilbert space, especially when focusing on single-photon entanglement. But this would amount to make an assumption about the system that we want to characterize. One can also estimate the dimension of the state from measurements but it is not clearly established how errors on this estimation can affect the conclusion about the presence of entanglement. More generally, the exponential increase of required measurements with the number of measured subsystems makes the tomography not suited to decide on the presence of entanglement in quantum networks, contrary to entanglement witnesses [32]. Homodyne tomography targets indeed a full information whereas an entanglement witness only tests the presence/absence of entanglement.

4- Local oscillator and photon-counting In 2004 the group of Björk proposed a scheme similar to a two-mode homodyne detection [35, 8]. Instead of using the subtraction of pho-

to currents, they use photon-counting. The rate of coincidence is therefore used as a witness of entanglement. From a general point of view, using photon-counting when the photon detector does not resolve the number of photons will require some assumptions on the measured state at some points. More practically, this is quite impossible in our experiment. Indeed, it would probably require additional filterings and more importantly the quantum efficiency of detectors at our wavelength (and a fortiori at telecom wavelength) are not enough to obtain a reasonable count rate of triple coincidence.

These two last methods are interesting. Indeed, although there are not completely satisfying, they can witness entanglement with local measurements only, in contrast to the two previous ones. Contrary to the polarization entanglement, here, simple photon counting locally is not enough. Hence, the use of a local oscillator as a shared phase-sensitive reference between Alice and Bob and thus can perform phase-sensitive measurements. Therefore it gives access to the relevant information for single-photon entanglement.

7.2 Principle

Although the two-mode homodyne tomography is not suited for an entanglement witness, the involved measurements are however a good way to extract the required information. Specifically, for entangled states like eq. (7.1), it can provide some phase information thanks to the local oscillator. That is why the scheme of homodyne tomography is here rethought in terms of acquisition of information. In other words, the measurement device is the same but the choice of the measurements and the exploitation of their results are different.

The idea of the protocol is first described in the ideal case i.e. when the state is fully described in the qubit subspace $\{|0\rangle, |1\rangle\}$. Then we consider the realistic case of a quantum network by considering typical issues like higher photon-number components and measurement accuracy. Eventually, we give the complete practical summary of the protocol.

7.2.1 Starting idea

When we talk about entanglement, we usually have in mind the well-known Bell-test. It was previously thought for polarization entanglement, but it has been generalized to other degrees of freedom. Here the entanglement concerns the number of photons and the measurements are in the phase space. We thus choose a basis of quadratures instead of polarization, as done in the standard Bell-test.

The idea is thus to apply a Bell-test scenario in the phase space. Alice performs some measurements among two quadratures $\{X, P\}$ while Bob does it in a basis rotated by 45° $\{X + P, X - P\}$. Contrary to the photon-counting measurement used in the standard Bell test, the results of quadrature measurements are continuous. So, in order to obtain some binary outcomes, we consider only the sign of the measurement results (+1 for positive measurement result and -1 for a negative one). Like in a Bell test, Alice and Bob randomly choose their quadrature measurements. With the four different combinations of quadratures, we obtain a measure of the Clauser-Horne-Shimony-Holt (CHSH) polynomial [13]

$$S = E_{X, X+P} + E_{X, X-P} + E_{P, X+P} - E_{P, X-P} , \quad (7.2)$$

where the correlators are defined by

$$E = p(1, 1) + p(-1, -1) - p(1, -1) - p(-1, 1) , \quad (7.3)$$

with $p(i, j)$ the probability that Alice measures i and Bob j simultaneously.

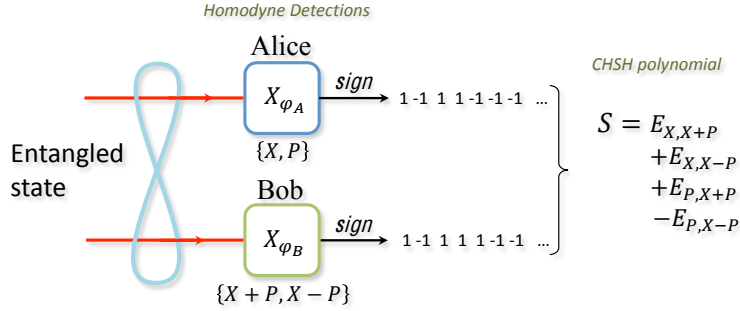


Figure 7.1: Like in a Bell test, Alice and Bob perform some measurements on specific basis but here, it is not on the basis of polarization but in phase space. To obtain some binary outcomes, Alice and Bob only consider the sign of their measurements. By repeating this measurement, they can estimate some correlators for different combinations of quadratures and, at the end, compute a CHSH polynomial.

Sign-binning of homodyne measurement in the qubit subspace $\{|0\rangle, |1\rangle\}$ is equivalent to a noisy spin measurement [94]. For instance, the operator associated with a sign-binned X -measurement corresponds to $\sqrt{2/\pi} \hat{\sigma}_x$ where $\hat{\sigma}_x$ is the standard Pauli matrix. A maximally entangled state, $(|1\rangle|0\rangle + |0\rangle|1\rangle)/\sqrt{2}$, thus leads to $S_{max} = 2\sqrt{2} \cdot 2/\pi \simeq 1.8$, the maximal value that one can obtain using the aforementioned measurements. The proposed witness cannot show any non-locality as the bound to violate in that case is 2, but this is not the purpose of this witness: we only want to conclude about the entanglement.

The question that arises now is the value of the separable bound. It can be demonstrated that the maximal value over the set of all the separable states is equal to $S_{sep} = 2\sqrt{2}/\pi \simeq 0.9$ [99]. A witness above 0.9 enables thus to conclude that the two modes are single-photon entangled.

7.2.2 Suitability for a realistic network

The bound $S_{sep} \simeq 0.9$ corresponds to the separable states limited to the subspace $\{|0\rangle, |1\rangle\}$. In practice, the Hilbert space to consider is larger as the states can contain more than one photon (Fig. 4.9 of Chap. 4). Unfortunately, these higher photon number components can contribute to the value of S and, in some cases, lead to a wrong conclusion by violating the separable bound whereas the state is separable. It is thus necessary to evaluate the separable bound in this larger space.

We need to bound the space of separable states. Indeed, for an infinite size of the Hilbert space, the S parameter for separable states can be as large as for entangled states. The idea is to bound the joint probability that at least one of the two modes contains more than one photon

$$p^* = 2 - p_0^A - p_1^A - p_0^B - p_1^B \geq p(n_A \geq 2 \cup n_B \geq 2), \quad (7.4)$$

with p_n^A the local probability of having n photons in the mode of Alice (idem for Bob). The important point to underline is that this bound is obtained with *local probabilities* only.

A simple way to determine these local probabilities without additional experimental abilities, is to perform a phase-averaged tomography by locally averaging the phase of the local oscillator. Indeed, by averaging the phase, the coherence terms vanish whereas the diagonal elements remain. Moreover, this average of phase is already required in the protocol for the measurements of the correlators. We can thus re-use the same quadrature measurements

to estimate the local photon number probabilities. This can be realized by applying the pattern function¹ as described in [58] (and in section 2.4.4 p.40)

$$p_n = \int d\theta \int_{\mathbb{R}} dx f_{nn}(x) P(x) , \quad (7.5)$$

with P the phase averaged marginal distribution.

Now we can divide a general density matrix like

$$\hat{\rho} = \left(\begin{array}{c|c} \hat{\rho}_{(0,1)^2} & \hat{\rho}_{coh} \\ \hline \hat{\rho}_{coh} & \hat{\rho}_{\geq 2} \end{array} \right) . \quad (7.6)$$

Since $\hat{\rho}_{\geq 2}$ possibly spans a Hilbert space of infinite dimension, there could be an infinite number of coherence terms. However, a few of them give a non-zero contribution to the CHSH polynomial if a phase-averaged homodyne detection is used at each location (random and equally distributed) in such a way that $\langle e^{ik\varphi_{A,B}} \rangle = 0$ with $k \in \mathbb{N}^*$. After simplifications, it can be shown that the CHSH polynomial corresponding to the state (7.6) is (see SI of ref. [73])

$$\begin{aligned} S^{\max} &= \frac{16}{\pi\sqrt{2}} \Re [\langle 01 | \hat{\rho}_{(0,1)^2} | 10 \rangle] \\ &+ \frac{8}{\pi} (\Re [\langle 20 | \hat{\rho}_{coh} | 11 \rangle] + \Re [\langle 02 | \hat{\rho}_{coh} | 11 \rangle]) \\ &+ 2\sqrt{2} p(n_A \geq 2 \cup n_B \geq 2) \end{aligned} \quad (7.7)$$

Fig. 7.2 gives the separable bound as a function of $p(n_A \geq 2 \cup n_B \geq 2)$. This figure mainly illustrate the importance to take into account the part of the state out of the qubit subspace. However, in this numerical optimization no specific constraints have been applied on each local probabilities, only on the global statistics. If we include the specific values of all this local probabilities, we add more information, more constraints on the compatible separable states. This, most of the time, yields to a tighter bound, easier to violate and makes this witness more robust contrary to what could suggest Fig.7.2.

7.2.3 Simplification and summary of the protocol

The fact that it is necessary to average the local phases (i.e. between the state and the two local oscillators) leads to some simplifications. Only the relative phase between Alice and Bob has to be controlled ($\pm\pi/4$ et $\pm 3\pi/4$). Furthermore, for an homodyne measurement, we have $x_\theta = -x_{\theta+\pi}$. Hence, the cases $\pi/4$ (resp. $-\pi/4$) correspond to the same measurements as $-3\pi/4$ (resp. $\pi/4$) with an opposite sign. As a consequence, we only needed to estimate two correlators.

¹ the article [77] use another expression

$$p_n = \int_{\mathbb{R}} dx M_n(x) P(x)$$

$M_n(x) = \sum_{m=0}^n \frac{(-1)^{m+n}}{(2m+1)!!} \binom{n}{m} 2^{2m+1} x^{2m} \Phi(m+1, m+\frac{1}{2}, -x^2)$ with the double factorial $n!! = n(n-2)(n-4)\dots$, $1!! = 1$ et $0!! = 1$, and the confluent hypergeometric function $\Phi(a, b, z) = \sum_{n=0}^{\infty} \frac{(a)_n z^n}{(b)_n n!}$ where $(a)_n = a(a+1)(a+2)\dots(a+n-1)$, $(a)_0 = 1$

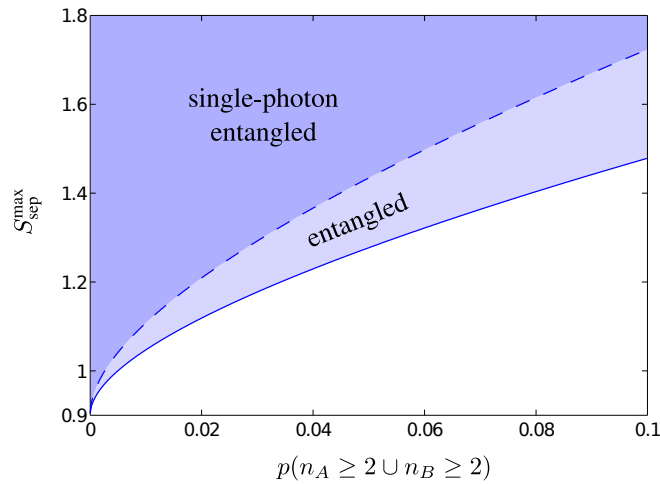


Figure 7.2: Separable bound $S_{\text{sep}}^{\text{max}}$ as a function of the probability that at least one of the two protagonists gets more than one photon $p(n_A \geq 2 \cup n_B \geq 2)$. The dashed curve allows one to know the maximum value of the CHSH polynomial $S_{\text{sep}}^{\text{max}}$ that a state that is separable in the $\{|0\rangle, |1\rangle\}^{\otimes 2}$ subspace can reach. If the observed CHSH value $S_{\text{obs}} > S_{\text{sep}}^{\text{max}}$, one can conclude that the projection of the state in the subspace with zero and one photon locally is entangled. The full curve gives the maximum value that a separable state can reach. If the observed CHSH value is higher than the latter, one can conclude about entanglement but without saying where the entanglement lies.

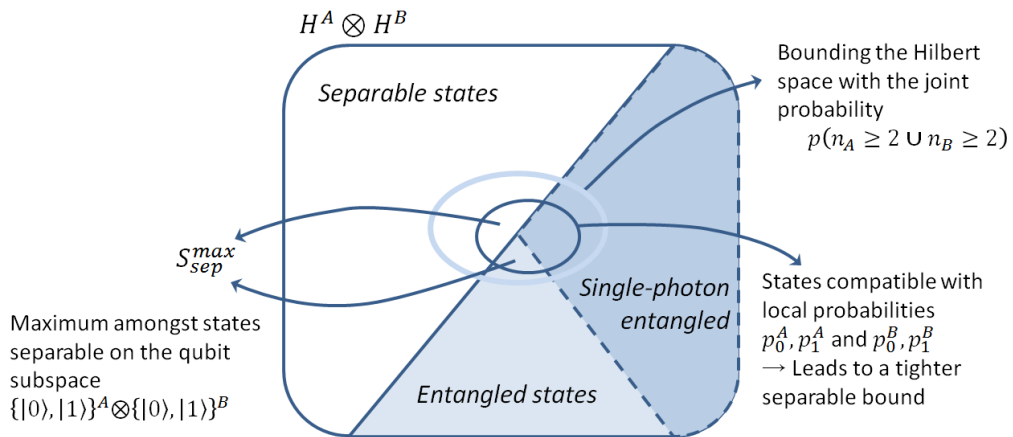


Figure 7.3: The idea of the separable bound calculation can be represented by a picture as above. The two-mode Hilbert space can be divided into two, the separable states and the entangled states. By bounding the joint probability with $p^* \geq p(n_A \leq 2 \cup n_B \leq 2)$, we reduce the space that can be occupied by the measured state. We find the separable bound $S_{\text{sep}}^{\text{max}}$ by maximizing the parameter S over all possible separable states in the bounded space. In order to witness the entanglement specifically in the qubit subspace, we also include in the maximization the states that are separable in the qubit subspace.

In order to make the witness suitable for realistic network, we have modified it compared to the initial idea. Now we can summarize the complete protocol in a practical way as follows.

- Quadrature measurements for two different dephasings between Alice and Bob: $+\pi/4$ and $-\pi/4$ and a local phase-averaging.
- For each phase, we thus have a set of N measurements $\{x_1^A, \dots\}$ for Alice and $\{x_1^B, \dots\}$ for Bob. From these measurements, we can estimate the two correlators

$$E = \frac{1}{N} \sum_{k=1}^N \text{sign}(x_k^A) \cdot \text{sign}(x_k^B) , \quad (7.8)$$

and then the CHSH parameter

$$S = 2E_{+\pi/4} + 2E_{-\pi/4} . \quad (7.9)$$

- With the same quadrature measurements, we can estimate the local photon-number probabilities in the qubit subspace, p_0^A, p_1^A for Alice and p_0^B, p_1^B for Bob

$$p_n = \frac{\pi}{N} \sum_{k=1}^N F_{nn}(x_k) \quad (7.10)$$

with F_{nn} the pattern function defined in section 2.4.4,

- and then the corresponding separable bound $S_{\text{sep}}^{\text{max}}$ can be calculated.

7.3 Experiment with different levels of entanglement

In this first experiment, we would like to test the entanglement witness for different “levels” of entanglement (cf figure 7.4). This is realized by sending a single-photon state on a tunable beam-splitter for different values of the transmission. The single-photon state is produced as described in Chap.4. The tunable beam-splitter is made of a half-wave plate and a polarizing beam-splitter. The state after the beam-splitter is given by

$$\cos(2\theta)|0\rangle_A|1\rangle_B + \sin(2\theta)|1\rangle_A|0\rangle_B , \quad (7.11)$$

where θ is the angle of the half-wave plate².

Choice of the basis For the two homodyne detection measurements, we use the setup already used in [53] mainly for two reasons. First, this scheme allows a passive stability of the relative phase of the local oscillator between the two local oscillators. Secondly, it seems more realistic, for a network, to use both polarizations: one as a quantum channel and the other one to share the local oscillator. This kind of strategies is already used in quantum key distribution protocols [24].

The relative phase is tuned with the help of a quarter-wave plate. If the axis of the quarter-wave plate aligned with the linear polarization of the input beam, the polarization remains the same, if it is turned by 45° the output polarization is circular. The setting of the relative phase is done *manually* by changing the angle of the wave-plates. The behavior of these wave-plates is not perfect and the relative phase is set precisely by monitoring the

²the polarization is turned by an angle 2θ

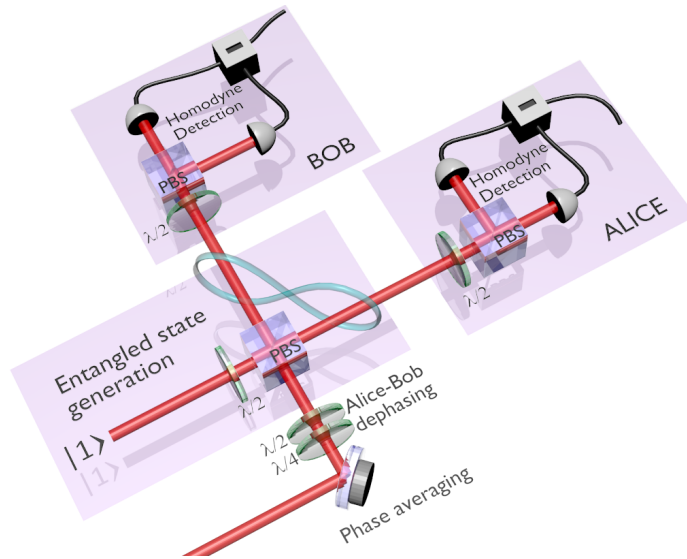


Figure 7.4: Experimental setup. A tunable single-photon entangled state is created by sending a heralded single-photon on a tunable beam-splitter based on a polarizing beam-splitter (PBS) and a half-wave plate ($\lambda/2$). The proposed witness is then tested with two independent homodyne detections (Alice & Bob). The local oscillator is superposed to each modes via the first PBS. Its global phase is swept with a piezoelectric actuator. The relative phase $\Delta\varphi$ is set with a combination of wave plates.

fringes of interference between the seed from the OPO (instead of the single-photon state) and each local oscillators. The relative phase resulting in a delay between the two fringes when swept. We adjust this delay to obtain the desired relative phase.^{3 4} In principle, the choice of basis should be random, but for practical reasons this is not the case here.

Eventually, to average the local phases, a PZT before the polarizing beam-splitter is swept over 2π exactly during the measurement time. This not only makes the local phase random but, above all, makes it equally distributed. Nevertheless, the state we have tested is not sensitive to this specific point, thus we do not expect any issue if this is not well-realized.

Data processing We perform the quadrature measurements by applying a temporal mode to the continuous signal from the homodyne detection (as described in Chap.4). We then perform the two processings required by the protocol. First, we compute the correlators for both relative phases via eq. (7.9) and (7.8), and with the same data we estimate the first two local probabilities with the pattern functions via eq. (7.10). It is important to note that this reconstruction method is preferred to the MaxLik algorithm because, contrary to this latter, it does not require assumption on the size of the Hilbert space. Nevertheless, for a Hilbert space up to 5 photons, the MaxLik algorithm gives the same results.

³The precision of this setting has been mainly inferred by processing the waveform of the two fringes. Some measurement of this kind are included in oscilloscopes softwares but the accuracy of this measurement is difficult to evaluate.

⁴The precise angles for the two wave plates have been found in a “semi-randomly” way: the behavior of the wave-plates being not perfect, the precise setting is found by playing a little bit around the theoretical positions. Nevertheless, by noting the angle of each wave-plates, it is possible to go back to the configuration and obtain a reproducible relative phase.

Error estimation As we want a trustworthy conclusion of entanglement, it is necessary to estimate the different sources of errors due to the experimental imperfections but also statistical estimations. Indeed, the computation of the separable bound consists in maximizing the S parameter with the constraint that the state is PPT. It also takes into account the various errors that we now enumerate.

Firstly, statistical errors affect the measured value of the CHSH polynomial S_{obs} . These errors are estimated in a standard way by using the central limit theorem. They are basically very small (see Table 7.5) because they were deduced from 200,000 results.

Secondly, the accuracy with which the relative phase $\Delta\varphi_{AB}$ between Alice & Bob's measurements is estimated to be 2° . This means that when Alice and Bob choose a measurement settings, the relative phase is not exactly equal to $\pm\pi/4$ as it should be, but $\Delta\varphi_{AB} = \pm\pi/4 + \delta\varphi$ where $-1^\circ \leq \delta\varphi \leq 1^\circ$. This error is taken into account into the separability bound.

Thirdly, errors also affect the local photon-number probabilities, which are estimated using the phase-averaged homodyne measurements [77]. Evaluating these errors is not a trivial task. We use the following method for estimating the overall error. The tomography that we use to access the local photon-number distributions leaves us with the diagonal elements of an estimated density matrix $\rho_{estimate}$. Using this matrix, we simulate the quadrature data, then reconstruct the diagonal elements of a simulated density matrix ρ_{simul} . This matrix is not perfectly equal to $\rho_{estimate}$ for the same reasons than this latter is not exactly equal to the real state. We simulate 200 matrices, always from the same initial state $\rho_{estimate}$. We can thus estimate the errors make on the state reconstruction for each local probability $p_0^A, p_0^B, p_1^A, p_1^B \dots$. The corresponding standard deviations provide $\delta p_0^A, \delta p_0^B, \delta p_1^A, \delta p_1^B \dots$.

angle	Alice						Bob						p^*		S_{obs}		S_{sep}^{max}
	p_0	error	p_1	error	$p>1$	error	p_0	error	p_1	error	$p>1$	error	p^*	error	S_{obs}	error	S_{sep}^{max}
0	99.8	0.1	0.2	0.1	0.01	0.01	30.6	0.2	65.4	0.3	3.94	0.19	3.9	0.262	0.104	0.001	0.235
5	98.9	0.2	1.1	0.2	0.06	0.04	30.6	0.2	65.5	0.3	3.84	0.20	3.9	0.258	0.353	0.003	0.355
10	92.9	0.2	7.0	0.2	0.10	0.06	36.9	0.2	60.4	0.3	2.70	0.18	2.8	0.274	0.776	0.004	0.643
15	83.6	0.2	16.1	0.2	0.32	0.10	45.6	0.2	52.1	0.3	2.28	0.17	2.6	0.294	1.085	0.004	0.893
20	72.3	0.2	27.2	0.3	0.54	0.13	55.5	0.2	43.2	0.3	1.26	0.17	1.8	0.314	1.289	0.004	1.017
22.5	65.0	0.2	34.0	0.3	0.95	0.16	63.1	0.2	35.8	0.3	1.06	0.16	2.0	0.338	1.326	0.004	1.060
25	59.4	0.2	39.3	0.3	1.33	0.17	67.3	0.2	31.8	0.3	0.90	0.13	2.2	0.312	1.330	0.004	1.072
30	48.3	0.2	49.6	0.3	2.17	0.17	78.2	0.2	21.3	0.2	0.47	0.10	2.6	0.292	1.235	0.004	0.989
35	38.8	0.2	58.4	0.3	2.77	0.18	89.5	0.2	10.5	0.2	0.05	0.06	2.8	0.283	0.951	0.004	0.755
40	32.2	0.2	64.2	0.3	3.66	0.20	96.9	0.2	3.1	0.2	0.05	0.04	3.7	0.265	0.527	0.003	0.493
45	30.1	0.2	66.3	0.3	3.59	0.19	99.7	0.1	0.2	0.1	0.02	0.01	3.6	0.224	0.112	0.001	0.233

Figure 7.5: Experimental estimation of local probabilities and their corresponding errors. The measured CHSH polynomial S_{obs} and the separable bound calculated from the local probabilities.

Results We can see on Fig. ?? the results of the witness for different levels of entanglement. For each angle, the separable bound has been numerically calculated. For $\theta = 0$, the state $|0\rangle|1\rangle$ is separable and of course S doesn't violate the bound S_{sep}^{max} . By continuously increasing the angle θ , we increase the entanglement and obtain a violation of the bound. The S parameter goes back below S_{sep}^{max} for the separable state $|1\rangle|0\rangle$ ($\theta = \pi/4$). We obtain the best violation of the bound for the maximally entangled state $(|0\rangle|1\rangle + |1\rangle|0\rangle)/\sqrt{2}$. However, the maximal value is $S = 1.3$, even though the maximal expected value is $S = 1.8$. This is due to the non-perfect single-photon resource and the losses of the homodyne detections. In the next section, we will see how losses can degrade the entanglement and how the witness

behaves in that case.

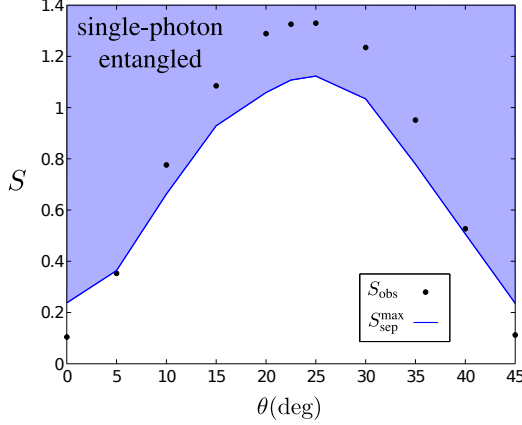


Figure 7.6: Observed CHSH values S_{obs} (the size of the points accounts for the statistical errors) and separable bound $S_{\text{sep}}^{\text{max}}$ as a function of the beam-splitter angle θ . When $S_{\text{obs}} > S_{\text{sep}}^{\text{max}}$, one can conclude that the measured state is entangled.

7.4 Sensitivity to losses

Another important question is the following: is the protocol robust to the losses? Indeed, one of the main issue of quantum networks is the losses which as a consequence limit its range. In this second experiment, we test the witness with some losses on the channels. Two cases can be distinguished, when the losses are symmetric, i.e. the same on both channels, and asymmetric, i.e. one channel is more lossy than the other.

It is thus not obvious to have an intuition of what are the expected results: the losses decrease the value of the parameter S but, in the same time, $S_{\text{sep}}^{\text{max}}$ is also affected as the local probabilities change too.

7.4.1 Theoretical study

For obvious reasons of simplicity, we first study the effect of the losses under the assumption that the state is only in the qubit subspace. The way we study the effect of losses is the following. We first consider the perfect single-photon entanglement of eq. (7.1). Then we calculate the state affected by some losses and then the corresponding S parameter. Secondly, from the corresponding local probabilities, we compute the separable bound and also the maximal value of S . This study is applied to two cases of lossy channels, with symmetric or asymmetric losses.

Bound with local probabilities For any state within the qubit subspace the CHSH parameter S is simply

$$S = \frac{16}{\pi\sqrt{2}} \Re[\langle 01|\hat{\rho}|10\rangle]. \quad (7.12)$$

We consider that the states, separable or not, which can maximize S are of the form (see SI of [12])

$$\hat{\rho} = \begin{pmatrix} p_{00} & 0 & 0 & 0 \\ 0 & p_{01} & d & 0 \\ 0 & d^* & p_{10} & 0 \\ 0 & 0 & 0 & p_{11} \end{pmatrix}. \quad (7.13)$$

This state should verify the following properties:

- $p_0^A = p_{00} + p_{01}$ and $p_0^B = p_{00} + p_{10}$ relationship between joint probabilities and local probabilities,
- $\text{Tr}[\hat{\rho}] = 1$ conservation of probabilities,
- $\hat{\rho} \geq 0$ physical state, all eigenvalues are positive, $p_{01}p_{10} \geq |d|^2$,
- $0 \leq p_{ij} \leq 1$ probabilities.

The maximization of $|d|$ under all these constraints gives the upper bound of S as

$$S^{\max} = \frac{16}{\pi\sqrt{2}} \begin{cases} \sqrt{p_0^A p_0^B} & \text{if } p_0^A + p_0^B \leq 1, \\ \sqrt{(1-p_0^A)(1-p_0^B)} & \text{if } p_0^A + p_0^B \geq 1. \end{cases} \quad (7.14)$$

If now we add the constraint of separability (PPT criterion)

$$\hat{\rho} \text{ is a separable state} \Rightarrow \hat{\rho}^{T_B} \geq 0 \Leftrightarrow |d|^2 \leq p_{00}p_{11} .$$

Once again, the maximization of $|d|$ gives the maximal value of S but this time for the separable states,

$$S_{\text{sep}}^{\max} = \frac{16}{\pi\sqrt{2}} \sqrt{p_0^A p_0^B (1-p_0^A)(1-p_0^B)} , \quad (7.15)$$

which is the separable bound.

Symmetric losses

The case of symmetric losses is equivalent to start with a mixture of vacuum and single-photon

$$\eta|1\rangle\langle 1| + (1-\eta)|0\rangle\langle 0| . \quad (7.16)$$

Obviously, the state after a 50:50 beam-splitter is

$$\hat{\rho}_{\text{sym}} = \eta\hat{\rho} + (1-\eta)|0\rangle\langle 0| \otimes |0\rangle\langle 0| \quad (7.17)$$

with $\hat{\rho}$ the ideal state (7.1) when one start from a perfect single-photon state.

To avoid any confusion, we note $S^{\text{Max}} \simeq 1.8$ the maximal value achievable by a maximally entangled state as explained at the beginning of the chapter and S^{\max} the maximal value compatible with the measured local probabilities. We have here the relationship

$$S^{\max} = \eta S^{\text{Max}} . \quad (7.18)$$

After the losses, the local probabilities become

$$p_1^A = p_1^B = \eta/2 . \quad (7.19)$$

Replaced in eq. (7.14), we obtain the maximal value

$$S^{\max} = \frac{16}{\pi\sqrt{2}} \eta/2 , \quad (7.20)$$

In this case, the single-photon entangled state (7.1) maximizes the parameter S (i.e. $S^{\max} = S(\hat{\rho}_\eta)$). Similarly, by replacing the local probabilities in eq. (7.15), we have the corresponding separable bound

$$S_{\text{sep}}^{\max} = \frac{16}{\pi\sqrt{2}} \frac{\eta}{2} (1-\eta/2) . \quad (7.21)$$

Asymmetric losses

We start by considering the ideal single-photon entanglement. We call η_A the transmission efficiency on Alice's channel and naturally η_B for Bob's one. The calculation gives, after propagation through the lossy channels, the state

$$\hat{\rho} = \frac{1}{2} \begin{pmatrix} 2 - \eta_A - \eta_B & 0 & 0 & 0 \\ 0 & \eta_A & \sqrt{\eta_B \eta_A} & 0 \\ 0 & \sqrt{\eta_B \eta_A} & \eta_B & 0 \\ 0 & 0 & 0 & 0 \end{pmatrix}. \quad (7.22)$$

In that case the CHSH polynomial provides the value

$$S(\hat{\rho}) = \frac{16}{\pi\sqrt{2}} \frac{\sqrt{\eta_A \eta_B}}{2}. \quad (7.23)$$

Furthermore, the losses change the local probabilities in

$$p_1^A = \eta_A/2, \quad (7.24)$$

$$p_1^B = \eta_B/2. \quad (7.25)$$

The maximal value of S^{\max} eq.(7.15) is again saturated by the state given in eq.(7.23) and the corresponding separable bound is in that case

$$S_{\text{sep}}^{\max} = \frac{16}{\pi\sqrt{2}} \sqrt{\frac{\eta_A}{2} \frac{\eta_B}{2} (1 - \eta_A/2)(1 - \eta_B/2)}. \quad (7.26)$$

Discussion The two cases are plotted on figure 7.7. One can be tempted to readily conclude that the parameter S is more sensitive to symmetric losses than asymmetric losses as $S_s(\eta) < S_{as}(\eta)$, but this is not relevant. Indeed, the question should be asked as following. The distance between Alice and Bob is fixed, let us call η_{AB} the overall transmission of the channel. The question is where to place the single-photon entanglement source? On Bob side? or in the middle?

These two situations are depicted on figure 7.8. If the source is on Bob side, this is equivalent to take in the model $\eta_A = \eta_{AB}$ and $\eta_B = 1$. If the source is in the middle, we have $\eta_A = \eta_B = \sqrt{\eta_{AB}}$. In order to compare both cases in terms of distance, we use a logarithmic scale (i.e. losses in dB). Indeed, the distance is proportional $AB \propto \log_{10} \eta$. Actually, in both cases, S is the same, but on the other hand the two separable bounds are different.

7.4.2 Experiment

Strategies The first obvious idea, to add some losses on a channel, is to add a variable attenuation (made of a polarizing beam-splitter and a half-wave plate) but, in that case, we introduce some losses in the experiment and we would like to start with a good state. Moreover, the local oscillator and the state being shared in the same spatial-mode but two orthogonal polarizations, the losses will be much more difficult to manage as it could also affect the homodyne detection.

Another possibility was to increase the dark count. Indeed, we increase in that case the vacuum component in the statistical mixture, which is equivalent to some losses. But this method has two drawbacks: first, it only allows to study symmetric losses and secondly, the experiment changes during time. Hence, we do not really study only the effect of

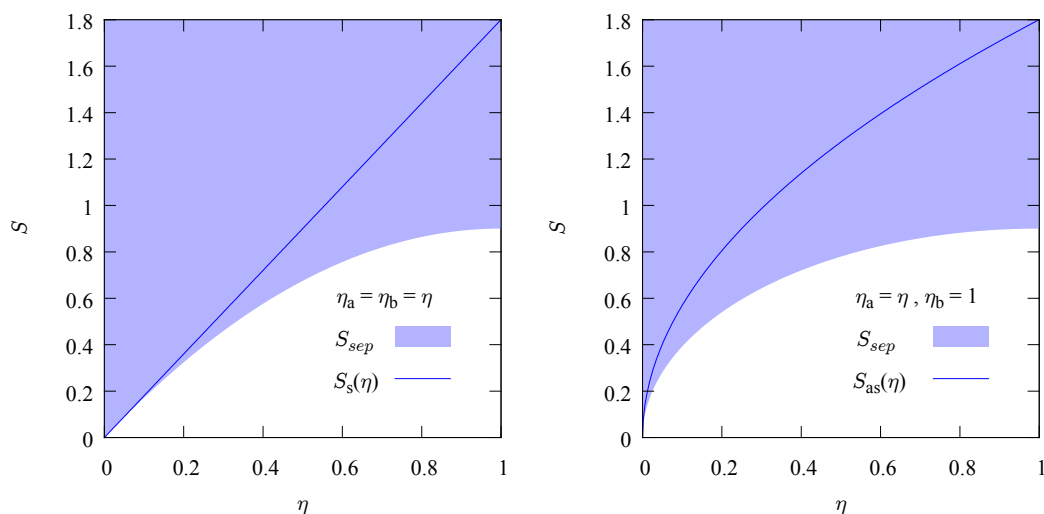


Figure 7.7: S parameter and associated separable bound for different values of the transmission channel. Left: symmetric losses. Right: asymmetric losses.

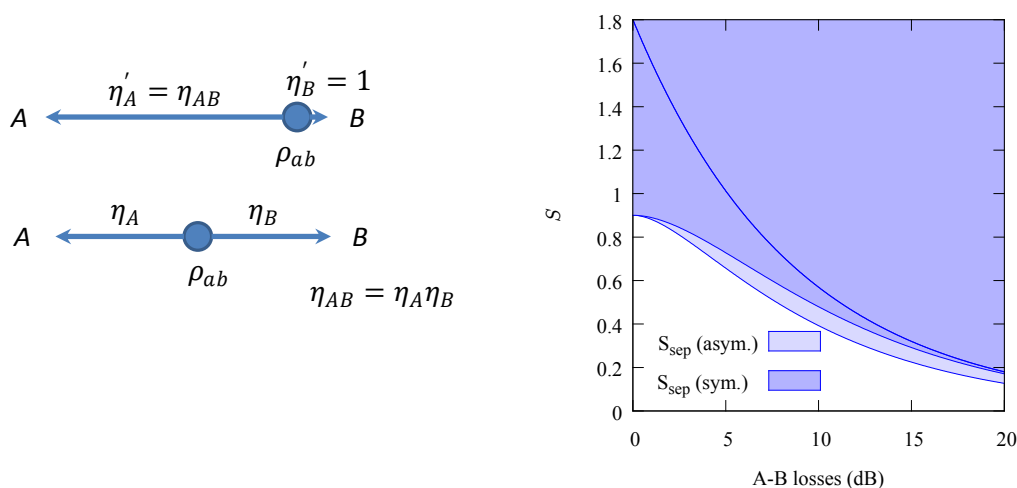


Figure 7.8: For a fixed distance between Alice and Bob, the source of entanglement can be on one site (Bob for instance) or in the middle (left). Depending on this position, losses will not be split in the same way, only the global losses is preserved $\eta_{AB} = \eta_A \eta_B$. It turns out that the measured parameter S is the same whatever the position of the source (right). However, this is not the case for the separable bound, and it is easier to violate the bound with asymmetric losses.

losses.⁵ Moreover, owing to the sensitivity of the separable bound it seems difficult to study the behavior of the witness with losses if, in the same time, the multi-photon components

⁵by increasing the polarization current of the SSPD, we have observed a decrease of the single-photon component and an increase of the vacuum component as expected but, in the same time, an increase of the two-photon component that is, on the other hand, unexpected. This behavior is not explained. The increase of the polarization current increases the quantum efficiency but in the same time the effect of the dark count should be slower. At least, we can expect to see a slower decrease of the two-photon compared to the single-photon.

change. So we have considered another strategy.

Eventually, we have taken advantage of the continuous-wave regime of our homodyne detections. If the temporal mode is not centered on the single-photon mode, there is a temporal mode mismatch, and the other modes being filled by the vacuum state (or a state extremely close with at least 98% of vacuum state), this is equivalent to optical losses. These losses are given by the overlap between the two temporal modes.

$$\eta(\tau) = \int f(t)f(t+\tau)dt = (1 + \gamma|\tau|)e^{-\gamma|\tau|}. \quad (7.27)$$

This strategy has many advantages: we work with exactly the same state, only the losses vary; we can make the losses asymmetric and we can a priori precisely control the value of the losses. Hence, we reuse the previous data in the case of the maximally entangled state and modify the temporal mode.

Results The results of the two situations are plotted on figure 7.9. In order to have a better illustration, we consider the whole losses, with $\eta = \eta_A\eta_B$. We roughly estimate the local losses (in a good approximation) with the local probability $\eta_A = 2p_1^A$ and $\eta_B = 2p_1^B$.

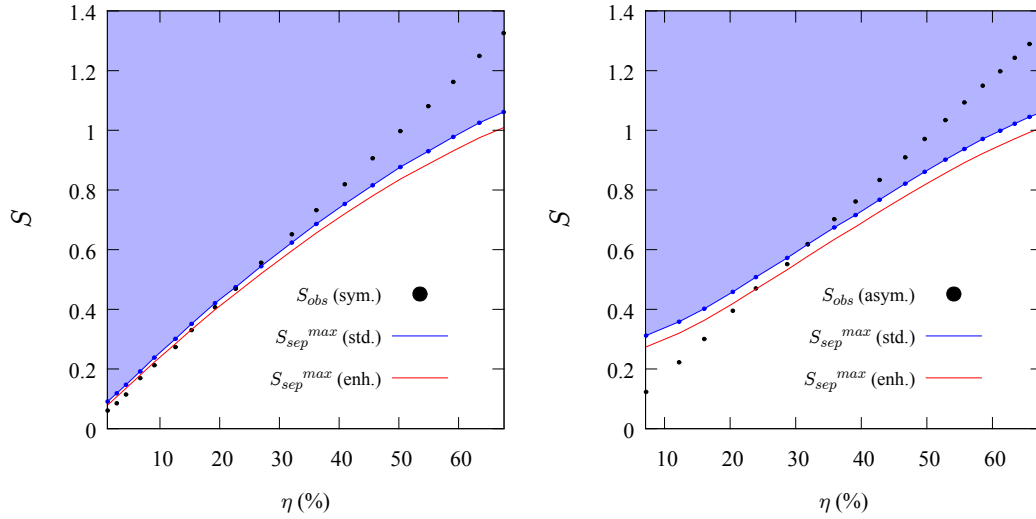


Figure 7.9: Single-photon entanglement witness for various losses. Left: the losses are applied in the same way for both homodyne detections. Right: the losses vary on only one side. For both we give the two separable bounds: the “standard” one based on local probabilities of 0 and 1 photon; and the “enhanced” bound based on the additional local probabilities of two photons.

Surprisingly, the symmetric losses allows to prove the entanglement further than the case of asymmetric, where the theoretical study lets us think that it would be the contrary. However, these results are quite recent and probably require deeper investigations. Indeed, for important value of losses, may be the small defects become less negligible.

7.5 Conclusion

We have presented and experimentally tested a witness for single-photon entanglement. This witness does not need post-selection and uses local measurements only. Moreover, it does not rely on assumptions about the dimension of the measured state. Our work thus brings experiments based on continuous variables into the realm of device independent quantum information processing. Note that our witness can be easily adapted to detect few-photon entanglement without additional complications. We believe that it will naturally find applications in long distance quantum communication, allowing users to check whether two remote nodes of a given quantum network are entangled. One important challenge in this context is to reveal the entanglement shared by a large number of parties. Finding Bell inequalities that could be used as witnesses for multi-partite single-photon entanglement is work for future.

Besides, we have shown that this witness is in the ideal case robust against losses. In the realistic case the range is limited by the photon component outside of the qubit subspace. Nevertheless we have shown that the range of the witness can be extended if we include the knowledge of the two-photon components which actually are the main part of the state outside of the qubit subspace.

To go further in the discussion, we have seen that in principle the witness is robust to any losses, but in practice this is not the case, the only limitation comes from the amount of state out of the qubit subspace. Could we reduce the effect in order to extend the range of the witness? Generally, the part out of the qubit subspace contains mainly some two-photon components. Without additional measurements, it is possible to measure the higher photon-number local probabilities. Therefore, the idea is to include the supplementary local probabilities p_2^A and p_2^B in the optimization of $S_{\text{sep}}^{\text{max}}$. As can be seen on figure 7.9, this additional knowledge makes the bound tighter and thus extends the range for which the bound can be violated.

However, as indicated by the previous theoretical study, as the losses increases, the violation becomes smaller, that is why we do not expect a strong decrease of the bound. Nevertheless, the violation should be always possible. One can thus wonder what is the limitation and how we can improve again this bound. It turns out that the two remaining limitations are the error on the local probabilities and the uncertainty on the phases. Nevertheless, even without any errors the bound is not improved a lot. Actually, the fact that a part of the state is outside of the qubit subspace makes necessarily this witness limited. In conclusion, to extend the range of the witness, the source itself should be enhanced with a lower part out of the qubit subspace.

8 | Hybrid Entanglement

I always think of music as interior decoration. So, if you have all kinds of music, you are fully decorated!

WAYNE SHORTER

The wave-particle duality of light has led to two different encodings for optical quantum information processing [86]. Several approaches have emerged based either on particle-like discrete-variable states [48], e.g. finite-dimensional quantum systems, or on wave-like continuous-variable states [107], e.g. infinite-dimensional systems. Moreover, none seems to be better than the other. Indeed, both have advantages and drawbacks. More interestingly, most of the time, it turns out that the weakness of one corresponds to a strong point for the other. The question that arise is: can we take advantage of both? Can a hybrid system be better?

Here, we demonstrate the first measurement-induced generation of entanglement between optical qubits of these different types, located at distant places and connected by a lossy channel [76]. Such hybrid entanglement, which is a key resource for a variety of recently proposed schemes [113], including quantum cryptography and computing, enables to convert information from one Hilbert space to the other via teleportation and therefore, connect remote quantum processors based upon different encodings. Beyond its fundamental significance for the exploration of entanglement and its possible instantiations, our optical circuit opens the promises for heterogeneous network implementations, where discrete and continuous-variable operations and techniques can be efficiently combined.

In this chapter, we first highlight the interest of hybrid strategy. Next, we describe the protocol for generating hybrid entanglement between field-like and wave-like optical qubits. Then the experiment is described and the obtained results are analyzed. After, we give more details about the the experimental setup. We end with a discussion of possible extensions and improvements.

8.1	Hybrid strategy	136
8.2	Protocol	136
8.2.1	Optical circuit	136
8.2.2	Calculation	138
8.2.3	Phase terms	138
8.3	Experimental demonstration	139
8.3.1	Global setup	139
8.3.2	Results and discussion	139
8.4	Details about the experiment	142
8.4.1	Connecting the two OPOs	143
8.4.2	Control and measurements of the phases	144
8.4.3	Timing	147
8.4.4	Data acquisition and processing	148
8.5	Further discussions	150
8.6	Conclusion	151

8.1 Hybrid strategy

The discrete and the continuous-variable approaches to linear optical quantum computing [96] and quantum communication rely on different physical states for their implementation. The first one involves single-photons [47], and the photonic qubits live in a two-dimensional space spanned for example by orthogonal polarizations or the absence or presence of a single-photon, as expressed by $c_0|0\rangle + c_1|1\rangle$. In the continuous alternative, the encoding is realized in the quadrature components of a light field, in an inherently infinite-dimensional space, and the qubits, also known as *qumodes* [113], can be implemented for instance as arbitrary superpositions of classical light waves with opposite phases [43, 95], $c_0|\alpha\rangle + c_1|-\alpha\rangle$, where $|\alpha\rangle$ is a coherent state with a mean photon number $|\alpha|^2$.

In parallel to the demonstration of groundbreaking experiments with single-photons, coherent state superpositions also spurred a considerable theoretical and experimental activity over the last years as reminiscent of the Schrödinger cat state but also as the main off-line resource for investigating continuous-variable-based protocols as seen in chapter 5. Quantum repeater architectures using this paradigm have been proposed [102, 9] and there is now a variety of schemes for quantum computing using such a computational basis, including fault tolerant operations with small amplitude coherent states [60].

Both encodings have their own advantages and drawbacks [90]. Continuous-variables can benefit from unconditional operations, high detection efficiencies, unambiguous state discrimination and more practical interfacing with conventional information technology. It is however well-known that they suffer from a strong sensitivity to losses and intrinsically limited fidelities. On the other side, discrete-variable approaches can achieve close to unity fidelity but usually at the expense of probabilistic implementations. Combining the two, i.e. achieving hybrid architectures, may offer serious advantages [113, 56]. In this endeavor, transferring information between the two encodings is a crucial requirement.

Hence, entangled states between modes using a different encoding are therefore labeled hybrid entanglement. These states are obviously useful resources to connect systems using different encodings.

8.2 Protocol

In contrast to proposals based on a daunting dispersive light-matter interaction [112] or Kerr non-linearities between single-photon and coherent states ([44] and references therein), we have proposed and implement a measurement-induced generation of such an entangled state at a distance. Similar to the Duan-Lukin-Cirac-Zoller protocol in the discrete variable regime [20], or the remote generation of quasi-Bell states in the continuous variable regime [87], our scheme relies on a probabilistic preparation heralded by the detection of a single-photon in an indistinguishable fashion. The fragile components remain local and only single-photons propagate between the two distant nodes. A lossy channel affects in this way the preparation rate but not the fidelity of the resulting state.

8.2.1 Optical circuit

The optical circuit is illustrated in Fig. 6.4a. Alice and Bob (denoted A and B in the following), who are using respectively discrete variable (DV) and continuous-variable (CV) encodings for information processing, are willing to establish hybrid entanglement. In order to establish this inter-node connection, they prepare locally two non-classical light fields: a two-mode squeezed state in the very low gain limit on Alice's side, $|\psi\rangle_{s,i} = |0_s, 0_i\rangle + \lambda|1_s, 1_i\rangle + O(\lambda)$ where s and i stand for the signal and idler modes and a single-mode even

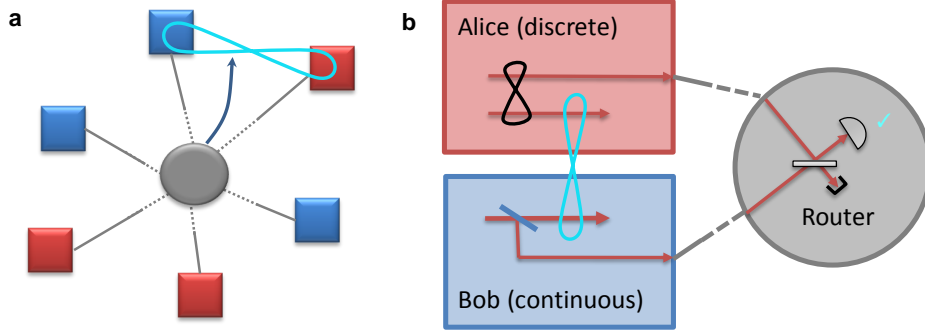


Figure 8.1: Distant nodes of a quantum network can rely on different information encodings, i.e. continuous (CV) or discrete (DV) variables. A Router enables at a distance to establish hybrid entanglement between the nodes. For instance, Alice sends one mode of a weak EPR state $|0\rangle|0\rangle + \lambda|1\rangle|1\rangle$ towards the Router while Bob transmits a small part of a cat state $|\alpha\rangle + |-\alpha\rangle$. The two modes interfere in an indistinguishable fashion on a beam-splitter. Each detection event at the output heralds the generation of qubit-qumode entanglement between Alice and Bob, which can be used for further processing or hybrid teleportation.

cat state on Bob's node, $|\text{cat}_+\rangle = |\alpha\rangle + |-\alpha\rangle$. A small fraction of the cat state is then tapped off and transferred to a router station, where it can be superposed on a tunable beamsplitter, in an indistinguishable way, with the idler mode of Alice's state. Conditioned on the detection of a single-photon at the output, and with a beamsplitter ratio adjusted to balance the two contributions, the resulting state is a maximally entangled state, which in the ideal case can be written as:

$$|\Psi\rangle_{AB} = |0\rangle_A |\text{cat}_-\rangle_B + e^{i\varphi} |1\rangle_A |\text{cat}_+\rangle_B, \quad (8.1)$$

where φ is the overall relative phase for the triggering modes, which can be controlled and adjusted, and $|\text{cat}_-\rangle = |\alpha\rangle - |-\alpha\rangle$ denotes an odd cat state.

This generation procedure can be understood in the following way: a detection event heralds either the subtraction of a single-photon from the even cat state, resulting in a parity change and leaving Alice's signal mode in a thermal state very close to vacuum, or the detection of a single-photon in the idler mode, resulting in projecting the signal into a single-photon state and leaving unchanged the initial cat state. Importantly, the generation process is not affected by the losses in the transfer to the router station as only single-photons propagate.

The resulting entangled state can also be written using for Alice the rotated qubit basis $\{|+\rangle = (|0\rangle + |1\rangle)/\sqrt{2}, |-\rangle = (|0\rangle - |1\rangle)/\sqrt{2}\}$ as:

$$|\Psi\rangle_{AB} = |+\rangle_A |\alpha\rangle_B + e^{i\varphi'} |-\rangle_A |-\alpha\rangle_B. \quad (8.2)$$

This state directly enables the teleportation of a qubit encoded in the $\{|+\rangle, |-\rangle\}$ basis to the coherent state computational basis $\{|\alpha\rangle, |-\alpha\rangle\}$. It also refers to the spirit of the Schrödinger Gedankenexperiment where the two classical states (in the sens of the Wigner function negativity) are entangled with a microscopic degree of freedom. Let us note also that a Hadamard gate, which can be performed with non-gaussian ancilla and projective measurements [67], would enable to convert this state into the state $|0\rangle_A |\alpha\rangle_B + |1\rangle_A |-\alpha\rangle_B$.

8.2.2 Calculation

Let us put in equation this protocol. We tap a small amount of the cat state with a beam-splitter of small reflection. This is written $\hat{B} = e^{\theta(\hat{a}\hat{b}^\dagger - \hat{a}^\dagger\hat{b})} \approx 1 + \theta(\hat{b}^\dagger\hat{a} - \hat{b}\hat{a}^\dagger)$ with $r = \sin\theta \approx \theta \ll 1$. The mode b being vacuum the second term becomes 0. The resulting state is $(1 + \theta\hat{b}^\dagger\hat{a})\hat{S}_a|0\rangle_a|0\rangle_b$. On the other side, the type-II OPO produce a weak EPR state $|0\rangle_c|0\rangle_d + \lambda|1\rangle_c|1\rangle_d$ with $\lambda \ll 1$. The full state is written

$$(1 + \theta\hat{b}^\dagger\hat{a})(1 + \lambda\hat{c}^\dagger\hat{d}^\dagger)|cat_+\rangle_a|0\rangle_b|0\rangle_c|0\rangle_d. \quad (8.3)$$

The mode b and c are mixed on a beam-splitter of transmission t and reflection r in amplitude. We then do the exchange $\hat{b}^\dagger \rightarrow t\hat{b}^\dagger + r\hat{c}^\dagger$ and $\hat{c}^\dagger \rightarrow t\hat{c}^\dagger - r\hat{b}^\dagger$. This yields to

$$(1 + \theta\hat{a}(t\hat{b}^\dagger + r\hat{c}^\dagger))(1 + \lambda\hat{d}^\dagger(t\hat{c}^\dagger - r\hat{b}^\dagger))|cat_+\rangle_a|0\rangle_b|0\rangle_c|0\rangle_d. \quad (8.4)$$

By neglecting the second order terms $\lambda\theta$, one obtain:

$$\left[1 + \theta\hat{a}(t\hat{b}^\dagger + r\hat{c}^\dagger) + \lambda\hat{d}^\dagger(t\hat{c}^\dagger - r\hat{b}^\dagger)\right]|cat_+\rangle_a|0\rangle_b|0\rangle_c|0\rangle_d. \quad (8.5)$$

We detect one photon on mode c , the state is then (without normalization)

$$\theta r|0\rangle_d\hat{a}|cat_+\rangle_a|0\rangle_b + \lambda t|1\rangle_d|cat_+\rangle_a|0\rangle_b. \quad (8.6)$$

Knowing that $\hat{a}|cat_+\rangle = \alpha|cat_-\rangle$ the state is rewritten as:

$$\theta r|0\rangle_d\alpha|cat_-\rangle_a|0\rangle_b + \lambda t|1\rangle_d|cat_+\rangle_a|0\rangle_b. \quad (8.7)$$

The mode b is not considered anymore and being not entangled with the other modes, it doesn't affect the state on mode a and d . The ratio of the superposition can be adjusted with the reflection of the beam-splitter.

8.2.3 Phase terms

In the previous calculation we did not include the phase, more specifically the effect of propagations. Let us modify this calculation to take them into account.

First, we do not consider the phase of the cat state and we include it in the amplitude α (i.e. $\alpha = e^{i\phi_0}|\alpha\rangle$). Similarly for the EPR state, lets say that λ is possibly a complex number. When the small part of squeezing is tapped on mode b , it then propagates to the second beam-splitter to be mixed with mode c , and similarly the mode c propagates to the beam-splitter too. During this propagation, we have a phase shift given by the Hamiltonian of evolution, in other words $\hat{b}^\dagger \rightarrow e^{i\varphi_I}\hat{b}^\dagger$ and $\hat{a}^\dagger \rightarrow e^{i\varphi_{II}}\hat{c}^\dagger$. Thus, the equation (8.3) becomes

$$(1 + e^{i\varphi_I}\theta\hat{b}^\dagger\hat{a})(1 + e^{i\varphi_{II}}\lambda\hat{c}^\dagger\hat{d}^\dagger)|cat_+\rangle_a|0\rangle_b|0\rangle_c|0\rangle_d. \quad (8.8)$$

This yields at the end to the state

$$\theta r|0\rangle_d\alpha|cat_-\rangle_a|0\rangle_b + e^{i(\varphi_{II}-\varphi_I)}\lambda t|1\rangle_d|cat_+\rangle_a|0\rangle_b. \quad (8.9)$$

Independently of the choice of the two output modes bases, the phase of the superposition can be adjusted by the path lengths of the two mixed modes. This is why this paths should be controlled as well as the phase of the two output states.

8.3 Experimental demonstration

8.3.1 Global setup

In this experiment, we run the single-photon experiment (Chap.4) and the cat experiment (Chap.5) together. On Bob's site, a type-I OPO is used to generate a single-mode squeezed vacuum with 3 dB noise reduction below shot noise level. For $|\alpha|^2 \lesssim 1$, this state has a close to unity fidelity with an even cat state $|\text{cat}_+\rangle$. A small fraction, $R = 3\%$, of the light is tapped off via a beam-splitter. Subtracting a single-photon from this state results in the generation of an odd cat state (cf chapter 5). On Alice's side, the required two-mode squeezed vacuum is generated by a type-II frequency-degenerate OPO. At the output, the orthogonally polarized signal and idler modes are spatially separated via a polarizing beam splitter. The device is operated very far below threshold (around 100 times below) in order to limit the multi-photon component to a few percents (cf chapter 4). The tapped mode and the idler mode are then brought to interfere. Before detection, frequency filtering elements are needed to remove the non-degenerate modes emitted by the OPOs. Finally, the filtered mode is detected by a superconducting single-photon detector (SSPD, Scontel) working at cryogenic temperature. The very low dark noise (below 1Hz) avoids false detection events, a crucial feature to achieve high-fidelity in the state generation.

To achieve entanglement, various parameters have to be strictly controlled. First, the superposed beams must be indistinguishable in all degrees of freedom. This stringent condition requires in particular to match the bandwidth of the two OPOs. Starting from similarly-built OPOs, a fine tuning of the cavity lengths is performed by adjusting the temporal modes in which the conditional states are emitted when operated separately.

Second, the relative phase φ has to be kept constant [111]. The different phases in the experiment are therefore controlled and actively stabilized by using auxiliary weak beams injected into both OPOs. The additional difficulty, compared to when the experiments are run independently, are the different phases to control. In particular, the stability of the relative phase between the two beams from each OPOs on the mixing point should be controlled otherwise the coherence part of the state is lost leading to a statistical mixture of the form $|1\rangle\langle 1| \otimes |\text{cat}_+\rangle\langle \text{cat}_+| + |0\rangle\langle 0| \otimes |\text{cat}_-\rangle\langle \text{cat}_-|$.

Eventually, to realize a two-mode tomography it is necessary to perform pairwise quadrature measurements $(x_I, \theta; x_{II}, \varphi)$ with all possible combinations of the phases θ and φ . We should either control the phases of the local oscillator or measure it. The control is more difficult, that is why we have chosen the option to measure the phases. For this purpose, we will use the information of the interference between the seed and the local oscillator.

8.3.2 Results and discussion

The heralded state $\hat{\rho}$ is characterized by a two-mode quantum tomography performed with two high-efficiency homodyne detections ($\eta = 85\%$), one on each node.

This new kind of hybrid state raises the question of how to represent it in a visual and illustrative manner. Indeed, density matrix is well suited for DV states and Wigner function for CV states. However, whatever the encoding, we consider qubits. Hence, a density matrix in the qubit basis specific to each mode should be appropriate... but the decoherence can be an issue. For the DV qubit, despite decoherence the state stays in the two-dimension basis, but this is not the case for the CV part. Therefore, we have chosen as a convenient representation to display the Wigner functions associated with the reduced density matrices $\langle k|\hat{\rho}|l\rangle$, where $|k\rangle, |l\rangle$ stand for the discrete qubit states. It is worth noting that the sub-matrices are not normalized (which actually would not make sense for the off diagonal matrix). Hence, as for a density matrix, each Wigner function is weighted by their

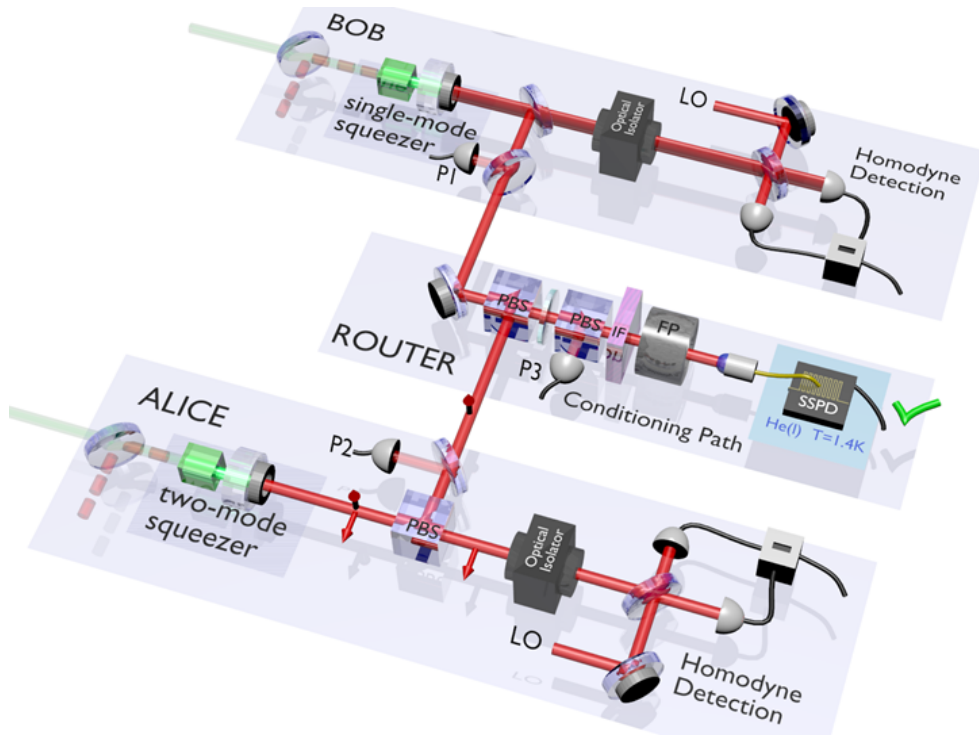


Figure 8.2: Experimental setup. Alice and Bob locally generate the required resources by using continuous-wave optical parametric oscillators operated below threshold. A two-mode squeezer and a single mode-squeezer are used respectively on Alice's and Bob's node. A small fraction of Bob's squeezed vacuum is tapped (3%) and mixed at a central station to the idler beam generated by Alice. The resulting beam is then frequency filtered (conditioning path) and detected by a superconducting single photon detector (SSPD). Given a detection event, which heralds the entanglement generation, the hybrid entangled state is characterized by two high-efficiency homodyne detections. Photodiodes P1, P2 and P3 are used for phase control and stabilization. The beam-splitter ratio in the central station enables to choose the relative weights in the superposition. FP stands for Fabry-Perot cavity, IF for interferential filter, PBS for polarizing beam-splitter and LO for local oscillator.

contribution in the whole state. Moreover, when $k = l$ the reduced matrix is Hermitian thus the corresponding Wigner functions have real values.

The experimental results are given in Fig.8.3a without and with correction for detection losses, for a phase set to $\varphi = \pi$ and a beam-splitter ratio tuned to balance the detection probability from each nodes. The diagonal elements, namely the projection $\langle 0|\hat{\rho}|0\rangle$ and $\langle 1|\hat{\rho}|1\rangle$, correspond respectively to a photon-subtracted squeezed state and to a squeezed state. The non-zero off-diagonal terms witness the coherence of the superposition. The generated state can also be represented using as another projection basis the rotated one $\left\{ |+\rangle = (|0\rangle + |1\rangle)/\sqrt{2}, |-\rangle = (|0\rangle - |1\rangle)/\sqrt{2} \right\}$ (Fig. 8.3b). As it can be clearly seen from the contour plots, the two projections $\langle +|\hat{\rho}|+\rangle$ and $\langle -|\hat{\rho}|-\rangle$ exhibit an opposite displacement in phase space, corresponding with large fidelity to the two states $|\alpha\rangle$ and $|\alpha - \alpha\rangle$. Corrected for detection losses, we obtain a fidelity $77 \pm 3\%$ with the targeted state with $\varphi = \pi$ and

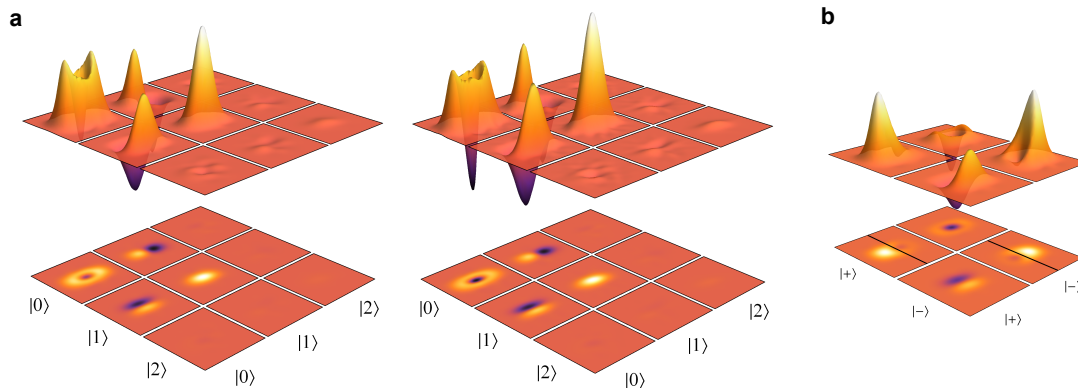


Figure 8.3: Experimental quantum state tomography. The relative phase is set to $\varphi = \pi$ and the beamsplitter ratio in the central station is adjusted to generate a maximally entangled state, i.e. with equal weights. **a**, Wigner functions associated with the reduced density matrices $\langle k|\hat{\rho}|l\rangle$ with $k, l \in \{0, 1\}$, without and with correction for detection losses ($\eta = 85\%$). The components with $k \neq l$ being not Hermitian, the corresponding Wigner functions are not necessarily real, but conjugate. The plot gives therefore the real part for $\langle 0|\hat{\rho}|1\rangle$ (back corner) and the imaginary part for $\langle 1|\hat{\rho}|0\rangle$ (front corner). **b**, Wigner functions associated with the reduced density matrices $\langle k|\hat{\rho}|l\rangle$ with $k, l \in \{+, -\}$, corrected for detection losses.

$|\alpha| = 0.9$.

There are numerous criteria for entanglement, in appendix E we describe few of them. The von Neuman entropy is not relevant in our case because we have mixed states. The concurrence will be not considered either because its generalization to mixed states is not straightforward to compute. To quantitatively assess the generated entanglement, we have computed the negativity [117] given by $\mathcal{N} = (\|\rho^{T_A}\|_1 - 1) / 2$, where T_A stands for the partial transposition. Here, we have used the useful form

$$\mathcal{N}(\hat{\rho}) = \frac{1}{2} \sum_i |\lambda_i| - \lambda_i, \quad (8.10)$$

where λ_i are the eigenvalues of the partial transpose (we could also use the *logarithmic negativity* $E_N(\hat{\rho}) = \log_2 \|\rho^{T_A}\|_1 = \log_2(2\mathcal{N} + 1)$). We remind that for a qubit the maximal value of the negativity is 0.5.

Ideally, the state reaches 0.5 (i.e. maximally-entangled state). Experimentally, $\mathcal{N} = 0.26 \pm 0.01$ is obtained without correction for detection losses and $\mathcal{N} = 0.37 \pm 0.01$ when corrected, demonstrating the hybrid entanglement remotely prepared between the two parties. The heralding rate is equal to 30 kHz, limited by an overall loss in the conditioning path equal to 97%. This lossy channel would be equivalent to 75 km of fiber at telecom wavelength. This value confirms the reliability of our method to establish entanglement connection on long distances.

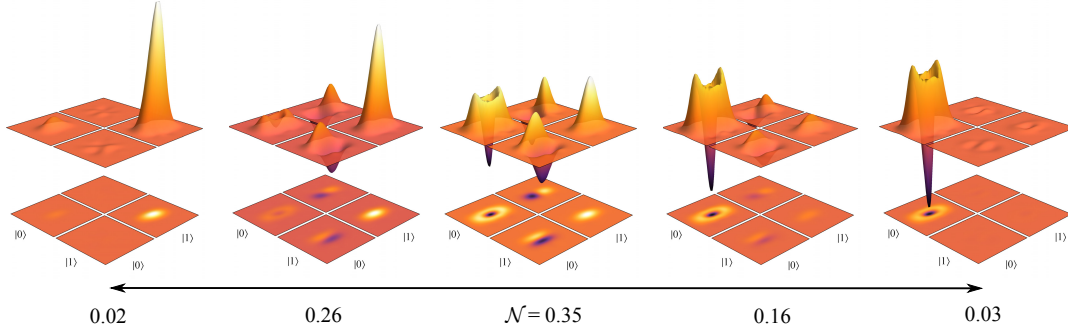


Figure 8.4: Experimental quantum states from separable to maximally entangled. The relative phase is set to $\varphi = 0$ and the beam-splitter ratio at the central station is tuned. The blocks provide the Wigner functions associated with the reduced density matrices $\langle k|\hat{\rho}|l\rangle$ with $k, l \in \{0, 1\}$. For each generated state, the negativity \mathcal{N} is computed, showing the transition from separable to maximally entangled state and back to separable.

The accurate control on the experimental parameters achieved in our implementation also enables the complete engineering of the hybrid state by choosing the relative phase φ and the superposition weights. Figure 8.4 provides the example of states with $\varphi = 0$, i.e. opposite to the one used in Fig.8.3, and for different ratio of the beam-splitter used for the mixing. The two extreme states result indeed from heralding events coming only from Alice’s node or Bob’s node. The figure in the middle provides the balanced case, which is very similar to the one provided in Fig.8.3a but with an opposite phase, as can be seen in the off-diagonal terms. The two other blocks give examples of intermediate ratios, showing the building up of the coherences. The negativity is provided in each case, showing the transition from separability to entanglement and back.

Experimental imperfections can be summarized on both nodes by an effective local efficiency, η_A and η_B , which mostly arises here from transmission losses, finite detection efficiency and escape efficiency of the OPO given by $T/(T + L)$ where T is the transmission of the output coupler and L the intracavity losses. Dark counts are negligible in our experiment. By using the value of the Wigner function at the origin for the states generated independently, these efficiencies are estimated to be $\eta_A = 76 \pm 2\%$ and $\eta_B = 71 \pm 2\%$. These values are in agreement with the observed negative value at the origin of the Wigner function for the odd cat state $\langle 0|\hat{\rho}|0\rangle$ given in Fig. 8.3a, $W_0 = -0.14 \pm 0.01$ (not corrected, ideally -1). Let us note that both local efficiencies contribute in this resulting value. Projecting on Alice’s side translates indeed into adding an extra vacuum contribution on Bob’s side resulting from her non-unity local efficiency. Achieving negativity without correction is thus a difficult task here and constitutes a notable feature of our work.

8.4 Details about the experiment

In this section, we discuss in detail the experimental setup. In particular, how are controlled the various phases, the acquisition of the data etc.

8.4.1 Connecting the two OPOs

The states emitted by the optical parametric oscillators (OPOs) have to be combined in an indistinguishable fashion. To meet this stringent requirement, the two OPOs are built with as close as possible cavity geometry and coupler transmissions. An additional fine tuning is performed for the spectral matching by adjusting the length of the cavities. This tuning is checked by computing the overlap between the reconstructed temporal modes. A value above 99% is obtained, as shown in Fig. 6.5b) (in Chap 6). This value may seem too high but if we make the calculation¹ we find that this matching is not extremely sensitive to the size of the cavities (see figure 8.5).

The two beams are put in the same spatial mode with the help of a polarizing beam-splitter, then a half-wave plate and another polarizing beam-splitter allows us to choose the ratio of the superposition. This ratio can be tuned with the respective count rate from each OPO, the seeds being not proportional to it, we cannot realize it by simply balancing the two seeds.

The two beams are also spatially matched and a visibility equal to 80% is obtained right after the beam-splitter where the modes interfere. However, the subsequent Fabry-Perot cavity in the heralding path as well as the optical fiber towards the detector plays the role of spatial filters. Indeed, only the mode spatially matched with the cavity is transmitted. In other words, the beams impinging on the single-photon detector are the projections in the same spatial mode of the two combined beams. The visibility before this filtering only affects the count rate.

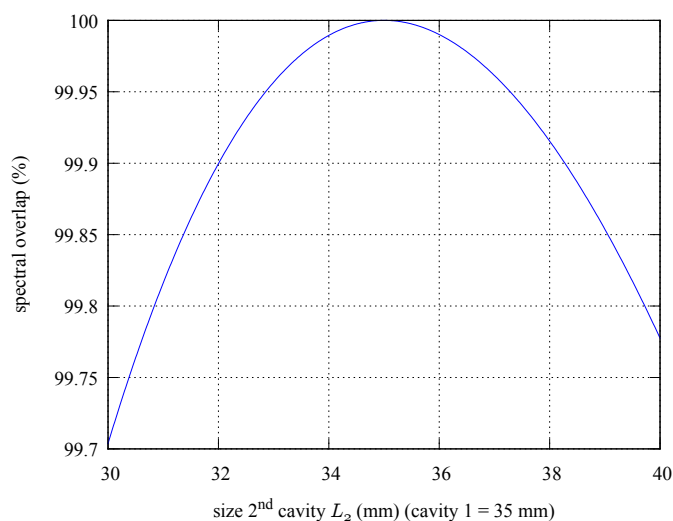


Figure 8.5: Spectral mode-matching. For a OPO cavity of length $L_1 = 35$ mm (and a 10% transmission of the output coupler) we plot the spectral overlap as a function of the second cavity length L_2 .

¹Thanks to Parseval's theorem we have $\int f_1(t)f_2(t)dt = \int f_1(\omega)f_2(\omega)d\omega$. Here we have $\frac{1}{\sqrt{\pi\omega_c}} \frac{1}{1 + (\omega/\omega_c)^2}$ with $\omega_c \propto 1/L$. We thus obtain $\int f_1(t)f_2(t)dt = \int \pi\sqrt{\gamma_1\gamma_2}e^{-\pi(\gamma_1+\gamma_2)|t|}dt = \frac{2\sqrt{\gamma_1/\gamma_2}}{1 + \gamma_1/\gamma_2} = \frac{2\sqrt{L_2/L_1}}{1 + L_2/L_1}$.

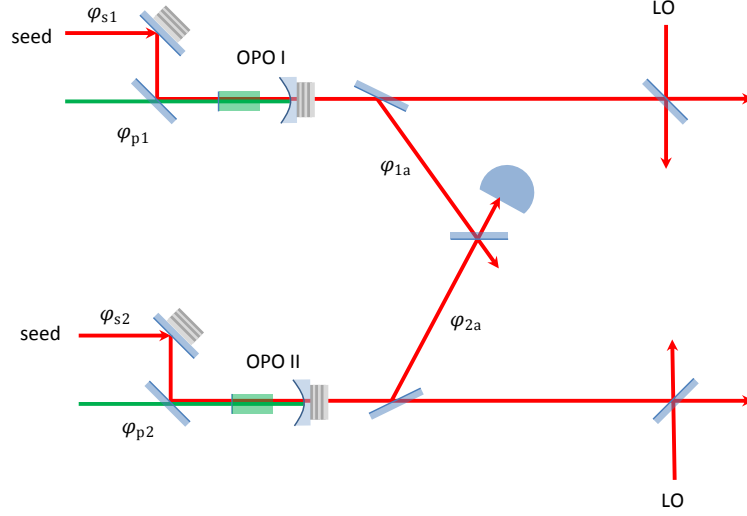


Figure 8.6: Locking of the relative phases.

8.4.2 Control and measurements of the phases

As in the previous experiments, we repeat a two step pattern: one for the measurements and one for the locking of the μ Cavity. Here, we use the time of locking, which is a dead time for the measurements, to also control the different phases. More precisely, during this time, some weak beams (coherent states the so-called seeds) are injected in the different parts of the setup and used as reference to adjust the different path lengths in order to control the relative phase between the two OPOs and the quadrature phases for each homodyne detections.

The various phases involved in the experiment are depicted in Fig. 8.6. After an heralding event, the generated state $|\Psi\rangle_{AB}$ can be in the ideal case written as:

$$|\Psi\rangle_{AB} = |0\rangle_A |\text{cat}_-\rangle_B \pm e^{i\varphi} |1\rangle_A |\text{cat}_+\rangle_B \quad (8.11)$$

where $\varphi = (\phi_{p1} + \phi_{1a}) - (\phi_{p2} + \phi_{2a})$. ϕ_{p1} and ϕ_{p2} are the overall propagation phases determined by the pumps, while ϕ_{1a} and ϕ_{2a} correspond to the phases acquired in propagation from the OPOs to the mixing beam-splitter. To achieve entanglement, φ has to be kept constant [111]. The \pm sign comes from the π phase shift between the two outputs of the beam-splitter. Only one output is used to herald the generation in our experimental implementation.

We actively stabilize the relative phase φ by using auxiliary weak beams injected into the two OPOs. The relative phase can be re-written as $\varphi = \beta_1 - \beta_2 + \xi$ with

$$\beta_i = (\phi_{pi} - \phi_{si}) \quad (8.12)$$

$$\xi = (\phi_{s1} + \phi_{1a}) - (\phi_{s2} + \phi_{2a}) \quad (8.13)$$

β_i represents the relative phase between the pump and the seed, while ξ is the relative phase between the two arms formed by the seeds and their propagations to the beam-splitter.

Another way to approach the problem of phases is to see the experiment in the Fresnel plane. First, a phase is never absolute, it is always defined thanks to a reference. The phase difference between two coherent states is easy to measure with interferences. For the states we consider and, above all, the power of these states, this is impossible. Hence, each seed will be the reference of the homodyne measurement. In other words, these coherent state

will be fixed in their respective Fresnel basis. We thus know the measured quadrature with the interference with the local oscillator. To obtain reliable tomography, we first need to locally fix the phase of the state in the basis of measurement. The state is π periodic so any uncertainty modulo π will be not an issue. Secondly, the two basis should be relatively fixed, in order to measure the quantum nature of the correlations. This is possible by locking the interference of the seeds on a fixed interference level.

All the trick lies in the fact that the propagation phase shift is assumed to be the same for the quantum state and the seeds, which is reasonable for short times.

NB: It was first considered using the pump beams exiting from the two OPOs to lock the different paths. But two problems make this technique not possible. First, the pump beam at 532 nm and the state at 1064 nm are not exactly in the same spatial mode from the output of the OPO and this separation increases through each optical element. This is due to the non-perfect normal incidence of these latter. In any case, even if we could reach a perfect alignment, the thermal fluctuations change the optical path of the two different wavelengths.

Phase reference β_i As depicted on figure 8.7, a weak 1064 nm beam (seed) is injected into each OPO. Owing to the parametric amplification, the amplitude of the beam depends on the relative phase β_i between the pump and the seed. Locking the output beam at a constant intensity level enables to set the phase of the output beam. For this purpose, a small ratio of the seed is tapped locally from the conditioning path and measured with a photodiode (P1 and P2 in Fig. 8.6). We then lock it on a maximum, by using the Dither-and-lock technique.

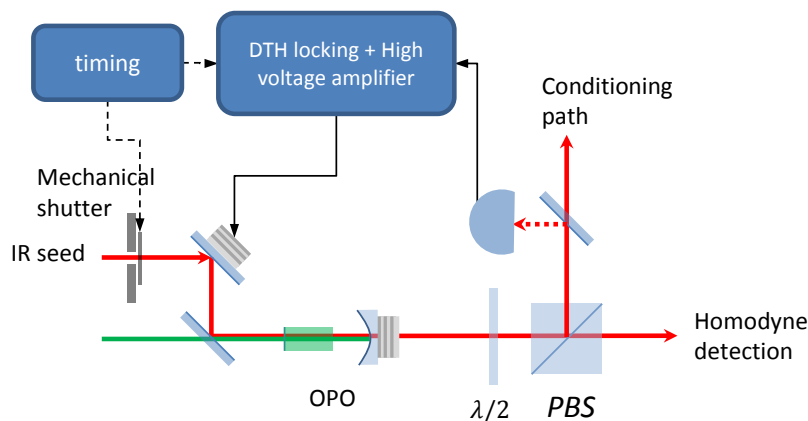


Figure 8.7: A weak IR beam is injected into the OPO (seed) and measured by tapping a small part of it on the conditioning path. The seed is lock in phase with the pump by using the effect of amplification (parametric gain) as the amplitude depends on the relative phase between the pump and the seed. A feed-back on a PZT changes the phase of the seed relatively to the pump. The seed has thus the same phase as the state from the output of the OPO.

Phase of superposition ξ The phase of the superposition ϕ in our state $|1\rangle|cat_+\rangle + e^{i\phi}|0\rangle|cat_-\rangle$ can be defined by the path difference between the two OPOs. (Actually, it is the path difference from the splitting of the two pump beams to the mixing point on the conditioning path.) It is thus necessary to lock it. For this purpose, we lock the phase with the help of the interference between the two seeds (cf fig 8.8).

After combination of the two modes, we lock the relative phase ξ using the interference between the two seeds, as shown in Fig. 8.7. The value of this phase can be chosen by the locking point. This capability enables to engineer the entangled state by choosing the relative phase φ . We note that the ratio of the beam splitter can also be modified to choose the relative weights.

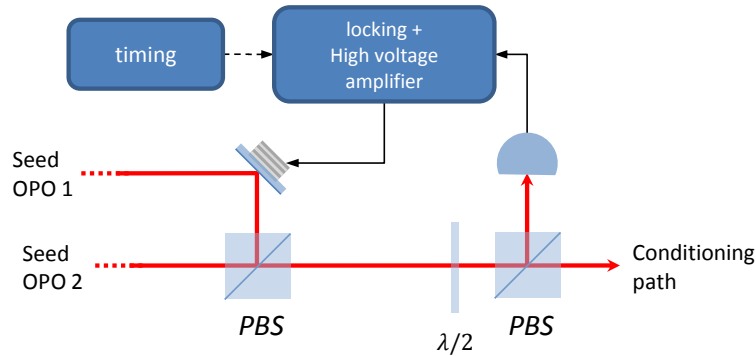


Figure 8.8: The beam from the two OPO are combined into the same spatial mode with a polarizing beam-splitter, they are then mixed with a second polarizing beam-splitter after rotating the polarization with a half-wave plate. This rotation that will define the ratio of the superposition. Thanks to the locking of the seed depicted on Fig. 8.7, the two seeds have the same phase than the states (output of the the two OPO). The interference between the two seeds gives the information of phase difference between the two OPO outputs including propagation up to this “mixing” point. This relative phase is the relative phase of the superposition. We can thus lock this phase by using the interference signal as an error signal.

Local phase The phase of the quadrature measured by the homodyne detection is not controlled: the random nature of the events gives us an homogeneous distribution of phases and we don’t need more for the two-mode tomography. However, failing to control the phase, we need at least to be able to measure it. This is quite easy for the CV part: we can measure the arches of squeezing. But for the DV part, we cannot use this trick. So we use the seed and look at its interference with the local oscillator to infer the phase (the level of the signal is linked to the relative phase between the two beams). Thus, if we know the relationship between the signal and the phase, we can estimate the current phase between two cycles. Unfortunately, the amplitude of the seed is not perfectly stable and, on the other hand, the precision is not the same for all phases. To overcome these two difficulties, the phase of the local oscillator is swept thanks to a PZT and we then fit the resulting signal (fringes of interference pattern) with a sine function. However, the response of the PZT is not linear. We take into account this non-linearity with a second order term ($\sin(at^2 + bt + c)$). a and b are intrinsic to the PZT and do not change when the sweep parameters (speed, voltage, offset) stay unchanged. The parameter c corresponds to the phase drift of the local

oscillator (change of path length by mechanical relaxation) and does not vary extremely fast. Thus, for one tomography, the complete fit is done once, after, only the parameter c is adjusted. Note that the interference is directly measured with the DC signal of the homodyne detection. Besides, this non-linearity also depends on the speed of the sweep. As the phase is also swept during the measurement, it is necessary to use the same sweep during the phase of measurement and during the phase of locking-calibration. As a consequence, it will be the same time duration for both: 50ms of calibration and 50ms of measurement.

NB: We need some quadrature measurements for all the different possible distributions of phase of the two homodyne detections. Due to the good stability of the experiment, the phase drift between the two homodyne detections is extremely slow (typically π after few minutes), the relative phase is thus constant during a too long time. An additional piezo is thus used to artificially create a phase drift.

In order to check the reliability of the lockings and calibration, we have use as a witness the sign correlation of the quadrature measurements $C(\delta\theta) = \langle \text{sign}(\hat{x}_\theta \hat{x}_{\theta+\delta\theta}) \rangle$. It should be a sine function with a phase function of $\delta\theta$. As can be seen in Fig. 8.9, when the phase is not properly locked, we can still observe some fringes due to the passive phase stability of the setup, but the fringes are drifting from one run to the other. When the phase is properly locked, the fringes are at the same position for every run.

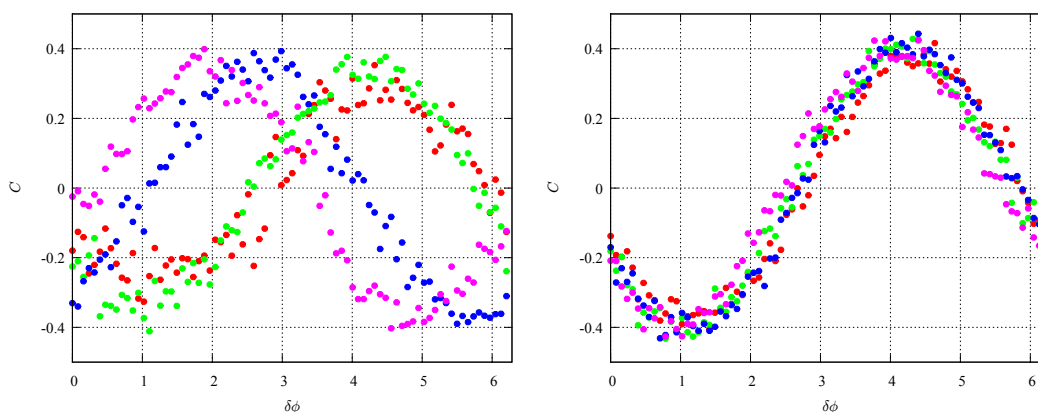


Figure 8.9: Witness of phase locking. On the left, the phase is not properly locked, nevertheless the stability of the experiment allows to see the fringes of correlations. The phase of the fringes drift from one run to the other. On the right the phases have been properly locked indeed the fringes are always at the same place

Improvement of the locking All the lockings here use analogical signals. The changes of phase mainly come from mechanical relaxation. For long optical path the length can change by many wavelengths. In an optical cavity, this is not the case. That is why, here, the piezos are, after a while, often out of range. Two strategies to compensate this problem can be considered. One consists in using piezos with longer range. This will probably increase the time of possible locking but not completely fixed the issue. The other, a priori robust over an unlimited time range, would be to use a numerical locking which is able to jump of 2π to the previous locking point each time the piezo reaches its range limit. This solution is currently investigated.

8.4.3 Timing

The choice of the timing is constrained by the different information/measurements we need. As in all the previous experiments, it is required to lock regularly the μ Cavity and to “freeze” it during the measurement. We thus use this period to also lock and calibrate the different phases. Three phases are locked: the two seeds with parametric gain, and the phase of the superposition. As for the μ Cavity, we use some sampler and holder to “freeze” the lockings during the measurement step and a shutter to turn on and off the seeds. Furthermore, it is important to do each transition step by step. As depicted on figure 8.10, if we start from a

measurement step the transition to the locking phase the transition should be done with the following sequence. First, we close the path to the SSPD, and then the shutter of the seeds is open. We can now release the locking of their phase. It is then possible to release the locking of the superposition and record a sweep of phase for each local oscillator. To do the other transition, i.e. from locking to measurements, we should follow exactly the opposite sequence.

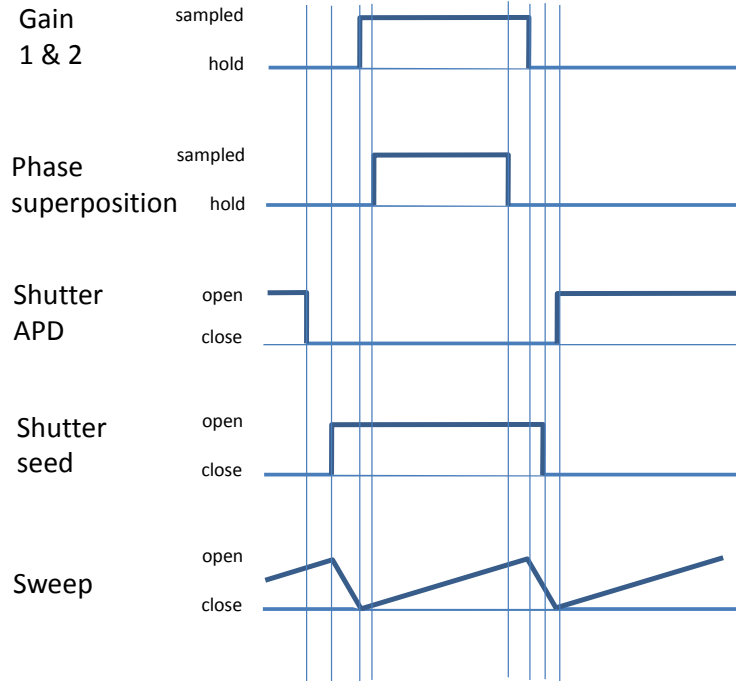


Figure 8.10: Timing of the experiment

The delays between the different steps are adjusted in order to obtain a reliable behavior. For instance, the locking cannot be released until we have an error signal and the error signal cannot be available until the locking beam is blocked.

8.4.4 Data acquisition and processing

We summarize in the following the data acquired on both homodyne detections in order to perform the two mode quantum tomography:

- During the locking/calibration period, for both homodyne detections, we record the fringes of interference and the voltage values on the PZTs. The fittings explained previously provide the relationships between the voltages and the phases $\theta(V_I)$ and $\phi(V_{II})$.
- During the data acquisition, for each heralding events we record the two homodyne signals (200 ns segments). These data are processed with the temporal mode and provide the two quadrature values x_I and x_{II} . We also record the voltages v_I and v_{II} , which are used to obtain the phase of the measured quadrature. We note that the voltage is swept all the time and thus the phase changes during the acquired segment. However, this change is extremely small: indeed, the phase is swept by almost 2π in

50 ms whereas the homodyne window is 200 ns, leading to a negligible phase change of the order of $2\pi 4.10^{-6}$.

In practice, this data corresponds to two different “sizes” of signals triggered by two different events. The short ones correspond to homodyne data and are triggered by the single-photon detector. The long ones correspond to each cycle of measurements and are triggered by the global timing. Therefore, two oscilloscopes are used: one oscilloscope records the “short” signals with a high sampling rate (Lecroy WaveRunner 610Zi) whereas the other records the “long” signals with a low sampling rate (Lecroy WaveSurfer 434). These two oscilloscopes are remotely controlled by a computer via a LAN connection. Contrary to the previous experiments, this time, all the experiment is controlled by a “master” computer. One of the computers included in the oscilloscope could be used as a master computer but this will increase the workload needlessly.

To summarize the different signals recorded by the oscilloscopes. For each single-photon detection event we record:

- homodyne signal from type I,
- homodyne signal from type II,
- piezo voltage (to infer the phases),
- trigger SSPD,
- trigger measurement time.

This oscilloscope is run in “sequence mode”, N detection events are accumulated in the memory of the oscilloscope. For this N events the second oscilloscope records once the different information for the phases:

- DC homodyne I (fringes between seeds and local oscillator),
- DC homodyne II (the same for the other part),
- pzt voltage,
- cycle’s trigger.

One tomography start with the shot noise calibration. Typically 50,000 data points of vacuum state are acquired with each homodyne detection, this gives us access to the normalization factor we should apply to the quadrature measurements.

Next, start the tomography of the state. The goal is to have the quadratures measurements for each heralding event and the corresponding phases. For this purpose, the two oscilloscopes are armed at almost the same time and the number of sequences is adjusted in order to have all the N events in a few numbers of cycles. Indeed, we assume that the calibration of the phase is reliable for few cycles, that is why N is adjusted in function of the rate of events. When the N measurements are completed, all the data are collected to the master computer. Since the data transfer is done, the oscilloscopes triggers are armed again for the next N detection events.

After accumulating typically 200,000 events, the state is reconstructed via the two-mode MaxLik algorithm (see ref.[65] and section 2.4.5).

8.5 Further discussions

Up to now we have been relatively general about the use of this state. Different points have to be addressed in more details.

The first interest, as illustrated by figure 8.1, is the use of hybrid state to connect two differently encoded nodes by using it as a resource for teleportation. An universal teleporter uses a bright EPR state as entangled resource. The first issue is its limitation for long distance. It is necessary to propagate the EPR state between the two nodes and unfortunately this will degrade the state and thus the quality of the teleportation. The advantage of our measurement-induced state is that the distance doesn't affect the entangled state. Secondly, if the state of the sender is teleported to the addressee, this latter has to convert it if using another encoding. The other interest of the hybrid entanglement is that both operations (i.e. teleportation and conversion) are done in the same time. However, it can be seen as conceptually different: here we want to transfer the information encoded in a qubit regardless of the encoding of the sender and the addressee, whereas the universal teleportation transfers a state whatever the state.

The question that one could ask now is how to teleport the state? Actually, various teleportation protocols already exist for each encoding. Interestingly, most of the time, the mode of the receiver is never affected by the nature of its encoding: the possibly required operations are only logic quantum gate. This means that these protocols can be directly reused with our state and choose it depending on the encoding of the sender.

Now, let us consider a situation in which the long distance feature is useless, for instance for a local quantum processor where the different algorithms use different encodings. Actually, the authors of [71] have proposed and demonstrated a qubit conversion between the two encodings (in both direction). To compare, their proposed conversion is deterministic, which is not our case. However, as prelude in the chapter 5, the main weakness of this protocol and of ours lies in the approximation of the squeezed vacuum as an even cat state.

Indeed, as can be seen in Fig.8.3b in the rotated basis, the projected states $\langle +|\hat{\rho}|+\rangle$ and $\langle -|\hat{\rho}|-\rangle$ are not completely round as expected for coherent states. This feature comes from the initial approximation consisting in starting with a squeezed vacuum in the experimental protocol. The maximum achievable fidelity with the targeted hybrid state is therefore 94% in this case. Moreover, starting from a squeezed vacuum within the region of -3 dB, after one and two subtractions leads to odd and even cat with the same α this is less the case for higher squeezing.

To go beyond this demonstrated result in future extensions, Bob can perform a local single-photon subtraction to initially prepare an odd cat state. Furthermore, this procedure would readily enable a larger distance in phase space between the two coherent states, paving the way to the study of squeezing induced micro-macro states [1]. After the non-local subtraction, the fidelity with an even cat state is higher for also a larger amplitude (typically $|\alpha|^2 \approx 1.1$ with a 99% fidelity).

Our optical circuit is well-suited for these operations and provides a platform for subsequent experiments. Higher values of squeezing with high purity will be necessary, and are readily available given our OPO escape efficiency. Furthermore, efficient photon detectors are also required for these cascaded detections however our detector is not efficient enough but some better one can be achieved by the new generation of superconducting devices working in the near infrared [69].

8.6 Conclusion

In summary, we have achieved entanglement between two remote nodes that are using different information encodings. Living in Hilbert space of different dimensionality, the two parties establish heralded qubit-qumode entanglement, which enables for instance to map particle qubits $\{|0\rangle, |1\rangle\}$ onto coherent state wave qubits $\{|\alpha\rangle, |-\alpha\rangle\}$. The work presented here constitutes the first demonstration of such hybrid entanglement enabling to link computational basis of different nature. This possibility, in combination with further works on high-fidelity quantum state engineering, provides a new resource for optical hybrid architecture and quantum network operation based on heterogeneous systems.

Furthermore, we have shown that the weakness of the used approximation can be overcome by a simple additional photon subtraction, which is a temporary technological limitation mainly due to the low quantum efficiency of single-photon detector at our wavelength, and that would be overcome in next years.

In addition, this type of state give rise to some more general questions beyond the quantum information framework. What kind of criteria could highlight the specificity of this state? What fundamental properties have this state compared to the usual states (e.g. $|0\rangle|1\rangle + |1\rangle|0\rangle$ or $|\alpha\rangle|\alpha\rangle + |-\alpha\rangle|-\alpha\rangle$)?

Conclusion

Friends applaud, the comedy is over.

LUDWIG VAN BEETHOVEN

During this work, we have developed two different sources of non-classical optical states: one generating a single-photon state and one generating a Schrödinger cat state. These sources have been used in two different protocols. A first one, using the single-photon state, has provided a proof of principle of a new single-photon entanglement witness. In another experiment we have combined both sources to generate hybrid entanglement between particle-like and wave-like optical qubits.

The single-photon source is the first one based on a degenerate type-II OPO. It allows to understand the different critical points of the conditional preparation technique. This source shows a fidelity as high as 80%, one of the highest value so far [74]. Moreover, the characterization with an auxiliary beam (local oscillator) witnesses the high level of control of the generated state. The same setup has been also used to generate a two-photon Fock state that we use in a deeper study of the temporal mode in which the states are generated.

The Schrödinger cat states have been generated via a single-photon subtraction from a squeezed vacuum state. Being based on an OPO identical to the previous one, except the crystal which is type-I phase-matched, we have obtained, as for the single-photon generation, a high fidelity and thus a strong signature of non-classicality in the sense of the negativity of the Wigner function.

Furthermore, we have studied in detail the temporal aspect of the generated non-Gaussian states and demonstrated an efficient method to extract the temporal mode from the raw measurements of the heralded state [75] without resorting to any a priori model of the system.

From a single-photon state, it is extremely easy to generate single-photon entanglement. However, it is extremely difficult to prove the entanglement by measurements without any assumption on the tested state, in particular in a realistic situation of long distance quantum networks. We have tested a new trustworthy single-photon entanglement witness in various situations, and showed its relevance [73].

The last experiment combines the two sources in order to generate entanglement between two (potentially) distant sites using different encodings [76]. The generated state is useful for long distance heterogeneous quantum networks or processors as it can bridge two nodes using different encodings. Indeed, it can be used as a suitable resource for quantum teleportation between the two. It also addresses further questions about the properties such kind of novel hybrid states.

Future of the experiment

Two experimental limitations have to be addressed: the improvement of the heralding detection losses, i.e. better efficiency and better photon-number resolution, and the overall losses of the setup.

First, thanks to the recent progresses of superconducting single-photon detectors these last years, we can expect an opening of many new possibilities. Indeed, a better efficiency will make possible more cascaded operations. Moreover, if the efficiency is close to unity,

the single-photon detector is also a good detector of vacuum. This will enlarge the feasible protocols.

Secondly, optimizations of the setup are still possible, so far there are no limitations intrinsic to the setup itself. Without going into details, we can give for instance few options. A ring cavity configuration would eliminate the issue of the backscattered light. The quality of the different optics used could be also improved, limiting in this way the loss but also the back scattering of the local oscillator that induced wrong conditioning events.

The stability of the experiment is good however, as its size increases, this stability has to be pushed further. All the lockings of the experiment are based on analog circuits, the next step is to replace or modify them to increase the autonomy of the experiment, for instance with programmable devices for re-locking. Various solutions are already under investigation.

Next challenges

Up to the actual knowledges, the possible technological applications of quantum processing are still far away. However, this last decade has seen tremendous progress on the generation of non-classical quantum states, i.e. non-Gaussian states. More recently, they started to be used in quantum operations. We can actually see that the different building-blocks are demonstrated one by one, and in a more reliable way.

The main difficulty of such experiments remains the control of the quantum systems to preserve it from decoherence. Here an important effort has been done to obtain quantum states of high “quality”. In our setup, the use of a cavity offer a strong advantage as it precisely defines the spatio-temporal mode of the state. In contrast, similar experiments realized with pulsed light using single pass in a non-linear crystal usually suffer from this control of mode. Moreover, it turns out that the control of the modal structure of generated quantum states, more than its knowledge, is of a crucial importance for nowadays and future quantum optics experiments. Indeed, apart from the competitive aspect of having good results, the quality of a quantum state is above all a necessary feature for further applications. Moreover, even some protocols can be insensitive to losses like the dual-rail encoding strategies, these losses turn into probabilistic any operations yielding to the vanish of the calculation speed up induced by quantum mechanics. Nevertheless, the bound of the required “qualities” remains blurred in general, and theoretical investigations on quantum error correction algorithms will probably clarify this problem.

Appendix

A | SSPD and APD

In this experimental work, we have used both an *avalanche photodiode* (APD) and a *superconducting single-photon detector* (SSPD), also called *superconducting nanowire single-photon detector* (SNSPD).

The advantages of the SSPD, compared to the APD, are its low noise (few hertz for the SSPD against 50 Hz or more for the APD) and its quantum efficiency. Our SSPD has indeed a QE of 7% for one detector and 4% for the other, when the APD is at 1.5%. The APD we used is based on Silicon, which is more sensitive to the visible light than the infrared. InGaAs is more sensitive to the infrared (one of the most sensitive) but make it working in the Geiger mode seems challenging at the moment. The quantum efficiency has never reached more than 30%. Nevertheless, this value is better than the two devices we used. Actually, InGaAs is an extremely noisy material and most of the time the dark count is above few kHz, which can be an important issue for our experiments.

One of the disadvantage of the SSPD is the necessity of cryogenic cooling. The detector is operated at 1.4 K by pumping of liquid Helium (expansion). This is why the APD is used first to align the experiment and then, the SSPD is used for the final measurements.

Table A.1: 2013 photon detector features. Some typical values reflecting the performances of each technologies at 1064 nm. For a more detailed review, see [33].

Detector	QE (%)	dark count (Hz)	jitter	dead-time/ max freq	working T°	number resolved
TES	>90	<1	100 ns	1 μ s	100 mK	yes (5)
SSPD Scontel	20	<10	60 ps	1 ns	1.4 K	no
SNSPD NIST/JPL	70 ?	0.1-1k	30 ps	1 ns	100mK- 1.5K?	not (yet?)
APD silicon	1.5-2	20-50	400 ps	100 ns	room T°	no
APD InGaAs	<40	>100	400 ps	>1 μ s	-80 °C	no

Principle of the SSPD The superconducting nanowire meander of typically 4 nm thickness is polarized with a current of few micro amps close to the critical value. By absorbing photon, the superconductivity is broken locally: the current tries then to bypass this hot-spot and this leads to an increase of the current density over the critical value resulting in a complete transition in the normal phase of the nanowire.

This technology is still under development and has progressed extremely fast this last few years. One of the critical issue that has been addressed by labs which work on this technology is the alignment of the fiber on the superconducting meander pattern. Indeed, the cycle of cooling and heating induced mechanical constraints and movements, this yielding to

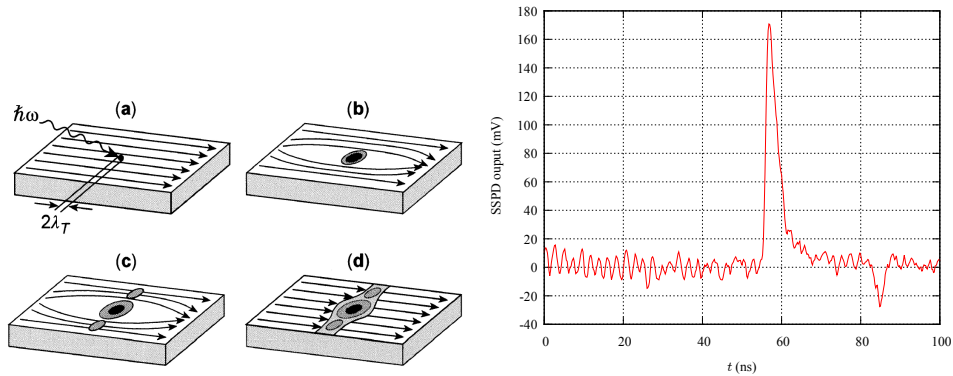


Figure 1.1: Widely used picture (but form unknown origin). Typical measured output signal from SSPD.

a misalignment. Hence, the light do not arrived to the detector and it becomes as inefficient as a Silicon APD. This is typically what happened to our detector during the last four years. The efficiency was at the beginning relatively good but, it decreased by jumps: 20% to 7% after 1 year, 7% to 4% 3 years after.

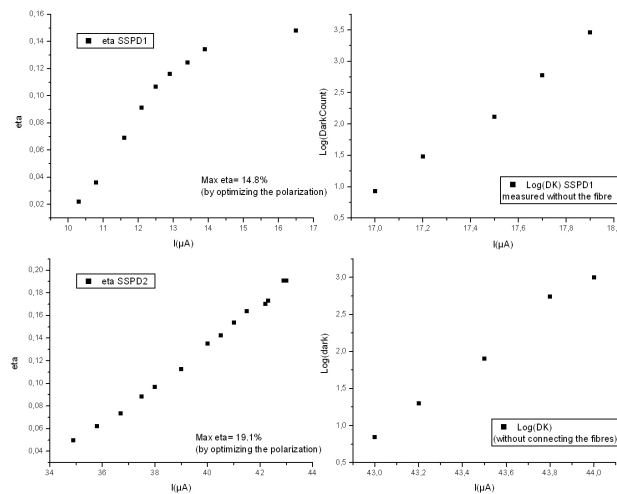


Figure 1.2: overall performance after delivering

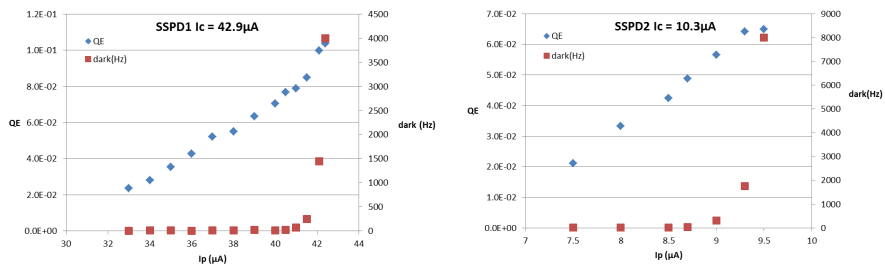


Figure 1.3: Overall performance two years after delivering.

B | Homodyne detection: technical considerations

In this appendix, we study step by step each part of the homodyne detection setup. However, we only consider the continuous regime, which is of interest in our case.

B.1 Introduction	161
B.2 Optics	161
B.2.1 Photodiodes	161
B.2.2 PBS, NPBS, plate BS	162
B.3 Electronics	162
B.3.1 Strategies	162
B.3.2 Model	163
B.3.3 Temporal mode	164
B.3.4 Electronic efficiency	165
B.3.5 Op Amp	165

B.1 Introduction

The model in section 2.3 shows only one defect: the efficiency of the homodyne detection η_{HD} . Below, we detail the contributions of each part of the homodyne detection.

- $\eta_{\text{vis}} = V^2$ efficiency given by the overlap of the spatial modes: the homodyne detection measure the state projected on the mode of the local oscillator, resulting in an efficiency given by the square of the visibility of the interferences [4],
- η_{phot} efficiency of the photodiodes,
- η_{noise} efficiency of the electronics,
- η_{prop} propagation losses.

We note the noise by lower cases. Rigorously, it corresponds to the standard deviations $i_{\gamma} := \sqrt{\langle i_{\gamma}^2 \rangle - \langle i_{\gamma} \rangle^2}$. Moreover, two noises with different origins are not correlated and consequently their variances are summed (and not their standard deviations).

B.2 Optics

B.2.1 Photodiodes

The conversion rate of photons into electrons is written as the ratio between the current generated in the diode (photocurrent) and the input beam power

$$\frac{I_d}{\mathcal{P}_{\text{phot}}} = \frac{e\lambda}{hc}. \quad (2.1)$$

with e the electron charge and $h\nu$ the energy of one photon. For a 1064 nm beam, we expect a response of $0.858 \text{ A}\cdot\text{W}^{-1}$ for a unity quantum efficiency. The response of the photodiode is thus written $R(A/W) = \frac{\eta_{\text{pd}}e}{h\nu}$ with η_{pd} the quantum efficiency of the photodiode.

The inefficiency can have various origins: transparency, absorption, reflection on the air-semiconductor interface. Typically, the transparency is reduced by increasing the thickness of the semi-conductor; and an anti-reflection coating reduces the reflection. However, a possible trick to increase the efficiency, if the main source of inefficiency is the reflection at the interface, is to send back the reflected beam to the photodiode. Nevertheless, in our quantum state engineering experiments, we are very sensitive to the back reflected lights and by doing this, we would generate a lot of other scattering.

B.2.2 PBS, NPBS, plate BS

The homodyne detection can be mounted with different optical elements: with polarizing beam splitter, non-polarizing beam-splitter or plate beam-splitter. The question is which one is the best?

Most of the time, polarizing beam-splitters have a bad transmission. However this defect does not come from neither AR coating nor absorptions. Actually, the missing part of the transmitted polarization is reflected. This yields to two defects: we have some losses on the transmitted polarization, and the reflected part has to be filtered to remove the remaining part of the polarization that should have been transmitted. The other solution consists in finding better PBS. But, most of the time, manufacturers “sacrifice” the transmission to obtain a better rejection of the reflected polarization. Unfortunately, this is not the main concern for our experiments.

The non-polarizing beam-splitter appears to be a reasonable solution but, most of the time, the balancing is obtained by playing on the polarization (the ratio being not the same for s and p polarizations), but this degrade the visibility. Finally, we found that the best strategy is to use plate beam-splitters with a custom coating precisely designed for 50:50 ratio for one polarization (Altechna).

B.3 Electronics

The following study is based on Ref.[38, 37].

B.3.1 Strategies

The subtraction of the photocurrents from the two photodiodes corresponds to the signal of our quantum measurement, the goal is to measure it. The most immediate idea is to use a resistance in order to convert the current into voltage. Unfortunately, the photodiodes have a parasitic capacitance, leading then to a RC filter. The current signal is extremely weak, it is thus relevant to use a high value of resistance but this will reduce the bandwidth of the RC filter. In addition, we will have a thermal noise, which translates into a current noise inside the resistance. This current noise is even lower that the resistance is high. It is thus necessary to have a high resistance to expect that our signal is not lost inside all these noises. An efficient strategy to improve the bandwidth with still the same resistance is to use the well-known *trans-impedance* scheme. Different architectures are possible:

- two separated photodiodes (i.e. an amplification circuit for each). The advantage is that we can easily and independently position the photodiodes. We can also compensate the difference of efficiency by playing with the gain of each circuit.

- Two photodiodes in the same amplification circuit. We intrinsically divide by two the electronics noise but we cannot look at the two signals separately and the beams are more difficult to align.

To separate the high and low frequency there is also two possible strategies: just after the photodiodes or after amplification.

- In the first case, we secure the op amp against any saturation. However, the circuit is more sensitive to the choice of the component, more difficult to model and potentially noisier. Indeed, the noise of the additional component will be amplified and this could be an important issue for our use.
- In the second case, the DC part is amplified by the same gain than the HF part. However, the DC is not used in our measurement as it is removed during the subtraction. Therefore, we are limited here by the saturation of the amp op.

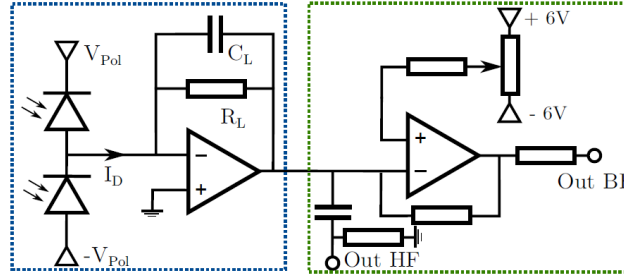


Figure 2.1: Electrical scheme of the homodyne detection.

As we will see below, the trans-impedance circuit is a well-known circuit and can be modeled with high accuracy. However, some other architectures are possible, for instance based on transistor or by combining two op amps with a feedback loop on both. We didn't try these other possibilities, first because these circuits are not well-known and secondly because the circuit we have is satisfying as we will see.

B.3.2 Model

With a reliable model we can estimate what is the best choice of settings for the different components.

The photon noise is $i_{ph} = \sqrt{2eI_d}$ A/ $\sqrt{\text{Hz}}$ with I_d the photo-current. The thermal noise from the resistance is $i_R = \sqrt{4kT/R}$.

Concerning the op amp, the open loop gain (tension) is

$$A_{Vol} = \frac{A_{dc}}{(1 + jf/f_{dom})(1 + jf/f_2)}, \quad (2.2)$$

A_{dc} is the zero frequency gain. The gain bandwidth product (GBWP) corresponds to a frequency for which the gain is equal to one, consequently we have $f_{dom} \approx GBWP/A_{dc}$ which is generally low for AOP with high gain. f_2 allows to take into account the effects from other stages of the op amp. Typically, $4 \cdot GBWP > f_2 > 1.2 \cdot GBWP$. For the LMH6624 amp op, this model is not reliable i.e. does not provide a model consistent with the measurements. However, by using the curves of the datasheet (amplitude and phase of the gain in open loop) the model is closer to the measurements. Finally,

$$Z_m = \frac{A_{Vol}Z_L}{1 + A_{Vol} + j2\pi f C_{pd}Z_L}, \quad (2.3)$$

with the load impedance $Z_L = \frac{1}{j2\pi f C_L + 1/R_L}$.

$$A_{Vcl} = \frac{A_{Vol}}{1 + A_{Vol}/(1 + j2\pi f C_{pd} Z_L)}, \quad (2.4)$$

with the LMH6624 amp op and a resistance of 3 k Ω , the noise of the resistance is comparable to the noise of the amp op and, the signal noise ratio is high. Hence, increasing the resistance beyond this value does not improve a lot.

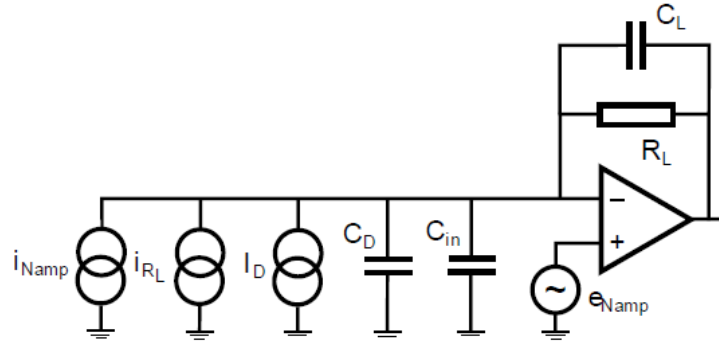


Figure 2.2: Electrical noise of the homodyne detection.

Note that all the current noises are amplified by the same gain, that is why the rising of the electronic noise comes from the voltage noise of the op amp, its amplitude is also linked to the capacity of the photodiodes and the input capacitance of the op amp.

B.3.3 Temporal mode

The temporal mode corresponding to the state we have generated (chap. 4, chap.5, ...) is $\sqrt{\gamma}e^{-\gamma|t|}$ (normalized function). Its Fourier transform (unitary) is $\frac{1}{\sqrt{\gamma}} \frac{2}{1 + (2\pi f/\gamma)^2}$ with $f_c = \gamma/2\pi$ the frequency. This latter corresponds to the half-width at half-maximum (HWHM) whereas the bandwidth, which is the full width at half-maximum (FWHM) is twice the cut-off frequency $BP = \gamma/\pi$.

It is preferable to have a cut-off frequency far from the typical frequency. Indeed, even if the information is not completely lost, it avoids some post-processings of signals which are delicate to do for non-specialists of signal processing (numerical deconvolution).

The bandwidth depending on the parasitic capacitance of the photodiodes, is could be interesting to reduce it. First, by increasing the voltage polarization of the photodiodes we can reduce the parasitic capacitance. However, the polarization we use already decrease it a lot and going further in voltage would not change it a lot. The other possibility is to use photodiodes with smaller sensitive area. However, we did not noticed big differences between the photodiodes of 300 μm large and 500 μm . In principle, we expected a change of bandwidth but, being not the main limitation, to increase the bandwidth we should reduce the other parasitic capacitance.

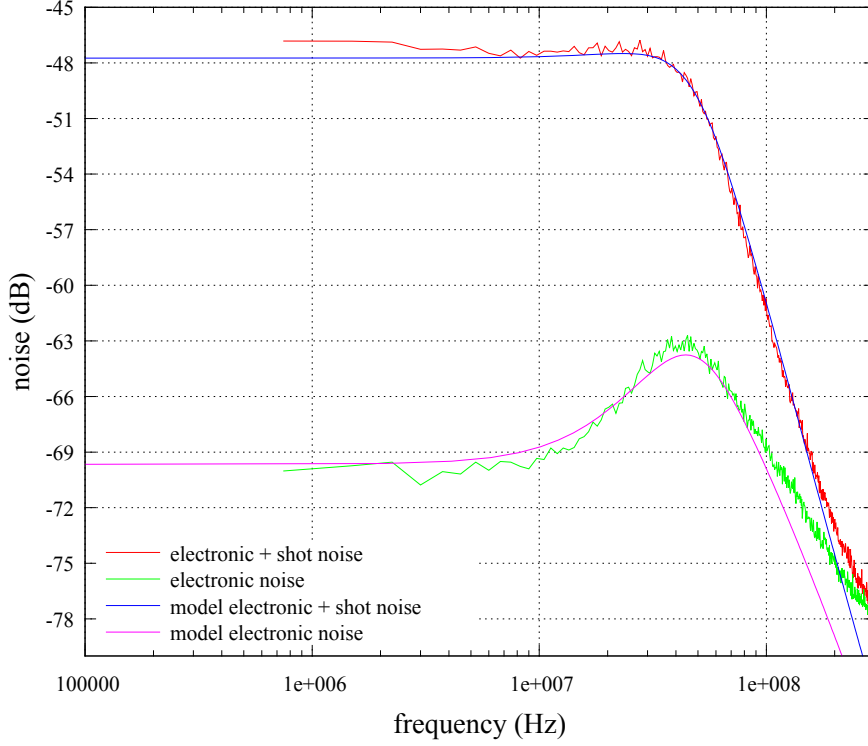


Figure 2.3: We note the the gain is well fitted by the model and that the noise not perfectly in particular the order of the slope at high frequency is not good.

B.3.4 Electronic efficiency

The way to quantify the equivalent efficiency of the homodyne detection when contaminated by noise is detailed in ref. [49]. This equivalent efficiency is equal to

$$\eta_e = 1 - \frac{\langle \hat{Q}_e^2 \rangle}{\langle \hat{Q}_{meas}^2 \rangle}, \quad (2.5)$$

The losses are given by the ratio of the electronic noise contribution by the whole noise. Moreover, these two terms depends on the part of the spectrum we look at. Indeed, if we call $\tilde{\psi}$ the Fourier transform of the temporal mode we want to measure, these two contributions are

$$\langle \hat{Q}_e^2 \rangle = \int S_e(\nu) |\tilde{\psi}(\nu)|^2 d\nu, \quad (2.6)$$

and similarly

$$\langle \hat{Q}_{meas}^2 \rangle = \int S(\nu) |\tilde{\psi}(\nu)|^2 d\nu, \quad (2.7)$$

with S_e the electronic noise spectrum, S the measured spectrum for the vacuum state (which thus also contains the contribution of the electronic noise). S_e and S are directly measurable with a spectrum analyzer.

B.3.5 Op Amp

Concerning the op amp, they are numerous but it seems that only 3 can currently lead to the best performances. First, the AOP847 is not really stable for moderate gains: for a load

resistance of $1\text{ k}\Omega$ we observe some self-oscillations. Moreover, its spectrum is difficult to predict with good accuracy. The one we have mainly use is the LMH6624. It is actually very stable and gives some very “clean” spectrum gain. The upper model is the op amp LMH6626 but this 4 GHz GBWP is under very small CMS package. Realizing circuits with this model requires high quality circuit facilities that we don’t have in the lab. Nevertheless, thanks to the characteristics of this latter op amp, we do not expect a big improvement compared to the LMH6624.

C | Optical cavities

We remind below various useful formula for optical cavities, and more precisely describe the μ Cavity used in the different experiments.

C.1 TEM₀₀ Gaussian beam	167
C.2 Optical cavity	167
C.3 micro-Cavity	168

C.1 TEM₀₀ Gaussian beam

- Intensity profile

$$I(r, z) = I_0(z)e^{-2r^2/w^2(z)} \quad (3.1)$$

- Rayleigh length

$$z_R = \frac{\pi w_0^2}{\lambda} \quad (3.2)$$

- Radius of curvature

$$R(z) = z \left[1 + \left(\frac{\pi w_0^2}{\lambda z} \right)^2 \right] = z \left[1 + \left(\frac{z_R}{z} \right)^2 \right] \quad (3.3)$$

- Beam size

$$w(z) = w_0 \sqrt{1 + \left(\frac{\lambda z}{\pi w_0^2} \right)^2} = w_0 \sqrt{1 + \left(\frac{z}{z_R} \right)^2} \quad (3.4)$$

other useful formula

$$w_0 = \frac{w^2}{1 + \left(\frac{\pi w^2}{\lambda R} \right)^2} \quad (3.5)$$

$$z = \frac{R}{1 + \left(\frac{\lambda R}{\pi w^2} \right)^2} \quad (3.6)$$

C.2 Optical cavity

In the case of low transmission i.e. $T_1 + T_2 + T_3 \ll 1$.

- Finesse

$$\mathcal{F} = \frac{2\pi}{T_1 + T_2 + T_3} \quad (3.7)$$

- Free spectral range

$$\mathcal{I} = \frac{c}{L} \quad (3.8)$$

- bandwidth

$$\Delta = \frac{\mathcal{I}}{\mathcal{F}} = \frac{c(T_1 + T_2 + T_3)}{2\pi L} \quad (3.9)$$

Resonance transmission for high finesse cavity

$$T = \frac{4T_1T_2}{(T_1 + T_2 + T_3)^2} \quad (3.10)$$

We can characterize an optical cavity with the following equations. First we scan the transmission of the cavity with a PZT. We then fit with a lorentzian profile the different peaks of resonance. The fitting will provide the center of the peaks c_{00}^I for the first TEM₀₀ mode, for instance. A_{00} the area of the peak, w_{00} its width

$$\text{rap} = \frac{c_{01}^I - c_{00}^I}{c_{00}^{II} - c_{00}^I} \quad (3.11)$$

$$\mathcal{F} = \frac{c_{00}^{II} - c_{00}^I}{w_{00}^I + w_{00}^{II}} \quad (3.12)$$

$$L = \text{ROC}(1 - \cos^2(\pi \text{rap})) \quad (3.13)$$

$$Cp = \frac{A_{00}^I}{A_{00} + A_{01} + A_{02} + \dots} \quad (3.14)$$

$$\Delta = \frac{c}{L\mathcal{F}} \quad (3.15)$$

$$\mathcal{I} = \frac{c}{L} \quad (3.16)$$

Note that L corresponds to the length of one round-trip in the cavity.

C.3 micro-Cavity

We have explained in chapter 4 the choice of the different parameters of the cavity. Figure 3.1 gives the drawing and a picture of it.

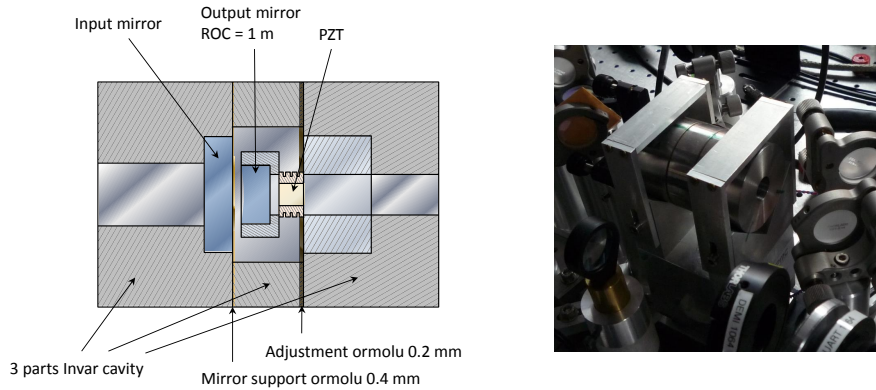


Figure 3.1: Scheme and picture of the μ Cavity. The length of the cavity is adjusted with the help of ormlu of 0.2 mm (*chrysocale* in french).

D | Useful mathematical formula

D.1 Gauss integrals

$$\int_{\mathbb{R}} e^{-ax^2+bx} dx = \sqrt{\frac{\pi}{a}} e^{b^2/4a} \quad (4.1)$$

$$\int_{\mathbb{R}} x^2 e^{-ax^2+bx} dx = \left(\frac{1}{2a} + \frac{b^2}{4a^2} \right) \int_{\mathbb{R}} e^{-ax^2+bx} dx \quad (4.2)$$

$$\int \frac{1}{\sqrt{2\pi}\sigma_0} x^4 e^{-x^2/2\sigma_0^2} = 3\sigma_0^4 \quad (4.3)$$

D.2 Laguerre polynomial

$$L_n^\alpha(x) = \sum_{i=0}^n (-1)^i \binom{n+\alpha}{n-i} \frac{x^i}{i!} \quad (4.4)$$

$$L_n^\alpha(x) = \frac{\alpha+1-x}{n} L_{n-1}^{\alpha+1} - \frac{x}{n} L_{n-1}^{\alpha+2}(x) \quad (4.5)$$

$$L_l^{k-l}(x) = \frac{k-l+1-x}{l} L_{l-1}^{k-(l-1)} - \frac{x}{l} L_{l-2}^{k-(l-2)}(x) \quad (4.6)$$

with $L_0^k = 1$, $L_1^{k-l} = -x + (k-1) + 1$. This way we have a recurrence relation on l only for each k

D.3 Hermite polynomials (*physicist version*)

This is the definition we use in the whole manuscript

$$H_{n+1}(x) = 2xH_n(x) - 2nH_{n-1}(x) \quad (4.7)$$

with $H_0(x) = 1$, $H_1(x) = 2x$, $H_2(x) = 4x^2 - 2$

E | Entanglement

The entanglement is a tricky property. Indeed, it is not only intrinsic to the state but also to the basis we use to describe it. We review in the following the usually used quantity to prove entanglement.

E.1 PPT criterion

The PPT criterion from Peres and Horodecki [91, 41] gives a necessary condition for separability. If we consider $\hat{\rho}$ a bi-partite state on mode A and B and one of its partial transpose¹ we have

$$\begin{aligned} \text{If } \hat{\rho}^{TA} \not\geq 0, \text{ the state } \hat{\rho} \text{ is entangled,} \\ \text{Any separable state has a positive partial transpose.} \end{aligned} \quad (5.1)$$

For small spaces $\mathcal{H}_2 \otimes \mathcal{H}_2$ and $\mathcal{H}_2 \otimes \mathcal{H}_3$ this condition is sufficient. For larger space, the condition is not sufficient: some entangled states can have a positive partial transpose.

E.2 Von Neumann entropy

The von Neumann entropy is defined by

$$S(\rho) = -\text{Tr}[\rho \log \rho] \quad (5.2)$$

and with the eigenvalues λ_i for ρ

$$S(\rho) = -\sum_i \lambda_i \log \lambda_i \quad (5.3)$$

This criteria is not often use for experimental demonstration as it is only appropriate to pure states.

E.3 Concurrence

The concurrence has been first designed for qubit entanglement [36, 120] (i.e. two Hilbert spaces each of dimension 2)

$$\mathcal{C}(\hat{\rho}) = \max(0, \lambda_1 - \lambda_2 - \lambda_3 - \lambda_4) , \quad (5.4)$$

where $\lambda_1, \lambda_2, \dots$ are the eigenvalues in the decreasing order of the matrix

$$R = \sqrt{\sqrt{\hat{\rho}} \tilde{\rho} \sqrt{\hat{\rho}}} , \quad (5.5)$$

¹ we remind that for a state $\hat{\rho} = \sum_{ijkl} |i\rangle\langle j|_A \otimes |k\rangle\langle l|_B$ its partial transpose on mode B is $\hat{\rho}^{TB} = \sum_{ijkl} |i\rangle\langle j|_A \otimes |l\rangle\langle k|_B$ (inversion of index k and l). Being partial, the symbol of transposition is sometimes noted Γ_B (a half of T).

with

$$\tilde{\rho} = (\sigma_y \otimes \sigma_y) \hat{\rho}^* (\sigma_y \otimes \sigma_y) \quad (5.6)$$

Another possible formulation but only valid for pure state is

$$C(|\psi\rangle) = \sqrt{1 - \text{Tr } \hat{\rho}_r^2} \quad (5.7)$$

where $\hat{\rho}_r$ is the density matrix of the state reduced by a tracing over one mode. This can be understand in the following way: the trace of the squared matrix correspond to the purity. Hence, if a state is separable the trace over one mode let the purity of the other equal to one, on the contrary if the state is entangled the trace over one mode yields to a statistical mixture for which the purity is small if the state is strongly mixed.

This can be generalized to spaces larger than qubit [100, 70, 31]

$$C(|\psi\rangle) = \sqrt{\frac{d}{d-1} (1 - \text{Tr } \hat{\rho}_r^2)} \quad (5.8)$$

and d the dimension of each party. The additional factor allows to keep the concurrence between 0 and 1. And generalized to mixed state by a convex roof

$$C(\hat{\rho}) = \min \sum_i p_i C(|\psi_i\rangle) \quad (5.9)$$

where the minimization is over all the possible decompositions of the state like $\hat{\rho} = \sum_i p_i |\psi_i\rangle \langle \psi_i|$.

E.4 Negativity

The *negativity* is also a measure of entanglement [117]. For a two-mode density matrix, it is defined by:

$$\mathcal{N}(\rho) = \frac{\|\hat{\rho}^{T_A}\|_1 - 1}{2}, \quad (5.10)$$

where T_A is the partial transpose in the subspace A et $\|X\|_1 = \text{Tr } |X| = \text{Tr } \sqrt{X^\dagger X}$ is the *trace norm*. An alternative expression is

$$\mathcal{N}(\hat{\rho}) = \frac{1}{2} \sum_i |\lambda_i| - \lambda_i, \quad (5.11)$$

with λ_i are the eigenvalues of the partial transpose. This formulation makes sense in the light of of the PPT criterion: a separable state having positive eigenvalues we measure how far the state is from this property.

This criterion is convex

$$\mathcal{N}(\sum p_i \hat{\rho}_i) \leq \sum p_i \mathcal{N}(\hat{\rho}_i), \quad (5.12)$$

and entanglement monotone

$$\mathcal{N}(P(\hat{\rho})) \leq \mathcal{N}(\hat{\rho}), \quad (5.13)$$

where P is LOOC (*Local Operations and Classical Communication*). In other words, this measure of entanglement cannot be increased with local operations.

A logarithmic version is also used [2, 92]:

$$E_N(\hat{\rho}) = \log_2 \|\rho^{T_A}\|_1 = \log_2(2\mathcal{N} + 1). \quad (5.14)$$

Note that for a system of qubit the logarithmic negativity cannot exceed 1 (or 0.5 for the negativity). However, we have equality when the state is maximally entangled. In contrast, with a two-mode squeezed vacuum, each mode lies in a Hilbert space of dimension above 2. Depending on the squeezing parameter, the state can show values of negativity above 0.5.

F | Acquisition and interface

What is the best strategy? Most of the time we have to deal with a compromise between the time needed to implement the acquisition system and how long this system will be useful. Nowadays, the possibilities of measurement acquisition are numerous and develop extremely fast. Thus, trying to find the best one can be extremely time consuming and true only few years. In our experiment, we need a good time resolution typically above 1GS/s, and with many channels. Therefore, an oscilloscope with integrated computer is preferred to an acquisition card integrated in a computer.

We have used some oscilloscopes from LeCroy. One of their strong advantage compared to others, is the speed of data transfer. In our case, this is not critical but, we can think that in the future experiments it could become necessary. We have developed two interfaces: one directly in the oscilloscope's computer (this is the fastest mode) and one via LAN communication.

F.1 Single-oscilloscope configuration

The data can be loaded with two strategies. The main difference between the two is the speed of the data transfer. The first one called "fastWaveform" (and later "multifastwaveform" for more than one channel) uses a shared memory managed by the operating system (here Windows) this strongly minimized the time of data transfer, actually probably the fastest solution. (The used shared memory is synchronized with the two processes by mutual exclusion *mutex*.)

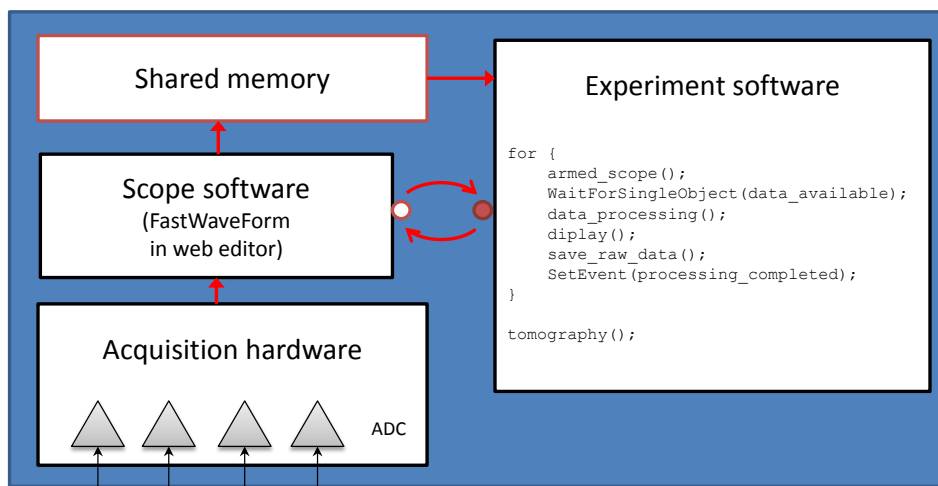


Figure 6.1: Single mode experiment. The data are transferred in a shared memory.

F.2 Two-oscilloscope configuration

The other possibility is to use a LAN connection. As we need more signals in the last experiment (chapter 8), we have used this technique. There are actually many libraries for this purpose, in particular, one for LeCroy but it requires to use additional libraries specific to Microsoft. Here, we use a library downloaded from internet “VICPClient.h” (sourceforge). This is a low-level input/output (quest/answer) of communication with a LeCroy oscilloscope. We have extended it with the library “dso.h”. This latter library manages some memories to load the contents of the different channels of the oscilloscope, save the raw data, and read back the data (for additional post-processings). In contrast to the previous configuration, the speed of data transfer is obviously slower.

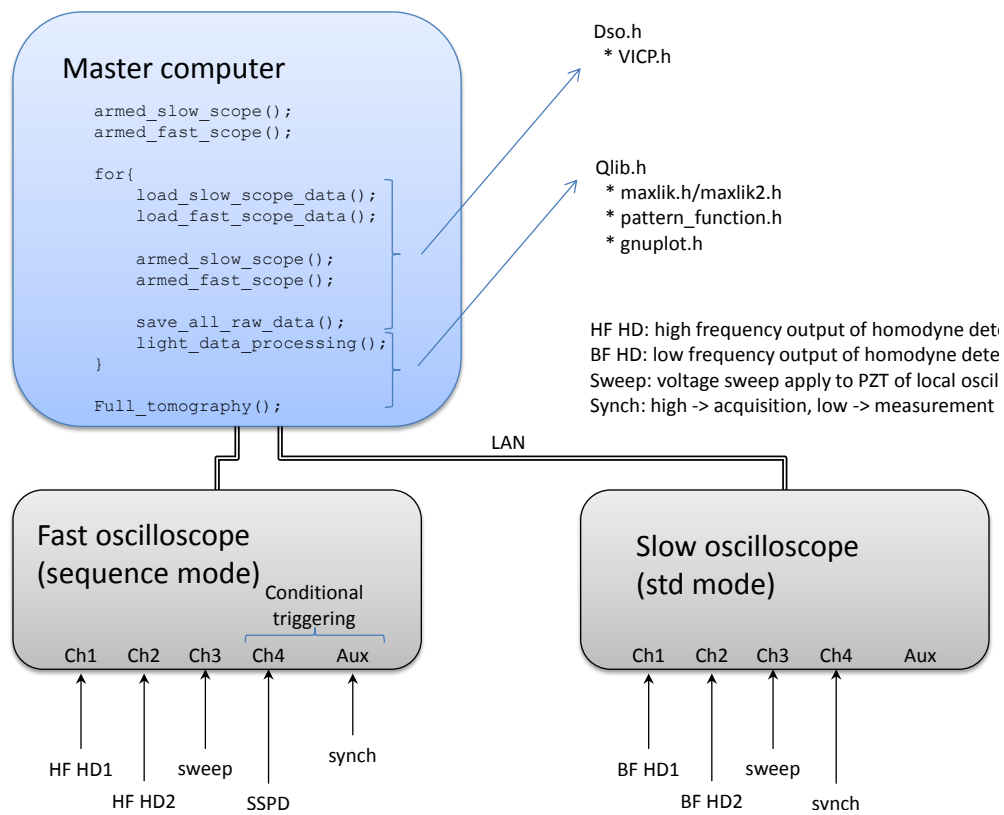


Figure 6.2: Acquisition setup for two-mode tomography (cf chapter 8)

As depicted on figure 6.2, the two oscilloscopes are controlled by a master computer.

G.1 Homodyne data simulation

The ability to simulate the measurement can be convenient mainly for two purposes. First, to test the reliability of the data processing. Secondly, to evaluate the accuracy of the reconstruction methods.

The goal is to generate some random numbers following a given probability distribution $\mathcal{P}(x, \theta) = |\langle x, \theta | \psi \rangle|^2$ (marginal distribution). Basically, a computer provides a random number generator equally distributed (which can be rescaled to the interval $[0, 1]$). The question is how to use this number generator to obtain the targeted marginal distribution? Starting from this, some efficient formulas exist for some particular case like the Gaussian distribution.

In all the other cases, we use the following method. Let us note Y the generated number from the computer's random number generator (equally distributed between 0 and 1) and X the random number following the distribution $f(x)$. Hence, we have the number X such

$$\int_{-\infty}^X f(x) dx = Y.$$

Note that computing the integral for each random number is potentially heavy! The trick is thus to compute once the distribution $\int_{-\infty}^x f(x) dx = y$. Therefore, the sampling dx small enough to assume a good accuracy, the interval X_{min}, X_{max} large enough, and the dy depending on the chosen resolution of the simulated measurement.

The two-mode case is a little bit trickiest. Indeed we need at least one local distribution probability but also the joint distribution probability. Below we give the corresponding formula for the single-photon entanglement. For the joint probability we have

$$\mathcal{P}(x_a, \theta_a, x_b, \theta_b) = \left| \langle x_a, \theta_a | \langle x_b, \theta_b | \frac{|0\rangle|1\rangle + |1\rangle|0\rangle}{\sqrt{2}} \right|^2 \quad (7.1)$$

$$= \frac{1}{4\pi\sigma_0^4} e^{-x_a^2/2\sigma_0^2 - x_b^2/2\sigma_0^2} [x_a^2 + x_b^2 + 2x_a x_b \cos(\theta_a - \theta_b)] \quad (7.2)$$

$$= \frac{e^{-x_a^2/2\sigma_0^2} e^{-x_b^2/2\sigma_0^2}}{\sqrt{2\pi\sigma_0^2} \sqrt{2\pi\sigma_0^2}} \left[\frac{x_a^2}{2\sigma_0^2} + \frac{x_b^2}{2\sigma_0^2} + \frac{x_a x_b}{\sigma_0 \sigma_0} \cos(\theta_a - \theta_b) \right]. \quad (7.3)$$

For the local probability

$$\mathcal{P}(x_a, \theta_a) = \int_{\mathbb{R}} dx_b \mathcal{P}(x_a, \theta_a, x_b, \theta_b) \quad (7.4)$$

$$= \frac{e^{-x_a^2/2\sigma_0^2}}{\sqrt{2\pi\sigma_0^2}} \left[\frac{1}{2} + \frac{x_a^2}{2\sigma_0^2} \right]. \quad (7.5)$$

Of course, we always have the probability conservation

$$\int_{\mathbb{R}} \int_{\mathbb{R}} dx_a dx_b \mathcal{P}(x_a, \theta_a, x_b, \theta_b) = 1 \quad (7.6)$$

Hence, we generate the random measurement by first ,generating the result X_a for a given phase θ_a thanks to the local probability distribution, and then the random measurement X_b for a given phase θ_b by using the distribution probability $\mathcal{P}(X_a, \theta_a, x_b, \theta_b)$ (one would have notice that only x_b is not fixed).

G.2 MaxLik in practice

In contrast to the other methods of reconstruction, it is necessary with MaxLik to make a choice for the value of the different parameters: the size of the Hilbert space, the number of iterations.

We start from N measurements $\{x_k, \theta_k\}$, depending on the sampling, the measurement results can be packed and associated with a frequency $\{f_i, x_i, \theta_i\}$ with f_i the frequency of the result i (if we obtain n_i times the results $\{x_i, \theta_i\}$ among a total number of N measurements $f_i = n_i/N$). In this case, the number of measurement is almost fixed. Indeed, the measurements are expected to be in $[x_{min}; x_{max}]$ and this interval is divided into N_x bins. The same for the phase: we divided it into N_θ , we thus obtain $N_x \cdot N_\theta$ measurements. However, this only speed up the algorithm if $N_x \cdot N_\theta < N$. In our experiments, speed of reconstruction was not an important criteria, thus we did not use this latter solution.

However, if implemented “brutally”, the algorithm can be heavy: with a never-ending time of computation! Hence, the goal is to take advantage of the various mathematical properties and recurrence relation to save the number of operation. For instance, we have used the following tricks to speed up the computation:

- we store all the calculated projectors and thus do not compute it for each iteration,
- the off-diagonal elements of the matrix product are not calculated when we want only the trace of this product for instance for the probability $p_i = \text{Tr}[\hat{\Pi}_i \hat{\rho}]$,
- we only compute the upper half elements of the matrix the other part being by definition complex conjugate (all the matrix are Hermitian),
- in order to compute faster the projectors we also have taken advantages of the recurrence relations

$$\langle n' | \hat{E}_\eta(\theta, x) | m' \rangle = \sum_{k > m', n'} B_{m', m'-k}(\eta) B_{n', n'-k}(\eta) \hat{\Pi}_{n'-k, m'-k}, \quad (7.7)$$

with

$$B_{n', n'-k+1} = \sqrt{\frac{k}{n' - k + 1} \frac{\eta}{1 - \eta}} B_{n', n'-k}, \quad (7.8)$$

and the initialization

$$B_{n', 0} = \sqrt{(1 - \eta)^{n'}}. \quad (7.9)$$

If we count the number of operation for on iteration of the algorithm, we find almost the following scale law in time

$$time \propto N_{Fock}^2 \cdot N_{data}. \quad (7.10)$$

This is confirmed by figure 7.1. Moreover, if we consider two modes of size each N_{Fock1} , N_{Fock2} , this is equivalent to work with a matrix of size $N_{Fock'} = N_{Fock1} N_{Fock2}$.

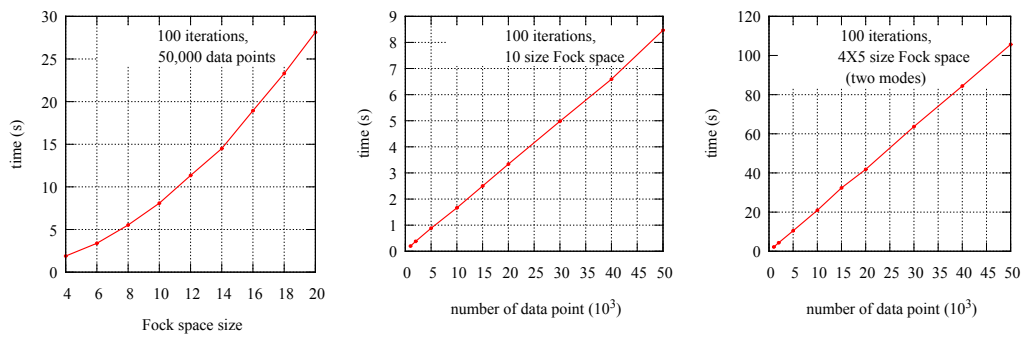


Figure 7.1: Scaling factor in time for the different parameters. Left, in function of the size of the Fock space, middle, versus the number of data point, Right, as before but for two-mode states. (Core 2 Duo, 2.53 GHz)

Bibliography

- [1] Ulrik L Andersen and Jonas S Neergaard-Nielsen. Heralded generation of a micro-macro entangled state. *Physical Review A*, 88(2):022337, 2013.
- [2] K. Audenaert, M. B. Plenio, and J. Eisert. Entanglement cost under positive-partial-transpose-preserving operations. *Phys. Rev. Lett.*, 90:027901, Jan 2003.
- [3] S. A. Babichev, J. Appel, and A. I. Lvovsky. Homodyne tomography characterization and nonlocality of a dual-mode optical qubit. *Phys. Rev. Lett.*, 92:193601, May 2004.
- [4] Hans-A Bachor and Timothy C Ralph. A guide to experiments in quantum optics, 2nd. *A Guide to Experiments in Quantum Optics, 2nd, Revised and Enlarged Edition, by Hans-A. Bachor, Timothy C. Ralph, pp. 434. ISBN 3-527-40393-0. Wiley-VCH, March 2004.*, 1, 2004.
- [5] S.M. Barnett and PM Radmore. *Methods in theoretical quantum optics*. Oxford University Press, USA, 1997.
- [6] D.W. Berry and A.I. Lvovsky. Linear-optical processing cannot increase photon efficiency. *Physical review letters*, 105(20):203601, 2010.
- [7] Erwan Bimbard, Nitin Jain, Andrew MacRae, and AI Lvovsky. Quantum-optical state engineering up to the two-photon level. *Nature Photonics*, 4(4):243–247, 2010.
- [8] Gunnar Björk, Per Jonsson, and Luis L. Sánchez-Soto. Single-particle nonlocality and entanglement with the vacuum. *Phys. Rev. A*, 64:042106, Sep 2001.
- [9] J. B. Brask, I. Rigas, E. S. Polzik, U. L. Andersen, and A. S. Sørensen. Hybrid long-distance entanglement distribution protocol. *Phys. Rev. Lett.*, 105:160501, Oct 2010.
- [10] G.S. Buller and R.J. Collins. Single-photon generation and detection. *Meas. Sci. Technol*, 21(1):012002, 2010.
- [11] Kyung Soo Choi, Hui Deng, Julien Laurat, and HJ Kimble. Mapping photonic entanglement into and out of a quantum memory. *Nature*, 452(7183):67–71, 2008.
- [12] Chin-Wen Chou, H De Riedmatten, D Felinto, SV Polyakov, SJ Van Enk, and H Jeff Kimble. Measurement-induced entanglement for excitation stored in remote atomic ensembles. *Nature*, 438(7069):828–832, 2005.
- [13] John F. Clauser, Michael A. Horne, Abner Shimony, and Richard A. Holt. Proposed experiment to test local hidden-variable theories. *Phys. Rev. Lett.*, 23:880–884, Oct 1969.
- [14] R. Courant and D. Hilbert. *Methods of Mathematical Physics Volume 1*. Interscience Publishers, Inc., New York, 1966.
- [15] M. Dakna, T. Anhut, T. Opatrný, L. Knöll, and D.-G. Welsch. Generating schrödinger-cat-like states by means of conditional measurements on a beam splitter. *Phys. Rev. A*, 55:3184–3194, Apr 1997.

-
- [16] Virginia D’Auria, Olivier , Claude Fabre, and Julien Laurat. Effect of the heralding detector properties on the conditional generation of single-photon states. *The European Physical Journal D*, 66(10):1–7, 2012.
- [17] Virginia D’Auria, Noriyuki Lee, Taoufik Amri, Claude Fabre, and Julien Laurat. Quantum decoherence of single-photon counters. *Physical Review Letters*, 107(5):050504, 2011.
- [18] Samuel Deleglise, Igor Dotsenko, Clement Sayrin, Julien Bernu, Michel Brune, Jean-Michel Raimond, and Serge Haroche. Reconstruction of non-classical cavity field states with snapshots of their decoherence. *Nature*, 455(7212):510–514, 2008.
- [19] P. D. Drummond and M. D. Reid. Correlations in nondegenerate parametric oscillation. ii. below threshold results. *Phys. Rev. A*, 41:3930–3949, Apr 1990.
- [20] L.-M. Duan, M.D. Lukin, J. Ignacio Cirac, and Peter Zoller. Long-distance quantum communication with atomic ensembles and linear optics. *Nature*, 414(6862):413–418, 2001.
- [21] D. Felinto, C. W. Chou, J. Laurat, E. W. Schomburg, H. de Riedmatten, and H. J. Kimble. Conditional control of the quantum states of remote atomic memories for quantum networking. *Nature Phys.*, 2:841, 2006.
- [22] Alessandro Ferraro, Stefano Olivares, and Matteo G. A. Paris. Gaussian states in continuous variable quantum information. [arXiv: 0503237v1](https://arxiv.org/abs/0503237v1), Mar 2005.
- [23] Jaromír Fiurášek. Improving the fidelity of continuous-variable teleportation via local operations. *Physical Review A*, 66(1):012304, 2002.
- [24] Simon Fossier, Eleni Diamanti, Thierry Debuisschert, André Villing, Rosa Tualle-Brouri, and Philippe Grangier. Field test of a continuous-variable quantum key distribution prototype. *New Journal of Physics*, 11(4):045023, 2009.
- [25] Akira Furusawa and Peter Van Loock. *Quantum teleportation and Entanglement*. Wiley. com, 2011.
- [26] Crispin Gardiner and Peter Zoller. *Quantum noise: a handbook of Markovian and non-Markovian quantum stochastic methods with applications to quantum optics*, volume 56. Springer, 2004.
- [27] C.C. Gerry and P.L. Knight. Quantum superpositions and schrödinger cat states in quantum optics. *American Journal of Physics*, 65:964, 1997.
- [28] A. Gilchrist, Kae Nemoto, William J. Munro, T.C. Ralph, S. Glancy, Samuel L. Braunstein, and G.J. Milburn. Schrödinger cats and their power for quantum information processing. *Journal of Optics B: Quantum and Semiclassical Optics*, 6(8):S828, 2004.
- [29] Nicolas Gisin and Rob Thew. Quantum communication. *Nature Photonics*, 1(3):165–171, 2007.
- [30] Yan-Xiao Gong, Xu-Bo Zou, Timothy C Ralph, Shi-Ning Zhu, and Guang-Can Guo. Linear optical quantum computation with imperfect entangled photon-pair sources and inefficient non-photon-number-resolving detectors. *Physical Review A*, 81(5):052303, 2010.
- [31] Gilad Gour. Family of concurrence monotones and its applications. *Phys. Rev. A*, 71:012318, Jan 2005.

- [32] Otfried Gühne and Géza Tóth. Entanglement detection. *Physics Reports*, 474(1):1–75, 2009.
- [33] Robert H Hadfield. Single-photon detectors for optical quantum information applications. *Nature Photonics*, 3(12):696–705, 2009.
- [34] Serge Haroche and Jean-Michel Raimond. *Exploring the Quantum : Atoms, Cavities, and Photons*. Oxford University Press, USA, 2006.
- [35] Björn Hessmo, Pavel Usachev, Hoshang Heydari, and Gunnar Björk. Experimental demonstration of single photon nonlocality. *Phys. Rev. Lett.*, 92:180401, May 2004.
- [36] Scott Hill and William K. Wootters. Entanglement of a pair of quantum bits. *Phys. Rev. Lett.*, 78:5022–5025, Jun 1997.
- [37] Philip CD Hobbs. Photodiode front ends: The real story. *Optics and Photonics News*, 12(4):44–47, 2001.
- [38] Philip CD Hobbs. *Building electro-optical systems: making it all work*, volume 71. Wiley. com, 2011.
- [39] David Höckel, Lars Koch, and Oliver Benson. Direct measurement of heralded single-photon statistics from a parametric down-conversion source. *Phys. Rev. A*, 83:013802, Jan 2011.
- [40] C. K. Hong and L. Mandel. Experimental realization of a localized one-photon state. *Phys. Rev. Lett.*, 56:58–60, Jan 1986.
- [41] Michał Horodecki, Paweł Horodecki, and Ryszard Horodecki. Separability of mixed states: necessary and sufficient conditions. *Physics Letters A*, 223(1):1–8, 1996.
- [42] S.R. Huisman, Nitin Jain, S.A. Babichev, Frank Vewinger, A.N. Zhang, S.H. Youn, and A.I. Lvovsky. Instant single-photon fock state tomography. *Optics letters*, 34(18):2739–2741, 2009.
- [43] H. Jeong and M. S. Kim. Efficient quantum computation using coherent states. *Phys. Rev. A*, 65:042305, Mar 2002.
- [44] Hyunseok Jeong. Using weak nonlinearity under decoherence for macroscopic entanglement generation and quantum computation. *Phys. Rev. A*, 72:034305, Sep 2005.
- [45] Richard Jozsa. Fidelity for mixed quantum states. *Journal of Modern Optics*, 41(12):2315–2323, 1994.
- [46] H.J. Kimble. The quantum internet. *Nature*, 453(7198):1023–1030, 2008.
- [47] Emanuel Knill, Raymond Laflamme, and Gerald J Milburn. A scheme for efficient quantum computation with linear optics. *nature*, 409(6816):46–52, 2001.
- [48] Pieter Kok, William J Munro, Kae Nemoto, Timothy C Ralph, Jonathan P Dowling, and GJ Milburn. Linear optical quantum computing with photonic qubits. *Reviews of Modern Physics*, 79(1):135, 2007.
- [49] Ranjeet Kumar, Erick Barrios, Andrew MacRae, AI Lvovsky, E Cairns, and EH Huntington. Versatile wideband balanced detector for quantum optical homodyne tomography. *Optics Communications*, 285(24):5259–5267, 2012.

- [50] Hudson R. L. When is the wigner quasi-probability density non-negative? *Report on Mathematical Physics*, 6:249, Jun 1974.
- [51] J. Laurat, K. S. Choi, H. Deng, C. W. Chou, and H. J. Kimble. Heralded entanglement between atomic ensembles: Preparation, decoherence, and scaling. *Phys. Rev. Lett.*, 99:180504, Nov 2007.
- [52] J. Laurat, H. de Riedmatten, D. Felinto, C.W. Chou, E.W. Schomburg, and H.J. Kimble. Efficient retrieval of a single atomic excitation stored in an atomic ensemble. *Physical Review A*, 70(4):042315, 2004.
- [53] Julien LAURAT. *Etats non-classiques et intrication en variables continues à l'aide d'un oscillateur paramétrique optique*. PhD thesis, Université Paris VI, 2004. [tel-00007442](tel:00007442).
- [54] Michel Le Bellac. *Quantum physics*. Cambridge University Press, 2006.
- [55] KC Lee, MR Sprague, BJ Sussman, J Nunn, NK Langford, X-M Jin, T Champion, P Michelberger, KF Reim, D England, et al. Entangling macroscopic diamonds at room temperature. *Science*, 334(6060):1253–1256, 2011.
- [56] Seung-Woo Lee and Hyunseok Jeong. Near-deterministic quantum teleportation and resource-efficient quantum computation using linear optics and hybrid qubits. *Physical Review A*, 87(2):22326, 2013.
- [57] U. Leonhardt and M. Munroe. Number of phases required to determine a quantum state in optical homodyne tomography. *Phys. Rev. A*, 54:3682–3684, Oct 1996.
- [58] U. Leonhardt, H. Paul, and G. M. D’Ariano. Tomographic reconstruction of the density matrix via pattern functions. *Phys. Rev. A*, 52:4899–4907, Dec 1995.
- [59] Ulf Leonhardt. *Measuring the Quantum State of Light*. Cambridge University Press, 1997.
- [60] A.P. Lund, T.C. Ralph, and H.L. Haselgrove. Fault-tolerant linear optical quantum computing with small-amplitude coherent states. *Physical review letters*, 100(3):030503, 2008.
- [61] N. Lütkenhaus and Stephen M. Barnett. Nonclassical effects in phase space. *Phys. Rev. A*, 51:3340–3342, Apr 1995.
- [62] A. I. Lvovsky and M. G. Raymer. Continuous-variable optical quantum-state tomography. *Rev. Mod. Phys.*, 81:299–332, Mar 2009.
- [63] AI Lvovsky. Iterative maximum-likelihood reconstruction in quantum homodyne tomography. *Journal of Optics B: Quantum and Semiclassical Optics 6 (2004) S556–S559*, 2003. [arXiv: quant-ph/0311097v2](https://arxiv.org/abs/quant-ph/0311097v2).
- [64] Alexander I Lvovsky, Hauke Hansen, T Aichele, O Benson, J Mlynek, and S Schiller. Quantum state reconstruction of the single-photon fock state. *Physical Review Letters*, 87(5):050402, 2001.
- [65] Alexander I Lvovsky and Michael G Raymer. Continuous-variable optical quantum-state tomography. *Reviews of Modern Physics*, 81(1):299, 2009.
- [66] A. Mandilara, E. Karpov, and N. J. Cerf. Extending hudson’s theorem to mixed quantum states. *Phys. Rev. A*, 79:062302, Jun 2009.

- [67] Petr Marek and Jaromír Fiurášek. Elementary gates for quantum information with superposed coherent states. *Physical Review A*, 82(1):014304, 2010.
- [68] A. Mari and J. Eisert. Positive wigner functions render classical simulation of quantum computation efficient. *Phys. Rev. Lett.*, 109:230503, Dec 2012.
- [69] F Marsili, VB Verma, JA Stern, S Harrington, AE Lita, T Gerrits, I Vayshenker, B Baek, MD Shaw, RP Mirin, et al. Detecting single infrared photons with 93% system efficiency. *Nature Photonics*, 7(3):210–214, 2013.
- [70] Florian Mintert, Marek Kuś, and Andreas Buchleitner. Concurrence of mixed bipartite quantum states in arbitrary dimensions. *Phys. Rev. Lett.*, 92:167902, Apr 2004.
- [71] Yoshichika Miwa, Jun-ichi Yoshikawa, Noriaki Iwata, Mamoru Endo, Petr Marek, Radim Filip, Peter van Loock, and Akira Furusawa. Unconditional conversion between quantum particles and waves. *arXiv preprint arXiv:1209.2804*, 2012.
- [72] K. Mølmer. Non-Gaussian states from continuous-wave Gaussian light sources. *Physical Review A*, 73(6):63804, 2006. [arXiv: quant-ph/0602202v1](https://arxiv.org/abs/quant-ph/0602202v1).
- [73] Olivier Morin, Jean-Daniel Bancal, Melvyn Ho, Pavel Sekatski, Virginia D’Auria, Nicolas Gisin, Julien Laurat, and Nicolas Sangouard. Witnessing trustworthy single-photon entanglement with local homodyne measurements. *Phys. Rev. Lett.*, 110:130401, Mar 2013.
- [74] Olivier Morin, Virginia D’Auria, Claude Fabre, and Julien Laurat. High-fidelity single-photon source based on a type ii optical parametric oscillator. *Opt. Lett.*, 37:3738–3740, Sep 2012.
- [75] Olivier Morin, Claude Fabre, and Julien Laurat. Experimentally accessing the optimal temporal mode of traveling quantum light states. *Phys. Rev. Lett.*, 111:213602, Nov 2013.
- [76] Olivier Morin, Kun Huang, Jianli Liu, Hanna Le Jeannic, Claude Fabre, and Julien Laurat. Remote creation of hybrid entanglement between particle-like and wave-like optical qubits. *arXiv preprint arXiv:1309.6191*, 2013.
- [77] M. Munroe, D. Boggavarapu, M. E. Anderson, and M. G. Raymer. Photon-number statistics from the phase-averaged quadrature-field distribution: Theory and ultrafast measurement. *Phys. Rev. A*, 52:R924–R927, Aug 1995.
- [78] J. S. Neergaard-Nielsen, B. Melholt Nielsen, C. Hettich, K. Mølmer, and E. S. Polzik. Generation of a superposition of odd photon number states for quantum information networks. *Phys. Rev. Lett.*, 97:083604, Aug 2006.
- [79] J.S. Neergaard-Nielsen, B. Meholt Nielsen, H. Takahashi, A.I. Vistnes, and E.S. Polzik. High purity bright single photon source. *Optics Express*, 15:7940–7949, 2007.
- [80] Jonas Schou Neergard-Nielsen. *Generation of single photons and Schrödinger kitten states of light*. PhD thesis, University of Copenhagen, 2008. <http://www.nbi.ku.dk/forskningsgrupper/Kvanteoptik/english/qoptlab>.
- [81] Anne E. B. Nielsen and Klaus Mølmer. Photon number states generated from a continuous-wave light source. *Phys. Rev. A*, 75:043801, Apr 2007.

- [82] Anne E. B. Nielsen and Klaus Mølmer. Single-photon-state generation from a continuous-wave nondegenerate optical parametric oscillator. *Phys. Rev. A*, 75:023806, Feb 2007.
- [83] Anne E. B. Nielsen and Klaus Mølmer. Transforming squeezed light into a large-amplitude coherent-state superposition. *Phys. Rev. A*, 76:043840, Oct 2007.
- [84] B Melholt Nielsen, JS Neergaard-Nielsen, and Eugene Simon Polzik. Time gating of heralded single photons for atomic memories. *Optics letters*, 34(24):3872–3874, 2009.
- [85] Michael A. Nielsen and Isaac L. Chuang. *Quantum computation and quantum information*. Cambridge university press, 2010.
- [86] Jeremy L O’Brien and Jelena Vučković and Akira Furusawa. Photonic quantum technologies. *Nature Photonics*, 3(12):687–695, 2009.
- [87] Alexei Ourjoumtsev, Franck Ferreyrol, Rosa Tualle-Brouri, and Philippe Grangier. Preparation of non-local superpositions of quasi-classical light states. *Nature Physics*, 5(3):189–192, 2009.
- [88] Alexei Ourjoumtsev, Rosa Tualle-Brouri, and Philippe Grangier. Quantum homodyne tomography of a two-photon fock state. *Phys. Rev. Lett.*, 96:213601, Jun 2006.
- [89] Alexei Ourjoumtsev, Rosa Tualle-Brouri, Julien Laurat, and Philippe Grangier. Generating optical schrödinger kittens for quantum information processing. *Science*, 312(5770):83–86, 2006.
- [90] Kimin Park and Hyunseok Jeong. Entangled coherent states versus entangled photon pairs for practical quantum-information processing. *Physical Review A*, 82(6):062325, 2010.
- [91] Asher Peres. Separability criterion for density matrices. *Phys. Rev. Lett.*, 77:1413–1415, Aug 1996.
- [92] M. B. Plenio. Logarithmic negativity: A full entanglement monotone that is not convex. *Phys. Rev. Lett.*, 95:090503, Aug 2005.
- [93] C. Polycarpou, K. N. Cassemiro, G. Venturi, A. Zavatta, and M. Bellini. Adaptive detection of arbitrarily shaped ultrashort quantum light states. *Phys. Rev. Lett.*, 109:053602, Aug 2012.
- [94] Marco Túlio Quintino, Mateus Araújo, Daniel Cavalcanti, Marcelo França Santos, and Marcelo Terra Cunha. Maximal violations and efficiency requirements for bell tests with photodetection and homodyne measurements. *Journal of Physics A: Mathematical and Theoretical*, 45(21):215308, 2012.
- [95] T. C. Ralph, A. Gilchrist, G. J. Milburn, W. J. Munro, and S. Glancy. Quantum computation with optical coherent states. *Phys. Rev. A*, 68:042319, Oct 2003.
- [96] Tim C Ralph and Geoff J Pryde. Optical quantum computation. *Progress in Optics*, 54:209–269, 2010.
- [97] Peter P. Rohde, Timothy C. Ralph, and Michael A. Nielsen. Optimal photons for quantum-information processing. *Phys. Rev. A*, 72:052332, Nov 2005.
- [98] Jonathan Roslund, Renné Medeiros De Araujo, Shifeng Jiang, Claude Fabre, and Nicolas Treps. Wavelength-multiplexed quantum networks with ultrafast frequency combs. *arXiv preprint arXiv:1307.1216*, 2013.

- [99] S. M. Roy. Multipartiteseparability inequalities exponentially stronger than local reality inequalities. *Phys. Rev. Lett.*, 94:010402, Jan 2005.
- [100] Pranaw Rungta, V. Bužek, Carlton M. Caves, M. Hillery, and G. J. Milburn. Universal state inversion and concurrence in arbitrary dimensions. *Phys. Rev. A*, 64:042315, Sep 2001.
- [101] Nicolas Sangouard, Christoph Simon, Hugues De Riedmatten, and Nicolas Gisin. Quantum repeaters based on atomic ensembles and linear optics. *Reviews of Modern Physics*, 83(1):33, 2011.
- [102] Nicolas Sangouard, Christoph Simon, Nicolas Gisin, Julien Laurat, Rosa Tualle-Brouri, and Philippe Grangier. Quantum repeaters with entangled coherent states. *JOSA B*, 27(6):A137–A145, 2010.
- [103] Nicolas Sangouard and Hugo Zbinden. What are single photons good for? *Journal of Modern Optics*, 59(17):1458–1464, 2012.
- [104] Masahide Sasaki and Shigenari Suzuki. Multimode theory of measurement-induced non-gaussian operation on wideband squeezed light: Analytical formula. *Phys. Rev. A*, 73:043807, Apr 2006.
- [105] Wolfgang P Schleich. *Quantum optics in phase space*. Wiley. com, 2011.
- [106] E. Schrödinger. *Naturwissenschaften*. 23, 807-812; 823- 828; 844-849 (1935).
- [107] A.K. Pati S.L. Braunstein. *Quantum Information with Continuous Variables*. Springer, 2003.
- [108] Hiroki Takahashi, Kentaro Wakui, Shigenari Suzuki, Masahiro Takeoka, Kazuhiro Hayasaka, Akira Furusawa, and Masahide Sasaki. Generation of large-amplitude coherent-state superposition via ancilla-assisted photon subtraction. *Phys. Rev. Lett.*, 101:233605, Dec 2008.
- [109] N. Treps, V. Delaubert, A. Maître, J. M. Courty, and C. Fabre. Quantum noise in multipixel image processing. *Phys. Rev. A*, 71:013820, Jan 2005.
- [110] Imam Usmani, Christoph Clausen, Félix Bussièeres, Nicolas Sangouard, Mikael Afzelius, and Nicolas Gisin. Heralded quantum entanglement between two crystals. *Nature Photonics*, 6(4):234–237, 2012.
- [111] Steven J van Enk, Norbert Lütkenhaus, and H Jeff Kimble. Experimental procedures for entanglement verification. *Physical Review A*, 75(5):052318, 2007.
- [112] P. Van Loock, T.D. Ladd, K. Sanaka, F. Yamaguchi, Kae Nemoto, W.J. Munro, and Y. Yamamoto. Hybrid quantum repeater using bright coherent light. *Physical review letters*, 96(24):240501, 2006.
- [113] Peter van Loock. Optical hybrid approaches to quantum information. *Laser & Photonics Reviews*, 5(2):167–200, 2011.
- [114] Michael Varnava, Daniel E. Browne, and Terry Rudolph. How good must single photon sources and detectors be for efficient linear optical quantum computation? *Phys. Rev. Lett.*, 100:060502, Feb 2008.
- [115] Victor Veitch, Christopher Ferrie, David Gross, and Joseph Emerson. Negative quasi-probability as a resource for quantum computation. *New Journal of Physics*, 14(11):113011, 2012.

-
- [116] Victor Veitch, Nathan Wiebe, Christopher Ferrie, and Joseph Emerson. Efficient simulation scheme for a class of quantum optics experiments with non-negative wigner representation. *New Journal of Physics*, 15(1):013037, 2013.
- [117] G. Vidal and R. F. Werner. Computable measure of entanglement. *Phys. Rev. A*, 65:032314, Feb 2002.
- [118] Kentaro Wakui, Hiroki Takahashi, Akira Furusawa, and Masahide Sasaki. Photon subtracted squeezed states generated with periodically poled ktiopo. *Optics Express*, 15(6):3568–3574, 2007.
- [119] Christian Weedbrook, Stefano Pirandola, Raul Garcia-Patron, Nicolas J. Cerf, Timothy C. Ralph, Jeffrey H. Shapiro, and Seth Lloyd. Gaussian quantum information. *Rev. Mod. Phys.*, 84:621–669, May 2012.
- [120] William K. Wootters. Entanglement of formation of an arbitrary state of two qubits. *Phys. Rev. Lett.*, 80:2245–2248, Mar 1998.
- [121] William K Wootters and Wojciech H Zurek. A single quantum cannot be cloned. *Nature*, 299(5886):802–803, 1982.
- [122] Alessandro Zavatta, Valentina Parigi, and Marco Bellini. Toward quantum frequency combs: Boosting the generation of highly nonclassical light states by cavity-enhanced parametric down-conversion at high repetition rates. *Phys. Rev. A*, 78:033809, Sep 2008.
- [123] Alessandro Zavatta, Silvia Viciani, and Marco Bellini. Tomographic reconstruction of the single-photon fock state by high-frequency homodyne detection. *Physical Review A*, 70(5):053821, 2004.

Résumé

Dans ce travail de thèse nous nous sommes intéressés à une catégorie spécifique d'états quantiques de la lumière : les états non-gaussiens. Ces états ont la particularité de présenter des fonctions de Wigner à valeurs négatives. Cette propriété est indispensable pour réaliser des opérations de calcul quantique mais trouve aussi des applications variées en communication quantique ou métrologie par exemple.

Différentes stratégies peuvent être utilisées pour générer de tels états. Ici, les ressources initiales sont des états dit gaussiens produits par des oscillateurs paramétriques optiques en régime continu (i.e. vide comprimé bi-mode et mono-mode). Le caractère non-gaussien ne peut être obtenu que par des phénomènes non-linéaires (hamiltonien sur-quadratique). Dans notre cas, la non-linéarité est induite par des mesures basées sur le comptage de photon (aussi appelées mesures non-gaussiennes).

Cette étude est principalement divisée en deux parties. Tout d'abord, la génération d'états non-classiques correspondants à deux types d'encodages de qubits : le photon unique, utilisé en information quantique dite à variables discrètes, et la superposition d'états cohérents (chat de Schrödinger optique), utilisée en information quantique dite à variables continues. Ces états ont ensuite été utilisés pour mettre en œuvre deux protocoles d'information quantique. Le premier porte sur un témoin d'intrication en photon unique, l'autre sur la génération d'intrication entre deux types d'encodages (aussi appelée intrication hybride).

Mots clés

optique quantique; information quantique; photon unique; chat de Schrödinger; intrication hybride; tomographie quantique

Abstract

In the present PhD work, we focus on a specific class of quantum states of light: the non-Gaussian states. These states have the particularity of exhibiting Wigner functions with some negative values. This quantum feature is a necessary condition to perform some quantum computation task; furthermore it is also useful for various other applications, including quantum communication and metrology.

Different strategies can be used to generate these states. Here, we start from Gaussian states produced by optical parametric oscillators in the continuous wave regime, (i.e. single-mode and two-mode squeezed vacuum states). The non-Gaussian feature can only be obtained by non-linear phenomena (over-quadratic Hamiltonian). In our case, the non-linearity is induced by photon-counting-based measurements (also called non-Gaussian measurements).

This study is mainly divided into two parts. First, the generation of non-classical states associated with two types of qubit encoding: the single-photon state, used for quantum information with discrete variables, and the coherent state superposition (the so-called optical Schrödinger cat state), used for quantum information with continuous variables. These two states have then been used to perform some quantum information protocols. The first one addresses the problem of single-photon entanglement witness, and the other the generation of entanglement between the two encodings (also called hybrid entanglement).

Keywords

quantum optics; quantum information; single photon; Schrödinger's cat; hybrid entanglement; quantum tomography